MICROSTRUCTURE AND CORROSION PERFORMANCE OF EXCIMER LASER-MELTED AA2124-T4 ALUMINIUM ALLOY AND SiC$_P$/AA2124-T4 COMPOSITE

A thesis submitted to the University of Manchester

for the degree of Doctor of Philosophy

in the Faculty of Engineering and Physical Sciences

2015

Daishu Qian

School of Materials

Corrosion and Protection Centre

Contents

54,508 words

List of Abbreviation

BSE = Backscattered Electron

CW = Continuous Wave

EIS = Electrochemical Impedance Spectroscopy

FEM = Finite Element Model

HAADF = High-Angle Annular Dark-Field

LSM = Laser Surface Melting

MA = Monolithic Alloy

MMC = Metal Matrix Composite

NOP = Number of Pulses

OCP = Open Circuit Potential

P = Pulses

SE = Secondary Electron

SEM = Scanning Electron Microscopy

SKPFM = Scanning Kelvin Probe Force Microscopy

SPH = Smoothed-Particle Hydrodynamics

STEM = Scanning Transmission Electron Microscopy

TEM = Transmission Electron Microscopy

XRD = X-ray Diffraction

List of Tables

List of Figures

Abstract

The University of Manchester
Daishu Qian
Doctor of Philosophy
Microstructure and corrosion performance of excimer laser-melted AA2124-T4
aluminium alloy and SiC$_p$/AA2124-T4 composite
2015

The present work studies the microstructure and corrosion behaviour of 25 vol.% SiC$_p$/AA2124-T4 metal matrix composites (MMCs) and AA2124-T4 aluminium alloy; and also the capability of excimer laser surface melting (LSM) to improve the corrosion resistance of the SiC$_p$/AA2124 MMC and the monolithic alloy (MA).

Microstructural characterization has shown significant influence of the presence and size of SiC particles on the fine Al$_2$Cu precipitate and Mg segregation at SiC/Al interfacial regions. Such precipitates are revealed to be active sites for corrosion initiation in the MMCs, while the preferential sites for corrosion initiation in the MA are the coarse intermetallics. Corrosion evaluation performed in a 0.6 M NaCl solution suggests that the corrosion resistance of the MMC reinforced with micrometre-sized SiC particles is inferior to that of the MA and the MMC reinforced with submicrometre-sized SiC particles. The submicrometre-sized SiC particles have little adverse effect on the corrosion resistance of the MMC due to the reduced interfacial precipitates.

Thin films of up to several micrometres have been achieved by excimer LSM on both the MMC and the MA. The surface roughness and the thickness of the melted layer increase with increasing laser fluence. High number of pulses (40 P) results in significant porosity in the MA and networks of cracking in the MMC. A homogeneous layer without chemical segregation except the Cu-rich segregation bands has been obtained on the MA; while complex microstructures are observed for the MMC, including the Cu-rich segregation bands, Al-Si eutectic structure and microsegregation-free structure laid in sequence from the bottom of the melted layer to the top surface. The modelling work suggest that the presence of SiC particles gives rise in high temperatures in the melt pool, which is useful to explain the materials responses upon laser irradiation, such as decomposition of SiC, evaporation of matrix alloy, and oxides formation. The fast cooling rate up to 10^{11} K/s is responsible for the formation of microsegregation-free structure.

Corrosion evaluation has indicated improvement of corrosion resistance of the MMC and the MA after excimer LSM due to the reduction of the intermetallics. For the laser-melted MA, the corrosion behaviour is governed by the surface morphology and the porosity. The significant rippled structure obtained under high laser fluence could lead to crevice corrosion in the valley between the ripples whilst the pores could provide penetrating routes for the chloride solution to reach the Cu-rich segregation bands, leading to the delamination of the melted layer. For the laser-melted MMC, corrosion mainly initiated at the SiC remnants, which are rich in Si. The corrosion sites of the laser-melted MMC are in the form of small cracked blisters.

Declaration

No portion of the work referred to in this thesis has been submitted in support of an application for another degree or qualification of this or any other university or other institution of learning.

Copyright Statement

i. The author of this thesis (including any appendices and/or schedules to this thesis) owns certain copyright or related rights in it (the "Copyright") and s/he has given The University of Manchester certain rights to use such Copyright, including for administrative purposes.

ii. Copies of this thesis, either in full or in extracts and whether in hard or electronic copy, may be made only in accordance with the Copyright, Designs and Patents Act 1988 (as amended) and regulations issued under it or, where appropriate, in accordance with licensing agreements which the University has from time to time. This page must form part of any such copies made.

iii. The ownership of certain Copyright, patents, designs, trademarks and other intellectual property (the "Intellectual Property") and any reproductions of copyright works in the thesis, for example graphs and tables ("Reproductions"), which may be described in this thesis, may not be owned by the author and may be owned by third parties. Such Intellectual Property and Reproductions cannot and must not be made available for use without the prior written permission of the owner(s) of the relevant Intellectual Property and/or Reproductions.

iv. Further information on the conditions under which disclosure, publication and commercialisation of this thesis, the Copyright and any Intellectual Property and/or Reproductions described in it may take place is available in the University IP Policy (see http://documents.manchester.ac.uk/DocuInfo.aspx?DocID=487), in any relevant Thesis restriction declarations deposited in the University Library, The University Library's regulations (see http://www.manchester.ac.uk/library/aboutus/regulations) and in The University's policy on Presentation of Theses.

Acknowledgements

First of all, I would like to express my greatest gratitude and appreciation to my supervisor, Dr. Zhu Liu, for her kindness, patience and invaluable support and guidance throughout my PhD project.

I would like to thank Ms. Xiangli Zhong for the operation of Quanta 3D FIB, Mr. Teruo Hashimoto for the operation of Titan G2 80-200 S/TEM, and their assistant operation of Tecnai TF30 TEM.

I would like to thank Dr. Michele Curioni for his valuable discussion and advice on the electrochemical tests and analysis.

I would like to thank Dr. Christopher Wilkins for proof-reading my papers and posters and the precious advice he has provided throughout my study in Manchester.

Special thanks go to Dr. Yuanfeng Yang, Dr. Bing Liu, and Gaoxiang Cao, who gave me encouragement and cheered me up during the hard times. Thank my friends Wei Shi, Jiantao Qi, Pei He, Zheling Li, Xinxin Zhang, Yingwei Fan, Wu Wei and Gunan Shang for sharing so much happy time together. Also, thank all my colleagues and staff in the School of Materials for their support during my study.

I also would like to thank China Scholarship Council for the financial support.

Last but not least I would like to thank my family for their love and care, without whom I can hardly achieve all the progress. Also, thank my girlfriend who supported me a lot.

Publications

D.S. Qian, X.L. Zhong, T. Hashimoto, and Z. Liu, *Effect of reinforcements on the corrosion behaviour of SiC$_P$/AA2124 metal matrix composites*, Corrosion, 71 (2015), 1083-1092.

D.S. Qian, X.L. Zhong, T. Hashimoto, Y.Z. Yan, Z. Liu, *Effect of excimer laser surface melting on the corrosion performance of a SiC$_P$/Al metal matrix composite*, Applied Surface Science, 330 (2015), 280-291.

D.S. Qian, Z. Liu, *Comparative study of microstructural and corrosion characteristics of excimer laser-melted AA2124-T4 and AA6061-T4 alloys*, Materials Science Forum, 794-796 (2014), 235-240.

Chapter 1 Introduction

1.1 General background

Aluminium alloys have been widely used in aerospace, automotive and marine industries due to their light weight. Aluminium-based metal matrix composites (MMCs) are developed as a result of the requirement for mechanical properties superior to aluminium alloys. They involve aluminium alloys as the matrix and a second material as the reinforcement, retaining the weight-saving advantage of aluminium alloys but exhibiting superior mechanical properties. The reinforcements are usually ceramics of carbide or oxide in the form of continuous fibres, whiskers or particles.

SiC particle reinforced aluminium (SiC_p/Al) MMCs make an important species of MMCs. SiC_p/Al MMCs find wide applications in aerospace, automotive, defence and sports equipment due to the advantages of high tensile strength, high elastic modulus, high specific stiffness, high strength to weight ratio, etc. The good wear resistance of SiC_p/Al MMCs make them favourable in producing wear resistant components, such as pistons and brakes. They are also employed for electronic packaging products due to balanced thermal properties of SiC_p/Al MMCs.

However, in general, aluminium alloys are susceptible to localised corrosion in chloride environments. This typically applies in the applications of aluminium alloys in marine or coastal environment. A number of investigations have demonstrated the localised corrosion of aluminium alloys associated with the heterogeneity and defects of the surface of aluminium alloys in chloride environments. For SiC_p/Al MMCs, the addition of SiC particles could further promote the localised corrosion of the MMCs by introducing high density dislocations, degrading the integrity of native oxide film, altering the intermetallics precipitation, or forming galvanic cells

between SiC and Al. The corrosion behaviour of SiC_p/Al MMCs significantly depends on the reinforcement size and volume fraction and the matrix microstructure. Submicrometre-sized SiC particles have been incorporated to enhance mechanical properties but the corrosion behaviour of the MMCs reinforced with such particles have not been given much attention. Understanding the effect of the presence and size of SiC reinforcement on the corrosion behaviour of MMCs forms a part of this research work.

The high susceptibility of aluminium alloys and their MMCs to localised corrosion requires suitable corrosion protection of these materials in chloride environments to reduce the failure risks and prolong their service life. Improving the corrosion resistance of materials can be achieved by altering the original composition and manufacturing process of the materials or surface treatment. Altering the original composition or manufacturing process could affect the mechanical properties and also means that the materials are no longer the originally designated materials. Therefore, surface treatment is preferable for providing corrosion protection whilst retaining the mechanical properties of the bulk materials. Conventional methods of corrosion protection of aluminium alloys include anodising, chemical conversion coatings and organic coatings, which have been applied to MMCs as well. However, these techniques usually bring about environment concerns and many of them have been reported to be less effective when used on MMCs than aluminium alloys due to the presence of SiC reinforcement. Laser surface melting (LSM), which is environment-friendly, has become a promising technique for corrosion protection in the last few decades. Investigations have demonstrated considerable corrosion protection for steels, aluminium alloys, magnesium alloys and MMCs provided by LSM.

LSM improves corrosion resistance of aluminium alloys and MMCs by generating a melted layer with refined microstructures. The thickness of the melted layer varies from several micrometres to several hundreds of micrometres depending on the types

of applied laser and the processing parameters. Reduction and/or refinement of coarse intermetallics, grain boundary precipitates and matrix-reinforcement interfaces, which could be active sites for corrosion initiation, contribute to LSM-induced improvement of corrosion resistance of aluminium alloys and MMCs. Ideally, the alloying elements are homogeneously distributed in the melted layer without chemical segregation, eliminating the electrochemical heterogeneity. Pulsed excimer lasers are advantageous in achieving such microstructure compared to frequently used continuous wave CO_2 and Nd:YAG lasers, being resulted from much higher cooling rates of excimer lasers (up to 10^{11} K/s) than continuous wave lasers (10^3-10^8 K/s).

Excimer LSM of aluminium alloys has been the subject of interest recently. A number of studies have devoted to the improvement of corrosion resistance of aluminium alloys by excimer LSM and show some prospering achievements. Excimer LSM has been also suggested to be a promising technique for corrosion protection of their MMCs. However, more understanding is needed for the corrosion mechanisms of the laser-melted aluminium alloys and their MMCs. The LSM process involving laser-material interaction and microstructure changes are far from understood. The correlation between the laser-induced microstructures and the corrosion behaviour of laser-melted aluminium alloys and their MMCs remains unknown.

1.2 Aims and objectives

One of the main aims of this research is to compare the corrosion behaviour of SiC_p/AA2124-T4 MMCs with the monolithic AA2124-T4 aluminium alloy and understand the effect of SiC particles on the corrosion behaviour of as-received SiC_p/AA2124 MMCs. This research employs two SiC_p/AA2124 MMCs; one is reinforced with micrometre-sized SiC particles and the other one with submicrometre-sized SiC particles. Investigations to date mainly focus on the

corrosion behaviour of MMCs reinforced with micrometre-sized SiC particles while the MMCs reinforced with submicrometre-sized SiC particles, which are beneficial for mechanical properties, are seldom involved.

The main objectives in this part are as follows:

- Microstructural characterization of both MMCs and the matrix alloy using various microscopic techniques, EDX and XRD analysis. The microstructure characterization is to find out the difference between the MMCs and the matrix alloy and to identify the possible active sites for corrosion initiation. The SiC/Al interfacial precipitates and intermetallics in the matrix are of great interest as these can be active sites for corrosion initiation.

- Evaluation of the corrosion behaviour of the MMCs and the matrix alloy in 0.6 M NaCl solution via potentiodynamic polarization and electrochemical impedance spectroscopy.

- Immersion test in 0.6 M NaCl solution to reveal the preferential sites for corrosion initiation and understand the corrosion mechanism of each investigated material.

This research also aims to generate protective thin films on AA2124-T4 aluminium alloy and SiC_p/AA2124 MMC to improve their corrosion resistance. The objectives include:

- Study the effect of laser operating parameters (laser fluence and number of pulses) on the surface morphology, thickness and microstructure of the melted layer formed on each material.

- Detailed microstructural characterization of the melted layers obtained with selected operating parameters using SEM/EDX, TEM/EDX, and XRD;

comparison of the surface potential distribution between the melted layer and the substrate using SKPFM.

- Simulation of LSM process involving single Al phase and dual phases (Al and SiC) with an analytical model, a finite element model and a smoothed-particle hydrodynamics model in order to understand the laser-material interaction and interpret the formation of the microstructures in the melted layer.

- Evaluation of the corrosion behaviour of the laser-melted MMCs and matrix alloy processed with selected operating parameters in 0.6 M NaCl solution via potentiodynamic polarization, electrochemical impedance spectroscopy and immersion test.

- Comparison of the corrosion resistance of both materials before and after excimer LSM to evaluate the improvement of corrosion resistance induced by excimer LSM; identification of the corrosion initiation sites to build up the correlation between the corrosion behaviour and the laser-induced microstructures.

1.3 Outline of thesis

The thesis comprises seven chapters in total. Following this chapter, Chapter 2 is devoted to providing the essential background information to this research work. The literature relevant to this research are also summarised in Chapter 2. In Chapter 3, an account of the experimental procedures and techniques utilised in this study will be presented. Chapters 4, 5 and 6 present the experimental results and discussion. Chapter 7 attempts to bring together the overall results from previous Chapters, deliver the main conclusions of this research work, and discuss possible future work.

Chapter 4 presents the results of the microstructural characterization and corrosion evaluation of the SiC_p/AA2124 MMCs and the monolithic AA2124 aluminium alloy.

The effect of SiC particles on the microstructures and corrosion behaviour of the MMCs and the corrosion mechanisms of the MMCs will be discussed.

Chapter 5 is dedicated to the characterization of the laser-induced microstructures in the melted layer of the MMC and the matrix alloy. The effect of laser operating parameters on the formation of the melted layer is assessed; the melted layer is detailedly studied using SEM/EDX, TEM/EDX, XRD and SKPFM; the formation of the microstructures is interpreted with the simulation results of various models, combined with the experimental observation.

Chapter 6 studies the corrosion performance of the laser-melted SiC_p/AA2124 MMC and AA2124 aluminium alloy in 0.6 M NaCl solution. Comparison of the corrosion resistance between the as-received and the laser-melted materials is made to evaluate the improvement of corrosion resistance induced by excimer LSM. The corrosion mechanism of the laser-melted samples will be discussed for each material.

Chapter 2 Literature review

2.1 Introduction

In this chapter, the literature on the corrosion and protection of aluminium alloys and their MMCs, and LSM are reviewed. This review logically includes two parts. In the first part, an introduction to aluminium alloys and MMCs, and basic related corrosion concepts is provided; the corrosion behaviour in chloride media and the prior art of corrosion protection of aluminium alloys and MMCs are reviewed. In the other part, basics and applications of laser are briefly reviewed. Understanding of laser-material interaction and laser surface processing based on the literature is stressed.

2.2 Aluminium alloys and MMCs

2.2.1 Aluminium and aluminium alloys

Table 2.1 Series of aluminium alloys [1].

Alloy series	Main alloying elements
1XXX	Aluminium 99%
2XXX	Copper
3XXX	Manganese
4XXX	Silicon
5XXX	Magnesium
6XXX	Magnesium and Silicon
7XXX	Zinc
8XXX	Lithium and Tin

Aluminium is the third abundant element and the most abundant metal in the Earth's crust. As a metallic engineering structural material, it is favourable due to its

remarkable low density of 2.7 g/cm^3, which is approximately two times lower than that of iron. Aluminium possesses a face-centred cubic crystal structure with the lattice parameter a=0.40496 nm.

Pure aluminium has good corrosion resistance because of the native oxide layer formed in air. However, pure aluminium has a low tensile strength, which constrains the applications of this light-weight metal. Therefore, aluminium alloys are developed by intentional addition of alloying elements, to obtain superior properties. Aluminium alloys are divided into eight series, which are listed in Table 2.1.

Cast alloys and wrought alloys are two main types of each series aluminium alloys. The wrought alloys can subject to secondary processing, such as rolling, forging and extrusion. For both types of aluminium alloys, some of them can be strengthened by heat treatment, known as heat-treatable alloys; the rest are non-heat-treatable alloys. The heat treatment tempers of heat-treatable aluminium alloys are shown in Table 2.2. Additional digits may be found after the first temper digit to specify the details of each type of heat treatment, such as the amount of cold working or the subsequent stress relieving process.

2.2.2 AA2124 aluminium alloy

AA2124 aluminium alloy is a heat-treatable wrought aluminium alloy alloyed with two main alloying elements, i.e. copper and magnesium. Other alloying elements include manganese, iron, silicon, etc. The effect of main alloying elements on the microstructure and properties of AA2124 aluminium alloy is summarised below.

(i) Copper

Copper provides the alloy with an increase in strength and hardness after solution heat treatment and subsequent aging. The maximum strengthening is achieved with 4-6 % copper, together with a comprehensive influence of other alloying elements.

Adding copper decreases the ductility and corrosion resistance of the alloy. Copper tends to precipitate at grain boundaries, forming copper-depleted zones in the surrounding aluminium. Thus, the grain boundaries are more cathodic than the vicinity, leading to the formation of galvanic cells, which makes the grain boundaries susceptible to corrosion [2].

(ii) Magnesium

Magnesium is added in combination with copper to obtain high strength. Magnesium accelerates the aging behaviour of this alloy at room temperature [3]. Artificial aging can further increase the strength of the alloy by precipitate hardening. Magnesium also tends to segregate at the grain boundaries, which has been related to the stress corrosion susceptibility of aluminium alloys [4]. The magnesium segregation makes the grain boundaries more anodic to the surrounding matrix and preferential dissolution of the grain boundaries could occur in corrosive environment.

(iii) Manganese

Manganese increases the tensile strength and yield strength of this alloy but decreases the ductility. Therefore, the content of manganese should be less than 1 %. Manganese could remarkably retard the grain growth by forming fine dispersoids, for example $Al_{20}Mn_3Cu$; and increase the recrystallization temperature. Manganese almost has no effect on the corrosion performance of aluminium-copper alloys.

(iv) Iron and silicon

Iron and silicon are the most and second common impurity in aluminium, respectively. Most of the iron exists in the form of intermetallics due to the very low solubility of iron in solid state aluminium (~0.04 %). Iron increases the strength of the alloy at elevated temperature. Silicon reduces cracking during processing of the alloy. However, as low as 0.5 % iron reduces the tensile properties in heat-treated

condition, if the amount of silicon is less than that is required to tie up the iron as αFeSi phase.

(v) Other elements

Other alloying elements of small amount also play important roles in the alloy. Titanium, zirconium and vanadium increase the recrystallization temperature and thus increase the stability of the alloy at elevated temperature. Chromium reduces the susceptibility to stress corrosion cracking.

Table 2.2 Heat treatment temper descriptions according to the standard EN 515 [5].

Temper	Definition
T1	Cooled from an elevated temperature shaping process and naturally aged.
T2	Cooled from an elevated temperature shaping process, cold worked and naturally aged.
T3	Solution heat-treated, cold worked and naturally aged.
T4	Solution heat-treated and naturally aged.
T5	Cooled from an elevated temperature shaping process and artificially aged.
T6	Solution heat-treated and artificially aged.
T7	Solution heat-treated and artificially overaged.
T8	Solution heat-treated, cold worked and artificially aged.
T9	Solution heat-treated, artificially aged and cold worked.

Due to the limited solubility of the alloying elements in solid-state aluminium, a number of intermetallics are formed during manufacture and subsequent heat treatment. The intermetallics can be divided into three types, i.e. constituents, dispersoids and precipitates. As the chemical composition of AA2124 aluminium alloy is very close to that of AA2024 aluminium alloy, the main intermetallic compounds in the two alloys are the same. The most common intermetallics in AA2124/AA2024 are summarized below.

(i) Constituents

Typical constituent intermetallics in AA2124/AA2024 includes Al_2Cu, Al_2CuMg, and AlCuMnFe(Si)-containing particles with various composition, such as $Al_{12}Si(Mn,Fe)$, Al_7Cu_2Fe, $(Al,Cu)_6Mn$, $Al_3(Mn,Fe)$, $Al_6(Mn,Fe)$, etc. These intermetallics are relative coarse micrometre-sized particles and can be present in the form of clusters up to tens of micrometres. The AlCuMnFe(Si)-containing intermetallics are insoluble while Al_2Cu and Al_2CuMg intermetallics are soluble during ingot homogenization or solution treatment. Therefore, coarse Al_2Cu and Al_2CuMg intermetallics are usually undissolved particles during homogenization or solution treatment.

(ii) Dispersoids

Fine dispersoids ranging from 0.05 to 0.5 μm form during homogenization. Typical examples of dispersoids in AA2124/AA2024 are Al-Cu-Mn-containing phases, for example $Al_{20}Mn_3Cu$. The dispersoids are homogeneously distributed in the matrix except the periphery of some intermetallic particles, which is depleted in solute atoms required to form the dispersoids. The dispersoids limit the grain growth and recrystallization during processing and heat treatment; and have less effect than the coarse constituent particles on the corrosion performance of the alloys.

(iii) Precipitates

For Al-Cu-Mg alloys, precipitation hardening is the most important mechanism for their high yield strength. After solution treatment and quenching, a supersaturated solid solution (*SSS*) is formed with the dissolve of the alloying elements into α-Al. Subsequent aging allows the solute atoms to precipitate in the form of very fine precipitates. The main strengthening precipitates in AA2124/AA2024 are the S-phase precipitates when the Cu/Mg ratio ranges between 1.5 and 4; if the Cu/Mg ratio increases to 4-8, both S-phase and θ-phase hardening could exists [6-8]. The

size of the precipitates is usually less than $0.1\mu m$. The precipitation of equilibrium S-phase from the *SSS* experiences the stages as GPB zones, S" and S'. GPB zones are characterised with the concentration of Cu and Mg atoms by diffusion during aging. There are some debates on the structure of the transient S" [9]. The S' phase is semi-coherent with the matrix and is considered to have the same structure with equilibrium S-phase but with slightly different lattice parameters. The S-phase is the incoherent equilibrium precipitates.

2.2.3 MMCs

MMC refers to a wide range of materials, which are usually consisted of a metallic matrix and the reinforcement for designed properties. The metallic matrix usually has excellent ductility, formability or high thermal conductivity, for example aluminium, magnesium and their alloys. The reinforcement is normally a ceramic, which has high stiffness, high strength, high hardness, good wear resistance and low coefficient of thermal expansion. Typical examples include SiC, Al_2O_3, and B_4C ceramics. The purpose of designing MMC is to overcome certain shortcomings of the matrix in mechanical or thermal properties without compromising too much of the advantages of the matrix. In other word, MMC utilises the advantages of both the matrix and the reinforcement, without seriously aggravating their shortcomings.

(i) Types of MMCs

According to the type of reinforcement, there are three types of MMC, as shown in Figure 2.1. The reinforcement can be in the form of mono filament, continuous fibres, short fibres/whiskers or particles. Mono filaments are large diameter fibres ranging from 100 to 150 μm while continuous fibres have small diameters of about 20 μm [10].

Continuous fibre reinforced MMCs arose interest in the 1960s. This type of MMC is typically of high volume fractions (~40-80%), which impart excellent axial

properties. The external load is mainly transferred and distributed by the matrix to the reinforcement and thus the reinforcement bears substantial proportions of the external load [11]. The anisotropy of continuous fibres results in poor workability of this type of MMC, limiting the applications of continuous fibre reinforced MMCs.
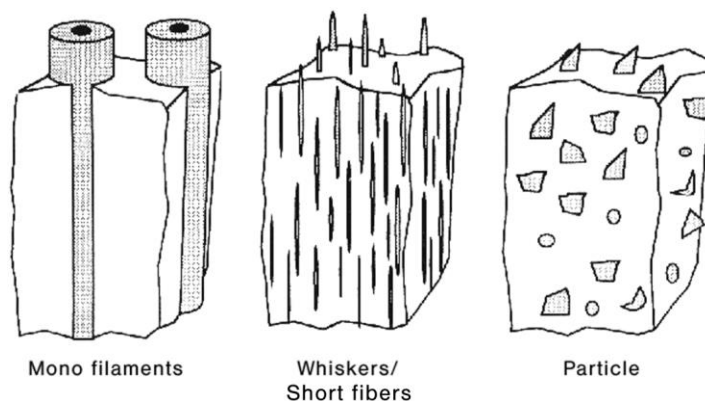
Figure 2.1 Schematic of three types of metal matrix composites [11].

MMCs reinforced with discontinuous reinforcements have been rapidly boosted in the 1980s. Compared with continuous fibre reinforced MMCs, discontinuous reinforced MMCs, especially particle reinforced MMCs have drawn more attention due to isotropic properties, low cost and high workability. For example, particle reinforced aluminium MMCs can be subjected to secondary forming used for aluminium alloys, such as rolling, forging and extrusion.

(ii) Manufacture of MMCs

Primary processes for manufacturing of MMCs include solid state processing and liquid state processing. Solid state processes include powder metallurgy processing, diffusion bonding, physical vapour deposition, etc. Liquid state processes include stir casting or compo casting, infiltration, spray casting, etc. The difference between solid state processing and liquid state processing is physical state of the matrix, that is, the matrix remains the powder form under its melting point in solid state processing while the converse comes under liquid state processing. The selection of

the manufacturing process depends on the type and fraction of the reinforcement and the degree of microstructural integrity desired [10]. The different processing temperatures for various processes could also significantly affect the chemical reactions between the reinforcement and the matrix. Whisker or particle reinforced MMCs have advantages over continuous fibre reinforced MMCs because whisker or particle reinforced MMCs are more flexible in processing routes.

2.2.4 SiC particle reinforced aluminium MMC

SiC particle reinforced aluminium (SiC_p/Al) MMCs make up an important species of MMC. SiC possesses stable chemical properties, high coefficient of thermal conductivity, low coefficient of thermal expansion and very high hardness. The addition SiC into aluminium and its alloys significantly improves the tensile strength, modulus and hardness whilst remains light-weight and controls the coefficient of thermal expansion without reducing too much of the thermal conductivity.

For instance, the hardness of aluminium reinforced with 20 wt.% SiC particles was twice of the pure aluminium whilst the tensile strength of the MMC tripled that of the pure aluminium according to Rahman and Rashed [12]. The strength of some high-strength aluminium alloy (2xxx) MMCs are close to some high-tensile steels. Al-Rubaie *et al.* [13] have reported three times improvement of the abrasion resistance of AA1100 aluminium alloy against 20 μm SiC abrasives by addition of 20 vol.% SiC_p reinforcement. The wear resistance of SiC_p/Al MMC increases with the reinforcement size and volume fraction [14]. SiC_p/Al MMCs have the equivalent thermal conductivity with the matrix alloy while the coefficient of thermal expansion (CTE) of the composites is well controlled. Depending on the volume fraction of SiC particles, the CTE of SiC_p/Al MMCs can be as low as 10 ppm/ °C, much lower than that of aluminium, 22.5 ppm/ °C.

With an excellent balance of physical and mechanical properties, SiC$_p$/Al MMCs have been widely used in the field of aerospace, defence, automotive, electronic industries, and sports equipment. The examples of their applications are aircraft structure and engine components, brakes, wheels, instrumentation, and satellite components; and also various applications in automotive such as pistons, cylinder liners, connecting rods, engine blocks, brake rotors, and gearbox parts. The excellent thermal properties of SiC$_p$/Al MMCs also make them favourable materials in electronic packaging.

2.2.5 Effect of reinforcements on microstructure development
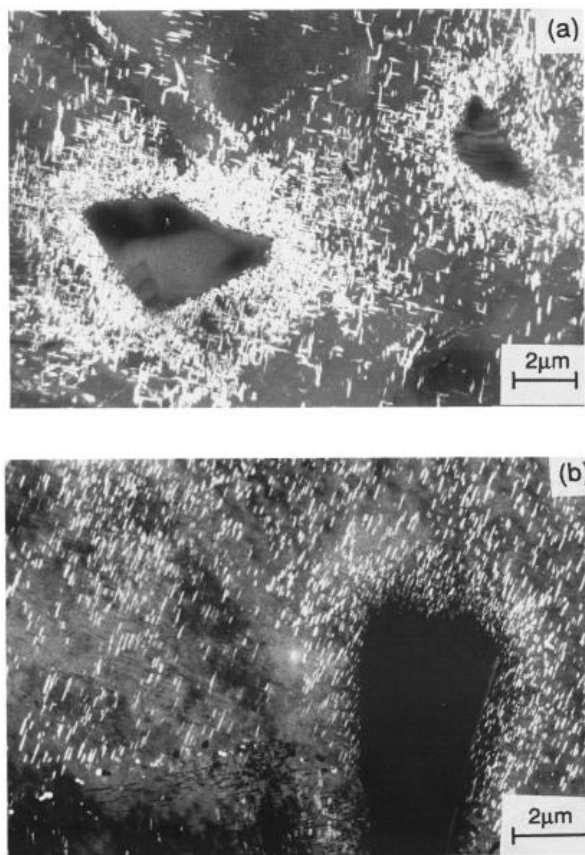
Figure 2.2 TEM micrographs showing the θ' precipitates around SiC particles in Al-4 wt.% Cu after aging at 190 ℃: (a) quenched sample prior to aging and (b) processed with 0.5% plastic strain prior to aging [15].

The matrix microstructure could be significantly influenced by the presence of reinforcements due to the thermal stress or deformation induced by the reinforcements. The literature regarding the microstructure of the matrix is reviewed and attention is focused on SiC/Al MMCs.

(i) Dislocations

Thermal stress is induced in MMCs when the MMCs are cooled down to the room temperature from elevated temperatures due to the mismatch of the CTE between the reinforcement and the matrix [16]. The mechanism of the relaxation of thermal stress has been proposed by Taya and Mori [17] to be prismatic punching as long as the energetics are favourable. The prismatic dislocation loops will be punched out into the matrix, giving rise to the dislocation density in the matrix around the reinforcement. The increased dislocation density in the vicinity of the reinforcements has been directly observed [18] or indicated by the precipitation of θ' phase in Al-Cu alloys [15]. Prangnell and Stobbs [15] observed the high density of θ' precipitates around the SiC particles after aging at 190 ℃, which favours dominant nucleation of θ' precipitates at dislocations (Figure 2.2(a)). It is clearly shown that the θ' precipitates decreased with the increase of distance from the SiC particles, indicating that the dislocation density decreased with the increase of distance from the SiC particles. Figure 2.2(b) shows the distribution of θ' phase precipitated with 0.5% plastic strain prior to aging, suggesting the possible local age-hardening effect in the matrix adjacent to the reinforcement. There are debates on the relationship between the thermal induced dislocation density and the reinforcement size. Arsenault and Shi [19] found the dislocation density to be inversely proportional to the particle size while Dutta and Bourell [20] suggested that the dislocation density was independent of particle size. But, Kim *et al.* [18] stated later that the average dislocation density decreased with the decrease of the particle size.

(ii) Grain refinement

Refinement of the matrix grains by the addition of reinforcements has been reported in different systems of MMC [21-29]. Kang and Chan [24] found that the grain size of the matrix aluminium of 5 vol.% Al_2O_3/Al MMC was about one fourth of that of the unreinforced alloy. The mechanism for grain refinement was attributed to the heterogeneous nucleation of the matrix alloy at the reinforcements. The reinforcements further acted as obstacles impeding the grain growth, giving enough time for more nuclei to form [25].

(iii) Intermetallics

Depending on the types of reinforcement, the species and the distribution of intermetallics could be significantly influenced by the presence of reinforcements. The addition of reinforcements could create new intermetallics which do not exist in unreinforced matrix alloys through chemical reactions; it could also alter the distribution of intermetallics in the matrix or aging behaviour of some age-hardenable aluminium alloys.

A comparative study of the microstructures of B_4C, Al_2O_3 and SiC reinforced pure aluminium alloy indicated that an interaction layer was formed at the interface of SiC/Al MMC; no reaction product was observed and the reinforcement-matrix interface was clean in Al_2O_3/Al MMC; and aluminium boroncarbide and some oxides were formed in B_4C/Al MMC [30]. B_4C interacts with solid or liquid aluminium to form ternary carbide Al_3BC, accompanied with the formation of AlB_2 or $Al_3B_{48}C_2$ in the temperature range of 627-1000 °C [30]. The reaction between SiC and liquid aluminium has been a main concern which affects both mechanical and corrosion performance of SiC/Al MMCs [31-44]. Although it has been reported that SiC could react with solid state aluminium during heating [45], more interest has been focused on the reaction between SiC and liquid aluminium because it simulates

the usual manufacturing conditions and the reaction takes place at significantly increased rates. Two main reactions may occur:

$$3SiC \ (s) + 4Al \ (l) = Al_4C_3 \ (s) + 3Si \ (s) \qquad \text{(Reaction 2.1)}$$

and

$$4SiC \ (s) + 4Al \ (l) = Al_4SiC_4 \ (s) + 3Si \ (s) \qquad \text{(Reaction 2.2)}$$
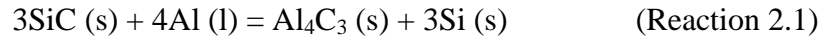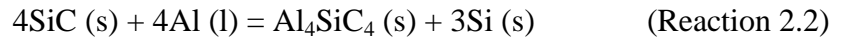
The Reaction 2.1 dominates the reaction process when the temperature ranges from 650 to 1200 ℃ while the Al_4SiC_4 compound starts to form by Reaction 2.2 when the temperature exceeds 1200 ℃ [46, 47]. There are three primary methods to prevent the degradation of SiC by liquid aluminium. (1) The processing temperature and holding time are controlled to limit the extent of the chemical reactions, which varies significantly depending on the composite manufacturing methods [34, 48, 49]. (2) Silicon is added to the matrix alloy to suppress the reactions between SiC and aluminium [41, 50-52]. (3) SiC reinforcement was coated or oxidised prior to composite fabrication to separate the reactants [32, 36, 39, 42, 43, 53].

It is obvious that the chemical reactions between the reinforcement and the matrix depend on the nature of the matrix and the reinforcement, the processing temperature and holding time. Alumina reinforcement does not react with pure aluminium but it can react with the matrix containing magnesium via the reactions below [54]:

$$3Mg + Al_2O_3 = 3MgO + 2Al \qquad \text{(Reaction 2.3)}$$

and

$$3Mg + 4Al_2O_3 = 3MgAl_2O_4 + 2Al \qquad \text{(Reaction 2.4)}$$
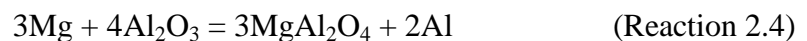
This is because MgO is more stable than Al_2O_3 according to Ellingham diagram. In SiC/Al-Mg alloy, Reactions 2.3 and 2.4 can also take place provided that silica is

present on the surface of SiC reinforcement. The silica can be native oxide layer or artificially oxidation product. Both Al_2O_3 and MgO could be formed via the reactions below:

$$SiO_2 + 2Mg = 2MgO + Si \qquad \text{(Reaction 2.5)}$$

and

$$3SiO_2 + 4Al = 2Al_2O_3 + 3Si \qquad \text{(Reaction 2.6)}$$

The resulting free Si can also promote the precipitation of some Si-containing intermetallics, for example Mg_2Si in Al-Mg alloy [55-57], or increase the content of Si in AlCuMnFeSi-containing intermetallics in AA2124 aluminium alloy [58].

The reinforcements can affect the amount and distribution of intermetallics in a more indirect way. Griffiths and Turnbull [59] reported a significant rise of intermetallics area fraction in 15-30 vol.% SiC/Al MMC compared to the unreinforced aluminium alloy. Buarzaiga and Thorpe [60] investigated the microstructure of SiC_p/A356 MMC compared to the unreinforced A356 aluminium alloy and concluded that the eutectic Si phase developed a different morphology in the MMC and nucleated preferentially adjacent to SiC particles; and the predominant intermetallic phase in the matrix changed from $FeMg_3Si_6Al_8$ to $FeSiAl_5$ due to the addition of SiC particles. This was explained by the segregation of Mg to SiC/Al interface, reducing the amount of Mg available for the formation of Mg-rich intermetallics. Mg segregation to SiC/Al interface has been reported by Nutt and Carpenter [61], Lin et al. [62], Imeson and Bartlett [58] and Kim et al. [63]. Apart from Mg segregation, Al_2CuMg [61, 62] and Al_2Cu [58, 61, 62] phases were also reported to preferentially precipitate at SiC/Al interface. The preferential precipitations to SiC/Al interface can be attributed to the high density of dislocations in this area, as discussed earlier, providing pipe tunnels for atom diffusion and promote the diffusion of solute atoms [11, 62].

(iv) Porosity

The porosity of the MMCs is calculated via the following equation [64]:

$$\%\text{porosity} = (1 - \rho_{ce}/\rho_{cth}) \times 100 \qquad \text{(Equation 2.1)}$$

where ρ_{ce} is the experimentally determined density of the MMCs and ρ_{cth} is theoretically calculated density of the MMCs. ρ_{cth} can be calculated using the rule of mixture:

$$\rho_{cth} = V_r\rho_r + V_m\rho_m \qquad \text{(Equation 2.2)}$$

where V_r and V_m are the volume fraction of the reinforcement and the matrix respectively; ρ_r and ρ_m are the density of the reinforcement and the matrix respectively.

Porosity of the MMCs is largely related to the reinforcement size and volume fraction. Singh et al. [64] found that the porosity of SiC_p/Al MMCs increased with the increase of the volume fraction of the reinforcement. Montoya-Dávila et al. [65] reported that the porosity could be reduced by reducing the particle size of SiC reinforcement. In their research, the volume fraction remained constant but a fraction of the reinforcement was replaced with smaller particles, which reduced the average particle size of the reinforcement. The porosity reduced from 4.42% to 0.49% by replacing the monomodal distribution of reinforcement (146 μm) with the cuatrimodal distribution of reinforcement (10, 54, 86 and 146 μm with the ratio of 1:1:1:3).

2.3 Localised corrosion in aluminium alloys

Aluminium and its alloys are corrosion resistant due to the presence of the native oxide layer formed in air. They may be subjected to corrosion in certain environment. General corrosion usually occurs in strong acid or alkaline solutions, which are

typically used during processing of aluminium and its alloys. Localised corrosion is the main corrosion form in neutral aggressive environments, typically when chloride ion is present.

2.3.1 Pitting corrosion

Pitting corrosion is localised accelerated dissolution of passivated metals due to the breakdown of the protective passive film on metal surface and it is the most common localised corrosion in aluminium alloys when exposed to aggressive, even neutral, environments. Chloride anion (Cl^-) is a typical corrosive medium leading to localised corrosion of aluminium and its alloys. Cl^- ion has a relatively small ion radius and a high diffusivity. Four stages are involved in pitting corrosion: 1) processes on the passive film and passive film/solution interface; 2) processes within in the passive film, when no visible microscopic changes occur in a film; 3) formation of metastable pits which initiate and grow for a short period of time below the critical pitting potential and then repassivate; and 4) stable pit growth above the critical pitting potential [66].

The first step of pitting initiation is the adsorption of Chloride anion (Cl^-). The passive film is not homogeneous on the surface of aluminium alloys due to the chemical or physical heterogeneity, such as inclusions, intermetallics, solute-segregated grain boundaries, dislocations, and morphological artefact, on the surface. Therefore, the adsorption energy for Cl^- ions varies from site to site, resulting in preferable Cl^- adsorption locally. Following the adsorption of Cl^- ions, passive film breakdown at the weak sites of the oxide film occurs due to the interaction between the Cl^- ions and pitting initiates. However, there are debates on the mechanism of the initial stages of pitting corrosion. The theories interpreting the pitting initiation process are classified into three categories: 1) ion migration/penetration model, 2) adsorption model leading to oxide thinning, and 3) breakdown repair model [67-70].
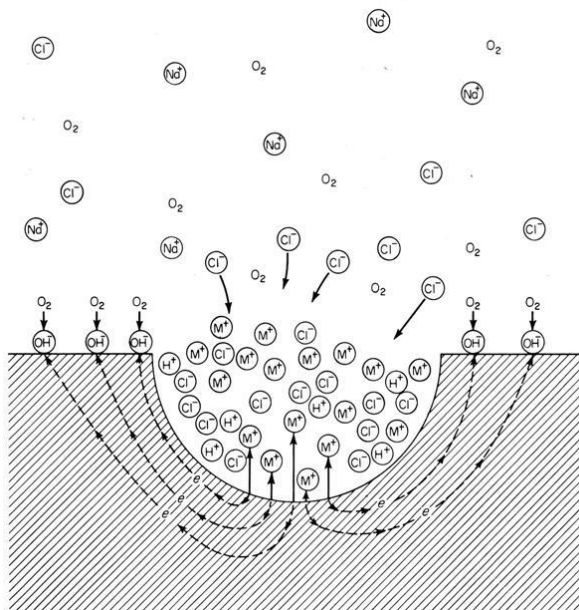
Figure 2.3 Autocatalytic processes within the pit [71].

The propagation of pitting corrosion involves the growth of metastable and stable pits. At the active sites, it is an autocatalytic process for the pits growth. The schematic of the autocatalytic process within the pit is shown in Figure 2.3. The anodic and cathodic reactions involved are separated inside the pits and at the outer surface, respectively. The cathodic reaction keeps the same at the outer surface involving the reduction of oxygen:

$$O_2 + 2H_2O + 4e^- = 4OH^- \text{ (neutral solution)} \qquad \text{(Reaction 2.7)}$$

The anodic reaction, oxidation of aluminium losing electrons and mass, occurs at the bottom:

$$Al = Al^{3+} + 3e^- \qquad \text{(Reaction 2.8)}$$

The formation of Al^{3+} ions generates an electric field and attracts more Cl^- ions into the pit to form a complex intermediate species $AlCl^{4-}$. The hydrolysis of $AlCl^{4-}$ acidifies the solution at the bottom to make it a very aggressive solution, which accelerates the pit propagation.

46

In fact, pitting corrosion of aluminium alloys is more frequently linked with the presence of intermetallics within the alloys. The intermetallics are either anodic or cathodic to the aluminium matrix. Mg-rich intermetallics, Al_2CuMg in AA2xxx aluminium alloys and Mg_2Si in AA6xxx aluminium alloys, are usually anodic to the aluminium matrix and subjected to dissolution of magnesium by a dealloying mechanism. Cu- and Fe-rich intermetallics are often cathodic to the aluminium matrix, supporting enhanced cathodic reaction. The cathodic reaction on the intermetallics creates an alkaline environment, leading to dissolution of passive layer and then aluminium matrix at the particle interface [72]. Different intermetallics show different significance of the effect on the pitting behaviour of aluminium alloys. Birbilis et al. [73] investigated the corrosion behaviour of an AA7075-T651 aluminium alloy, suggesting that Al_7Cu_2Fe intermetallics can support oxygen reduction reaction at rates three times greater than Al_2Cu and up to two times greater than $Al_{20}Cu_2Mn_3$ intermetallics. Ilevbare et al. [74] suggested that it required large intermetallic particle clusters to form stable pits in AA2024 aluminium alloy.

2.3.2 Crevice corrosion

Crevice corrosion has an extreme similar mechanism to pitting corrosion after its initiation. The difference is whether the corrosion initiates at an open site or at an occluded site [68]. The latter is called crevice corrosion. The majority of materials susceptible to crevice corrosion are passive in bulk environments and the preferable dimensions of the crevice are typically between 0.1 and 100 μm [75]. Crevice corrosion initiates often as a result of changes in local chemistry such as depletion of oxygen, increase in pH, and increase of Cl^- ions in the crevice [76]. The oxygen depletion creates an oxygen concentration cell, which makes the metal occluded in the crevice net anodic, while the outer surface net cathodic, providing the driven force for corrosion initiation [75]. It is the autocatalytic process, the same with that in pitting corrosion, sustaining the propagation of crevice corrosion. The damage of

crevice corrosion can be eliminated or reduced using proper sealants and protective coatings [76].

2.3.3 Intergranular corrosion

Intergranular corrosion refers to the corrosion damage due to selective dissolution of grain boundaries or the close vicinity without attack of the grains themselves [77]. The driven force of intergranular corrosion is the difference in corrosion potential between the matrix of grains and the grain boundaries, resulted from precipitation of fine intermetallic particles and segregation of alloying elements at grain boundaries. The precipitates at grain boundaries can be anodic, cathodic, or change from anodic to cathodic to the adjacent matrix of grains. The first situation leads to preferential dissolution of the grain boundaries themselves, while the second situation results in the attack of adjacent matrix. The last situation exists in specific aluminium alloys such as Al-Cu-Mg alloy. Al_2CuMg at grain boundaries is anodic to adjacent matrix and subjected to dealloying of Mg at the beginning; afterwards, this phase is left with Al and Cu, and becomes cathodic to adjacent matrix.

During precipitation of intermetallics at grain boundaries, solute atoms such as Cu and Mg diffuse towards the grain boundaries, leading to the formation of a solute atom depleted zone close to the grain boundaries. For example, in AA2xxx aluminium alloys, a typical Cu-depleted zone makes a lower potential of this zone than adjacent matrix and the grain boundaries [75]. Therefore, the Cu-depleted zone preferentially dissolves during corrosion.

Susceptibility to intergranular corrosion can be reduced by optimization of fabrication practices reducing intergranular precipitates and proper heat treatment [77].

2.4 Galvanic corrosion

Galvanic corrosion is induced due to the coupling of two dissimilar metals in a corrosive electrolyte. When a galvanic couple forms, one of the metals in the couple becomes the anode and corrodes faster than it would all by itself, while the other becomes the cathode and corrodes slower than it would alone [78]. The driven force for galvanic corrosion is the potential difference (E) between the anode and cathode. Ohm's law, $E = IR$, is applicable, where I is the current and R is the galvanic cell resistance. High E results in high tendency of galvanic corrosion; otherwise the galvanic tendency is limited. However, the corrosion rates are also dependent on the galvanic resistance [76].

It is important to point out that the area ratio of anode and cathode plays an important role in galvanic corrosion. Current density on both anode and cathode is defined as $i = I/A$, where A is the surface area. A small area anode coupled with a large area cathode could corrode much faster than a large area anode coupled with a small area cathode.

2.5 Effect of SiC reinforcement on the corrosion behaviour of SiC/Al MMCs

2.5.1 Pitting susceptibility

The addition of SiC reinforcement into aluminium alloys makes the corrosion processes more complex than monolithic aluminium alloys. Localised corrosion is the main corrosion form for SiC/Al MMCs in chloride environments. There are quite a few investigations on the pitting susceptibility of SiC/Al MMCs in aggressive media. There are some debates on the effect of SiC reinforcement on the pitting susceptibility of SiC/Al MMCs.

Aylor and Moran [79] reported that the corrosion potential (E_{corr}) of SiC/AA6061 MMC was not affected by the SiC reinforcement and the addition of SiC did not increase the pitting susceptibility of the MMC. Trzaskoma and McCafferty [80] had similar conclusions that the SiC reinforcement would not affect the pitting susceptibility of SiC reinforced AA6061 and AA5456 aluminium alloys but AA2024 aluminium alloy. The SiC/AA2024 MMC showed a noticeable shift of pitting potential (E_{pit}) to more negative direction compared with AA2024 aluminium alloy, indicating a higher pitting susceptibility of the MMC than the matrix alloy. In contrast, Kiourtsidis et al. [81] concluded that the E_{pit} was independent on the presence and the volume fraction of SiC reinforcement in SiC/AA2024 MMC. Bhat et al. [82] suggested that the SiC/AA6061 MMC, regardless of as-cast or extruded, had more active E_{corr} than AA6061 aluminium alloy. Hwang and Kim [83] found that the SiC reinforcement did not alter the E_{pit} of AA2124 aluminium alloy but polarized the matrix to a higher potential equalling to the E_{pit}. It can be concluded that the pitting susceptibility of SiC/Al MMC depends on various factors, such as matrix composition, manufacturing process, purity and conductivity of SiC. The E_{corr} cannot be simply determined by mixed potential theory.

Although some researchers have stated that the pitting susceptibility of MMCs is not affected by the SiC reinforcement, it is believed that the SiC reinforcement has significant influence on pitting distribution and propagation after initiation of corrosion. Aylor and Moran [79] found that the pits in SiC/AA6061MMC were increased in number but reduced in size and depth. Corrosion was found to be confined to the SiC/Al interface [82]. It is frequently reported that MMCs corroded at higher rates than their monolithic aluminium alloys [59, 83-85]. Therefore, the SiC reinforcement has an indirect influence, related to matrix microstructures, processing history, etc, on the corrosion behaviour of MMCs, rather than a direct influence.

2.5.2 Galvanic coupling effect

SiC is a semi-conductive ceramic and its conductivity is largely dependent on its purity. The electrical resistivity of SiC varies from 10^{-5} to 10^{13} Ω.cm depending on its purity [86], which may contribute to the conflicting results when studying the galvanic effect between SiC particles and the Al matrix. In a study conducted by Griffiths and Turnbull [59], SiC reinforcement was found to support similar cathodic current density with AA6061 aluminium alloy, which indicated that there was no basis for galvanic corrosion in this composite system. Hihara and Latanision [87] suggested a low galvanic current density of 10^{-5} A/cm^2 between SiC and AA6061-T6 aluminium alloy using mixed potential theory. Castle et al. [88] employed scanning auger microscopy to locate the cathodic sites during corrosion of SiC_p/AA6061 MMC in chloride solution. The results showed that the oxygen reduction rates on SiC particles cannot exceed 10^{-4} A/cm^2 but the cathodic intermetallics can support the oxygen reduction current density exceeding $7x10^{-4}$ A/cm^2. These works indicate that the galvanic corrosion between SiC and aluminium alloys is insignificant and can be neglected.

Subsequently, Nunes and Ramanathan [89] suggested that SiC acted as one of the active sites supporting cathodic oxygen reduction when it was added to an Al-7.5% Si-1% Mg alloy. Monticelli et al. [85] and Diaz-Ballote et al. [90] revealed the SiC reinforcement acting as an effective cathode using electrochemical noise analysis and scanning electrochemical microscopy, respectively. The conflicting results in previous work suggest that galvanic coupling effect during corrosion of SiC/Al MMCs cannot be excluded but the significance of galvanic corrosion could be different from one specific MMC system to another.

2.5.3 Reinforcement size and volume fraction

If galvanic corrosion cannot be neglected, the size and volume fraction of SiC reinforcement plays an important role in determining the corrosion resistance of the MMCs. Monticelli et al. [85] reported that the MMC with higher volume fraction of SiC corroded at a higher rate due to the galvanic coupling effect between SiC and the matrix. Even if there is no significant galvanic corrosion tendency, the reinforcement size and volume fraction can still remarkably affect the corrosion behaviour of the MMCs [59, 60, 64, 65, 91-93]. The influence of the reinforcement size and volume fraction is mainly attributed to the related microstructural changes, such as porosity [64, 65] and amount of intermetallics in the matrix [59] or at SiC/Al interface [93].

2.5.4 Interfacial matrix microstructure

As discussed earlier, the addition of SiC reinforcement has a significant effect on the interfacial microstructure in the view of intermetallics species and distribution. The intermetallics can be the centre of electrochemical heterogeneity, acting as effective anodes or cathodes coupled with the matrix alloy. Many researchers reported concentrated corrosion at SiC/Al interface, associated with intermetallics preferentially precipitated at the interface [94, 95], disruption of the integrity of passive film [88, 96] and high dislocation density [97] at the interface.

The reaction product Al_4C_3, located at the interface, is detrimental to the corrosion performance of SiC/Al MMCs because it is water reactive. The hydrolysis of this compound leads to corrosion initiation at the interfacial region [86]. In SiC/Al-Cu-Mg alloys, the Al_2CuMg intermetallic and segregation of Mg to the interface make the interface anodic to adjacent matrix, whilst the Al_2Cu intermetallic results in cathodic interface compared to adjacent matrix, leading to the formation of galvanic cells between the interface and adjacent matrix [97]. Imeson and Bartlett [58] reported that the microstructure responsible for the corrosion initiation of

SiC/AA2124 MMC was Mg segregation to the interface, while the coarse Al_2Cu intermetallic in the matrix played a minor role in corrosion initiation.

After corrosion initiation, crevices could be created at SiC/Al interface, which could further promote the corrosion process with the mechanism of crevice corrosion [98]. There can be pre-existing crevices at SiC/Al interface due to the poor bonding between the reinforcement and the matrix, contributing largely to the porosity of MMCs. Therefore, there is a basis for crevice corrosion to occur during corrosion of MMCs [97]. The crevices, together with the intermetallics, could disrupt the integrity of the passive film in the interfacial region [88, 96], being another mechanism for corrosion initiation at the interface. Castle et al. [88] found crevice corrosion at the interface which was probably due to the poor quality of the oxide film.

Although the microstructure in the interfacial region is altered, the bulk matrix can still exhibit similar microstructure with unreinforced aluminium alloys. The intermetallics in the matrix were reported by some researchers to be the preferential sites for corrosion initiation rather/other than SiC/Al interface [60, 81].

2.6 Corrosion protection of aluminium alloys and their MMCs

Appropriate corrosion protection is required for aluminium alloys and their MMCs due to their high susceptibility to localised corrosion in chloride environment. Materials corrosion protection can be achieved by altering the bulk composition and microstructure, or surface treatment. The former might not be able to maintain the properties or performance the materials would have. Surface treatment is an effective and favourable resort for corrosion protection. Common methods of corrosion protection for aluminium alloys and their MMCs include anodising [99-104], chemical conversion coatings [105-113], organic coatings [114], plasma electrolytic oxidation [115-118] and laser surface treatment [119-125].

As a conventional method, anodising has been successfully applied to aluminium alloys as an effective measure for corrosion protection [126]. Many researchers also applied this technique on MMCs with an aluminium matrix but found that it was not as effective as it was applied on aluminium alloys [99, 101]. He et al. [101] studied the corrosion behaviour of AA2024 aluminium alloy and SiC_p/AA2024 MMC anodised in sulphuric acid. The anodic film on the MMC was found more porous than that on the aluminium alloy. They attributed the decrease of protection efficiency for the MMC to the structural change of the anodized layer due to the presence of SiC particles and the intermetallics preferentially precipitated at the interface between the matrix and the reinforcement. SiC particles were difficult to be oxidized during anodising, hindering the growth of a continuous oxide film. Anodising usually forms a porous film and thus requires further sealing process [102, 104].

Lanthanide conversion coating has been reported to be a promising alternative for dichromate conversion coating [105, 106], which is forbidden due to environment concern. However, Hamdy et al. [111] found that direct treatment in cerium solution did not provide good corrosion protection for MMCs. Localized corrosion was always present, even after a long cerium treatment. Mansfeld et al. [112] indicated that the presence of crevices at SiC/Al interfaces could decrease the corrosion resistance of the passivated MMC.

Organic coatings are usually applied as the outer most protection layer for aluminium alloys. The organic coatings can be very thick and provide effective protection. Defects or scratches in the coatings can lead to corrosion initiation, typically in the form of filiform corrosion. Anti-corrosion pigments are often added in the organic coatings. McMurray and the co-researchers have applied many pigments in organic coatings on aluminium alloys, such as AA2024 and AA6111 aluminium alloys, providing effective inhibition to filiform corrosion [127-129].

Laser surface treatment is a promising technique to increase the corrosion resistance of aluminium alloys and their MMCs. Considerable attention has been drawn to LSM and Laser surface alloying (LSA) for corrosion protection [130]. LSM provides protection to aluminium alloys and their MMCs by producing a rapidly solidified surface layer, in which the microstructure is refined. LSA, where a new material is introduced to the melted layer during laser melting process, changes the microstructure and the corrosion performance. Laser surface treatment was reported to be able to increase the resistance of aluminium alloys to pitting corrosion [119-125], stress corrosion cracking [131-133], and corrosion fatigue [134]. Compared with other techniques, the most advantageous characteristic of laser surface treatment is the chemical free processing of materials without any environmental concerns.

For LSM, four types of lasers are often employed, including CO_2 lasers, Nd:YAG lasers, high power diode lasers (HPDL), and excimer lasers. LSM conducted using the first three types of lasers can generate hundreds of micrometres thick melted layers and refine the microstructure in the melted layer to some extent depending on the processed materials. Chong et al. [135] reported that LSM using continuous wave Nd:YAG laser increased the pitting potential of AA2014 aluminium alloy and changed the corrosion morphology. Copper segregation in the melted layer was responsible for the corrosion initiation of the laser-melted aluminium alloy. In another comparative study of the corrosion behaviour of CO_2 laser-melted AA2014 and AA2024 aluminium alloys, re-precipitation of Al_2Cu and Al_2CuMg were observed in the melted layer, respectively [136]. Therefore, the microstructure refinement obtained from LSM did not play an important role in pitting performance. An Al-Si alloy subjected to CO_2 LSM was also found with no improvement of corrosion resistance [137]. Benedetti et al. [138] investigated the capability of HPDL for LSM of AA7075-T6 aluminium alloy and suggested that small intermetallics, mainly Al_2CuMg and $MgZn_2$, were located at grain boundaries after LSM. It is a

potential risk of involving the grain boundaries as the preferential sites for corrosion initiation.

LSM performed with excimer lasers normally produces thin melted layers less than 20 μm on aluminium alloys. The thin melted layer provides corrosion protection to aluminium alloys due to its highly refined microstructure. The ns-pulsed excimer lasers are capable to create segregation-free microstructures as a result of the fast cooling rate, improving the corrosion performance of aluminium alloys and their MMCs [125, 139].

2.7 Laser surface engineering

2.7.1 Introduction

LASER is short for Light Amplification by Stimulated Emission of Radiation, which can be produced by over 15 000 energy transitions. However, only about 40 active media are used for commercial lasers [140]. The lasers producing light with the wavelengths in the infrared, visible and ultraviolet range have been the subject of considerable interest in materials processing applications. All laser beams are monochromatic and share the unique features of high coherence, high brightness and low divergence. Material processing often utilizes the thermal or photonic effects, combined with the high accuracy of laser.

2.7.2 Generation of laser

Quantum mechanics define that all particles (atoms, ions and molecules) have discrete energy states, also referred to as energy levels. The lowest possible energy level is ground state (energy level E_1), while the other states are excited states (absorption level or levels E_2). A prerequisite for the generation of laser is called population inversion. Normally, particles tend to keep in the ground state to give a state of thermodynamic equilibrium. However, the normal energy distribution can be

altered by external energy stimulation. A state with population inversion is achieved when the population of higher energy levels exceeds that of the ground state. A variety of external energy sources, such as electrical, optical and chemical means, are used to excite the particles to gain population inversion.

To create an efficient population inversion, the particles must possess a large group of upper absorption energy levels, which are termed as upper laser levels (E_3). This enables enough energy absorption over an appreciable frequency. Below the upper laser levels lie the lower laser states. Laser light generation involves transitions from the upper to the lower laser states (E_4). In order to maintain a population inversion, the lifetime of the upper laser state must be longer than that of the lower state [140].

Einstein proposed that a photon interact with a particle by absorption of a photon, spontaneous emission of a photon, or stimulated emission of a photon. Spontaneous emission do not generate laser as it is a random process. Stimulated emission makes the excited particles emit a photon identical with the incident photon during transition from energy level E_3 to energy level E_4. For an effective luminescent substance, the upper energy level E_3 is an excited state, where the possibility for spontaneous emission is remote. Therefore, the lifetime of the upper energy level E_3 can be relatively long. E_3 is normally lower than E_2 and the transition from E_2 to E_3 occurs without the emission of a photon, termed as non-radiative decay. The energy level E_4 can be equal to or higher than the energy level E_1, referred as three-energy level or four-energy level laser system, respectively. If $E_4 > E_1$, it is easier to obtain population inversion since it is not necessary to invert the entire population [140-142]. Finally, an optical cavity is required to gain the light amplification.

2.7.3 Industrial lasers

The types of industrial lasers can be generally classified into four categories according to the physical nature of the active medium: solid-state lasers, gas lasers,

semiconductor lasers and dye lasers. The important lasers in each category are listed in Table 2.3. The operating principles of all the lasers are out of the scope of this review. Hereby, a brief introduction is given to the lasers that are most commonly used for LSM.

Table 2.3 Typical lasers in each category and their typical wavelengths [142].

Laser type	Wavelength (nm)
Solid-state lasers	
Nd:YAG	1064
Ruby	694
Nd: glass	1062
Alexandrite	700-820
Ti-sapphire	700-1100
Er: YAG	2940
Nd: YLF	1047
Gas lasers	
HeNe	632.8
Argon	488514.5
Krypton	520-676
HeCd	441.5, 325
CO_2	10600
ArF	191
KrF	248
XeCl	308
XeF	351
Copper vapour	510.6, 578.2
Gold vapour	628
Semiconductor lasers	
InGaAs	980
AlGaInP	630-680
InGaAsP	1150-1650
AlGaAs	780-880
Liquid dye lasers	
Rhodamine 6G	570-640
Coumarin 102	460-515
Stilbene	403-428

(i) Nd:YAG laser

The active medium of Nd:YAG lasers consists of crystalline YAG (chemical formula $Y_3Al_5O_{12}$), in which the yttrium ion sites in the lattice replaced by Nd^{3+} ions with a maximum doping level of around 2%. This is a typical four-energy level laser system, which is advantageous for achieving population inversion easily. Nd:YAG laser can be operated in three modes: continuous, pulsed and Q-switched. Several laser wavelengths are possible but 1064 nm is the strongest one. Nd:YAG lasers can be operated in frequency-doubled (532 nm), frequency-tripled (355 nm) and frequency-quadrupled (266 nm) modes [142].

Due to the flexibility of operating mode, Nd:YAG lasers find many applications in material processing, such as welding, drilling, cutting and surface modifications. Frequency-doubled green light is often used for machining colour-sensitive materials such as nitrides and polyimides. Frequency-tripled ultraviolet light involves applications in micromachining, marking polymers and glass, as well as in rapid manufacturing systems. Nd:YAG lasers have the ability to deliver laser beam through optical fibres, being an advantage for robotic or multi-axis applications [140].

(ii) CO_2 laser

The carbon dioxide (CO_2) laser is an infrared gas laser using CO_2 gas as the active medium. The active medium is actually a gas mixture of CO_2, helium (He), and nitrogen (N_2). The CO_2 molecule can undergo three vibration forms, i.e. symmetric stretching, bending, and asymmetric stretching, in addition to which the molecule can also rotate. The vibrational energy levels are split into closely spaced rotational sublevels since the energy associated with the rotations is much smaller than the vibrations [142]. The excitation of CO_2 molecules starts with the excitation of N_2 molecules, which transfer the excitation energy to CO_2 molecules through collision

because the vibrational excitation of the nitrogen molecules is metastable and closely corresponds to the (001) vibrational levels of CO_2 [140]. The addition of He is to increase the output power.

Laser transitions occur between upper laser level (001) and lower laser levels (100) and (020), giving 10.6 and 9.6 μm wavelength, respectively. However, the laser radiation at 10.6 μm is the strongest and most frequently used mode [142]. CO_2 laser can be operated in both continuous and pulsed mode. One advantage of CO_2 lasers is the extreme high efficiency of ~30%. Output power of several kilowatts can be obtained from CO_2 lasers, making their ability in material welding, cutting and drilling [143].

(iii) Excimer laser

The term excimer is from the term 'excited dimer', which refers to a diatomic molecule that dissociates in the ground state but is stable in its first excited state, although the lifetime of the excited state is only of the order of 10^{-9} s [144]. Examples of excimers are ArF, KrF, XeCl, and so on. In the case of excimer laser, a population inversion can be easily achieved since the molecules in ground state are much less than those in excited state. Laser transition takes place between the bound excited electronic state and the dissociative ground state. Take KrF excimer as an example, when the mixture of krypton and fluorine is excited by electrical discharge, the following processes can take place:

a. Electron attachment: $e + F_2 \rightarrow F^- + F$

b. Formation of excited molecule: $Kr^+ + F^- \rightarrow (KrF)^*$

c. Dissociation of excited molecule: $(KrF)^* \rightarrow Kr + F + h\nu$

The emitted energy (hν) in the form of a photon causes the molecule fall into the

ground state so that the molecule dissociates [142, 144]. Excimer lasers usually produce light in the ultraviolet range with 15−20% efficiency [141]. They find extensive applications in material processing, micromachining, marking, annealing, doping, vapour deposition, and other surface modification techniques with a wide range of materials including metals, ceramics and polymers [140].

2.7.4 Laser-material interactions
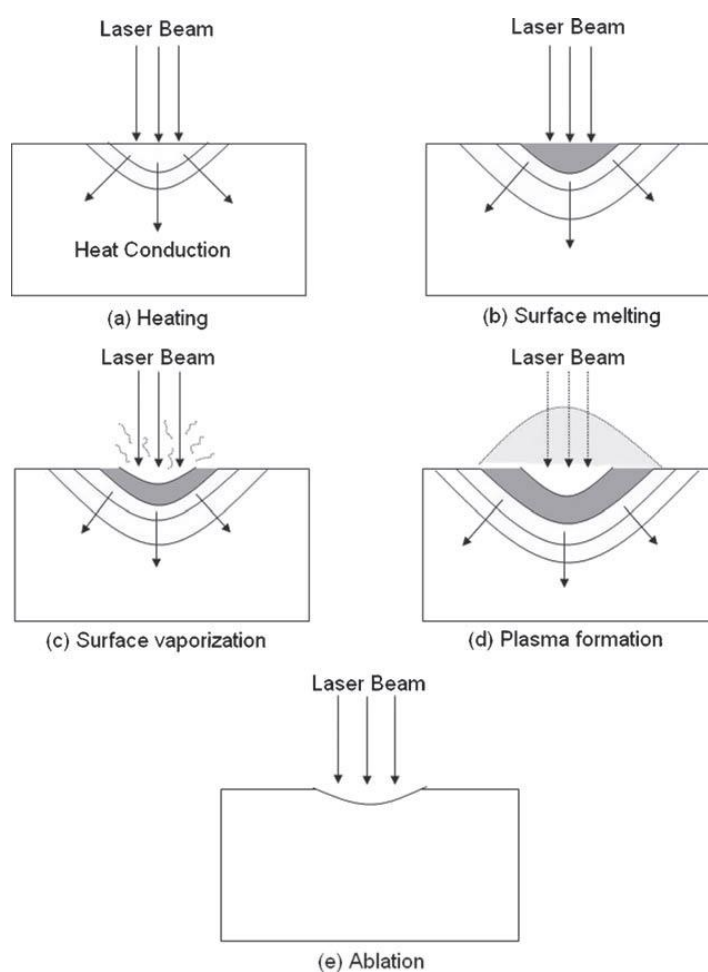
Figure 2.4 Various laser-material interactions: (a) heating; (b) surface melting; (c) surface vaporization; (d) plasma formation; and (e) ablation [142].

To apply the suitable laser for material processing, it requires the understanding of the interactions between the laser beam and the materials. When a laser beam is incident on the surface of a material, various optical processes could occur. These

61

include reflection, absorption, transmission, scattering and refraction. The energy of the photons is transformed into heat by absorption, resulting in heating, melting, vaporization, plasma formation, etc. These processes are largely dependent on the characteristic of the laser beam and the thermal-physical properties of the processed materials. If the processed material is melted by the laser radiation, the latent solidification process is of much interest. This is particularly important in laser surface modification for achieving desirable microstructures. Figure 2.4 shows the schematic of the important laser-material interactions.

(i) Absorption

The absorption of laser radiation is expressed by the Beer-Lambert law [145]:

$$I_{(z)} = I_0 e^{-\alpha z} \qquad \text{(Equation 2.3)}$$

where I is the intensity of the incident light at the depth z from the material surface, I_0 is the intensity just inside the surface after considering reflection loss, α is the material's absorption coefficient. The Beer-Lambert law describes the energy decay of the light with the depth inside the material. The penetration or absorption depth is defined as $1/\alpha$, at which the intensity falls to $1/e$ of the initial value I_0. For common metals, such as aluminium, iron, copper, etc., the penetration depth is on the order of 10 nm for ultraviolet, visible and near-infrared light.

The nature of absorption of light is the interaction between the electromagnetic radiation and the electrons (either free or bound). Therefore, α is a function of wavelength and temperature. At shorter wavelengths, more photons can be absorbed by a greater number of bound electrons and thus the absorptivity increases. The increase of temperature also enhances the energy exchanges and thus increases the absorptivity [146].

Surface roughness is another factor which has a significant influence on absorption. Keilmann [147] explained the effect of surface roughness with a mechanism of stimulated absorption due to the formation of periodic ripple pattern, acting as an anti-reflective coating.

(ii) Heating

Absorption of light results in the excess energy of the charged particles, giving rise to the temperature of irradiated material as a function of the depth from the surface. The temperature distribution can be assessed by simple one-dimensional heat conduction equation with the following assumptions [142]:

a. Material is homogeneous. The thermo-physical properties are independent of temperature.

b. The initial temperature of the material is constant.

c. Heat input is uniform during the irradiation time.

d. The convection and radiation losses from the surface are negligible.

The boundary condition assumes that the laser energy absorbed at the surface equals the energy conducted. The one-dimensional thermal diffusion equations were expressed as [148]:

$$T\left(z,t\right) = T_0 + \frac{2AI}{k\tau}\sqrt{\alpha t}\ \mathrm{ierfc}\left(\frac{z}{2\sqrt{\alpha t}}\right), 0 < t < \tau \qquad \text{(Equation 2.4)}$$

$$T'(z,t) = T_0 + \frac{2AI}{k\tau}\left(\sqrt{\alpha t}\ \mathrm{ierfc}\left(\frac{z}{2\sqrt{\alpha t}}\right) - \sqrt{\alpha(t-\tau)}\ \mathrm{ierfc}\left(\frac{z}{2\sqrt{\alpha(t-\tau)}}\right)\right),$$

$$t > \tau \qquad \text{(Equation 2.5)}$$

where T and T' are temperature distributions in the materials when the laser is on and off, respectively. A is the absorptivity of the materials at the 248 nm wavelength, I is the laser fluence, k is the thermal conductivity of the materials, τ is the pulse duration, t is the time and z is the depth from the material top surface. T_0 is the initial temperature. The thermal diffusivity (α) and the function ierfc(x) are determined by [148].

$$\alpha = \frac{k}{\rho c} \qquad \text{(Equation 2.6)}$$

$$\text{ierfc}(x) = \frac{1}{\sqrt{\pi}}\{e^{-x^2} - x(1 - \text{erf}(x))\} \qquad \text{(Equation 2.7)}$$

$$\text{erf}(x) = \frac{2}{\sqrt{\pi}}\int_0^x e^{-\xi^2}\,d\xi \qquad \text{(Equation 2.8)}$$

where ρ is the material mass density, c is the specific heat capacity, and erf(x) is error function. The temperature evolution in a material during laser irradiation can be summarized as [149]:

a. At the surface ($z = 0$), the temperature increases with t, reaches maximum at the end of irradiation ($t = \tau$), and then rapidly decreases.

b. At certain depths below the surface ($z > 0$), the temperature follows the same evolution with the position $z = 0$. However, the temperature reaches maximum at the longer time ($t > \tau$). The time ($t > \tau$) to reach the maximum temperature increases with increasing depth from the surface.

(iii) Melting

Laser power density above the threshold of melting can result in the formation of melt pool on the surface. According to the heating process discussed above, the material at the surface ($z = 0$) is heated up prior to melting and reaches the melting

point first. With the increase of irradiation time, the surface temperature increases to maximum at the end of irradiation ($t = \tau$) and the melt depth increases. Dahotre and Harimkar [142] take the melt depth at the end of irradiation as the maximum during the melting phase, followed by subsequent solidification phase. However, if we define the time t > τ as the cooling phase, solidification may not take place right at the beginning of the cooling stage. As the melt rapidly cools down because heat is absorbed by the bulk material, the latent heat from the melt can lead to further melting of the underlying substrate. Therefore, the melt depth can further increase and reach maximum at a point t > τ, after which solidification starts [150]. At this point, the temperature at the surface deceases to a temperature between the maximum and the melting point. The maximum melt depth increases with the laser fluence and the radiation time (pulse width for pulsed lasers) [142]. The positions of solid-liquid interface can be located by tracing the melting point in the temperature profile.

(iv) Vaporization

The melt depth cannot increase infinitely with the increase of laser power density and radiation time because surface evaporation occurs when the radiation reaches the threshold of vaporization. The vaporization limits the maximum surface temperature that can be achieved. Once the vaporization is initiated at the surface, further increase of laser fluence or radiation time will not affect the melt depth, but the liquid-vapour interface will move into the material, accompanied with the removal of material above the liquid-vapour interface [142].

(v) Plasma formation

If the laser power density is sufficiently high, the vapour or ambient gas can become ionized. The highly ionized vapour is termed as plasma, which strongly absorbs the laser irradiation. If the plasma attaches to the substrate when the laser power density

is just above the threshold for generating plasma, the plasma can transfer the absorbed energy to the substrate and thus improve the absorption of laser energy by the substrate. Such plasma coupling effect is particularly important in conditions where the substrate has a poor absorption of the laser energy. When the laser power density is significantly beyond the threshold for generating plasma, the formed plasma detaches from the substrate, stopping the laser beam from reaching the substrate and thus reducing the efficiency of the laser radiation in the applications of drilling, cutting, ablation, etc. Amoruso et al. [151] has proved the saturation of absorption due to the formation of highly absorbing or reflective plasma during laser irradiation of an Al target.

(vi) Ablation

Laser ablation is the removal of material from a substrate by direct breaking of molecular bonds above a threshold of laser fluence. The ablation threshold is the minimum energy required to remove the material by ablation. Below the ablation threshold, the material is thermal effects dominate. Typical threshold fluences are 1-10 J/cm^2 for metals, 0.5-2 J/cm^2 for inorganic insulators, and 0.1-1 J/cm^2 for organic materials [152]. Pulsed laser ablation finds extensive applications in materials processing, including micromachining, marking, grooving, cutting, drilling, and patterning of wide range of materials [142].

2.7.5 Rapid solidification

Solidification is very important for laser surface engineering because the behaviour of the melt during solidification determines the microstructure of the processed region. Two important parameters, the cooling rate (*CR*) and the temperature gradient (*G*), have strong influence on the development of microstructure during solidification. An important relationship between the two parameters is [153]:

$$CR = G \cdot SR \qquad \text{(Equation 2.9)}$$

where *SR* is the solidification rate, which is also referred to as growth front velocity. Some important features of the evolution of the three parameters are [142]:

a. The temperature gradient (*G*) is the maximum at the start of solidification and approaches zero at the end of solidification.

b. The cooling rate (*CR*) experiences a short transient period from zero to very high value at the beginning of solidification.

c. At the start of solidification, the solidification rate (*SR*) is zero and then approaches infinity as it proceeds towards the surface of the material.

The planar interface become instable to form a cellular, columnar, or dendritic structure when

$$\frac{G_{\text{Tl}}}{SR} \leq \frac{T_1 - T_s}{D_1} \qquad \text{(Equation 2.10)}$$

where G_{Tl} is the temperature gradient of the liquid close to the solid-liquid interface, D_1 is the diffusion coefficient of the solute in the liquid, T_1 is the liquidus temperature, and T_s is the solidus temperature [154]. This is the general estimation for the presence of constitutional supercooling, resulting from the ejection of solute. The tendency of the formation of dendritic structure increases with the decrease of the ratio between G_{Tl} and *SR*. The scale of the microstructures reduce with the increase of the cooling rate since it can be deduced that the cooling rate is inversely proportional to the square of the cell spacing [146], that is, the higher the cooling rate, the finer the microstructure. To eliminate the instability of the interface, a very large G_{Tl} is often required.
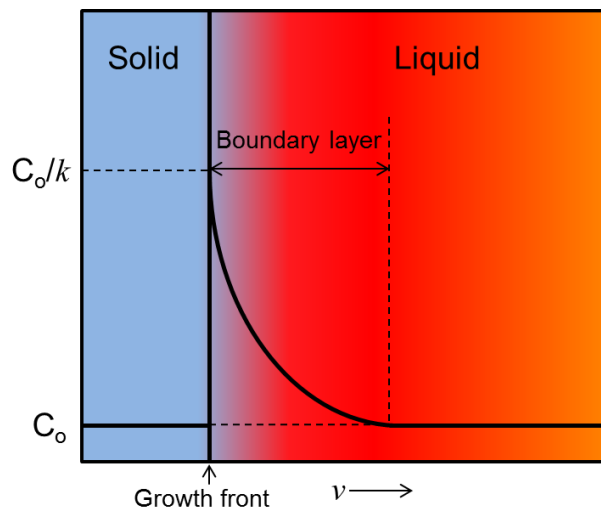
Figure 2.5 Schematic of the boundary layer at the solid-liquid interface during solidification [155]. C_o is the solute concentration in the liquid away from the solid/liquid interface and k is the partition coefficient.

The constitutional supercooling theory is limited to the solidification process at low *SR*, where the equilibrium condition presents. For laser material processing, which involves rapid solidification occurring under nonequilibrium conditions, the morphological stability theory is more applicable. The constitutional supercooling theory is a limiting case of the morphological stability theory, which further estimates the capillary effect that retards the growth of a perturbation and predicts a more stable interface during rapid solidification. The mathematical solution of this effect is not to be discussed here and can be found in [156].
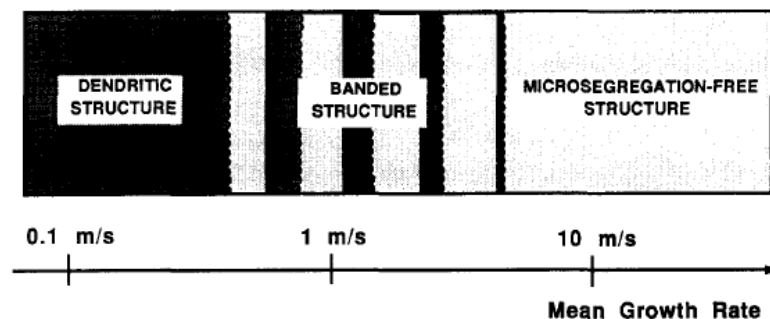
Figure 2.6 Schematic of the transition from dendritic structure to banded structure, and to microsegregation-free structure [157].

68

During solidification, solute enrichment will occur in the liquid close to the growth front of solidification due to the lower solubility of the solute atoms in the solid than that in the liquid alloy [155]. Therefore, a boundary layer is built up at the solid-liquid interface as shown in Figure 2.5. Under local equilibrium hypothesis at very low SR, the solute concentration in the solid equals to that in the liquid far from the interface that is not affected by the solute enrichment and the solute atoms ejected to the solid-liquid interface equals to that is taken away from the solid-liquid interface due to diffusion. Thus, the solute concentration in the liquid exponentially decreased from C_o/k to C_o as shown in Figure 2.5. k increases with the increase of SR as there is insufficient time for the solute to diffuse from the interface to the bulk liquid. At the same time, solute segregation at the cell boundaries and the interdendritic areas could occur during the formation of cellular or dendritic structure. This usually takes place in laser material processing using continuous wave lasers, which results in cellular or dendritic structure.

If the *SR* is sufficiently high, the solidification process obtains absolute stability and a microsegregation-free structure could be formed. In this case, k approaches 1 and complete solute trapping occurs. The growth mode changes from dendritic to planar. This typically occurs in laser material processing using short-pulsed lasers, such as excimer lasers, resulting in SR high enough to obtain absolute stability. The transition from dendritic structure to microsegregation-free structure could involve a banded structure, as shown in Figure 2.6 [157]. The formation of the banded structure has been reported during rapid solidification of various aluminium based alloys using various techniques such as laser- or electron-beam remelting, melt spinning or splat quenching [157]. The origin of the banded structure is possibly attributed to the oscillatory morphological instability of the planar interface, which is correlated with the SR dependent partition coefficient k and solid-liquid interface temperature [158-161].

The microstructural refinement achieved by different lasers could be different from each other due to the different cooling rates resulted from different lasers. The cooling rates during solidification vary from 10^5 to 10^{11} K/s according to the laser source applied [162, 163]. The solidification microstructure also depends on the composition of the processed materials. The microstructural refinement due to rapid solidification is the basis of LSM for corrosion protection.

2.8 Research progress on LSM of aluminium alloys and MMCs

Laser surface treatment has been applied to aluminium alloys since about four decades ago. By introducing refined microstructures, LSM shows the potential application for improvement of corrosion resistance of aluminium alloys. Later on, LSM was introduced to MMCs but the available literature is much less than that of aluminium alloys. In this section, research progress on LSM for improvement of corrosion resistance of aluminium alloys and MMCs is summarized.

2.8.1 LSM of aluminium alloys

LSM of aluminium alloys can be performed with continuous wave (CW) lasers and short-pulsed lasers. The laser-induced microstructure refinement and corrosion behaviour of laser-melted aluminium alloys have been extensively investigated.
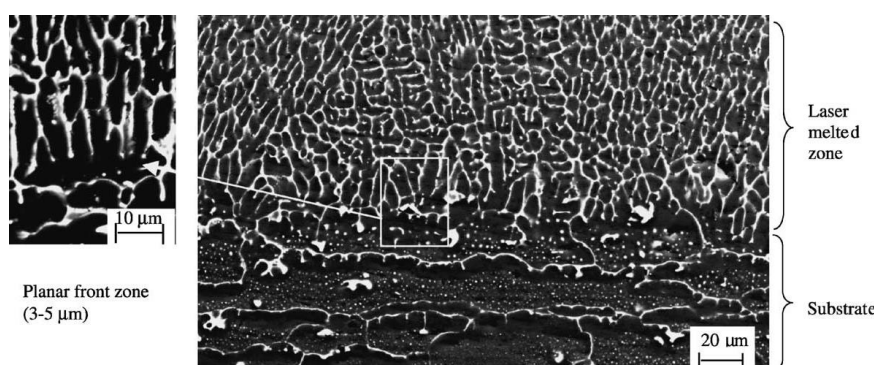
Figure 2.7 SEM micrograph showing the cross-section of a 3 kW CW Nd:YAG laser-melted AA2014-T6 aluminium alloy [135].

(i) CW lasers

CO_2 and Nd:YAG lasers are main industrial CW lasers used for corrosion protection of aluminium alloys. CW lasers are capable to generate thick melted layers with the thickness of several hundreds of micrometres due to the high energy input. An AA2014-T6 aluminium alloy was found to be of greater corrosion resistance after LSM using both CW CO_2 laser [136] and Nd:YAG laser [135]. The improvement of corrosion resistance was attributed to the extension of solubility of Cu in aluminium matrix. The increase of Cu in the solid solution increased the corrosion potential of the α-Al phase, reducing the driven force for the formation of galvanic cells between the Al_2Cu phase and the α-Al phase. Surekha et al. [164] suggested similar results on AA2219 aluminium alloy with reduced amount of Al_2Cu intermetallic particles after CW CO_2 LSM. It was also indicated that the solid solubility of Cu in Al matrix increased with the increasing cooling rate.

However, such intermetallics cannot be completely eliminated by CW CO_2 or Nd:YAG LSM. CW LSM usually results in the formation of cellular and/or dendritic structure in aluminium alloys. For AA2xxx aluminium alloys, Cu-bearing intermetallics were reduced in amount but still present in finer sizes at the cell or dendrite boundaries after CW CO_2 or Nd:YAG LSM [135, 165]. A typical cross-section of the melted region is shown in Figure 2.7. The re-melted microstructure started with a planar front zone (PFZ) at the fusion zone boundary, and then rapidly changed from cellular to cellular-dendritic/dendritic structure. The PFZs were reported to be of lower Cu concentration than the substrate (Figure 2.8) and extended from the bottom of the melt track to the surface of the alloy [135, 166]. Figure 2.8 also shows an increase of Cu concentration in the cellular/cellular-dendritic region and it is clearly that Cu was concentrated at the cell or dendrite boundaries. Such interdendritic Cu segregation could significantly affect the corrosion behaviour of the laser-melted aluminium alloys. It was found that the cell or dendrite cores were preferentially dissolved, leaving semi-networks of the Cu-rich boundaries, as shown

in Figure 2.9. This is strong evidence of the formation of galvanic cells between the cell/dendrite boundaries (cathode) and the cell/dendrite cores (anode).
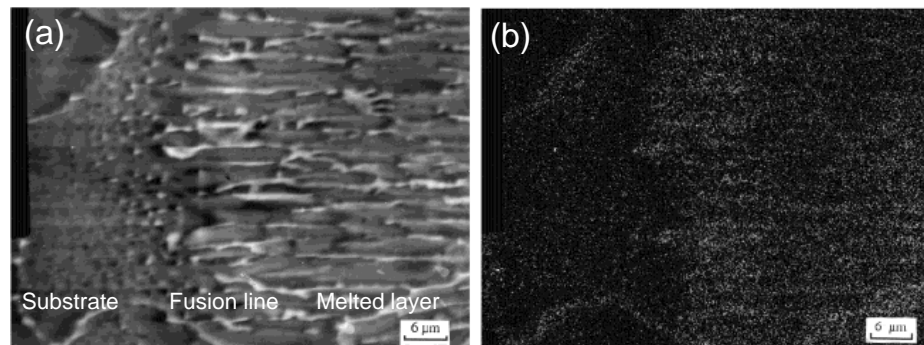
Figure 2.8 Cu distribution map in the PFZ of a 2 kW CW CO_2 LSM AA2014 aluminium alloy: (a) SEM micrograph and (b) Cu distribution in the corresponding zone [166].
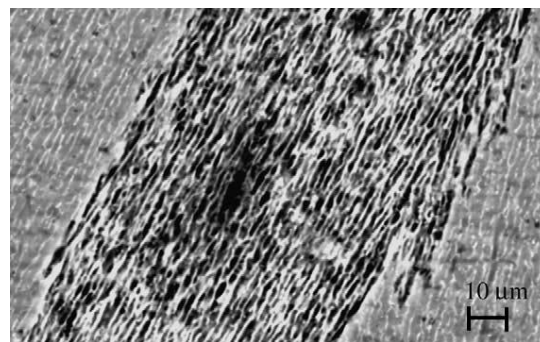
Figure 2.9 Pitting morphology of a 3 kW CW Nd:YAG laser-melted AA2014-T6 aluminium alloy after polarization to 530 mV_{SCE} [135].

Regarding the formation mechanism of Cu segregation at cell/dendrite boundaries, it can be explained as follows. As discussed above, when solidification begins, Cu is rejected from the solid due to the lower solubility of Cu in solid Al than liquid Al. Thus, a Cu-rich boundary layer is built up in the liquid right ahead of the solid-liquid interface, resulting in the formation of precipitates at the dendrite boundaries [166]. It was suggested that the extent of Cu segregation is largely dependent on the cooling rate during solidification; increasing laser power density and/or scan rate result in

higher cooling rate, extending the solubility of Cu in Al matrix and thus reducing the Cu segregation [135].

In AA2024 aluminium alloy, which is added with higher amount of Mg compared to AA2014 aluminium alloy, the CW CO_2 or Nd:YAG LSM could affect the corrosion behaviour in different mechanisms. Li et al. [165] reported the elimination of intergranular corrosion of AA2024-T351 aluminium alloy by LSM using a 2 kW CW CO_2 laser, being attributed to the elimination of Al_2CuMg intermetallic phase at grain boundaries. After LSM, the Al_2CuMg intermetallic phase distributed along the rolling direction or at grain boundaries changed into interdendritic Al_2Cu phase as a result of selective evaporation of Mg. However, Liu et al. [136] suggested that AA2024-T351 aluminium alloy subjected to CW CO_2 LSM showed no improvement in corrosion resistance. The difference of corrosion potential between Al matrix and the fine Al_2CuMg precipitates was enlarged by the extension of solubility of Cu in aluminium matrix, giving rise to galvanic corrosion. Pokhmurska et al. [167] also reported that the pitting susceptibility of AA2024-T3 aluminium alloy was not improved by CW CO_2 LSM due to the non-uniform structure of the laser-melted surface. The controversial results also imply that the corrosion performance of laser-melted aluminium alloys could vary with the operation conditions of LSM.
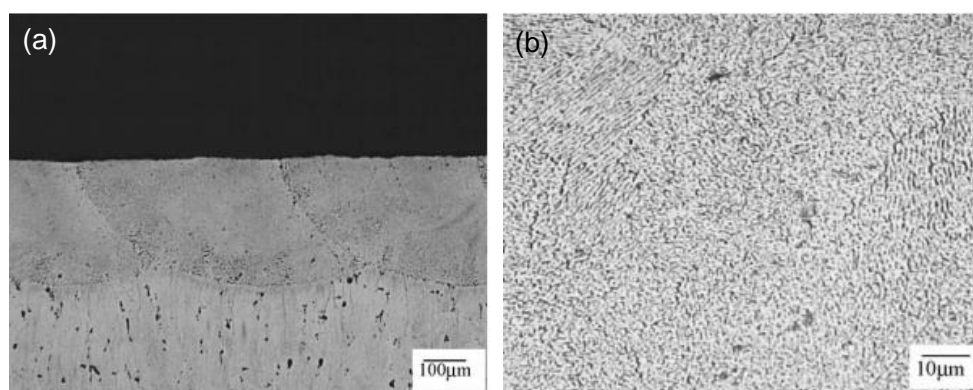
Figure 2.10 SEM micrographs showing the cross-section of LSM AA7075 aluminium alloy using CW Nd:YAG laser [133].

Yue et al. [133] investigated the pitting corrosion and stress corrosion cracking resistance of AA7075 aluminium alloy treated with a 2 kW CW Nd:YAG laser. A thick layer of 300 μm was formed (Figure 2.10(a)), primarily consisting of fine cellular/dendritic structure (Figure 2.10(b)). Their results indicated that both pitting corrosion and stress corrosion cracking resistance of AA7075 aluminium alloy was improved by Nd:YAG LSM. Similar results were reported in Nd:YAG LSM of AA6013-T651 aluminium alloy, which was found with significant improvement with pitting and pitting corrosion fatigue resistance [120]. However, the melted layers were formed with interdendritic phases without exception, which results in electrochemical potential differences leading to localised dissolution.

LSM performed with 1 kW CW CO_2 laser provided significant microstructure refinement to an Al-9% Si aluminium alloy with the dendritic arm spacing reduced to one fifth of the as-cast alloy [168, 169]. According to them, however, the corrosion resistance was not improved due to the laser-induced precipitation of Si; the Al-Si interface is susceptible to corrosion attack. Wong and Liang [170] suggested that the solubility of Si was extended over its saturated content in primary Al after CW CO_2 LSM of Al-Si alloys (0-13wt.% Si) and the corrosion resistance of the Al-Si alloys in 10% H_2SO_4 and 10% HNO_3 solutions was improved. But, it is noticeable that their corrosion resistance in chloride-containing 10% HCl and 5% NaCl solutions was not improved.

The discussion above indicates that the microstructural refinement induced by CW LSM could play minor role in the corrosion performance of laser-meted aluminium alloys. This could be due to the fact that the solidification rate is limited to the laser scan rate. According to Equation 2.9, the cooling rates resulted from CW LSM are thus limited to the order of 10^5-10^8 K/s for aluminium alloys, which can be found in literature [139, 171]. It can be concluded that the cooling rates in this range can result in microstructure refinement, such as reducing the size of secondary phases

and elimination of defects, to some extent, but the resulted microstructure could still somehow facilitate the corrosion initiation.
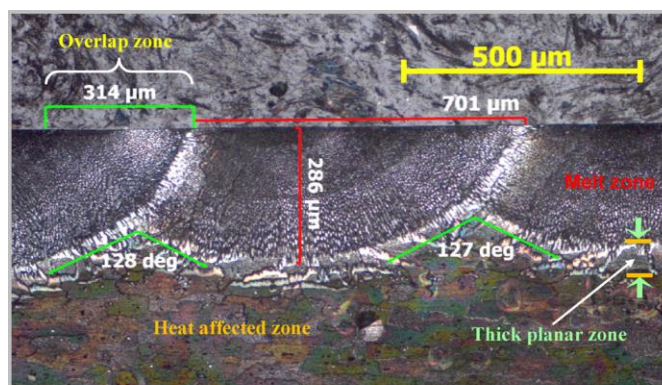
Figure 2.11 Optical micrograph showing the cross-section of the laser-melted frition stir weld of AA2024-T351 using a 1 kW fibre coupled diode laser [172].

Recently, HPDL was employed for LSM of friction stir weld of AA2024-T351 aluminium alloy [172]. The melted layer obtained using HPDL can be as thick as that obtained from CW CO_2 or Nd:YAG lasers due to its high thermal and energy efficiency. Figure 2.11 shows the cross-section morphology of the melted region consisting of a thick planar zone and epitaxially grown columnar structure, as well as a heat affected zone in the substrate. After LSM, the coarse intermetallics were dissolved and the alloying elements were uniformly distributed in the melted zone (Figure 2.12). However, EDX elemental mapping analysis at higher magnifications revealed slight Cu segregation at the columnar boundaries. The LSM weld showed an improved corrosion resistance compared to the untreated weld in chloride solution as shown in Figure 2.13, where the corrosion initiated at the substrate and the thick planar zone while the melted region was largely free from corrosion. Another study conducted by Benedetti et al. [138] suggested the microstructure of AA7075-T6 aluminium alloy could be refined after LSM using HPDL. However, the extent of improvement of corrosion performance of the laser-melted AA7075 aluminium alloy remains to be estimated since fine AlCuMg and $MgZn_2$ secondary phases are present.

Similar to the aluminium alloys processed by CW CO2 and Nd:YAG lasers, corrosion associated with the precipitates in interdendritic spaces could occur.
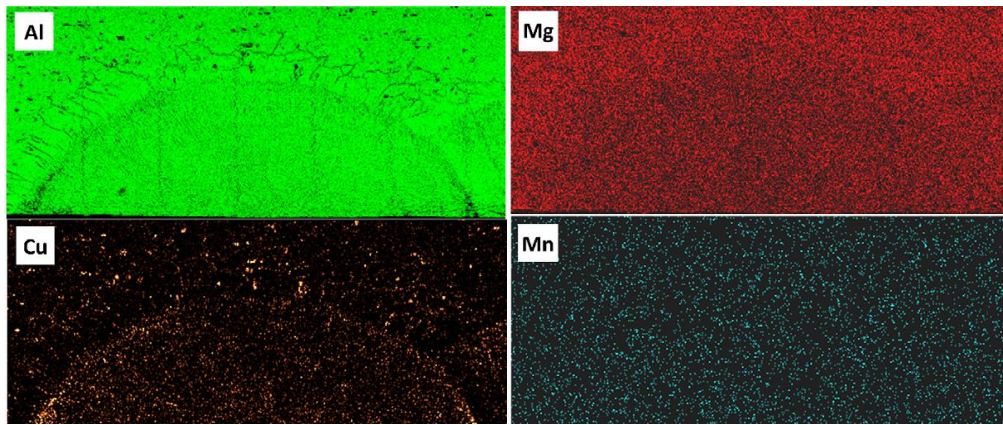
Figure 2.12 EDX elemental mapping for Al, Cu, Mg and Mn in a LSM friction stir weld of AA2024-T351 aluminium alloy [172].

(ii) Short-pulsed lasers
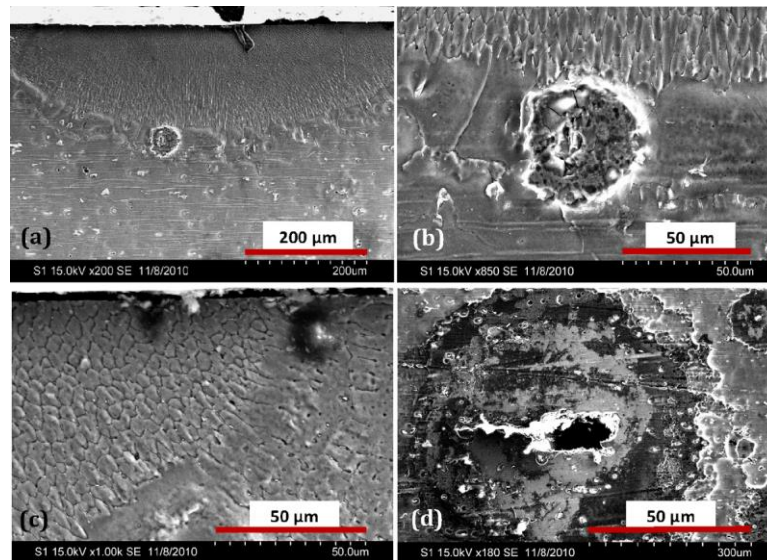
Figure 2.13 SEM micrographs after immersion test: (a) a complete melt track with no pitting inside and a small pit in the thick planar zone, (b) enlarges pit in the planar zone, (c) overlap region demonstrating no pitting and (d) large pit with extensive corrosion in the unmelted region [172].

Short-pulsed lasers, especially excimer lasers operated in the ultraviolet range, are of great interest for LSM applications. Although short-pulsed lasers produce thinner melted layers than CW lasers, the microstructure of the melted layer could be highly refined due to the extreme fast cooling rates up to the order of 10^{11} K/s [125].
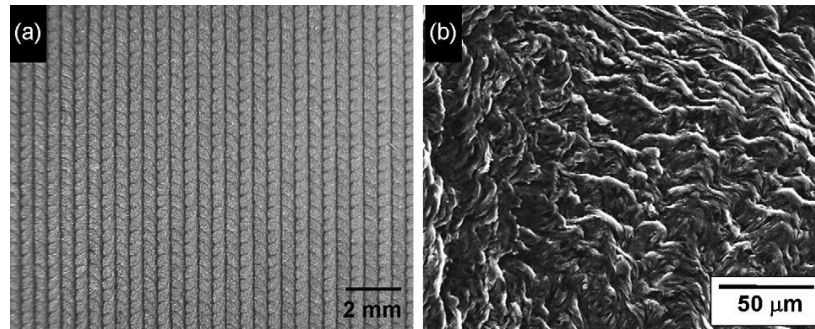
Figure 2.14 (a) Optical and (b) SEM micrographs of the surface of the excimer laser-melted AA2024 aluminium alloy [161].

Yilbas et al. [173] studied the corrosion behaviour of laser-melted AA8022 aluminium alloy treated with a pulsed CO_2 laser. They suggested that the corrosion current increased significantly after LSM due to the irregular surface morphology induced by LSM. Oxygen diffusion into the melted layer was confirmed by EDX analysis, indicating the oxidation of aluminium in the near-surface region. However, this did not contribute to any improvement of corrosion resistance. The results indicate that the corrosion behaviour of laser-melted aluminium alloys can be significantly affected by the surface morphology.

Excimer lasers have been employed for LSM of AA2050-T8 [125, 139, 174] and AA2024-T3 [174-176] aluminium alloys. The aluminium alloys were typically processed with the laser fluence of 5-6 J/cm^2 and number of pulses (NOP) ranging from 10 to 50. With such operation conditions, rippled structure forms over the melted surface (Figure 2.14). The formation of rippled structure could be attributed to the surface tension of the melt and the shear stresses generated from the surface tension gradients [177]. The surface gradient is associated with the non-uniform

distribution of temperature in the melt pool, that is, the temperature radially decreases from the centre of the melt pool to the circumference. The surface tension of a liquid may be written as $\sigma = \sigma_0 - ST$, where σ_0 is the surface enthalpy, S is the surface entropy and T is the temperature. Therefore, the temperature coefficient of the surface tension $(\partial\sigma/\partial T)$ is written as $\partial\sigma/\partial T = -S$. The radial decrease of temperature, which results in a decrease of S, contributes to the increase of surface tension from the beam centre to the circumference as the entropy S is always positive. After melting of the alloy occurred, the melt is pulled away from the centre by the surface tension and rapidly re-solidified, freezing up the flowing melt to form the rippled structure [177].

Excimer LSM could generate thin melted layers of a few microns. A typical cross-sectional morphology of the melted layer is shown in Figure 2.15(a), where the melted layer is free from visible precipitates with such resolution. The surface potential map indicates more homogeneous distribution of surface potential in the melted layer than the substrate (Figure 2.15(b)). A few micro-pores are present in the melted layer. Significant porosity was reported for the samples treated with 50 pulses [125]. The thickness of the melted layer generally increased with increasing NOP and oxide layer could be formed on the top surface with a thickness from a few nanometres to about 100 nm [125]. The corrosion performance of laser-melted aluminium alloys was improved compared to the as-received ones, being attributed to the formation of a homogeneous microstructure without chemical segregation. Yue et al. [178] investigated the pitting corrosion resistance of AA7075 aluminium alloy after excimer LSM and concluded that the formation of two oxide layers on the top surface was the main factor leading to the improvement of corrosion resistance of AA7075 aluminium alloy.

The potential application of excimer LSM as a pre-treatment prior to conventional anodising was also investigated. It was found that the corrosion resistance of the anodised aluminium alloys with excimer LSM as the pre-treatment was significantly

improved compared to that without excimer LSM [125, 174]. This was due to the high quality oxide film formed on the laser-melted surface as a result of the dissolution of intermetallics that may interfere with the anodising of aluminium.
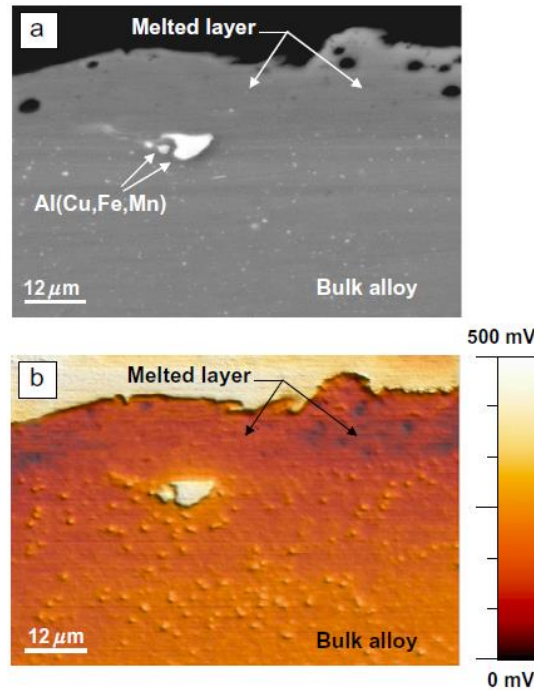
Figure 2.15 Backscattered SEM micrograph of the cross-section of KrF excimer laser-melted AA2050-T8 aluminium alloy and (b) the corresponding surface potential map obtained using SKPFM [139].
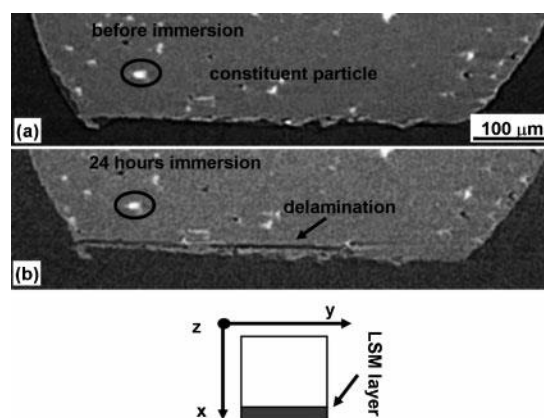
Figure 2.16 Cross-section SEM micrographs of excimer laser-melted AA2024-T351: (a) before immersion and (b) after immersion in 0.1 M NaCl for 24 h. Delamination of the melted layer was observed in (b) [179].

Excimer LSM is an effective way to increase the intergranular corrosion resistance of aluminium alloys. Chan et al. [124] and Yue et al. [180] suggested increase in both pitting corrosion and intergranular corrosion resistance of AA6013 and AA8090 aluminium alloy, respectively. The improvement of intergranular corrosion resistance was due to the elimination of the precipitates at grain boundaries in the melted layer. Further improvement can be achieved by LSM performed in N_2 gas, which facilitated the formation of stable AlN phase. Excimer LSM was also suggested to increase the resistance of aluminium alloys to stress corrosion cracking [131, 132] and corrosion fatigue [121, 134].

Application of excimer LSM has been extended to welds of aluminium alloys recently. Padovani et al.'s work on excimer LSM of welds of AA2024-T351 [179] and AA7449-T7951 [181] aluminium alloys have shown promising results for improvement of corrosion resistance of the weld region. However, during propagation of corrosion, delamination of the melted layer occurred for both alloys. The delaminated melted layer of AA2024-T351 aluminium alloy is shown in Figure 2.16.

The delamination of melted layer has been reported earlier in excimer laser-melted aluminium alloys during immersion in EXCO solution [174, 175], which is attributed to the formation of solute-rich segregation bands in the melted layer. Figure 2.17 shows the morphology of the segregation bands formed in excimer laser-melted AA2050-T8 aluminium alloy. The segregation bands are roughly parallel with the sample surface and concentrated at the melted layer/substrate interface. Yuan et al. [175] studied the composition of the segregation bands and found that the segregation bands formed in an AA2024-T351 aluminium alloy was rich in Cu (Figure 2.18). Ryan and Prangnell [161] suggested the segregation bands were probably in the form of Al_2CuMg. The formation of the segregation bands is believed to be due to the morphological instability of the solid-liquid interface during initial stages of solidification [161]. The delamination phenomenon of the melted

layer is considered as a main limitation of excimer LSM for corrosion protection of Al-Cu aluminium alloys.
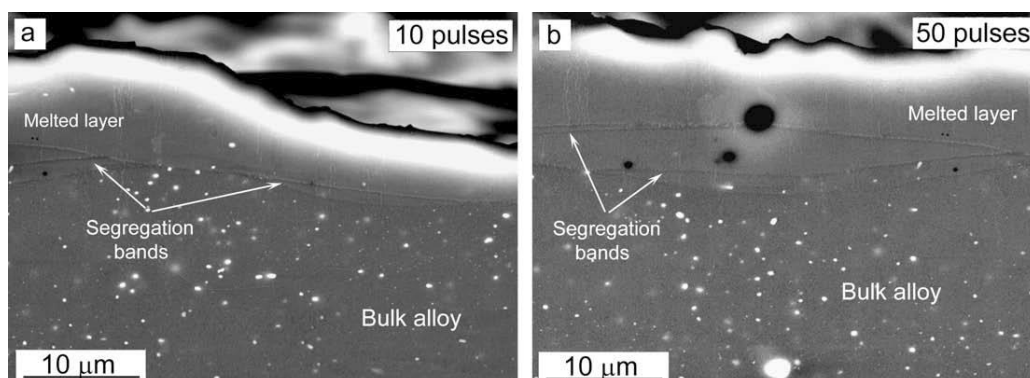
Figure 2.17 Cross-sectional SEM micrographs showing the morphology of the solute-rich segregation bands in the melted layer with different NOP: (a) 10 and (b) 50 [139].

2.8.2 LSM of SiC/Al MMCs
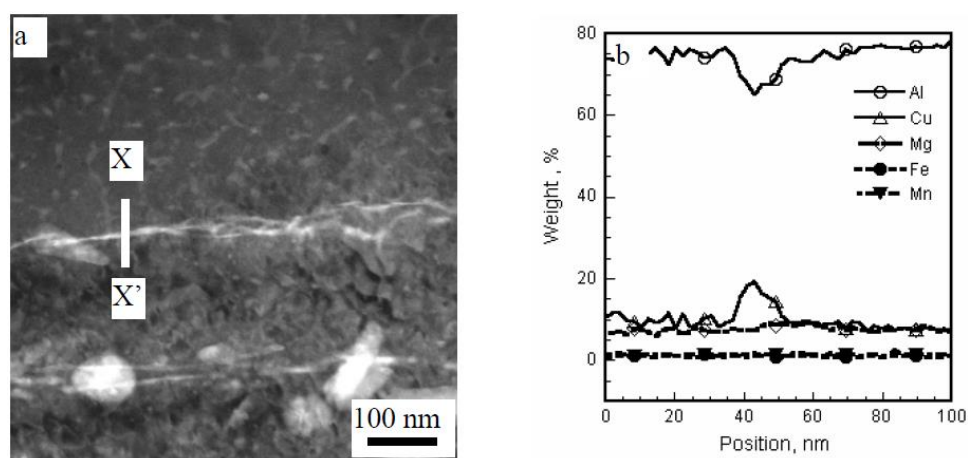
Figure 2.18 (a) High-angle annular dark-field (HAADF) transmission electron micrograph of the melted layer and (b) EDX elemental line profiles across the line X-X' [175].

LSM of SiC/Al MMCs for corrosion protection is less common in literature than LSM of aluminium alloys. Several investigators have done some initial work with various lasers. The results obtained are summarized below.

(i) CW lasers
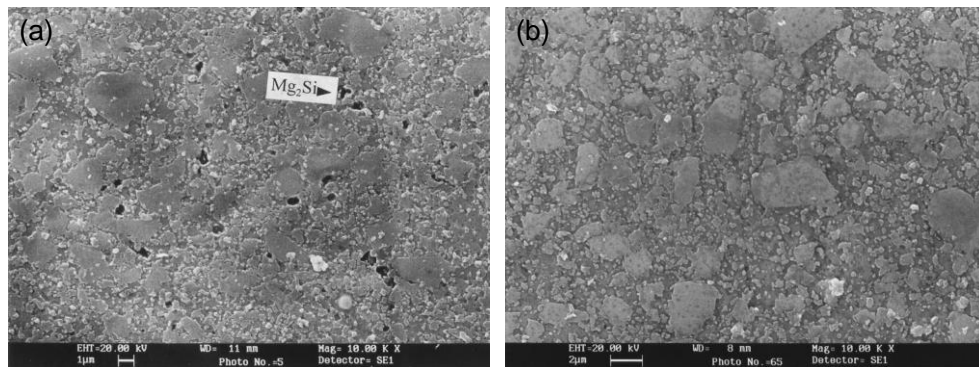
Figure 2.19 SEM micrographs of SiC$_p$/AA6013 MMC: (a) before LSM and (b) after LSM using CW Nd:YAG laser [123].
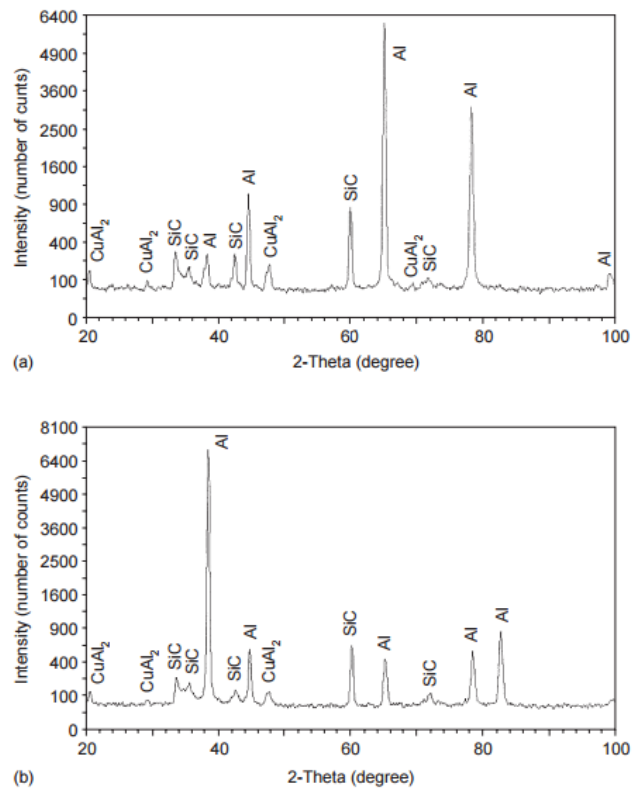
Figure 2.20 XRD analysis of SiC$_w$/AA2009 MMC: (a) before LSM and (b) after LSM [182].

Effort has been spent on the improvement of corrosion resistance of SiC/Al MMCs using CW Nd:YAG lasers. Yue et al. [123] employed a 2 kW CW Nd:YAG laser for

LSM of SiC_p/AA6013 MMC. According to them, the Mg_2Si precipitates on the surface were reduced (Figure 2.19), and the corrosion potential and pitting potential were increased by up to 230 mV and 60 mV after LSM, respectively. The pits size and amount were reduced in the laser-melted MMC due to the reduction and refinement of Mg_2Si precipitates, which were found to be sites for corrosion initiation in unmelted MMC [123].

The same authors also reported the improvement of corrosion resistance of SiC_w/AA2009 MMC induced by CW Nd:YAG LSM, being attributed to the reduction of SiC reinforcement, probably as a result of vaporization, and the reduction of Al_2Cu intermetallics that were susceptible to corrosion initiation [182]. It can be concluded that CW Nd:YAG lasers have the capability to reduce and refine the intermetallic phases in aluminium alloys. However, they can hardly eliminate such intermetallics completely. Figure 2.20 indicates that Al_2Cu phase is still observed after LSM.

HPDL was recently employed and found to be beneficial for corrosion performance of SiC_p/Al MMC by inducing a refined microstructure with homogeneous microdendrites and dissolution of cathodic intermetallic compounds (Figure 2.21) [183, 184].
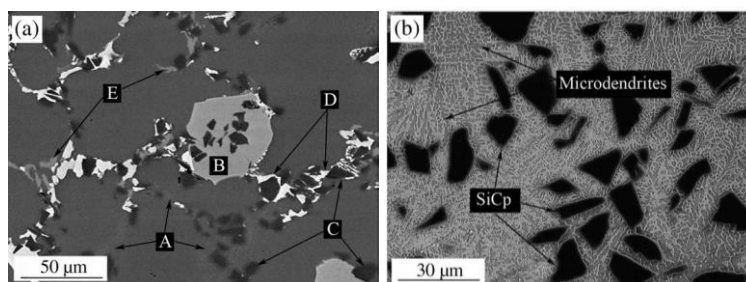
Figure 2.21 SEM micrographs of A380/SiC/10p MMC: (a) as-received and (b) laser-melted (HPDL). In (a), the different phases are marked as *A* Si eutectic; *B* AlFeSiMn-α intermetallic; *C* SiC particles; *D* $Al_2Cu(Mg)$ and *E* AlCuFe(Ni, Mn) [184].

Since LSM gives rise to the great increase of temperature in the melt pool, the chemical reactions between SiC and Al could take place. Although the above work discussed revealed no formation of the reaction product Al_4C_3, Shaban et al. [185], Hu and Baker [186], and Man et al. [187] reported that the detrimental Al_4C_3 compound was formed by CW Nd:YAG and CO_2 lasers melting or alloying. Therefore, excessive energy input and long interaction time during LSM should be avoided [188]. However, reducing the input energy or increase of the scan speed sacrifices the extent of the microstructure refinement, which could result in limited improvement of corrosion resistance [184].

(ii) Short-pulsed lasers

Compared to CW Nd:YAG lasers, excimer lasers are advantageous due to the pulsed operation mode and fast cooling rates, which significantly reduced the time for reactions between SiC reinforcement and Al matrix to take place. Nevertheless, there are few references regarding excimer LSM of SiC/Al MMCs.
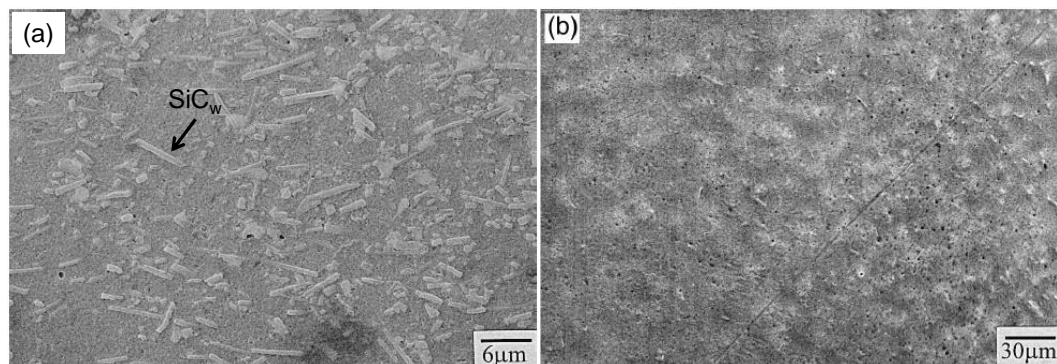
Figure 2.22 SEM micrographs showing the surface morphology of SiCw/AA2009 MMC: (a) before excimer LSM and (b) after excimer LSM [122].

Zhang et al. [119] and Yue et al. [122] suggested that the corrosion performance of SiC/Al MMCs could be improved by excimer LSM and they attributed the enhanced corrosion resistance to reduction of the SiC reinforcement and Cu-rich intermetallic phases on the surface. Figure 2.22 shows the reduction of the SiC whiskers exposed

on the surface after excimer LSM. Yue et al. [122] found that LSM carried out in N_2 gas further improved the corrosion resistance of SiC_w/AA2009 MMC as a result of the formation of AlN compound on the surface.

As indicated in these studies, relative low laser fluence was applied in their studies, and thus the melted layer was thin and there was still considerable amount of SiC reinforcement present on the surface. Furthermore, the mechanism of the microstructure refinement and laser-material interaction involving two phases (Al and SiC) remains to be investigated. The microstructural characterization limited to SEM observation is also insufficient to reveal such mechanism. The corrosion mechanism of the MMC after LSM remains unclear.

References

[1]   D. Altenpohl. Aluminium viewed from within: an introduction into the metallurgy of aluminium fabrication, Aluminium-Verlag, Dusseldorf, 1982.

[2]http://aluminium.matter.org.uk/content/html/eng/default.asp?catid=214&pageid=2144417081

[3]   L. Wang, M. Strangwood, D. Balint, J. Lin, T.A. Dean, *Formability and failure mechanisms of AA2024 under hot forming conditions*, Materials Science and Engineering a-Structural Materials Properties Microstructure and Processing, 528 (2011), 2648-2656.

[4]   G.M. Scamans, N.J.H. Holroyd, C.D.S. Tuck, *The role of magnesium segregation in the intergranular stress-corrosion cracking of aluminum-alloys*, Corrosion Science, 27 (1987), 329-347.

[5]   BS EN 515: Aluminium and aluminium alloys. Wrought products. Temper designations, BSI, 1993.

[6]   Y.C. Lin, Y.C. Xia, Y.Q. Jiang, H.M. Zhou, L.T. Li, *Precipitation hardening of 2024-T3 aluminum alloy during creep aging*, Materials Science and Engineering a-Structural Materials Properties Microstructure and Processing, 565 (2013), 420-429.

[7]   C.G. Cordovilla, E. Louis, *Characterization of the microstructure of a commercial Al-Cu alloy (2011) by differential scanning calorimetry (DSC)*, Journal of Materials Science, 19 (1984), 279-290.

[8]   L.F. Mondolfo. Al–Cu–Mg Aluminum–Copper–Magnesium system. in: Mondolfo LF, (Ed.). Aluminum Alloys, Butterworth-Heinemann, 1976. pp. 497-505.

[9]   S.C. Wang, M.J. Starink, *Two types of S phase precipitates in Al-Cu-Mg alloys*, Acta Materialia, 55 (2007), 933-941.

[10]   M.K. Surappa, *Aluminium matrix composites: Challenges and opportunities*, Sadhana-Academy Proceedings in Engineering Sciences, 28 (2003), 319-334.

[11]   T.W. Clyne, P.J. Withers. An Introduction to Metal Matrix Composites, Cambridge University Press, 1993.

[12]   M.H. Rahman, H.M.M.A. Rashed, *Characterization of silicon carbide reinforced aluminum matrix composites*, Procedia Engineering, 90 (2014), 103-109.

[13]   K.S. Al-Rubaie, H.N. Yoshimura, J.D.B. de Mello, *Two-body abrasive wear of Al-SiC composites*, Wear, 233 (1999), 444-454.

[14] S. Kumar, V. Balasubramanian, *Effect of reinforcement size and volume fraction on the abrasive wear behaviour of AA7075 Al/SiC(p) P/M composites-A statistical analysis*, Tribology International, 43 (2010), 414-422.

[15] P. Prangnell, W. Stobbs. Effect of internal stresses on precipitaiton behaviour in particulate reinforced Al matrix MMCs. Metal Matrix Composites- Processing, Microstructure and Properties. Proc. 12 th Riso Int. Symp. on Materials Science Roskilde, vol. 2, 1991.

[16] S. Ho, E.J. Lavernia, *Thermal residual stresses in metal matrix composites: A review*, Applied Composite Materials, 2 (1995), 1-30.

[17] M. Taya, T. Mori, *Dislocations punched-out around a short fiber in a short fiber metal matrix composite subjected to uniform temperature change*, Acta Metallurgica, 35 (1987), 155-162.

[18] C.T. Kim, M.R. Plichta, J.K. Lee, *Microstructural development and plastic relaxation of thermoelastic stress in Al/ceramic composites*, Fundamental Relationships between Microstructures and Mechanical Properties of Metal Matrix Composites, (1990), 371-386.

[19] R.J. Arsenault, N. Shi, *Dislocation generation due to differences between the coefficients of thermal-expansion*, Materials Science and Engineering, 81 (1986), 175-187.

[20] I. Dutta, D.L. Bourell, D. Latimer, *A theoretical investigation of accelerated aging in metal-matrix composites*, Journal of Composite Materials, 22 (1988), 829-849.

[21] H.Z. Ye, X.Y. Liu, *Review of recent studies in magnesium matrix composites*, Journal of Materials Science, 39 (2004), 6153-6171.

[22] A.A. Mahdy, *Fabrication and characterizations of Mg/SiC composite via compo-casting Technique*, Journal of American Science, 10 (2014), 196-202.

[23] D. Yadav, R. Bauri, *Processing, microstructure and mechanical properties of nickel particles embedded aluminium matrix composite*, Materials Science and Engineering a-Structural Materials Properties Microstructure and Processing, 528 (2011), 1326-1333.

[24] Y.C. Kang, S.L.I. Chan, *Tensile properties of nanometric Al_2O_3 particulate-reinforced aluminum matrix composites*, Materials Chemistry and Physics, 85 (2004), 438-443.

[25] X. Zhang, H. Hu, *Solidification of Magnesium (AM50A)/vol%. SiC_p composite*, 3rd International Conference on Advances in Solidification Processes, 27 (2012).

[26] H. Asgharzadeh, S.H. Joo, H.S. Kim, *Consolidation of carbon nanotube reinforced aluminum matrix composites by high-pressure torsion*, Metallurgical and

Materials Transactions a-Physical Metallurgy and Materials Science, 45A (2014), 4129-4137.

[27]   Y.D. Huang, K.U. Kainer, N. Hort, *Mechanism of grain refinement of Mg-Al alloys by SiC inoculation*, Scripta Materialia, 64 (2011), 793-796.

[28]   L. Zhao, H. Lu, Z. Gao, *Microstructure and mechanical properties of Al/graphene composite produced by high-pressure torsion*, Advanced Engineering Materials, 17 (2015), 976-981.

[29]   K.K.A. Kumar, A. Viswanath, T.P.D. Rajan, U.T.S. Pillai, B.C. Pai, *Physical, mechanical, and tribological attributes of stir-cast AZ91/SiC$_p$ composite*, Acta Metallurgica Sinica-English Letters, 27 (2014), 295-305.

[30]   K.M. Shorowordi, T. Laoui, A.S.M.A. Haseeb, J.P. Celis, L. Froyen, *Microstructure and interface characteristics of B$_4$C, SiC and Al$_2$O$_3$ reinforced Al matrix composites: a comparative study*, Journal of Materials Processing Technology, 142 (2003), 738-743.

[31]   J.C. Romero, R.J. Arsenault, *Anomalous penetration of Al into SiC*, Acta Metallurgica et Materialia, 43 (1995), 849-857.

[32]   J.C. Lee, J.P. Ahn, J.H. Shim, Z.L. Shi, H.I. Lee, *Control of the interface in SiC/Al composites*, Scripta Materialia, 41 (1999), 895-900.

[33]   H. Ribes, R. Dasilva, M. Suery, T. Bretheau, *Effect of interfacial oxide layer in Al-SiC particle composites on bond strength and mechanical-behavior*, Materials Science and Technology, 6 (1990), 621-628.

[34]   J.C. Lee, J.Y. Byun, C.S. Oh, H.K. Seok, H.I. Lee, *Effect of various processing methods on the interfacial reactions in SiC$_p$ 2024 Al composites*, Acta Materialia, 45 (1997), 5303-5315.

[35]   J.C. Romero, L. Wang, R.J. Arsenault, *Interfacial structure of a SiC/Al composite*, Materials Science and Engineering a-Structural Materials Properties Microstructure and Processing, 212 (1996), 1-5.

[36]   J.C. Lee, J.P. Ahn, Z.L. Shi, J.H. Shim, H.I. Lee, *Methodology to design the interfaces in SiC/Al composites*, Metallurgical and Materials Transactions a-Physical Metallurgy and Materials Science, 32 (2001), 1541-1550.

[37]   S. Long, O. Beffort, C. Cayron, C. Bonjour, *Microstructure and mechanical properties of a high volume fraction SiC particle reinforced AlCu$_4$MgAg squeeze casting*, Materials Science and Engineering a-Structural Materials Properties Microstructure and Processing, 269 (1999), 175-185.

[38]   S.D. Peteves, P. Tambuyser, P. Helbach, M. Audier, V. Laurent, D. Chatain, *Microstructure and microchemistry of the Al/SiC interface*, Journal of Materials Science, 25 (1990), 3765-3772.

[39]   J.C. Lee, J.P. Ahn, Z. Shi, Y. Kim, H.I. Lee, *Modification of the interface in SiC/Al composites*, Metallurgical and Materials Transactions a-Physical Metallurgy and Materials Science, 31 (2000), 2361-2368.

[40]   R.D. Evans, J.D. Boyd, *Near-interface microstructure in a SiC/Al composite*, Scripta Materialia, 49 (2003), 59-63.

[41]   J.C. Lee, J.Y. Byun, S.B. Park, H.I. Lee, *Prediction of Si contents to suppress the formation of Al_4C_3 in the SiC_p/Al composite*, Acta Materialia, 46 (1998), 1771-1780.

[42]   Z. Shi, S. Ochiai, M. Gu, M. Hojo, J.C. Lee, *The formation and thermostability of MgO and $MgAl_2O_4$ nanoparticles in oxidized SiC particle-reinforced Al-Mg composites*, Applied Physics a-Materials Science & Processing, 74 (2002), 97-104.

[43]   Z.L. Shi, J.M. Yang, J.C. Lee, D. Zhang, H.I. Lee, R.J. Wu, *The interfacial characterization of oxidized $SiC(_p)$/2014 Al composites*, Materials Science and Engineering a-Structural Materials Properties Microstructure and Processing, 303 (2001), 46-53.

[44]   Z.P. Luo, Y.G. Song, S.Q. Zhang, *A TEM study of the microstructure of SiC_p/Al composite prepared by pressureless infiltration method*, Scripta Materialia, 45 (2001), 1183-1189.

[45]   B. Noble, A.J. Trowsdale, S.J. Harris, *Low-temperature interface reaction in aluminium-silicon carbide particulate composites produced by mechanical alloying*, Journal of Materials Science, 32 (1997), 5969-5978.

[46]   S. Bao, K. Tang, A. Kvithyld, T. Engh, M. Tangstad, *Wetting of pure aluminium on graphite, SiC and Al_2O_3 in aluminium filtration*, Transactions of Nonferrous Metals Society of China, 22 (2012), 1930-1938.

[47]   D. Walter, I.W. Karyasa, *Solid state reactions in the Al-Si-C system*, Journal of the Chinese Chemical Society, 52 (2005), 873-876.

[48]   J.C. Lee, H.K. Seok, H.I. Lee, *Alloy design of thixoformable wrought SiC/Al alloy composites*, Materials Research Bulletin, 34 (1999), 35-42.

[49]   T.X. Fan, D. Zhang, Z.L. Shi, R.J. Wu, T. Shibayanagai, M. Naka, H. Mori, *The effect of Si upon the interfacial reaction characteristics in SiC_p/Al-Si system composites during multiple-remelting*, Journal of Materials Science, 34 (1999), 5175-5180.

[50]   A.C. Ferro, B. Derby, *Wetting behaviour in the Al-Si/SiC system: interface reactions and solubility effects*, Acta Metallurgica et Materialia, 43 (1995), 3061-3073.

[51]   J.C. Viala, P. Fortier, J. Bouix, *Stable and metastable phase-equilibria in the chemical interaction between aluminum and silicon-carbide*, Journal of Materials Science, 25 (1990), 1842-1850.

[52]   H. Ribes, M. Suery, G. Lesperance, J.G. Legoux, *Microscopic examination of the interface region in 6061-Al/SiC composites reinforced with as-received and oxidized SiC Particles*, Metallurgical Transactions a-Physical Metallurgy and Materials Science, 21 (1990), 2489-2496.

[53]   A. Urena, M.D. Escalera, P. Rodrigo, J.L. Baldonedo, L. Gil, *Active coatings for SiC particles to reduce the degradation by liquid aluminium during processing of aluminium matrix composites: study of interfacial reactions*, Journal of Microscopy-Oxford, 201 (2001), 122-136.

[54]   A.D. Mcleod, C.M. Gabryel, *Kinetics of the growth of spinel, $MgAl_2O_4$, on alumina particulate in aluminum-alloys containing magnesium*, Metallurgical Transactions a-Physical Metallurgy and Materials Science, 23 (1992), 1279-1283.

[55]   S. Candan, E. Bilgic, *Corrosion behavior of Al–60 vol.% SiC_p composites in NaCl solution*, Materials Letters, 58 (2004), 2787-2790.

[56]   S. Candan, E. Bilgic, *Corrosion behavior of Al-60 vol.% SiCp composites in NaCl solution*, Materials Letters, 58 (2004), 2787-2790.

[57]   S. Candan, *An investigation on corrosion behaviour of pressure infiltrated Al-Mg alloy/SiC_p composites*, Corrosion Science, 51 (2009), 1392-1398.

[58]   D. Imeson, D.L. Bartlett, *Microstructural origins of corrosion in a 20-percent SiC_P/2124 aluminum-alloy metal-matrix composite*, Journal of Microscopy-Oxford, 177 (1995), 347-356.

[59]   A.J. Griffiths, A. Turnbull, *An investigation of the electrochemical polarization behavior of 6061-aluminum metal-matrix composites*, Corrosion Science, 36 (1994), 23-35.

[60]   M.M. Buarzaiga, S.J. Thorpe, *Corrosion behavior of as-cast, silicon-carbide particulate-aluminum alloy metal-matrix composites*, Corrosion, 50 (1994), 176-185.

[61]   S.R. Nutt, R.W. Carpenter, *Non-equilibrium phase distribution in an Al-SiC composite*, Materials Science and Engineering, 75 (1985), 169-177.

[62]   J.S. Lin, P.X. Li, R.J. Wu, *Aging evaluation of cast particulate-reinforced SiC/Al(2024) composites*, Scripta Metallurgica Et Materialia, 28 (1993), 281-286.

[63]   W.J. Kim, D.W. Kum, H.G. Jeong, *Interface structure and solute segregation behavior in SiC/2124 and SiC/6061 Al composites exhibiting high-strain-rate superplasticity*, Journal of Materials Research, 16 (2001), 2429-2435.

[64]   I.B. Singh, D.P. Mandal, M. Singh, S. Das, *Influence of SiC particles addition on the corrosion behavior of 2014 Al-Cu alloy in 3.5% NaCl solution*, Corrosion Science, 51 (2009), 234-241.

[65]   M. Montoya-Davila, M.I. Pech-Canul, M.A. Pech-Canul, *Effect of SiC_p multimodal distribution on pitting behavior of Al/SiCp composites prepared by reactive infiltration*, Powder Technology, 195 (2009), 196-202.

[66]   Z. Szklarska-Smialowska, *Pitting corrosion of aluminum*, Corrosion Science, 41 (1999), 1743-1767.

[67]   P.M. Natishan, W.E. O'Grady, *Chloride ion interactions with oxide-covered aluminum leading to pitting corrosion: A review*, Journal of the Electrochemical Society, 161 (2014), C421-C432.

[68]   G.S. Frankel, *Pitting corrosion of metals - A review of the critical factors*, Journal of the Electrochemical Society, 145 (1998), 2186-2198.

[69]   E. McCafferty, *Sequence of steps in the pitting of aluminum by chloride ions*, Corrosion Science, 45 (2003), 1421-1438.

[70]   J. Kruger, *Passivity of metals - a materials science perspective*, International Materials Reviews, 33 (1988), 113-130.

[71]   G. Frankel, *Pitting corrosion*, 2003.

[72]   J.O. Park, C.H. Paik, Y.H. Huang, R.C. Alkire, *Influence of Fe﹣rich intermetallic inclusions on pit initiation on aluminum alloys in aerated NaCl*, Journal of the Electrochemical Society, 146 (1999), 517-523.

[73]   N. Birbilis, M.K. Cavanaugh, R.G. Buchheit, *Electrochemical behavior and localized corrosion associated with Al7Cu2Fe particles in aluminum alloy 7075-T651*, Corrosion Science, 48 (2006), 4202-4215.

[74]   G.O. Ilevbare, O. Schneider, R.G. Kelly, J.R. Scully, *In situ confocal laser scanning microscopy of AA 2024-T3 corrosion metrology - I. Localized corrosion of particles*, Journal of the Electrochemical Society, 151 (2004), B453-B464.

[75]   R.A. Cottis, L.L. *Shreir. Shreir's Corrosion*, Elsevier Science, 2009.

[76]   N. Perez. *Electrochemistry and Corrosion Science*, Springer US, 2004.

[77]   J.R. Davis. *Corrosion of Aluminium and Aluminium Alloys*, ASM International, 1999.

[78]   *https://www.nace.org/Corrosion-Central/Corrosion-101/Galvanic-Corrosion/*

[79]   D.M. Aylor, P.J. Moran, *Effect of reinforcement on the pitting behavior of aluminum-base metal matrix composites*, Journal of the Electrochemical Society, 132 (1985), 1277-1281.

[80]   P.P. Trzaskoma, E. Mccafferty, C.R. Crowe, *Corrosion behavior of SiC Al metal matrix composites*, Journal of the Electrochemical Society, 130 (1983), 1804-1809.

[81]   G.E. Kiourtsidis, S.M. Skolianos, E.G. Pavlidou, *A study on pitting behaviour of AA2024/SiC$_P$ composites using the double cycle polarization technique.*, Corrosion Science, 41 (1999), 1185-1203.

[82]   M.S.N. Bhat, M.K. Surappa, H.V.S. Nayak, *Corrosion behavior of silicon-carbide particle reinforced 6061/Al alloy composites*, Journal of Materials Science, 26 (1991), 4991-4996.

[83]   W.S. Hwang, H.W. Kim, *Galvanic coupling effect on corrosion behavior of Al alloy-matrix composites*, Metals and Materials International, 8 (2002), 571-575.

[84]   A.J. Trowsdale, B. Noble, S.J. Harris, I.S.R. Gibbins, G.E. Thompson, G.C. Wood, *The influence of silicon carbide reinforcement on the pitting behaviour of aluminium*, Corrosion Science, 38 (1996), 177-191.

[85]   C. Monticelli, F. Zucchi, F. Bonollo, G. Brunoro, A. Frignani, G. Trabanelli, *Application of electrochemical noise-analysis to study the corrosion behavior of aluminum composites*, Journal of the Electrochemical Society, 142 (1995), 405-410.

[86]   B. BOBIĆ, S. MITROVIĆ, M. BABIĆ, I. BOBIĆ, *Corrosion of metal-matrix composites with aluminium alloy substrates*, Tribology in industry, 32 (2010), 3-11.

[87]   L.H. Hihara, R.M. Latanision, *Galvanic corrosion of aluminum-matrix composites*, Corrosion, 48 (1992), 546-552.

[88]   J.E. Castle, L. Sun, H. Yan, *The use of scanning auger microscopy to locate cathodic centers in SiC$_P$/6061 Al MMC and to determine the current-density at which they operate*, Corrosion Science, 36 (1994), 1093-&.

[89]   P.C.R. Nunes, L.V. Ramanathan, *Corrosion behavior of alumina-aluminum and silicon carbide-aluminum metal-matrix composites*, Corrosion, 51 (1995), 610-617.

[90]   L. Diaz-Ballote, L. Veleva, M.A. Pech-Canul, M.I. Pech-Canul, D.O. Wipf, *Activity of SiC particles in Al-based metal matrix composites revealed by SECM*, Journal of the Electrochemical Society, 151 (2004), B299-B303.

[91]   R.L. Deuis, L. Green, C. Subramanian, J.M. Yellup, *Corrosion behavior of aluminium composite coatings*, Corrosion, 53 (1997), 880-890.

[92]   M. Metzger, S.G. Fishman, *Corrosion of aluminum-matrix composites - status-report*, Industrial & Engineering Chemistry Product Research and Development, 22 (1983), 296-302.

[93]   S. Candan, *Effect of SiC particle size on corrosion behavior of pressure infiltrated Al matrix composites in a NaCl solution*, Materials Letters, 58 (2004), 3601-3605.

[94]   Y.L. Saraswathi, S. Das, D.P. Mondal, *A comparative study of corrosion behavior of Al/SiC$_p$ composite with cast iron*, Corrosion, 57 (2001), 643-653.

[95]   B. Dikici, M. Gavgali, C. Tekmen, *Corrosion behavior of an artificially aged (T6) Al-Si-Mg-based metal matrix composite*, Journal of Composite Materials, 40 (2006), 1259-1269.

[96]   S.L. Coleman, V.D. Scott, B. Mcenaney, *Corrosion behavior of aluminum-based metal-matrix composites*, Journal of Materials Science, 29 (1994), 2826-2834.

[97]   Z. Feng, C. Lin, J. Lin, J. Luo, *Pitting behavior of SiC$_p$ 2024 Al metal matrix composites*, Journal of Materials Science, 33 (1998), 5637-5642.

[98]   Y. Shimizu, T. Nishimura, I. Matsushima, *Corrosion-resistance of Al-based metal-matrix composites*, Materials Science and Engineering a-Structural Materials Properties Microstructure and Processing, 198 (1995), 113-118.

[99]   S. Lin, H. Greene, H. Shih, F. Mansfeld, *Corrosion protection of Al/SiC metal matrix composites by anodizing*, Corrosion, 48 (1992), 61-67.

[100] F. Mansfeld, S.L. Jeanjaquet, *The evaluation of corrosion protection measures for metal matrix composites*, Corrosion Science, 26 (1986), 727-&.

[101] C.L. He, C.S. Liu, F.Q. Li, Q.K. Cai, Z.M. Shi, L.Q. Chen, J. Bi, *Corrosion behavior and protection efficiency of 2024Al and SiC$_p$/2024Al metal matrix composite*, Journal of Materials Science & Technology, 18 (2002), 351-353.

[102] H. Herrera-Hernandez, J.R. Vargas-Garcia, J.M. Hallen-Lopez, F. Mansfeld, *Evaluation of different sealing methods for anodized aluminum-silicon carbide (Al/SiC) composites using EIS and SEM techniques*, Materials and Corrosion-Werkstoffe Und Korrosion, 58 (2007), 825-832.

[103] C. Chen, F. Mansfeld, *Corrosion protection of an Al 6092/SiC$_p$ metal matrix composite*, Corrosion Science, 39 (1997), 1075-1082.

[104] H.J. Greene, F. Mansfeld, *Corrosion protection of aluminum metal-matrix composites*, Corrosion, 53 (1997), 920-927.

[105] Z. Ahmad, B.J.A. Aleem, *The effect of inhibitors on the susceptibility of Al 6013/SiC interface to localized corrosion*, Journal of Materials Engineering and Performance, 18 (2009), 129-136.

[106] I. Aziz, Z. Qi, X. Min, *Corrosion inhibition of SiC$_P$/5A06 aluminum metal matrix composite by cerium conversion treatment*, Chinese Journal of Aeronautics, 22 (2009), 670-676.

[107] I. Aziz, Q. Zhang, M. Xiang, *Using EIS to evaluate anti-corrosion properties of the SiC$_p$/5A06 aluminium MMC treated by cerium conversion coatings*, Journal of Rare Earths, 28 (2010), 109-116.

[108] A. Pardo, M.C. Merino, R. Arrabal, S. Merino, F. Viejo, A.E. Coy, *Effect of La surface treatments on corrosion resistance of A3xx.x/SiC$_p$ composites in salt fog*, Applied Surface Science, 252 (2006), 2794-2805.

[109] A. Pardo, M.C. Merino, R. Arrabal, F. Viejo, M. Carboneras, A.E. Coy, *Improvement of corrosion behavior of aluminum alloy/silicon carbide composites with lanthanum surface treatments*, Corrosion, 62 (2006), 141-151.

[110] F. Mansfeld, F.J. Perez, *Surface modification of Al/15%SiC metal matrix composite in molten salts containing CeCl$_3$*, Surface & Coatings Technology, 86 (1996), 449-453.

[111] A.S. Hamdy, A.M. Beccaria, P. Traverso, *Corrosion protection of aluminium metal-matrix composites by cerium conversion coatings*, Surface and Interface Analysis, 34 (2002), 171-175.

[112] F. Mansfeld, S. Lin, S. Kim, H. Shih, *Surface modification of Al-alloys and A1-based metal matrix composites by chemical passivation*, Electrochimica Acta, 34 (1989), 1123-1132.

[113] A.J. Lopez, A. Urena, M.D. Lopez, J. Rams, *Protection against corrosion of aluminium-SiC composites by sol-gel silica coatings*, Surface & Coatings Technology, 202 (2008), 3755-3763.

[114] S. Lin, H. Shih, F. Mansfeld, *Corrosion protection of aluminum-alloys and metal matrix composites by polymer-coatings*, Corrosion Science, 33 (1992), 1331-1349.

[115] S.H. Cui, J.M. Han, Y.P. Du, W.J. Li, *Corrosion resistance and wear resistance of plasma electrolytic oxidation coatings on metal matrix composites*, Surface & Coatings Technology, 201 (2007), 5306-5309.

[116] W.B. Xue, X.L. Wu, X.J. Li, H. Tian, *Anti-corrosion film on 2024/SiC aluminum matrix composite fabricated by microarc oxidation in silicate electrolyte*, Journal of Alloys and Compounds, 425 (2006), 302-306.

[117] J.M. Lee, K.B. Lee, J.H. Nam, S.Y. Ryu, D.S. Bae, J.T. Park, S.C. Kim, S.D. Cha, K.R. Kim, S.Y. Song, S.B. Kang, *Prognostic factors in FIGO stage IB-IIA small cell neuroendocrine carcinoma of the uterine cervix treated surgically: results of a multi-center retrospective Korean study*, Annals of Oncology, 19 (2008), 321-326.

[118] P. Zhang, X. Nie, H. Henry, J. Zhang, *Preparation and tribological properties of thin oxide coatings on an Al383/SiO$_2$ metallic matrix composite*, Surface & Coatings Technology, 205 (2010), 1689-1696.

[119]   X.M. Zhang, H.C. Man, T.M. Yue, *Corrosion properties of excimer laser surface treated Al-SiC metal matrix composite*, Scripta Materialia, 35 (1996), 1095-1100.

[120]   W.L. Xu, T.M. Yue, H.C. Man, *Nd : YAG laser surface melting of aluminium alloy 6013 for improving pitting corrosion fatigue resistance*, Journal of Materials Science, 43 (2008), 942-951.

[121]   W.L. Xu, T.M. Yue, H.C. Man, C.P. Chan, *Laser surface melting of aluminium alloy 6013 for improving pitting corrosion fatigue resistance*, Surface & Coatings Technology, 200 (2006), 5077-5086.

[122]   T.M. Yue, S.M. Mei, K.C. Chan, H.C. Man, *The effect of excimer laser surface treatment on corrosion resistance of aluminium 2009/SiC$_w$ composite*, Materials Letters, 39 (1999), 274-279.

[123]   T.M. Yue, Y.X. Wu, H.C. Man, *Laser surface treatment of aluminium 6013/SiC$_p$ composite for corrosion resistance enhancement*, Surface & Coatings Technology, 114 (1999), 13-18.

[124]   C.P. Chan, T.M. Yue, H.C. Man, *Effect of excimer laser surface treatment on corrosion behaviour of aluminium alloy 6013*, Materials Science and Technology, 18 (2002), 575-580.

[125]   F. Viejo, A.E. Coy, F.J. Garcia-Garcia, M.C. Merino, Z. Liu, P. Skeldon, G.E. Thompson, *Enhanced performance of the AA2050-T8 aluminium alloy following excimer laser surface melting and anodising processes*, Thin Solid Films, 518 (2010), 2722-2731.

[126]   J.W. Diggle, T.C. Downie, C.W. Goulding, *Anodic oxide films on aluminum*, Chemical Reviews, 69 (1969), 365-&.

[127]   A.J. Coleman, H.N. McMurray, G. Williams, A. Afseth, G. Scamans, *Filiform corrosion on 6000 series aluminium: Kinetics and inhibition strategies*, Aluminium Alloys 2006, Pts 1 and 2, 519-521 (2006), 629-633.

[128]   G. Williams, H.N. McMurray, *Anion-exchange inhibition of filiform corrosion on organic coated AA2024-T3 aluminum alloy by hydrotalcite-like pigments*, Electrochemical and Solid State Letters, 6 (2003), B9-B11.

[129]   G. Williams, H.N. McMurray, *Inhibition of filiform corrosion on organic-coated AA2024-T3 by smart-release cation and anion-exchange pigments*, Electrochimica Acta, 69 (2012), 287-294.

[130]   K.G. Watkins, M.A. McMahon, W.M. Steen, *Microstructure and corrosion properties of laser surface processed aluminium alloys: a review*, Materials Science and Engineering a-Structural Materials Properties Microstructure and Processing, 231 (1997), 55-61.

[131] W.L. Xu, T.M. Yue, H.C. Man, *Stress corrosion cracking behaviour of excimer laser treated aluminium alloy 6013*, Materials Transactions, 49 (2008), 1836-1843.

[132] T.M. Yue, C.F. Dong, L.J. Yan, H.C. Man, *The effect of laser surface treatment on stress corrosion cracking behaviour of 7075 aluminium alloy*, Materials Letters, 58 (2004), 630-635.

[133] T.M. Yue, L.J. Yan, C.P. Chan, *Stress corrosion cracking behavior of Nd : YAG laser-treated aluminum alloy 7075*, Applied Surface Science, 252 (2006), 5026-5034.

[134] C.P. Chan, T.M. Yue, H.C. Man, *The effect of excimer laser surface treatment on the pitting corrosion fatigue behaviour of aluminium alloy 7075*, Journal of Materials Science, 38 (2003), 2689-2702.

[135] P.H. Chong, Z. Liu, P. Skeldon, G.E. Thompson, *Large area laser surface treatment of aluminium alloys for pitting corrosion protection*, Applied Surface Science, 208 (2003), 399-404.

[136] Z. Liu, P.H. Chong, A.N. Butt, P. Skeldon, G.E. Thompson, *Corrosion mechanism of laser-melted AA 2014 and AA 2024 alloys*, Applied Surface Science, 247 (2005), 294-299.

[137] W.R. Osório, N. Cheung, J.E. Spinelli, K.S. Cruz, A. Garcia, *Microstructural modification by laser surface remelting and its effect on the corrosion resistance of an Al–9 wt%Si casting alloy*, Applied Surface Science, 254 (2008), 2763-2770.

[138] A. Benedetti, M. Cabeza, G. Castro, I. Feijoo, R. Mosquera, P. Merino, *Surface modification of 7075-T6 aluminium alloy by laser melting*, Surface and Interface Analysis, 44 (2012), 977-981.

[139] F. Viejo, A.E. Coy, F.J. Garcia-Garcia, Z.L.P. Skeldon, G.E. Thompson, *Relationship between microstructure and corrosion performance of AA2050-T8 aluminium alloy after excimer laser surface melting*, Corrosion Science, 52 (2010), 2179-2187.

[140] J. Ion. *Laser Processing of Engineering Materials - Principles, Procedure and Industrial Application*. Elsevier.

[141] S.C. Singh, H. Zeng, C. Guo, W. Cai. *Lasers: Fundamentals, Types, and Operations*. Nanomaterials, Wiley-VCH Verlag GmbH & Co. KGaA, 2012. pp. 1-34.

[142] N.B. Dahotre, S. Harimkar. *Laser Fabrication and Machining of Materials*, Springer US, 2008.

[143] K. Thyagarajan, A. Ghatak. *Lasers: Fundamentals and Applications*, Springer US, 2011.

[144] K.F. Renk. *Basics of Laser Physics for Students of Science and Engineering*, Springer Berlin Heidelberg, 2012.

[145] M.S. Brown, C.B. Arnold. *Fundamentals of Laser-Material Interaction and Application to Multiscale Surface Modification*. in: Sugioka K, Meunier M, Piqué A, (Eds.). Laser Precision Microfabrication, Springer Berlin Heidelberg, 2010.

[146] W.M. Steen, J. Mazumder. *Laser Material Processing*, Springer London, 2010.

[147] F. Keilmann. *Stimulated absorption of CO_2 laser light on metals*. in: Draper C, Mazzoldi P, (Eds.). Laser Surface Treatment of Metals, Springer Netherlands, 1986. pp. 17-22.

[148] J.F. Ready, D.F. Farson. *LIA handbook of laser materials processing*, Laser Institute of America Orlando, 2001.

[149] J. Wilson, J.F.B. Hawkes. *Lasers : principles and applications*, New York; London: Prentice Hall, 1987.

[150] E. Carpene, D. Höche, P. Schaaf. *Fundamentals of Laser-Material Interactions*. in: Schaaf P, (Ed.). Laser Processing of Materials: Fundamentals, Applications and Developments Springer Berlin Heidelberg, 2010.

[151] S. Amoruso, M. Armenante, V. Berardi, R. Bruzzese, N. Spinelli, *Absorption and saturation mechanisms in aluminium laser ablated plasmas*, Applied Physics a-Materials Science & Processing, 65 (1997), 265-271.

[152] D.W. Bäuerle. *Laser Processing and Chemistry*, Springer-Verlag Berlin Heidelberg, 2011.

[153] M.C. Flemings. *Solidification Processing*, McGraw-Hill, 1974.

[154] E. Kannatey-Asibu. *The Microstructure, Principles of Laser Materials Processing*, John Wiley & Sons, Inc., 2008. pp. 281-333.

[155] W. Kurz, D.J. Fisher. *Fundamentals of solidification*, Trans Tech Publications, 1986.

[156] E. Kannatey-Asibu. *Solidification. Principles of Laser Materials Processing*, John Wiley & Sons, Inc., 2008. pp. 334-360.

[157] M. Carrard, M. Gremaud, M. Zimmermann, W. Kurz, *About the banded structure in rapidly solidified dendritic and eutectic alloys*, Acta Metallurgica et Materialia, 40 (1992), 983-996.

[158] S.L. Sobolev, *Influence of local nonequilibrium on the rapid solidification of binary alloys*, Technical Physics, 43 (1998), 307-313.

[159] S.R. Coriell, R.F. Sekerka, *Oscillatory morphological instabilities due to non-equilibrium segregation*, Journal of Crystal Growth, 61 (1983), 499-508.

[160]   G.J. Merchant, S.H. Davis, *Morphological instability in rapid directional solidification*, Acta Metallurgica et Materialia, 38 (1990), 2683-2693.

[161]   P. Ryan, P.B. Prangnell, *Grain structure and homogeneity of pulsed laser treated surfaces on Al-aerospace alloys and FSWs*, Materials Science and Engineering: A, 479 (2008), 65-75.

[162]   C. Kim, L.S. Weinman, *Porosity formation in laser surface melted aluminum-alloys*, Scripta Metallurgica, 12 (1978), 57-60.

[163]   C.W. Draper, C.A. Ewing, *Laser surface alloying - a bibliography*, Journal of Materials Science, 19 (1984), 3815-3825.

[164]   K. Surekha, B.S. Murty, K.P. Rao, *Comparison of corrosion behaviour of friction stir processed and laser melted AA2219 aluminium alloy*, Materials & Design, 32 (2011), 4502-4508.

[165]   R. Li, M.G.S. Ferreira, A. Almeida, R. Vilar, K.G. Watkins, M.A. McMahon, W.M. Steen, *Localized corrosion of laser surface melted 2024-T351 aluminium alloy*, Surface & Coatings Technology, 81 (1996), 290-296.

[166]   K.G. Watkins, Z. Liu, M. McMahon, R. Vilar, M.G.S. Ferreira, *Influence of the overlapped area on the corrosion behaviour of laser treated aluminium alloys*, Materials Science and Engineering a-Structural Materials Properties Microstructure and Processing, 252 (1998), 292-300.

[167]   H. Pokhmurska, L. Kwiatkowski, W. Kalita, J. Hoffman, *Corrosion behaviour of laser remelted aluminium alloy*, Laser Technology Vii: Applications of Lasers, 5229 (2003), 260-265.

[168]   W.R. Osorio, N. Cheung, J.E. Spinelli, K.S. Cruz, A. Gacia, *Microstructural modification by laser surface remelting and its effect on the corrosion resistance of an Al-9 wt% Si casting alloy*, Applied Surface Science, 254 (2008), 2763-2770.

[169]   W.R. Osorio, N. Cheung, L.C. Peixoto, A. Garcia, *Corrosion resistance and mechanical properties of an Al 9wt%Si alloy treated by laser surface remelting*, International Journal of Electrochemical Science, 4 (2009), 820-831.

[170]   T.T. Wong, G.Y. Liang, *Effect of laser melting treatment on the structure and corrosion behaviour of aluminium and Al-Si alloys*, Journal of Materials Processing Technology, 63 (1997), 930-934.

[171]   P.W. Leech, *The laser surface melting of aluminum silicon-based alloys*, Thin Solid Films, 177 (1989), 133-140.

[172]   S.J. Kalita, *Microstructure and corrosion properties of diode laser melted friction stir weld of aluminum alloy 2024 T351*, Applied Surface Science, 257 (2011), 3985-3997.

[173] B.S. Yilbas, M. Khaled, C. Karatas, *Corrosion properties and morphology of laser melted aluminum alloy 8022 surface*, Journal of Materials Engineering and Performance, 18 (2009), 1-7.

[174] F. Viejo, Z. Aburas, A.E. Coy, F.J. Garcia-Garcia, Z. Liu, P. Skeldon, G.E. Thompson, *Performance of Al alloys following excimer LSM-anodising approaches*, Surface and Interface Analysis, 42 (2010), 252-257.

[175] Y. Yuan, Z. Aburas, T. Hashimoto, Z. Liu, P. Skeldon, G. Thompson, *Microstructure analysis and corrosion study of excimer laser modified AA2024-T351*, ECS Transactions, 11 (2008), 49-58.

[176] O. Kachurina, T.L. Metroke, K. Dou, *Laser-induced electrochemical characteristics of aluminum alloy 2024-T3*, Journal of Laser Applications, 16 (2004), 46-51.

[177] T.R. Anthony, H.E. Cline, *Surface pippling induced by surface-tension gradients during laser surface melting and alloying*, Journal of Applied Physics, 48 (1977), 3888-3894.

[178] T.M. Yue, L.J. Yan, C.P. Chan, C.F. Dong, H.C. Man, G.K.H. Pang, *Excimer laser surface treatment of aluminum alloy AA7075 to improve corrosion resistance*, Surface and Coatings Technology, 179 (2004), 158-164.

[179] C. Padovani, A.J. Davenport, B.J. Connolly, S.W. Williams, E. Siggs, A. Groso, M. Stampanoni, *Corrosion protection of AA2024-T351 friction stir welds by laser surface melting with Excimer laser*, Corrosion Engineering, Science and Technology, 47 (2012), 188-202.

[180] T.M. Yue, C.P. Chan, L.J. Yan, H.C. Man, *Effect of excimer laser surface melting on intergranular corrosion cracking of the aluminum-lithium alloy 8090*, Journal of Laser Applications, 16 (2004), 31-39.

[181] C. Padovani, A.J. Davenport, B.J. Connolly, S.W. Williams, E. Siggs, A. Groso, M. Stampanoni, *Corrosion protection of AA7449-T7951 friction stir welds by laser surface melting with an Excimer laser*, Corrosion Science, 53 (2011), 3956-3969.

[182] T.M. Yue, Y.X. Wu, H.C. Man, *Improvement in the corrosion resistance of aluminum 2009/SiC$_w$ composite by Nd:YAG laser surface treatment*, Journal of Materials Science Letters, 18 (1999), 173-175.

[183] J. Rams, A. Pardo, A. Urena, R. Arrabal, F. Viejo, A.J. Lopez, *Surface treatment of aluminum matrix composites using a high power diode laser*, Surface & Coatings Technology, 202 (2007), 1199-1203.

[184] F. Viejo, A. Pardo, J. Rams, M.C. Merino, A.E. Coy, R. Arrabal, E. Matykina, *High power diode laser treatments for improving corrosion resistance of*

A380/SiC$_p$ aluminium composites, Surface & Coatings Technology, 202 (2008), 4291-4301.

[185]   A. Shaban, W.Q. Hong, L.G. Yu, H.M. Wang, *Microstructure of a laser surface melted SiC particle reinforced aluminum metal metal composite*, 1999 International Conference on Industrial Lasers (Il'99), 3862 (1999), 453-457.

[186]   C. Hu, T.N. Baker, *Laser processing to create in-situ Al-SiC$_p$ surface metal-matrix composites*, Journal of Materials Science, 30 (1995), 891-897.

[187]   H.C. Man, C.T. Kwok, T.M. Yue, *Cavitation erosion and corrosion behaviour of laser surface alloyed MMC of SiC and Si$_3$N$_4$ on Al alloy AA6061*, Surface & Coatings Technology, 132 (2000), 11-20.

[188]   A. Grabowski, G. Moskal, *Laser surface treatment of aluminium matrix composites*, Laser Technology 2012: Applications of Lasers, 8703 (2013).

Chapter 3 Experimental procedure

3.1 Materials

The materials used in the present study were SiC_p/AA2124 MMCs reinforced with 25 vol.% SiC particles, and the monolithic AA2124 alloy (MA), supplied by Materion Corporation, UK. Two types of MMCs were involved and the average dimensions of SiC particles were 3 μm and 0.7 μm, termed as composite A and composite B, respectively. The MMCs were manufactured in solid state in a powder metallurgy route using hot isostatic pressing technique and supplied in 5 mm thick slices. T4 heat treatment was employed on such MMCs. The chemical composition of AA2124 alloy was (wt.%): 3.98 Cu, 1.77 Mg, 0.68 Mn, 0.12 Fe, 0.12 Si, <0.1 Cr, <0.1 Ti, 0.24 Zn, and Al as balance.

3.2 Sample preparation

3.2.1 Mechanical grinding and polishing

The slices of the as-received materials were cut into small pieces with the dimensions of 20 mm x 20 mm x 5 mm. Before all the experiments, the samples were mechanically wet ground with 240, 400, 800 and 1200 grit silicon carbide papers sequentially, then rinsed in deionized water and ethanol, and finally dried in warm air. The ground samples were used for excimer LSM and corrosion tests of the as-received materials.

For microstructural characterization, the ground samples were polished sequentially using 6, 3 and 1 μm diamond paste; and finally finished with oxide polishing suspension to achieve the mirror finish. For cross-sectional observation, the samples were cut along the section to be examined and mounted in a conductive resin. Then, the samples were ground and polished following the procedure mentioned above.

3.2.2 Ultramicrotomy

Ultramicrotomy is a technique firstly employed in biological field and then extended to the preparation of thin films with electron transparency of some relative soft materials, such as aluminium [1]. In the present study, ultramicrotomy was used to prepare the samples of both as-received and laser-melted AA2124 aluminium alloys for transmission electron microscopy (TEM). Since the SiC particles are relatively hard, the diamond knife can be easily damaged, and thus, the TEM samples of the MMCs cannot be prepared using ultramicrotomy.

The following procedure was applied to obtain the ultramicrotomed slices for TEM observation on the cross-section. The AA2124 aluminium alloy was cut into the dimensions of 20 mm x 7 mm x 2 mm and then encapsulated in embedding resin. After curing the resin at 60 ^{o}C for 24 hours, the sample was wet ground to obtain a sharp tip, which was then trimmed with a glass knife prepared by Leica EM KM2 glass knife maker to determine a cutting area of approximately 200 x 50 μm^2. The ultramicrotomed slice was finally obtained by cutting using a Micro Star diamond knife with a step size of 15 nm at the cutting speed of 0.15 mm/s. The thin slices floated on the water bath, which were then collected using the ATHENE $^®$ 400 mesh nickel grids with the diameters of 3.05 mm and examined using TEM. The surface of the cut tip for laser-melted AA2124 aluminium alloy was examined using SEM to investigate the cross-section of the melted layer.

3.2.3 Focused ion beam milling

Focused ion beam (FIB) system is a versatile system widely used in the scientific and industrial communities. It is commonly employed as a milling tool in tasks such as TEM cross-section sample preparation. FIB milling removes (sputters) the target material using a beam of positively charged ions emitted from liquid metal ion source, which is mostly consisted of gallium in commercial FIB systems. The FIB

systems are also available for material deposition, usually Pt or W, by gas ion injection, allowing areas of interest to be protected during sample preparation.

The FIB is similar to a scanning electron microscope (SEM) in many ways, except involving an ion beam instead of an electron beam. The FIB system employed in the present work is an FEI Quanta 3D FEG, which is a DualBeam instrument that combines a traditional Field Emission column with a FIB column mounted at an angle of 52°. The stage is untilted in SEM mode so that the surface is perpendicular to the electron beam while the stage is tilted through 52° in FIB mode so that the surface is perpendicular to the ion beam. The maximum acceleration voltage of the ion beam is 30 kV with the resolution of 7 nm. The ion probe current varies from 1 pA–65 nA, allowing both fast etching of materials and fine polishing to remove surface damage from cross-sectioned samples.

The cross-section samples were prepared using the FIB milling and lift-out technique. The operation followed the procedures detailedly described in [2].

3.2.4 Precision ion polishing system

Precision ion polishing system was also employed to prepare the TEM samples of as-received MMCs. Samples were wet ground with the finish of 4000 grit silicon carbide papers and mechanical polished to obtain a thin foil with the thickness less than 100 μm, and then punched into 3 mm discs. After precision ion polishing, ultrathin region was generated in the middle part of the sample, which can be evaluated with TEM.

The equipment employed in the present work for precision ion polishing is Gatan 691 Precision Ion Polishing System. The 3 mm disc was put into a holder made for PIPS (DuoPost ™, clamp type 3mm, by Gatan Inc.), and the holder with the disc was placed in the chamber of the machine. The sample was ion polished initially with the angles of ± 8° at 5 keV. Once light transmission was achieved, the ion polishing

parameters were changed to ± 3°, 3 keV in order to larger ultrathin area.

3.2.5 Sample preparation for corrosion evaluation

For electrochemical tests and immersion test, the samples were connected to a copper wire by a spot welder. All the surfaces and the connection were masked using a 45-stopping off lacquer and dried in air to define a 1 x1 cm^2 area to be tested.

3.3 Excimer LSM
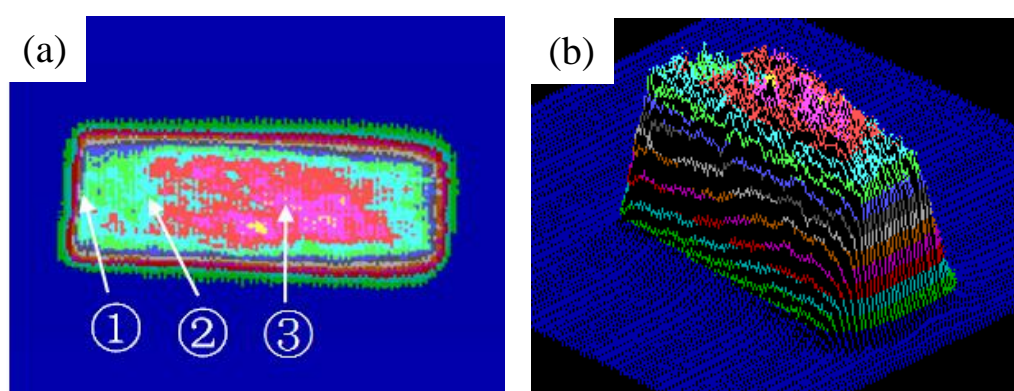
Figure 3.1 The KrF excimer laser beam intensity distribution in (a) 2-dimensions and (b) 3-dimensions [3]. The central area in red possesses higher energy density than surrounding areas.

LSM was performed on the ground sample surfaces in air using a 248 nm Lumonics IPEX848 KrF excimer laser with pulse width of ~15 ns. The laser can be operated with maximum energy input of 450 mJ and maximum repetition rate of 200 Hz. However, the actual maximum energy input measured on arrival of the sample surface is less than 400 mJ. The spot size of the laser beam was set at 3 x 1.5 cm^2. The laser beam was non-polarized and had an energy distribution within the beam profile as shown in Figure 3.1. A schematic of the LSM processing used in this research work is shown in Figure 3.2. The red dotted rectangle represents the beam spot, which scans the sample surface along the short side of the spot at the selected

velocity. Therefore, each track has a width of 3 mm with an overlapped area and a re-heated area between adjacent tracks, covering selected area of the sample surface.
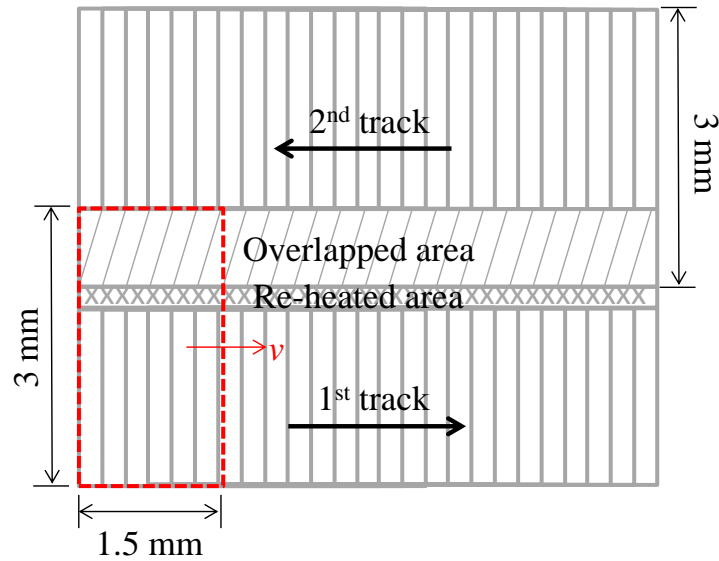
Figure 3.2 Schematic of LSM processing in this research work.

The main variables during LSM include:

(i) Laser fluence

Laser fluence (F) is the energy of the laser pulse per unit area. It is also referred to as the energy density and expressed as:

$$F = E/A \qquad\qquad \text{(Equation 3.1)}$$

where E is the input energy and A is the irradiated area (beam spot size). Once F is set, the peak power density P_p is determined. The peak power density is expressed as:

$$P_p = F/\tau \qquad\qquad \text{(Equation 3.2)}$$

where τ is the pulse width.

(ii) Number of pulses

NOP is the number of pulses per unit area. It is expressed as:

$$\text{NOP} = \frac{W}{v} f \qquad \text{(Equation 3.3)}$$

where W is the width of one side of the rectangle laser beam, along which the laser beam scans the surface, v is the scan rate, and f is the frequency.

(iii) Overlapping ratio

For large area coverage, overlapping of adjacent tracks is necessary due to multiple passes of the laser beam. The overlapped area between adjacent tracks will be subjected to an extra pass of the laser beam compared to the track centres. Between the overlapped area and the first track, there will be a re-heated area as shown in Figure 3.2.

3.4 Microscopy

3.4.1 Optical microscopy

Optical microscopy was mainly involved in the current work as one of the main techniques to observe the microstructure of AA2124 aluminium alloy and the MMCs. Observation was made by AxioCam ERc 5s Zeiss microscope camera and JVC TK-C1380 colour video camera. The images were then processed by AxioVision SE64 Rel. 4.9 Software.

3.4.2 Scanning electron microscopy

Scanning electron microscopy (SEM) is one of the techniques involved in microstructural characterization. In SEM, the sample surface is scanned by a focused beam of electrons and signals are collected by various detectors for imaging and

analysis of chemical composition. Essential components of a scanning electron microscope includes vacuum chamber, electron source (gun), condenser lens, scanning coils, sample chamber and detectors for various signals. There are two types of electron guns, i.e. thermionic guns and field emission guns (FEG). The thermionic guns are usually made of tungsten, generating electron beam by applying thermal energy to the tungsten filament. FEG pull the electrons away from the atoms by a strong electrical field, and more electrons with smaller diameters can be generated, compared with that of the thermionic guns. The electron beam is focused to a spot by the condenser lenses. The resolution of a scanning electron microscope is determined by the dimension of the focused spot. The scanning coils make the focused electron beam scan the sample surface and control the scan size so that the magnification of the image can be precisely controlled.

The electron beam interacts with the sample surface, generating signals of secondary electrons (SE), backscattered electrons (BSE), characteristic X-rays and auger electrons which provide the information about surface morphology and chemical composition of the investigated sample. Secondary electrons are generated as a consequence of inelastic scattering of the loosely bound electrons, the energy of which is typically less than 50 eV. Since the secondary electrons are generally from very superficial volume of the samples, topographical information can be obtained by detecting such electrons. Backscattered electrons are ejected as a result of an elastic collision between the incident electron and the atom nuclei. As the energy loss is very limited after the collision, backscattered electrons have high energy close to the incident electrons. Due to the high energy, they can be ejected from a relatively deeper volume of the sample. The signal of backscattered electrons increases with the increase of atomic number and the contrast resulted from different atomic numbers can be used to study the distribution of elements within the examined area.

Zeiss EVO50, Zeiss ultra55 and Philips XL30 scanning electron microscopes, equipped with energy dispersive X-ray (EDX) detector, were employed in the

present study for microstructural characterization and examination of the corrosion morphologies of the materials.

3.4.3 Energy dispersive X-ray spectroscopy

Energy dispersive X-ray spectroscopy is a technique to obtain the chemical composition of the alloy by analysing the characteristic X-ray generated when an inner shell electron is excited by the incident electron beam. The excited inner shell electron is emitted from the atom in the sample or transmitted to a higher unoccupied energy level, leaving a vacancy that is subsequently filled by an electron from a higher energy level. Simultaneously, an X-ray photon is emitted. The characteristic X-ray is unique for each element so that the elements in a material can be determined using EDX. EDX analysis can be operated in spot, line or mapping modes. Semi-quantitative analysis is normally involved to determine the chemical composition by calculating the peak-height ratio relative to a standard.

3.4.4 Transmission electron microscopy

Transmission electron microscopy is one of the techniques employed in the field of materials science and engineering for microstructural characterization. Bright-field (BF) and dark-field (DF) images, as well as the diffraction pattern can be obtained by transmission electron microscopy, which provide essential information on the microstructure and composition of the material. Images are formed by either the incident beams (BF image) or the diffraction beams (DF image). The wavelength of electron is smaller than that of other source, such as natural light, leading to relatively higher resolution of the TEM images, compared with the conventional optical images. Generally, the bright-field images present basic features of the examined area while the dark-field images reveal other useful information, such as planar defects, stacking faults, dislocations and particle size, etc., since the diffracted beams have interacted with the sample. The electron beams can also be diffracted by

certain crystal planes of the sample, thus the diffraction pattern of the material within the selected area can be obtained by collecting such diffracted electrons, which, in combination with the BF-TEM and DF-TEM images, reveals the microstructure and chemical composition of the material.

In the present work, an JOEL 2000 FXII TEM, an FEI Tecnai TF30 FEG AEM operated at 300 kV, and an aberration-corrected Titan G2 80-200 S/TEM operated at 200 kV were used in this investigation. The FEI TF30 FEG-AEM was equipped with an Oxford Instruments Xmax80 Silicon Drift Detector (SDD) and an AZTEC analysis system, and the Titan was equipped with Super X (4 quadrant EDX SDDs) and an X-FEG for optimised EDX analysis to assess the composition of ultra-fine microstructures and the distribution of the alloying elements in the melted layer. The TEM micrographs were processed using Gatan Digital Micrograph software.

3.4.5 Scanning Kelvin probe force microscopy

Since Schmutz and Frankel found the linear relation between the Volta potential measured in air and the corrosion potential in aqueous solution for a range of pure metals [4], scanning Kelvin probe force microscopy (SKPFM) has been widely used to evaluate the corrosion performance of materials. Volta potential refers to the potential drop from the infinity to a position just outside the surface. SKPFM images the Volta potential of the sample by measuring the difference of the work functions of the sample and the probe, as the following correlation between the two applies [5]:

$$e(\psi^{sample} - \psi^{KP}) = \Phi^{KP} - \Phi^{sample} \qquad \text{(Equation 3.4)}$$

where ψ^{sample} and ψ^{KP} are the Volta potential of the sample and the Kelvin probe, Φ^{KP} and Φ^{sample} are the work function of the Kelvin probe and the sample, respectively. The working mechanism is described more detailedly in [5].

During the measurement, the probe firstly scans the sample surface in the tapping mode to obtain the topography line by line. Then, a rescan is performed and the tip of the Kelvin probe is lifted from the sample surface for a fixed distance, which is the so-called the lift mode. During the rescan, an alternating current and direct current bias is applied to the probe. The alternating current bias is applied at the probe's fundamental resonance frequency. The null state is observed when the applied direct current bias exactly balances the Volta potential difference between the sample and the probe. However, the measurement of the Volta potential of different phases within a sample can be affected by the surface condition [6].

SKPFM analysis was carried out using a Nanoscope Dimension™ 3100 atomic force microscope in the present study. The surface topography and the surface potential distribution were measured simultaneously on a line-by-line basis in the tapping/lift mode sequence with a scan frequency rate of 0.25 Hz. A silicon tip with a 20-nm thick platinum-coating was used as the reference electrode. All measurements were undertaken in air at room temperature.

3.5 X-ray diffraction
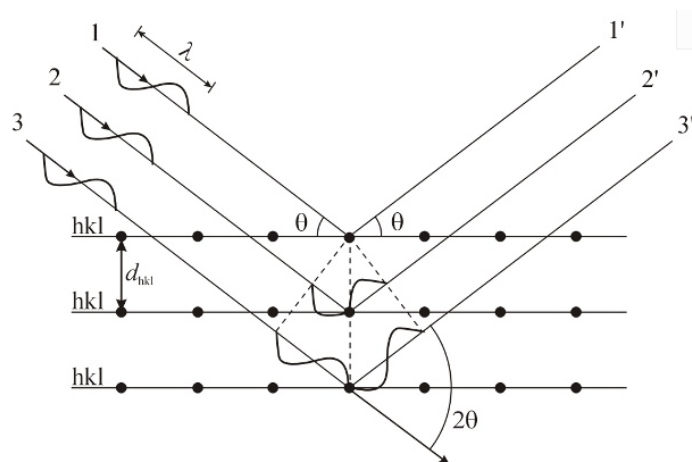
Figure 3.3 Basic principle of X-ray diffraction.

X-ray diffraction (XRD) is a powerful tool to identify the crystallography of materials. The theory is based on the Bragg's law. When incident X-rays interacts with a crystalline material, the part reflecting from the top surface travel less distance than the part reflecting from a lattice plane of crystal below the surface, as shown in Figure 3.3. Constructive interference occurs when the beams reflecting from different layers of parallel lattice planes keep in phase, which requires their path difference equal to an integer number of wavelength of incident X-rays. It is known as Bragg's law and expressed as:

$$2d_{hkl}\sin\theta = n\lambda \qquad \text{(Equation 3.5)}$$

where λ is the wavelength of the incident X-rays, θ is the angle between the incident X-rays and the surface of the crystal and d_{hkl} is the spacing between layers of the parallel lattice planes.

XRD is employed to identify the crystallographic structure of AA2124 aluminium alloy and the MMCs before and after excimer LSM. XRD analysis was carried out using an X'Pert MPD diffractometer with a Cu Kα radiation source (λ=1.5406 Å) with a glancing angle of 1° and 2°.

3.6 Interferometry

Interferometry was employed to measure the surface roughness of the laser-melted surfaces. Investigation was carried out using Veeco Contour GT-K1 high resolution surface measurement system. The surfaces were scanned from 20 μm above the surface to 20 μm below the surface with white light. 10x objective lens and 1% threshold were employed in the measurements. The surface roughness was obtained by averaging the values of three measurements and the maximum and the minimum values were recorded as an indication of the distribution range of the measured roughness values.

3.7 Corrosion evaluation

3.7.1 Potentiodynamic polarization

Potentiodynamic polarization was performed in a naturally aerated 0.6 M NaCl solution at room temperature. A conventional three-electrode system was employed, with a Pt wire counter electrode and a saturated calomel electrode (SCE) as the reference, to which all potentials were referred. The open circuit potential (OCP) measurement was performed for 1 hour to establish a stable state before potentiodynamic polarization. The current-potential curves were recorded from −200 mV$_{OCP}$ with a scanning rate of 0.5 mV/s until the current density reached a limit of 1 mA/cm^2.

3.7.2 Electrochemical impedance spectroscopy

Electrochemical impedance spectroscopy (EIS) tests were carried out by applying alternating current voltage amplitude of 10 mV at the steady free corrosion potential after immersion in naturally aerated 0.6 M NaCl solution for 1 hour. The EIS responses were recorded in the frequency range from 100 kHz to 10 mHz with 10 points per decade. The tests were repeated three times to ensure the reproducibility of the results for all electrochemical tests.

3.7.3 Immersion test

Evaluation of the mechanism of corrosion initiation for the investigated materials was achieved by immersing the samples in the 0.6 M NaCl solution for up to 24 hours. After immersion, the samples were retrieved and dried for SEM examination.

References

[1]   R.C. Furneaux, G.E. Thompson, G.C. Wood, *The application of ultramicrotomy to the electronoptical examination of surface films on aluminium*, Corrosion Science, 18 (1978), 853-881.

[2]   R.M. Langford, A.K. Petford-Long, *Preparation of transmission electron microscopy cross-section specimens using focused ion beam milling*, Journal of Vacuum Science & Technology a-Vacuum Surfaces and Films, 19 (2001), 2186-2193.

[3]   Y.F. Joya, Titanium dioxide films prepared by sol-gel/laser-induced technique for inactivation of bacteria, 2011, PhD Thesis, The University of Manchester

[4]   P. Schmutz, G.S. Frankel, *Characterization of AA2024-T3 by scanning Kelvin probe force microscopy*, Journal of the Electrochemical Society, 145 (1998), 2285-2295.

[5]   M. Rohwerder, F. Turcu, *High-resolution Kelvin probe microscopy in corrosion science: Scanning Kelvin probe force microscopy (SKPFM) versus classical scanning Kelvin probe (SKP)*, Electrochimica Acta, 53 (2007), 290-299.

[6]   B.S. Tanem, G. Svenningsen, J. Mardalen, *Relations between sample preparation and SKPFM Volta potential maps on an EN AW-6005 aluminium alloy*, Corrosion Science, 47 (2005), 1506-1519.

Chapter 4 Microstructure and corrosion behaviour of the MA and the MMCs

4.1 Introduction

Prior to excimer LSM, the microstructure and corrosion behaviour of the MA and the MMCs have been studied in order to reveal the corrosion mechanisms of the as-received materials. The MMCs, composites A and B as specified in Chapter 3, is employed. In comparison with the MA, the effects of SiC particles on the microstructure and corrosion behaviour of the MMCs will be discussed in this chapter. The correlation between the microstructure and corrosion behaviour of the materials has been established.

4.2 Microstructural characterization

4.2.1 SEM characterization

(i) MA

Figure 4.1(a) shows a typical microstructure of the MA, which presents a large number of intermetallics. Two main types of intermetallic particles were observed. The irregularly or rod-shaped intermetallics were revealed to be AlCuMnFe(Si)-containing particles. A typical EDX spectrum of AlCuMnFe(Si)-containing particles is shown in Figure 4.2(a). However, the AlCuMnFe(Si)-containing particles exhibit a range of compositions including Al_7Cu_2Fe, Al_6MnFe_2, $(Al,Cu)_6Mn$, and a number of undetermined compositions in the class $Al_6(Cu,Fe,Mn)$ [1]. The round-shaped intermetallics, which are usually smaller than the AlCuMnFe(Si)-containing particles, are Mg-rich S-phase particles, being consisted of mainly Al, Cu, and Mg as shown in

Figure 4.2(b). Both kinds of intermetallics were also observed at the grain boundaries, as indicated in Figure 4.1(a).
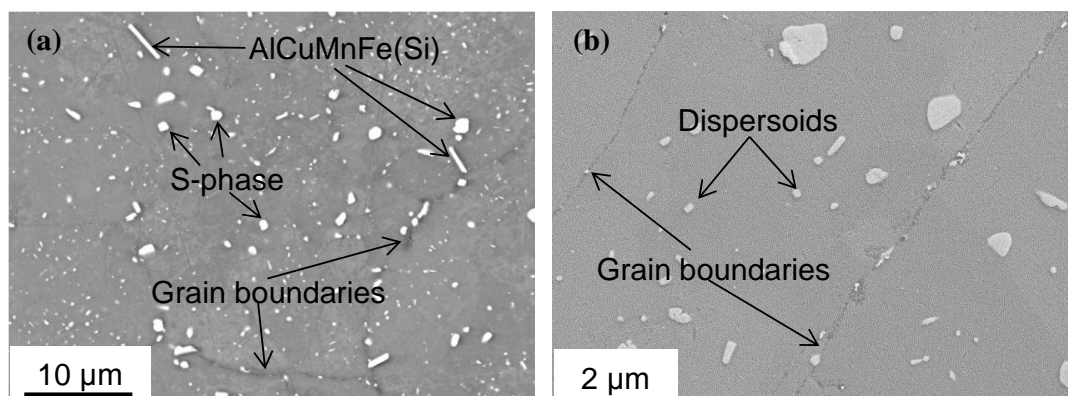
Figure 4.1 SEM micrographs of the MA: (a) low magnification and (b) high magnification.
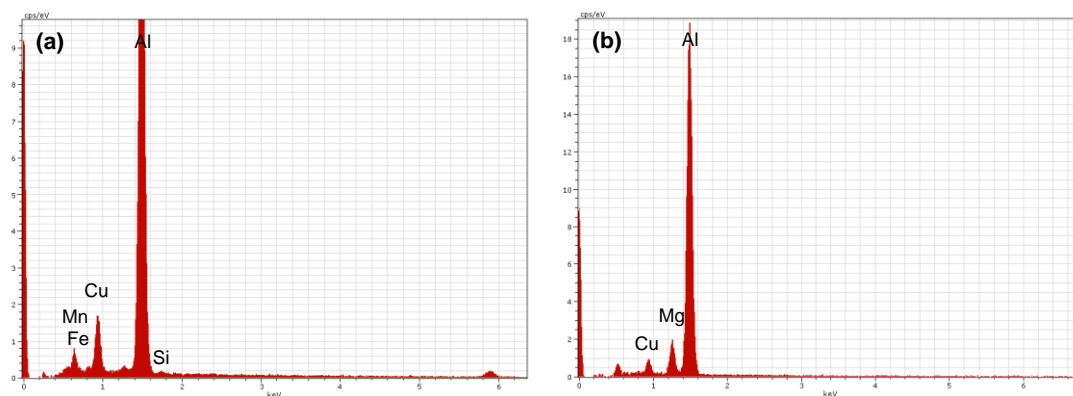
Figure 4.2 Typical EDX spectra of (a) AlCuMnFe(Si)-containing particles and (b) S-phase particles.

Additionally, numerous fine dispersoids, ranging from several tens of nanometres to several hundreds of nanometres, are randomly distributed in the Al matrix, as shown in Figure 4.1(b). The dispersoids usually contains one or more transition metals, such as $Al_{20}Mn_3Cu$, $Al_{12}Mg_2Cr$ and Al_3Zr [2]. Together with the AlCuMnFe(Si)-containing particles, the dispersoids are formed during homogenization and are insoluble. However, these fine dispersoids have been reported to play a minor role in

the corrosion process of aluminium alloys [2]. Therefore, they are not specifically identified and distinguished from each other in current work.

(ii) MMCs

A typical microstructure of composite A is shown in Figure 4.3(a), which reveals the uniform distribution of SiC particles in the Al matrix. Eventually, cracked SiC particles were observed. At a higher magnification, slight agglomeration of SiC particles is shown in Figure 4.3(b), which also shows micro-pores and micro-crevices close to the SiC particles, especially those agglomerated SiC particles. In composite B, the SiC particles are also uniformly distributed in the matrix, as shown in Figure 4.4. The size of SiC particles in composite B is much smaller than that in composite A. Although agglomeration of SiC particles is also present, significantly reduced porosity is revealed in composite B.
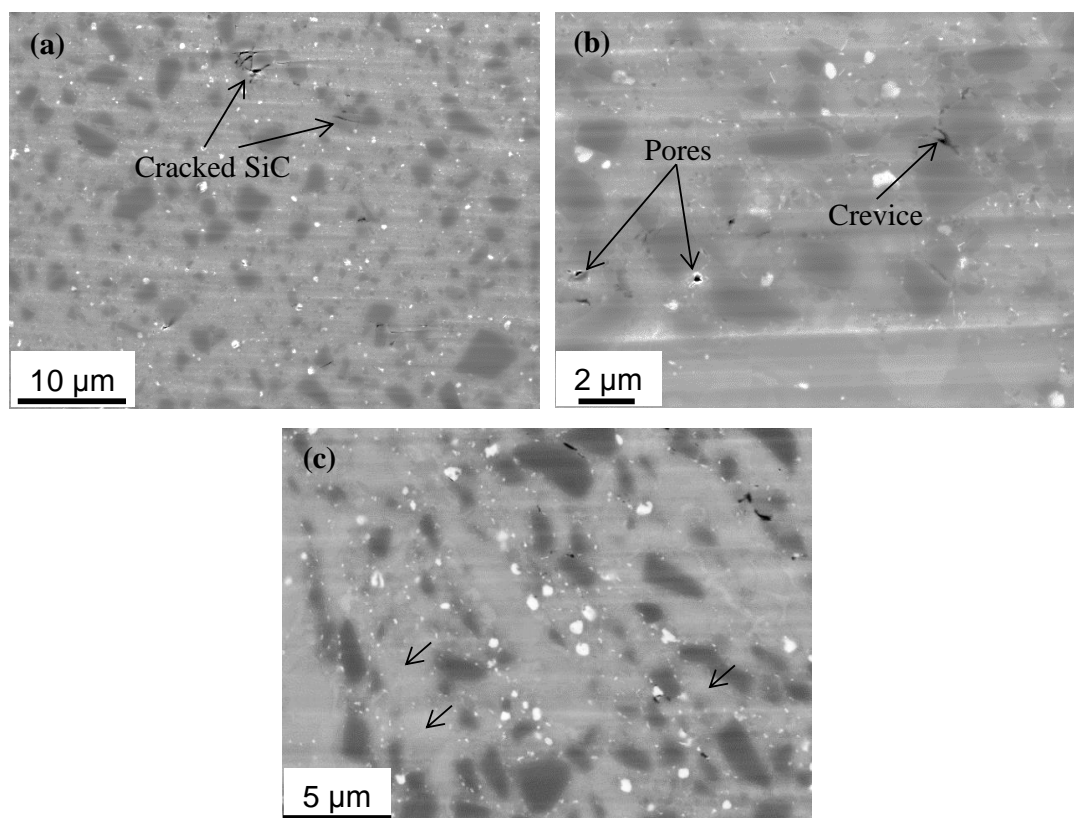
Figure 4.3 (a) and (b) SE-SEM, and (c) BSE-SEM micrographs of composite A.

The intermetallics in composite A and composite B were revealed using backscattered electron (BSE) detector, as shown in Figure 4.3(c) and Figure 4.4(c), respectively. Compared with the intermetallics in the MA (Figure 4.1(a)), it is noticed that the intermetallics in both composites are much smaller in size. For composite A, it is evident that most SiC particles are decorated with numerous fine intermetallic particles, typically smaller than 200 nm in the SiC/Al interfacial regions, while these fine particles are significantly reduced in the matrix away from the SiC particles as the arrows indicates in Figure 4.3(c). However, this characteristic is not evidently shown in composite B in Figure 4.4(c). More details were further studied using TEM to reveal the distribution and composition of the intermetallics in the MMCs.
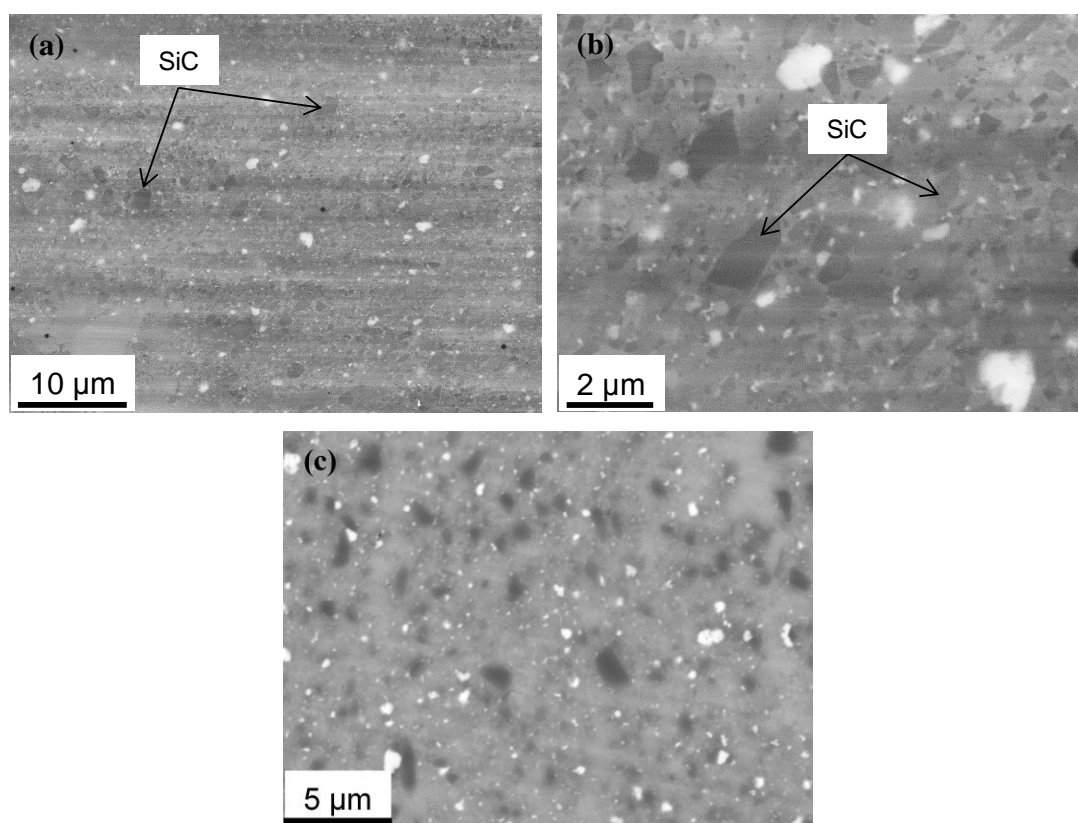
Figure 4.4 (a) and (b) SE-SEM, and (c) BSE-SEM micrographs of composite B.

4.2.2 TEM characterization

(i) MA

Table 4.1 Typical chemical compositions of the AlCuMnFe(Si)-containing intermetallics in the MA (at.%).

	Al	Cu	Mn	Fe	Si	Mg
Rod-shaped	73.7	16.1	1.8	7.6	0.7	-
Irregularly-shaped	79.7	7.0	10.9	0.8	1.5	0.1
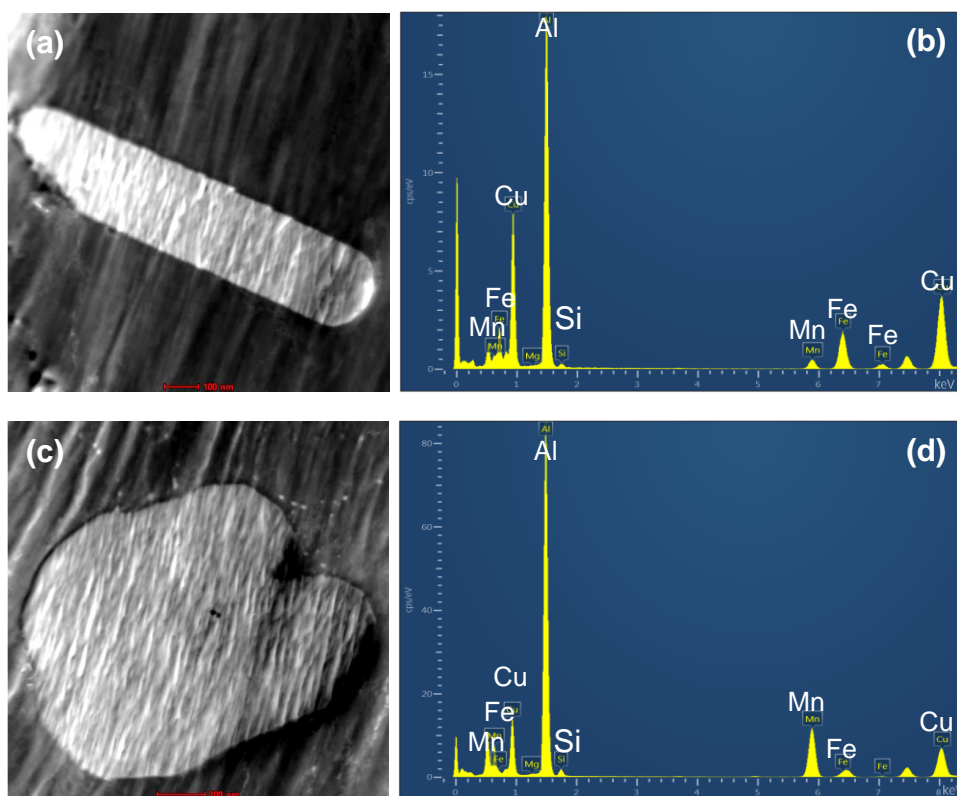
Figure 4.5 High-angle annular dark-field (HAADF) images and EDX spectra of the AlCuMnFe(Si)-containing particles in the MA: (a) and (b) rod-shaped particles; (c) and (d) irregular-shaped particles.

Figure 4.5 shows two typical AlCuMnFe(Si)-containing particles in the MA. The results of the quantitative analysis of the EDX spectra are shown in Table 4.1 and show that the rod-shaped particle has higher percentage of Cu and Fe while the

irregular-shaped particle has higher percentage of Mn. Both kinds of particles exhibit low content of Si. The AlCuMnFe(Si)-containing intermetallic particles are almost free of Mg.

Co-precipitation of S-phase and AlCuMnFe(Si)-containing intermetallic particles was observed in the MA, as indicated in Figure 4.6(a). The cluster of intermetallics has an AlCuMnFe(Si)-containing particle in the centre, surrounded with S-phase. The high-resolution lattice image of the S-phase in the [100] zone axis is shown in Figure 4.6(b). Al_2CuMg has an orthorhombic structure with the lattice parameters of a=0.401 nm, b=0.925 nm, and c=0.715 nm. The d-spacing values (d_1 and d_2) indicate two lattice planes of Al_2CuMg with the index {023}, the standard d-spacing of which is 2.18 Å. The measured angle (54.5°) between the two planes is in good agreement with the theoretical angle between the two lattice planes (023) and (0$\bar{2}$3), confirming the presence of S-phase.
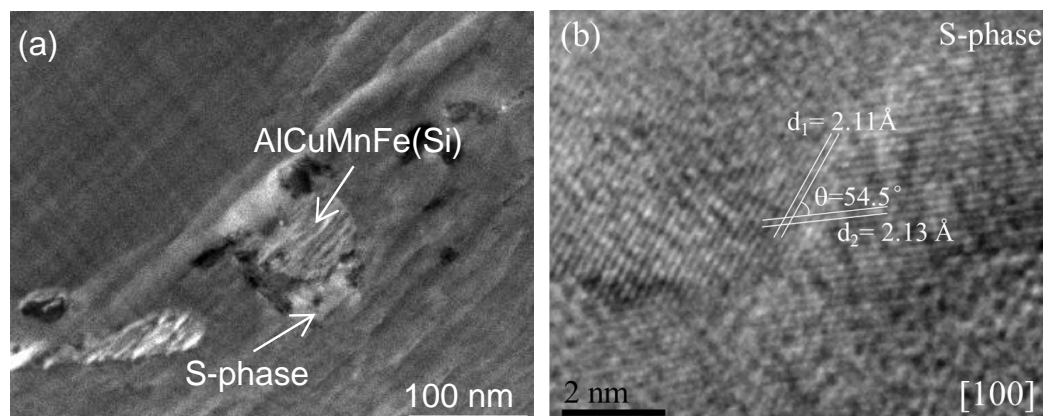
Figure 4.6 Co-precipitation of S-phase and AlCuMnFe(Si)-containing intermetallic particles: (a) HAADF image; (b) high-resolution lattice image of the S-phase particle.

Figure 4.7 shows the results of EDX analysis of the grain boundaries in the MA. In the HAADF image, except several fine bright particles, a string of dark spots are revealed along the grain boundary. The dark spots seem to be pores as these areas are blank in the individual STEM-EDX spectrum images. The STEM-EDX spectrum images reveal Mg segregation at the grain boundaries.

119
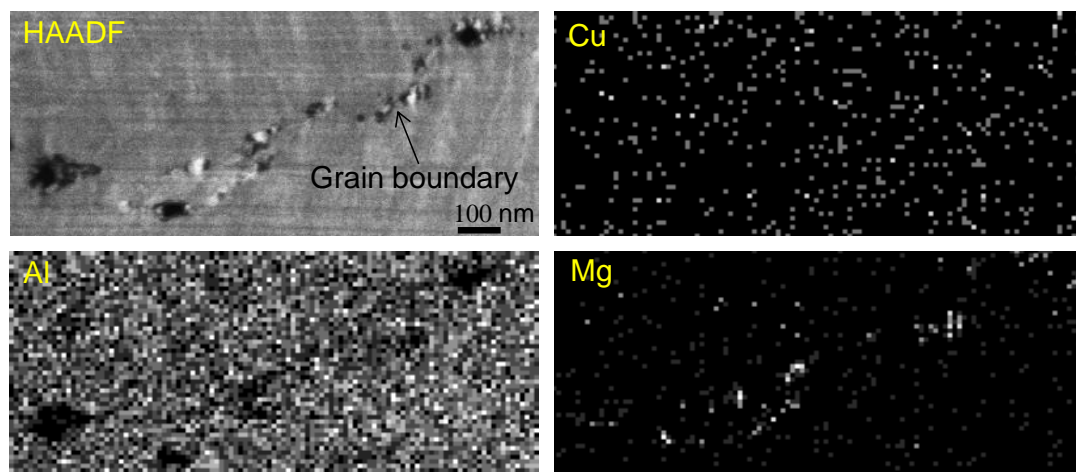
Figure 4.7 HAADF image and corresponding STEM-EDX spectrum images of the main alloying elements at the grain boundaries in the MA.

(ii) MMCs

Figures 4.8(a) and (b) show the general view of composite A and B, respectively. The bright-field (BF) TEM micrographs show the uniformly dispersed SiC particles in the matrix and the fine matrix grains in both composites. The fine grains and precipitates at grain boundaries are indicated in the HAADF images in Figures 4.8(c) and (d) for composite A and Figure 4.8(e) for composite B. In composite A, the grain size is typically smaller than 2 μm. Compared with Figure 4.8(d), the matrix grains in composite B are even finer in Figure 4.8(e). The grain size in composite B is in the sub-micron range. The bright features at the grain boundaries indicate the precipitation of intermetallic particles containing elements with high atomic numbers, such as Cu, Mn and Fe in the MMCs. It seems that the grain boundary precipitation is more significant in composite A than composite B.
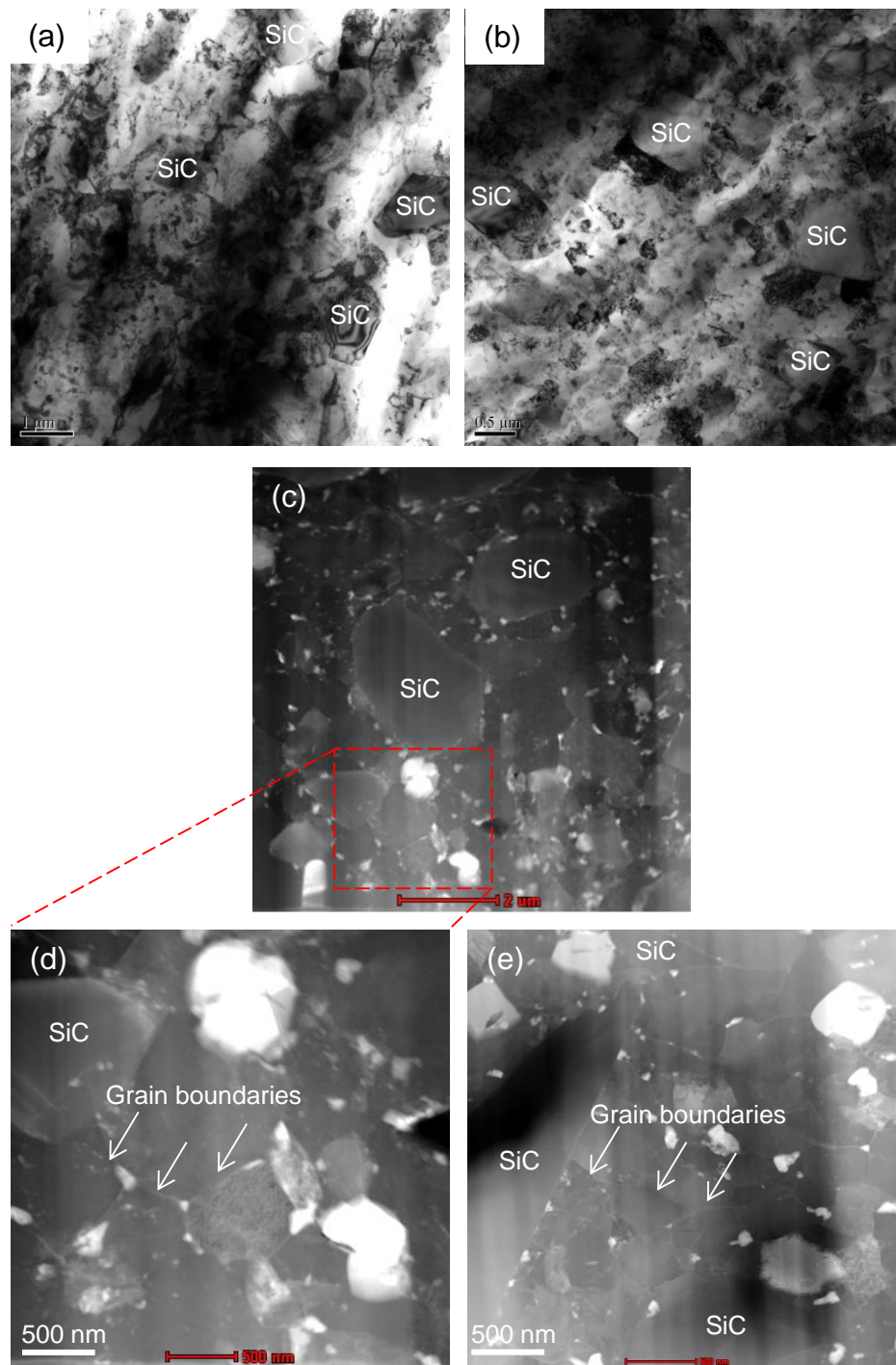
Figure 4.8 BF-TEM micrographs of the general view of (a) composite A and (b) composite B; HAADF images of (c) and (d) composite A and (e) composite B, showing the grains of Al matrix and the distribution of intermetallic particles.
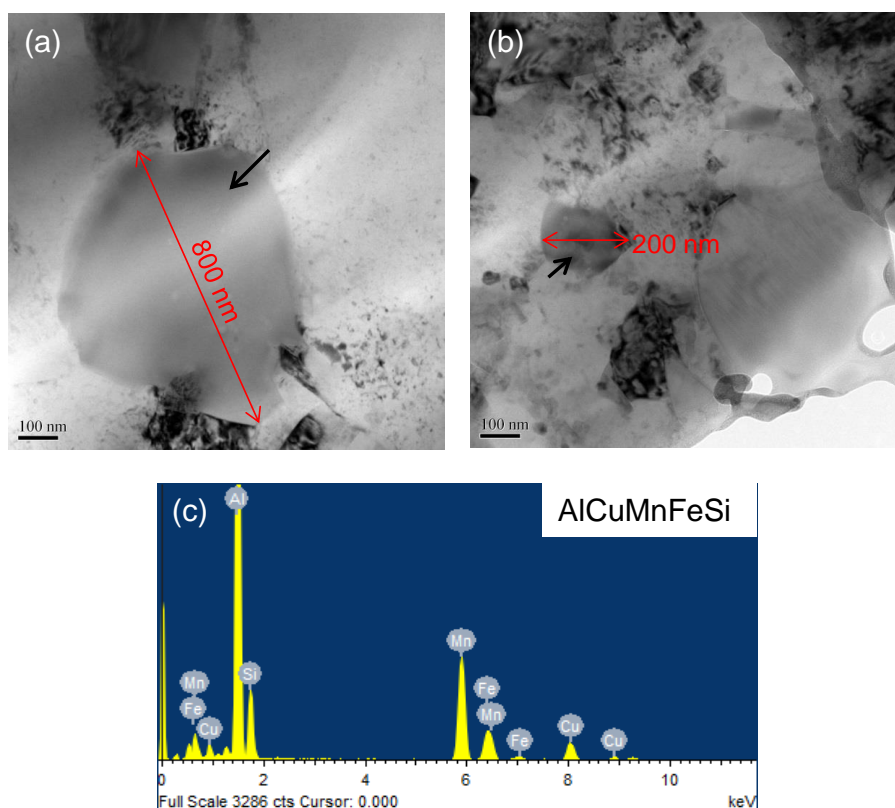
Figure 4.9 The AlCuMnFe(Si)-containing intermetallic particles in the MMCs: (a) and (b) BF-TEM micrographs and (c) typical EDX spectrum of such particles.

Furthermore, the HAADF images indicate the distribution of intermetallic particles in the MMCs. A few bright coarse particles are randomly distributed in the matrix in both MMCs (Figures 4.8(c)-(e)). This is in agreement with the SEM observation in Figures 4.3(c) and 4.4(c). However, some fine bright intermetallic particles, as small as 100 nm, possess similar compositions with these coarse intermetallic particles. Figure 4.9(a) and (b) present two particles with the dimensions up to 800 nm and 200 nm, respectively. A typical EDX spectrum in Figure 4.9(c) suggests that such particles are mainly consisted of Al, Cu, Mn, Fe and Si. Similar to that in the MA, these particles have a variety of compositions; they are generally termed as AlCuMnFe(Si)-containing particles to be coincidence with that in the MA. However, EDX analysis reveals that in most cases, significant amount of Si is included in the AlCuMnFe(Si)-containing particles in the MMCs.
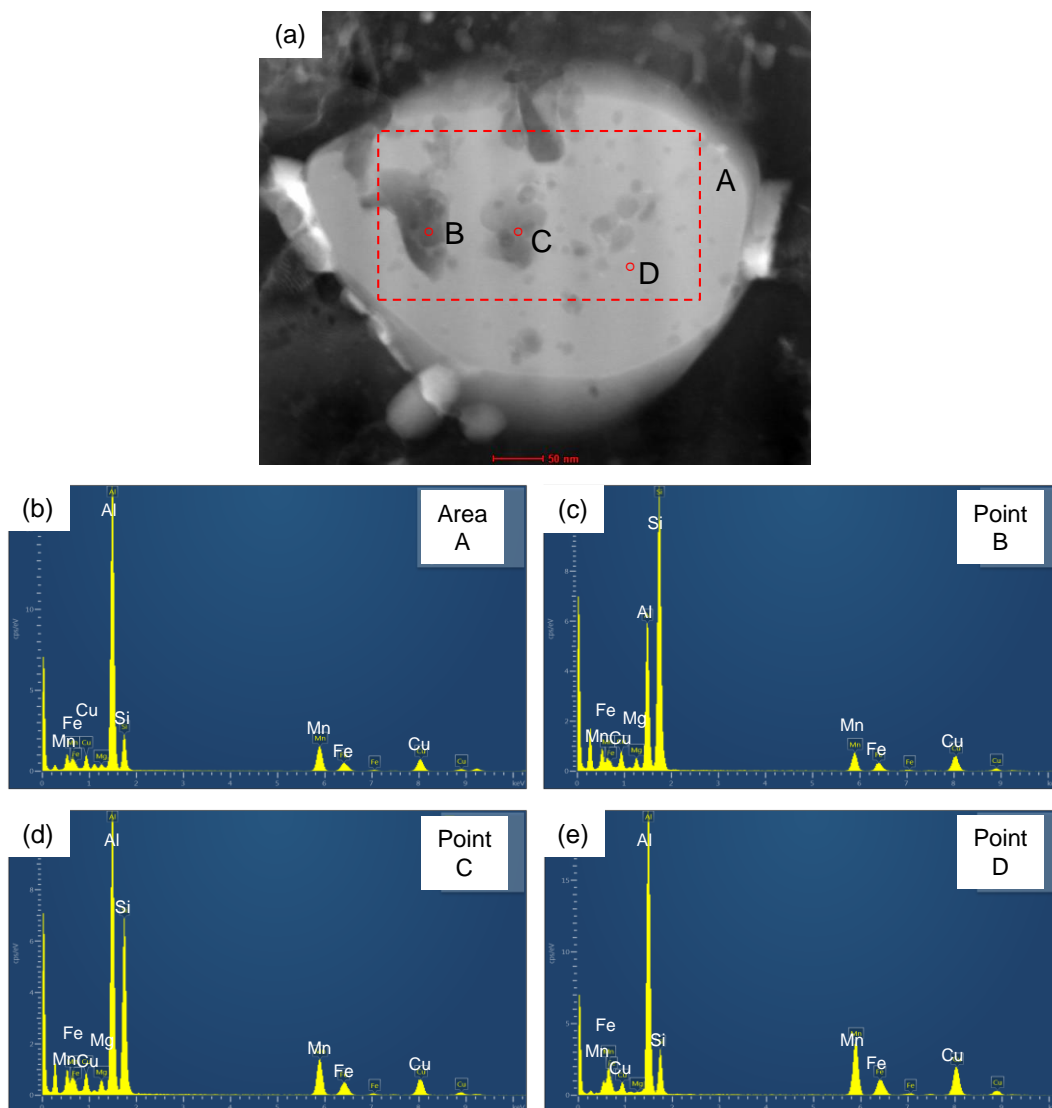
Figure 4.10 (a) HAADF image of an AlCuMnFe(Si)-containing particle; (b)-(e) EDX spectra obtained from area A, and point B, C and D, respectively.

Figure 4.10(a) presents the HAADF image of an AlCuMnFe(Si)-containing particle, where the dark areas within the particle indicate different composition from the rest. The EDX spectra of the area A, and point B, C, and D are shown in Figures 4.10(b)-(e), respectively. The results of the quantitative analysis are shown in Table 4.2. The data obtained from area A represents the average chemical composition of the particle, which involves a percentage of Si close to 10 at.% in the particle. The chemical composition of point B and point C is revealed with 58 at.% and 32.5 at.% Si, respectively, indicating that the dark areas are rich in silicon. It is graphically

indicated that the darker the area is, the higher the proportion of silicon is, as shown in Figure 4.10(a). The chemical composition of point D is close to the average chemical composition obtained from area A. Also, compared with point D, which contains very little magnesium, there is an increase in magnesium at point B and point C. It is evident that the percentage of Si and Mg in the AlCuMnFe(Si)-containing particles in the MMCs is much higher than that in the MA by comparing the data in Table 4.1 and Table 4.2.

Table 4.2 Corresponding chemical composition of area A, and point B, C and D in Figure 4.9(a) (at.%).

	Al	Cu	Mn	Fe	Si	Mg
Area A	78.2	3.1	6.1	1.7	9.6	1.3
Point B	31.4	3.2	3.4	1.5	58	2.6
Point C	53.8	3.0	6.2	1.8	32.5	2.7
Point D	68.5	6.6	11.4	2.8	10.5	0.2

Apart from the relative coarse intermetallic particles, fine intermetallics were observed in the SiC/Al interfacial regions in both MMCs. As shown in Figures 4.8(c) and (e), the SiC particles are surrounded by bright fine particles, which have dimensions up to 200 nm. This indicates the preferential precipitation of intermetallics in the SiC/Al interfacial regions. These particles were studied with EDX elemental mapping analysis, as shown in Figure 4.11, revealing that the fine intermetallic particles at the SiC/Al interfacial region are rich in Cu. Furthermore, magnesium segregation to the SiC/Al interface is indicated in Figure 4.11(a), which is accompanied with a gradual change of the aluminium and silicon concentrations at the interface, indicating the diffusion or chemical reactions between Al and SiC particles and this could be a source of free Si in the MMC. However, this can hardly explain the relatively high level of Si in the AlCuMnFe(Si)-containing intermetallic particles in the MMCs as the possibility is remote for the free Si to interact with the already-existing AlCuMnFe(Si)-containing intermetallic particles in the solid-state

manufacturing process. The different levels of Si in the AlCuMnFe(Si)-containing intermetallic particles in the MA and the MMC might be due to the use of different batches of aluminium alloy powders during manufacturing process. Magnesium segregation to the SiC/Al interface is not shown in Figure 4.11(b), suggesting that such segregation is not always present in the MMCs.
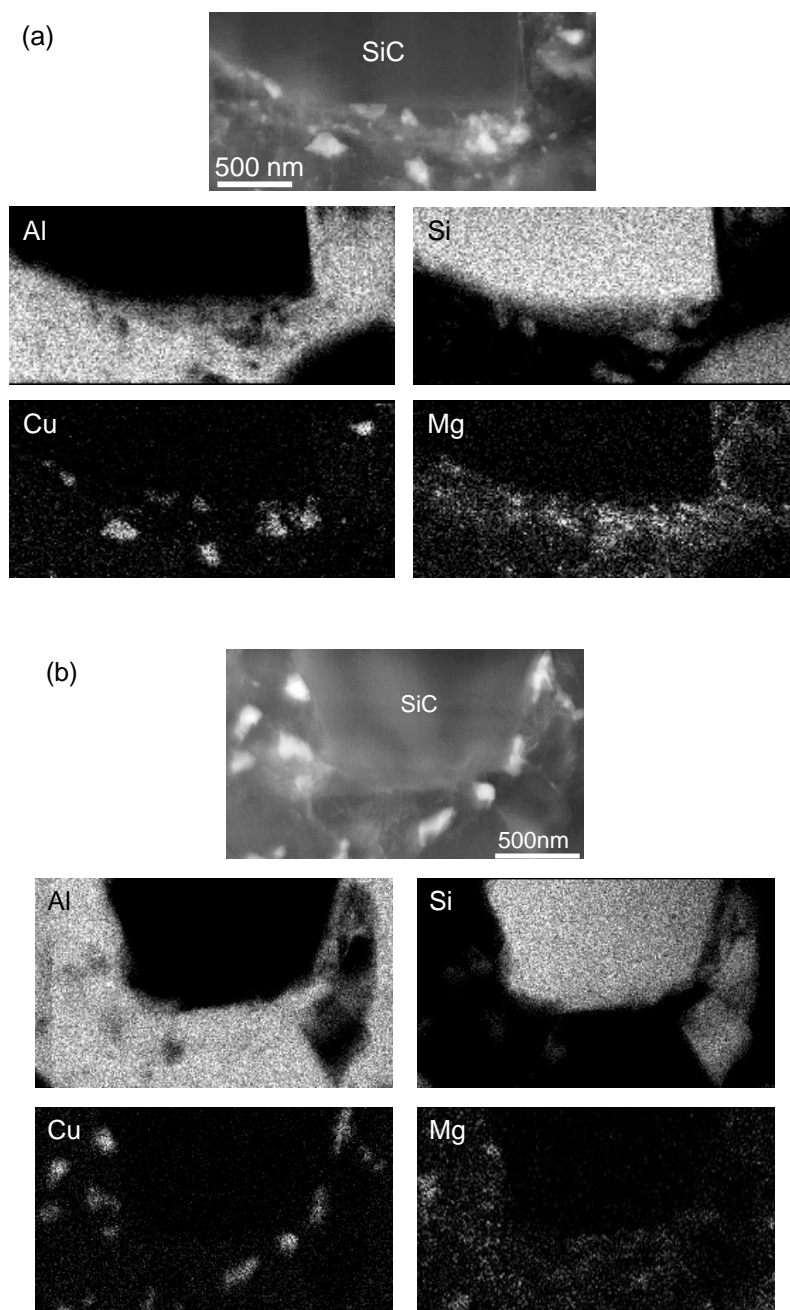
Figure 4.11 EDX elemental mapping analysis of the SiC/Al interfacial regions of two SiC particles.

Figure 4.12(a) shows a copper-rich particle in the SiC/Al interfacial region, which is mainly consisted of aluminium and copper as suggested in the EDX spectrum in Figure 4.12(b). The atomic proportion of aluminium and copper is 70.3% and 28.7%, respectively, being close to the composition of Al_2Cu (θ-phase). The θ-phase has a tetragonal structure with the lattice parameters of a=b=0.606 nm and c=0.487 nm. The high-resolution lattice image in the [$1\bar{1}\bar{1}$] zone axis confirms two lattice planes of θ-phase, i.e. (110) and (211), with the angle of 34.97° between the two lattice planes. The measured angle is in good agreement with the theoretical angle between the two lattice planes of Al_2Cu, which is 34°, confirming the copper-rich intermetallic particles are in the form of θ-phase.

In the present study, AlCuMnFe(Si)-containing particles and θ-phase particles were identified to be the two main species of intermetallic particles in the MMCs, although some other species were observed. Both AlCuMnFe(Si)-containing particles and θ-phase particles are rather bright under STEM because the elements with high atomic number are included, i.e. Cu, Mn, and Fe. Some intermetallic particles, which exhibit similar dimensions but darker colour than the θ-phase particles, were observed, as shown in Figure 4.13(a). The EDX spectrum of the particle shows that it is mainly composed of aluminium, copper and silicon (Figure 4.13(b)), being randomly distributed either in the Al matrix or at the SiC/Al interfacial areas.

Occasionally, thin layer or discrete particles rich in oxygen were observed near the SiC/Al interface, as shown in Figure 4.14. The bright-field and dark-field TEM micrographs indicate a thin layer with the thickness less than 20 nm, which is mainly consisted of Al, Mg, Si and O as shown in Figure 4.14(c). Such interface layer has been reported in the SiC-reinforced aluminium-based MMCs manufactured in powder metallurgy routes [3, 4]. According to the equation below:

$$2SiO_2 \text{ (s)} + 2Al \text{ (l)} + Mg \text{ (l)} = MgAl_2O_4 \text{ (s)} + 2Si \text{ (l)} \qquad \text{(Reaction 4.1)}$$

$MgAl_2O_4$ could be formed when native silicon oxide is present at the surface of the SiC particles [5]. However, it should be noted that in Reaction 4.1, Al and Mg are in liquid state. The MMCs employed in the present work were manufactured in the solid-state powder metallurgy route. Therefore, the possibility for the above reaction is rare. The possible origin of the spinel phase is more likely to be due to some pre-treatments of the SiC particles.
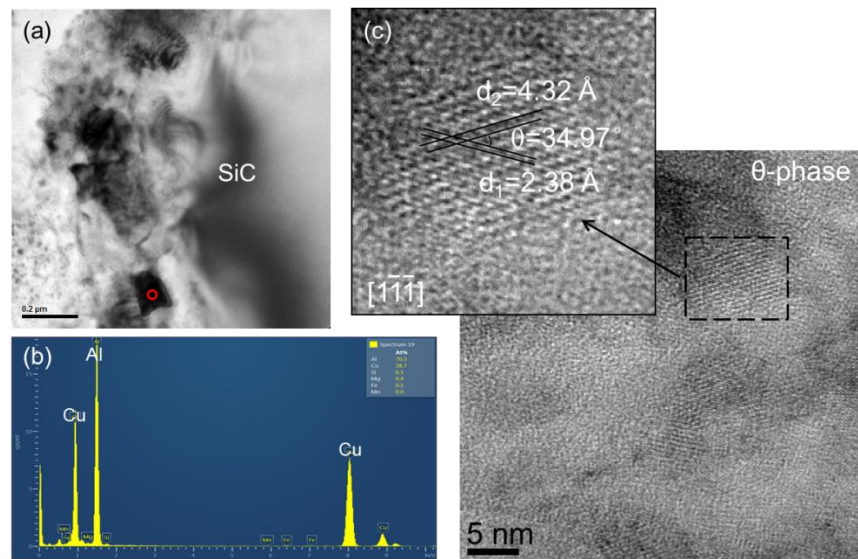
Figure 4.12 (a) BF-TEM micrograph of the SiC/Al interface; (b) EDX spectrum of the particle indicated by the red circle in (a); (c) high-resolution TEM image from the particle.
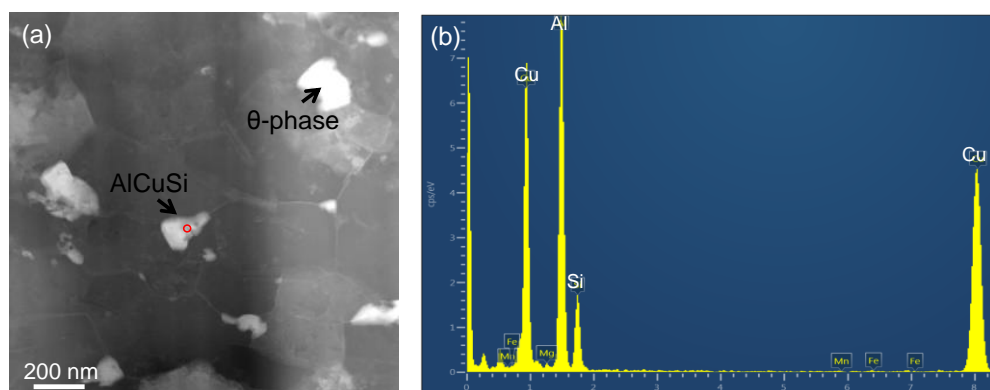
Figure 4.13 (a) HAADF image and (b) EDX spectrum of the AlCuSi particle in the MMCs.
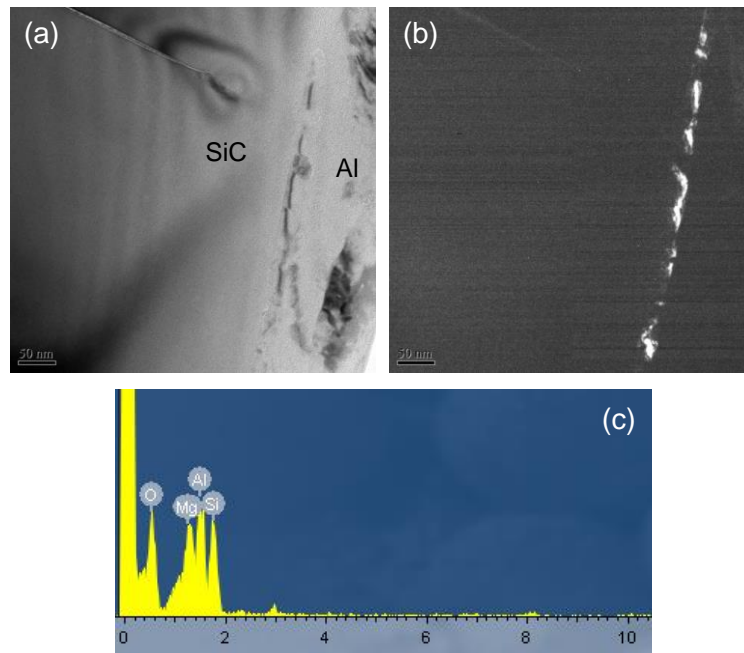
Figure 4.14 Thin interfacial layer at the SiC/Al interface: (a) BF-TEM micrograph; (b) DF-TEM micrograph; (c) EDX spectrum from the thin layer.
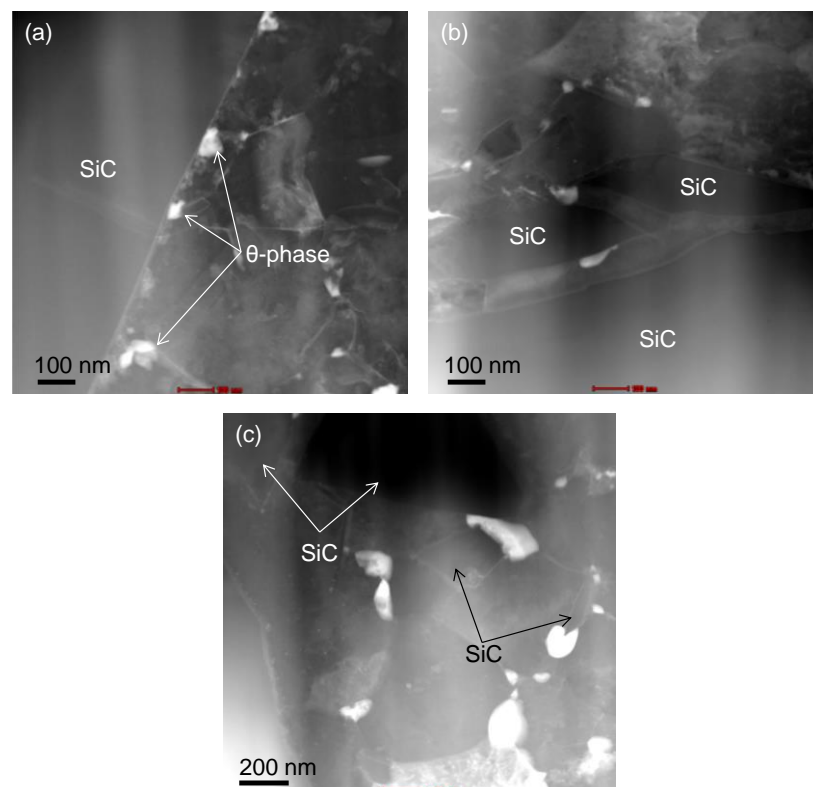
Figure 4.15 HAADF images showing the SiC/Al interfacial regions in composite B: (a) relative coarse SiC particles; (b) and (c) submicrometre-sized SiC particles.

The above features observed using TEM are shared by both MMCs, suggesting that both MMCs have the same species of the intermetallic particles. However, some significant difference between the two MMCs was observed. As shown in Figure 4.8(c), there is a high density of θ-phase particles in the vicinity of micrometre-sized SiC particles. This is also true for the relative coarse SiC particles in composite B, as shown in Figure 4.15(a). By further examining the SiC particles of different sizes in composite B, it is revealed that the density of θ-phase particles is reduced in the vicinity of fine SiC particles in the submicrometre range, as shown in Figures 4.15(b) and 4.15(c). The SiC/Al interfaces in Figures 4.15(b) and 4.15(c) are rather smooth and clean. This indicates that the size of the SiC particles significantly affect the precipitation of intermetallic particles in the SiC/Al interfacial regions. Figure 4.16(a) shows a submicrometre-sized SiC particle in composite B, which interface is smooth and clean without any precipitates as shown in Figure 4.16(b).
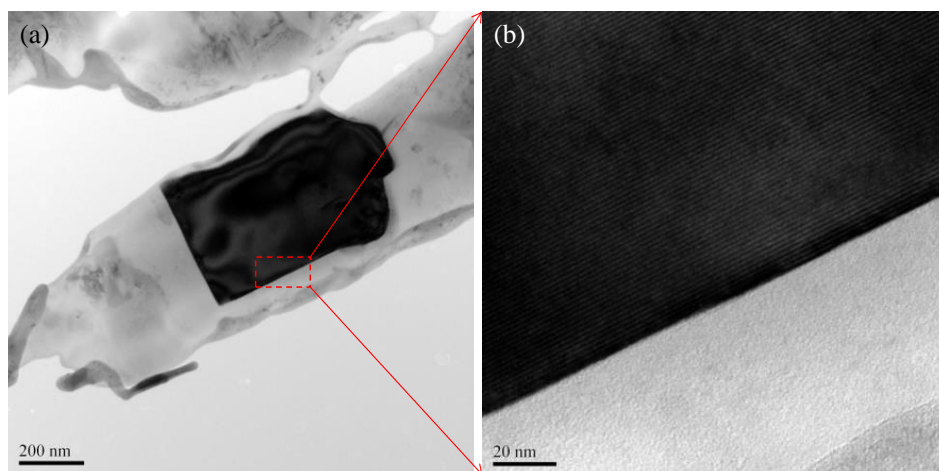
Figure 4.16 BF-TEM micrographs showing (a) a submicrometre-sized SiC particle and (b) smooth SiC/Al interface.

4.2.3 XRD characterization
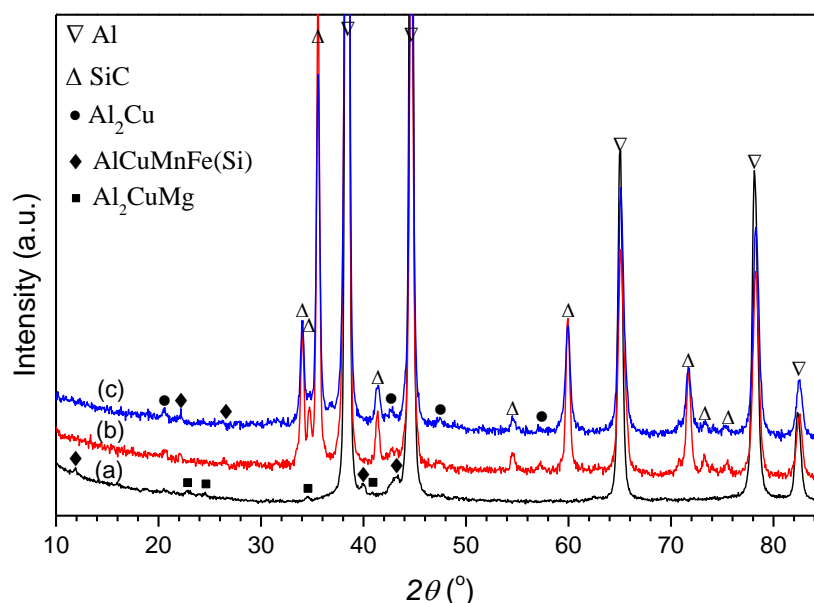
Figure 4.17 XRD patterns of (a) MA, (b) composite A, and (c) composite B.

Based on the SEM and TEM observations, it is suggested that the species of the intermetallics in the Al matrix are altered by the addition of SiC particles. An evident characteristic of the MMCs is the precipitation of θ-phase particles in the SiC/Al interfacial regions. The difference in crystallography between the MMCs and the MA was further investigated with XRD analysis. The XRD profiles, obtained at a glancing angle of 2°, for all the materials are shown in Figure 4.17. The AlCuMnFe(Si)-containing phase, as a common constituent in AA2124 aluminium alloy, is identified in all the materials. Besides, S-phase (Al_2CuMg) is indicated in the MA while θ-phase (Al_2Cu) is indicated in the MMCs, clearly demonstrating the impact of SiC on the microstructures of the MMCs. The S-phase particles in the MA are probably undissolved particles during solution treatment while the θ-phase in the MMCs is attributed to its preferential precipitation in the SiC/Al interfacial regions.

4.3 Corrosion evaluation

4.3.1 Open circuit potential
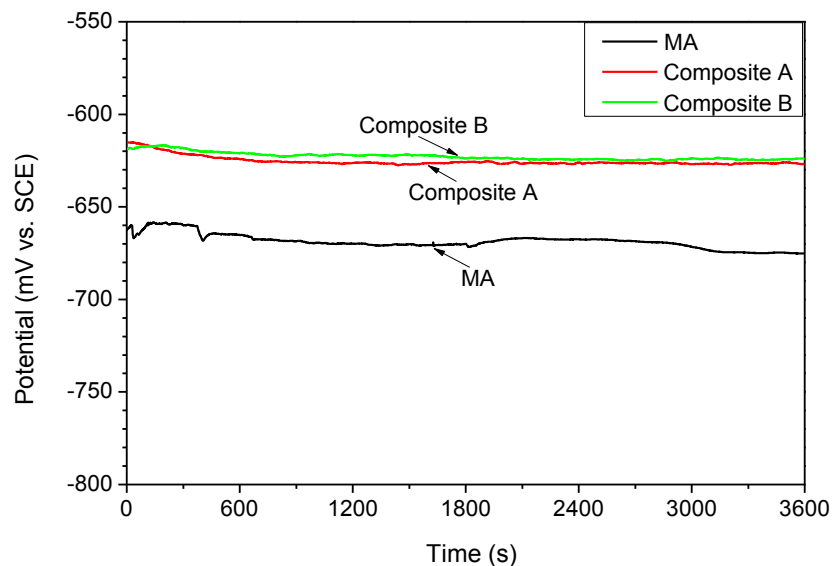
Figure 4.18 OCP-time curves of the MA and MMCs during immersion in naturally aerated 0.6 M NaCl solution.

The evolution of open circuit potential (OCP) of the investigated materials was recorded for 1 h in naturally aerated 0.6 M NaCl solution in order to obtain a steady state before potentiodynamic polarization (Figure 4.18). The OCP-time curves show that all the materials remains in a steady state throughout immersion. The OCP values of the MMCs are slightly higher than that of the MA. As is known that SiC has a more positive OCP than Al [6], the MMCs could be polarized to more positive potentials compared with the MA according to the mixed potential theory.

4.3.2 Potentiodynamic polarization
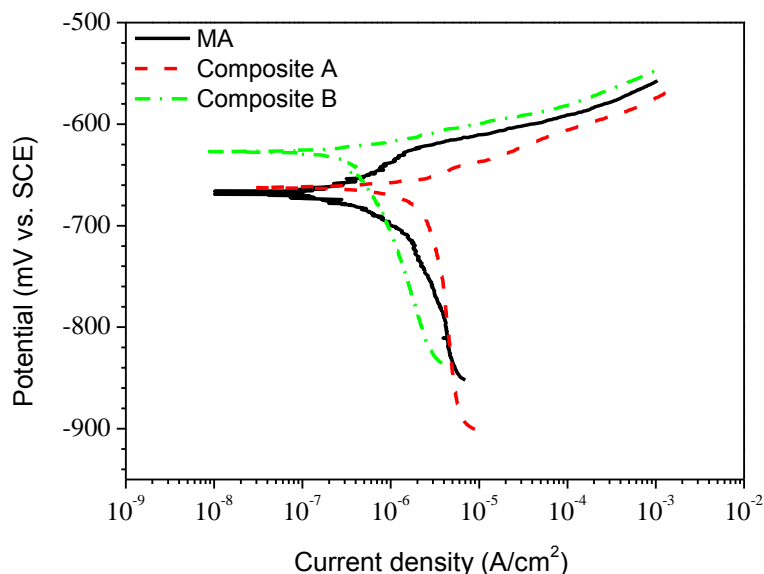
Figure 4.19 Potentiodynamic polarization curves of the MA and MMCs obtained in naturally aerated 0.6 M NaCl solution.

The potentiodynamic polarization curves for the MA, composite A and composite B following 1 h immersion in naturally aerated 0.6 M NaCl solution are presented in Figure 4.19. For all the samples, the polarization curves exhibit little change in current density in the cathodic part, suggesting the diffusion-controlled reduction of oxygen. No passivation occurs for both composites while the MA shows partial passivation during anodic polarization. This could be due to the presence of SiC particles disrupting the integrity of the passive layer. The average electrochemical parameters obtained from the polarization curves of three measurements are shown in Table 4.3. As a result of the addition of SiC particles, the area fraction of aluminium decreases. However, due to the semi-conductive nature of SiC, possibly supporting cathodic reaction, the area of SiC is not subtracted when calculating the corrosion current density (i_{corr}). At the corrosion potential (E_{corr}), the MA and composite B exhibit similar i_{corr}, compared with which a three-fold higher i_{corr} is

registered for composite A, indicating that the corrosion resistance of composite A is inferior to that of the MA and composite B.

Table 4.3 Average electrochemical parameters interpreted from the polarization curves of three measurements of each material.

	E_{corr} (mV)	i_{corr} (μA/cm^2)	E_{pit} (mV)
MA	-658±10	0.55±0.22	-613±17
Composite A	-655±16	1.84±0.85	-
Composite B	-638±19	0.65±0.19	-

4.3.3 Electrochemical impedance spectroscopy

Figure 4.20 shows the Nyquist plots of the EIS responses for the investigated materials after immersion in naturally aerated 0.6 M NaCl solution for 1 h. The Nyquist plots for all the samples are characterized by two depressed capacitive loops. The high-medium frequency capacitive loop corresponds to the electrolyte-metal interface behaviour and provides a measurement of the charge transfer resistance, which is proportionally related to the corrosion resistance of the MA/MMC when the surface undergoes corrosion in aggressive media. The low frequency capacitive loop is related to the mass transport during corrosion (e.g. diffusion of chloride or aluminium ions through the surface). The EIS spectra were fitted using the equivalent circuit as shown in Figure 4.21, where R_s is the electrolyte resistance, Q_{dl} is the constant phase element (CPE) related to the double layer capacitance, R_{ct} is the charge transfer resistance and R_w and Q_w are diffusion related Warburg elements.

The CPE used in the equivalent circuit is to signify the non-ideal capacitance with varying n. The impedance of CPE (Z_{CPE}) is a function of the angular frequency and is related to that for a capacitance:

$$Z_{CPE(\omega)} = (Cj\omega^{-n})^{-1} \qquad \text{(Equation 4.1)}$$
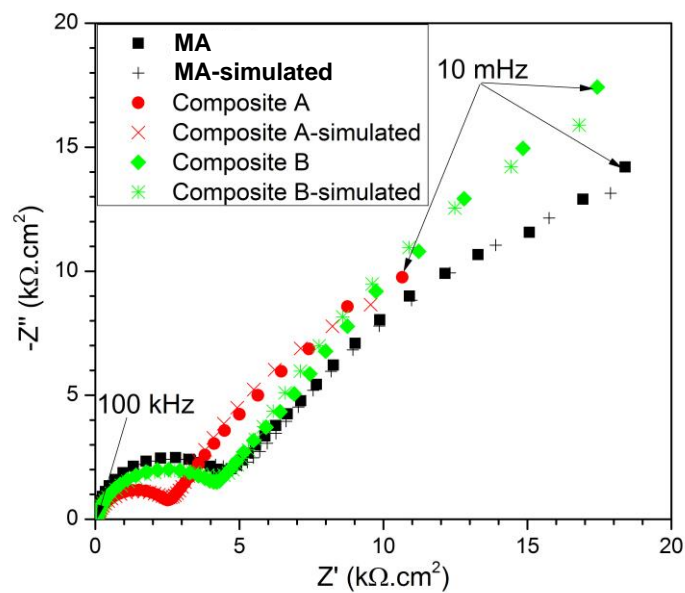
Figure 4.20 Nyquist plots of the EIS responses of the MA and MMCs after immersion in naturally aerated 0.6 M NaCl solution.
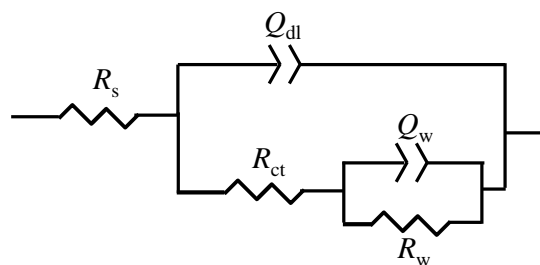
Figure 4.21 Equivalent circuit used to fit the EIS spectra.

where $j^2=-1$, and n is an empirical exponent between 0 and 1. The variation of n is due to the dispersion introduced by the heterogeneity of the surface. When $n=1$, the CPE represents a pure capacitor associated with a smooth surface and when $n=0$ the CPE represents a resister. Particularly, the *CPE* represents Warburg impedance when $n=0.5$.

The good agreement between experimental and simulated results was obtained using the Zview software as shown in Figure 4.20 and the fitting results are shown in Table 4.4. The Q_{dl} follows the sequence: composite A > composite B > MA. This is

probably related to the passive film on the surfaces [7]. The distance of charge separation could be different for the MA and the MMCs depending on the quality of the passive film. The presence of SiC particles could interrupt the integrity of the passive film and result in weak sites at the SiC/Al interfaces. The relative high porosity in composite A could further deteriorate the formation of passive layer. Therefore, the increase in Q_{dl} for the MMCs can be related to the passive layer with more defects compared with that of the MA. The MA and composite B have similar R_{ct} values while the composite A has a much lower R_{ct}, suggesting that the corrosion resistance of the MA and composite B is higher than that of the composite A. The order of the R_{ct} values is in good agreement with that of the i_{corr}. The polarization resistance (R_p) can be correlated with the steady-state corrosion current density at OCP using the Stern-Geary equation:

$$i_{\text{corr}} = \frac{\beta_a \beta_c}{2.303 R_P (\beta_a + \beta_c)} \qquad \text{(Equation 4. 2)}$$

Table 4.4 Average fitted values for the components in the equivalent circuit.

	R_s ($\Omega.cm^2$)	R_{ct} ($k\Omega.cm^2$)	Q_{dl} (10^{-6}) ($\Omega^{-1}.cm^{-2}.s^n$) (n_1)	R_w ($k\Omega.cm^2$)	Q_w (10^{-6}) ($\Omega^{-1}.cm^{-2}.s^n$) (n_2)
MA	8.4±0.3	4.9±0.3	16.2±7.4 (0.92±0.02)	45.2±9	404±114 (0.8±0.04)
Composite A	8.5±0.2	3.1±0.1	29.4±6.6 (0.86±0.03)	24.8±13	689±80 (0.83±0.04)
Composite B	8.3±0.3	4.8±0.2	21.6±6.1 (0.85±0.02)	50.8±5	409±23 (0.84±0.01)

where β_a and β_c are the Tafel constants for anodic and cathodic reactions, respectively. In current work, the R_{ct} is a good indication of the polarization resistance because the EIS spectra at low frequencies are attributed to the diffusion process. Therefore, a low corrosion current density is expected when a high R_{ct} value is registered. Both potentiodynamic polarization and EIS measurements suggest that

135

composite B possesses higher corrosion resistance than composite A and the submicrometre-sized SiC particles in composite B have very little detrimental influence on the corrosion performance of the MMC.

4.3.4 Immersion test

Figure 4.22 BSE-SEM micrographs of (a) MA, (b) composite A, and (c) composite B after immersion in 0.6 M NaCl solution for 30 min.

Figure 4.22 shows the surface morphology of the three materials after immersion in 0.6 M NaCl solution for 30 min. It is evident that the corrosion initiation is closely related with the intermetallic particles for all the three materials. Specifically, Figure 4.22(a) indicates the corrosion initiation at the Al matrix around the AlCuMnFe(Si)-containing intermetallic particles. Also, dealloying of the S-phase was observed in the MA. As shown in Figure 4.23(a), there are some remnants at the sites of the dealloyed particles, which are rich in copper and magnesium as indicated in the EDX spectrum in Figure 4.23(b). For the MMCs, the relative coarse AlCuMnFe(Si)-

containing intermetallic particles seem to remain inert after immersion in 0.6 M NaCl solution while the fine θ-phase particles are the preferential sites for corrosion initiation as shown in Figures 4.22(b) and 4.22(c).
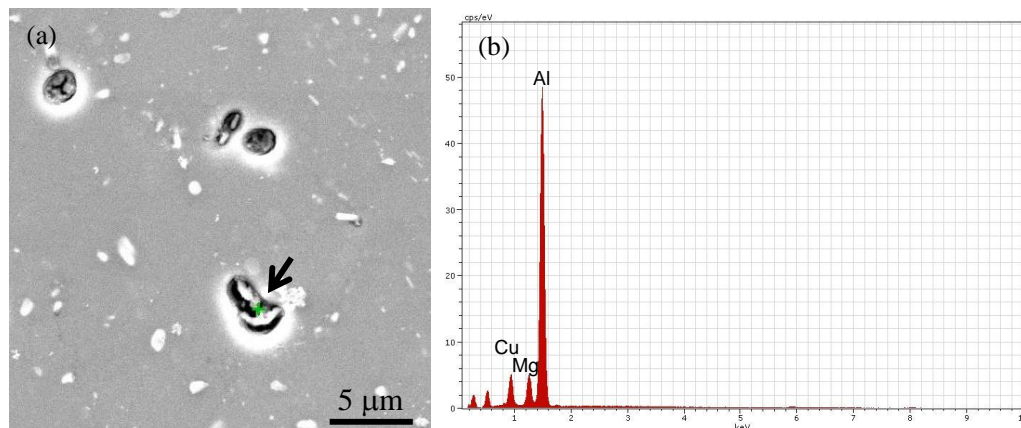
Figure 4.23 Dealloying of the S-phase in the MA after immersion in 0.6 M NaCl for 30 min: (a) SEM micrograph; (b) EDX spectrum.
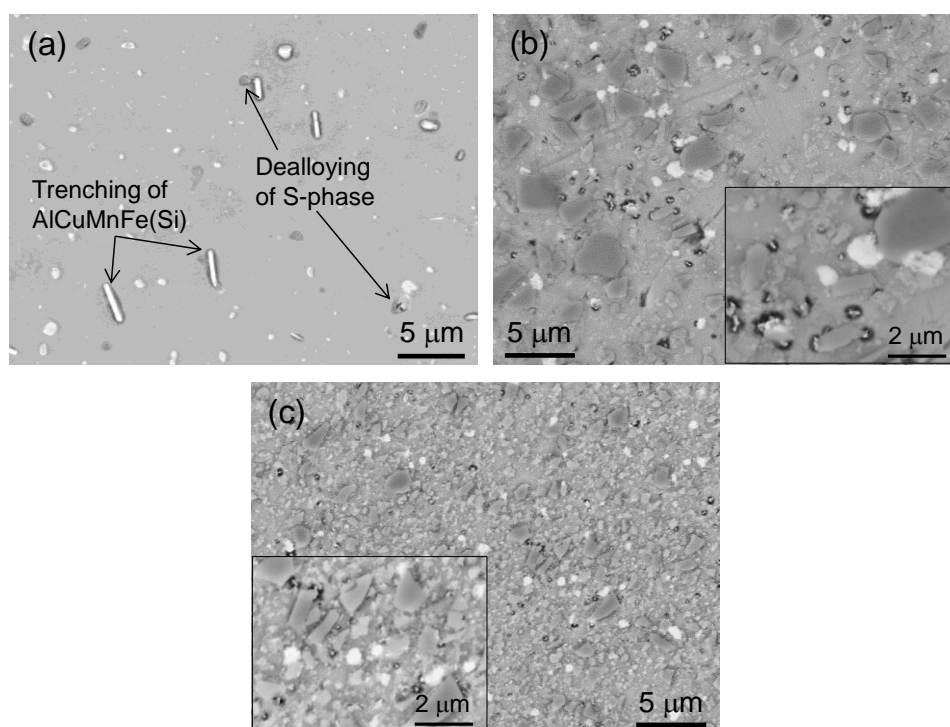
Figure 4.24 BSE-SEM micrographs of (a) MA, (b) composite A, and (c) composite B after immersion in 0.6 M NaCl solution for 1 h.

Figure 4.24 shows the morphology of the corroded samples after immersion in 0.6 M NaCl solution for 1 h. Trenching around the AlCuMnFe(Si)-containing intermetallic particles is revealed on the whole periphery of the particles in the MA (Figure 4.24(a)), while the AlCuMnFe(Si)-containing intermetallic particles still remains unattacked in the MMCs. However, the corrosion of the MMCs initiated at the θ-phase particles has developed into severer attack, especially for the θ-phase particles close to the SiC/Al interfaces as shown in the inserted images in Figures 4.24(b) and 4.24(c). There is more obvious corrosion around the coarse SiC particles than those submicrometre-sized SiC particles in both MMCs. It is evident in composite B that the vicinity of most submicrometre-sized SiC particles is unattacked, as shown in Figure 4.24(c).

After immersion in 0.6 M NaCl solution for 2 h, corrosion attack along the grain boundaries is revealed for the MA, as shown in Figure 4.25(a). The pits morphologies of the corroded MMCs are shown in Figures 4.25(b) and 4.25(c), with the magnified pit centres shown in Figures 4.25(d) and 4.25(e), respectively. Started at isolated areas in the SiC/Al interfacial regions (Figures 4.24(b) and 4.24(c)), corrosion is revealed to propagate along the perimeter of the SiC particles, resulting in large dissolution of the matrix around the SiC particles.

4.4 Discussion

4.4.1 Effect of SiC particles on the microstructure of the MMCs

Comparing Figure 4.1 and Figure 4.8, it is evident that the grain size of Al matrix is reduced by the addition of SiC particles in the MMCs. Refined matrix grains by reinforcements has been reported elsewhere [8]. During manufacture, SiC particles act as obstacles which prevent the grain boundaries movement and therefore result in reduced grain sizes in the MMCs compared with the MA. Due to the reduction of

particle size in composite B, the distance (λ) between dispersed SiC particles decreases because λ is written as:

$$\lambda = \frac{4(1-f)r}{3f}$$

(Equation 4. 3)

where λ is the distance between SiC particles, f is the volume fractions of SiC particles, r is the particle radius [9]. Therefore, the number obstacles in the matrix increases with the decrease of particle size so that the matrix grains in composite B are finer than those in composite A.
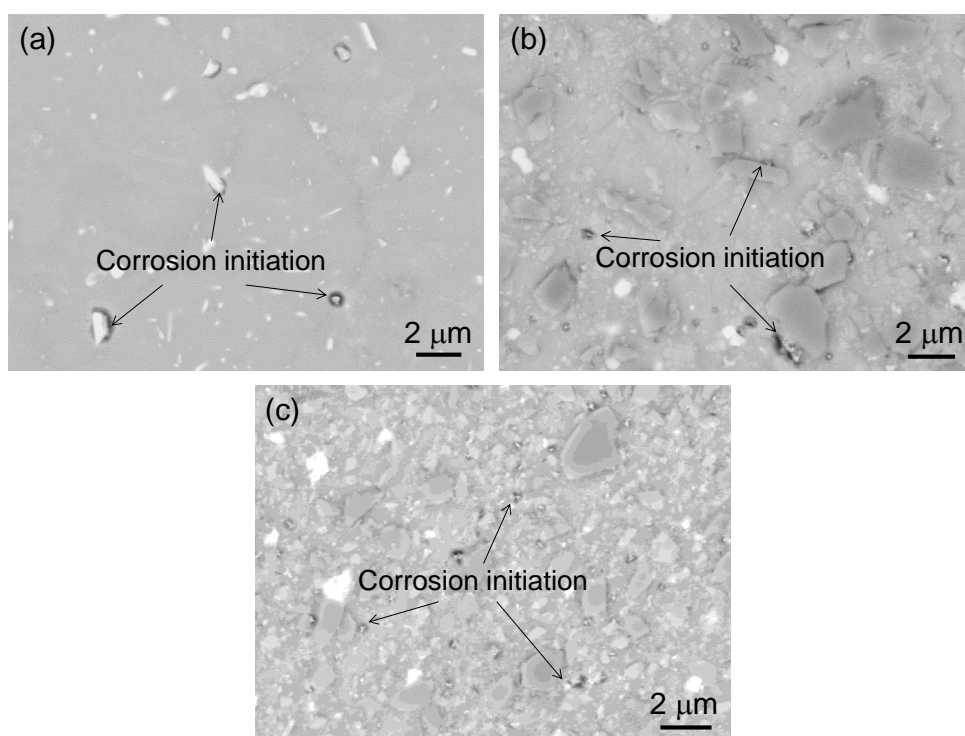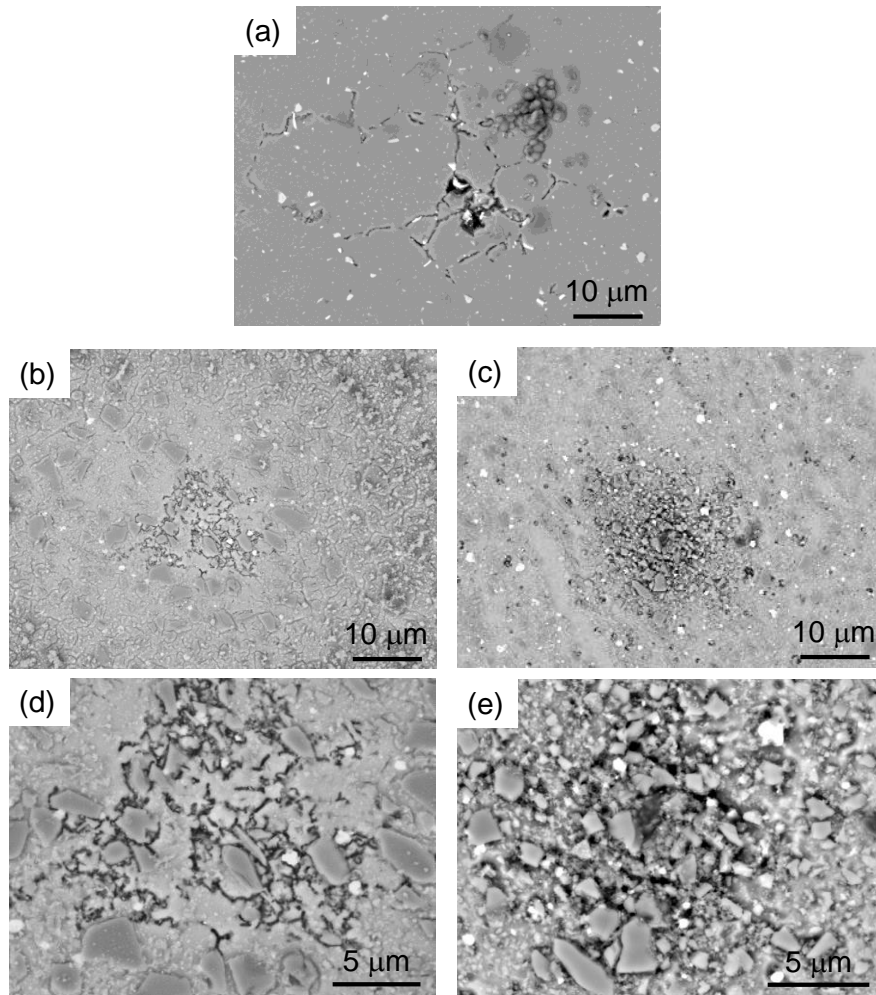

Figure 4.25 BSE-SEM micrographs of (a) MA, (b) and (d) composite A, and (c) and (e) composite B after immersion in 0.6 M NaCl solution for 2 h.

Furthermore, the rod-shaped AlCuMnFe(Si)-containing particles in the MA disappear in the MMCs. These particles contain low concentration of Si and probably belong to the Al_7Cu_2Fe phase according to the EDX analysis in Table 4.1. With the addition of SiC particles, it appears that the rod-shaped particles are replaced with round particles with high concentration of Si (Figures 4.9 and 4.10). This could be due to the increase of Si in the MMCs since SiC particles could be the source of free Si due to chemical reactions. The formation of spinel results in free Si in the matrix according to the Reaction 4.1. A recent study of the SiC_p/AA2124 MMC reported two types of coarse intermetallic particles containing significant Si, which are Fe_2SiAl_8 and $Al_{15}(Fe, Mn)_3Si$ [10]. Another possibility for the generation of free Si is the interdiffusion between Al and SiC, which has been reported to be possible [3, 11, 12]. Via interdiffusion, Al atoms take the positions of Si atoms and Si atoms are dissolved in the Al matrix. The degree of interdiffusion depends on the solubility of Si in Al [12]. The interdiffusion between Al and SiC is indicated in the present study in Figure 4.11(a).

More importantly, the results confirm that the addition of SiC particles results in the preferential precipitation of θ-phase and Mg segregation in the SiC/Al interfacial regions (Figure 4.11). Such interfacial precipitation has been reported by other researchers as discussed in the literature review [10, 13-16]. In current work, the interfacial precipitation is reduced by incorporating submicrometre-sized SiC particles in composite B, indicating that the size of the SiC particles has great impact on the distribution of the intermetallics in the MMCs. Previous research has demonstrated that the interfacial precipitates increase with the decrease of the size of SiC particles (from several tens of micrometres to about 10 μm) due to the increase of the areas of SiC/Al interfaces [17]. This somewhat contradicts our observations, which could be probably attributed to the incorporation of extra-fine SiC particles in submicron range. It has been reported that the addition of SiC particles results in high density of dislocation in their adjacent matrix due to the mismatch of the

thermal expansion coefficients between SiC and Al, providing pipe tunnels for atom diffusion and promoting the diffusion of solute atoms [16, 18, 19]. Prangnell et al. [20] reported the preferential precipitation of θ' phase around the reinforcements and concluded that the density of θ' precipitates around the SiC reinforcement is proportional to the dislocation density due to the fact that the density of θ' phase decreases with the increase of the distance from the reinforcements, leading to the decrease of dislocation density. Kim et al. [21] suggested the decrease in average dislocation density with deceasing particle size of the reinforcements. Therefore, high density dislocations could accelerate the diffusion of solute atoms during solution treatment, such as Cu and Mg. The migration of solute atoms stops when the solute atoms encounter with the SiC/Al interfaces so that they can be segregated to the SiC/Al interfaces. According to above discussion, the dislocation density in the SiC/Al interfacial regions could be reduced in composite B due to the decrease in particle size, resulting in the decrease of solute atoms migration during solution treatment and thus the interfacial precipitation is reduced in composite B, compared with composite A.

In addition, the compound Al_4C_3 was not observed in both composites. It normally requires a minimum temperature of 650 ℃ with sufficient holding time for the formation of Al_4C_3 [16, 22]. In the present study, the MMC was manufactured in solid state; and therefore the temperature did not exceed 650 ℃. Also, the subsequent solution heat treatment was performed at 505 ℃. Therefore, the chance of the formation of Al_4C_3 was slim.

4.4.2 Corrosion mechanisms of the MA and MMCs

A number of previous reports have demonstrated that the corrosion initiation of Al-Cu-Mg alloys is related to the intermetallics, such as Al_2CuMg, Al_2Cu, and AlCuMnFe(Si)-containing intermetallics [1, 23-28]. In current work, dealloying of S-phase particles and the dissolution of Al matrix around AlCuMnFe(Si)-containing

particles are responsible for the corrosion initiation of the MA in chloride solution as indicated by the immersion tests (Figures 4.23-4.25). As is known, S-phase has a more negative OCP than the aluminium matrix and the OCPs of the AlCuMnFe(Si)-containing intermetallics are close to or more positive than that of the aluminium matrix [23, 27, 28]. S-phase and AlCuMnFe(Si)-containing intermetallics could form galvanic couples with the aluminium matrix, being anode and cathode, respectively, and lead to the initiation of corrosion. As indicated in Figure 4.1 and Figure 4.7, the electrochemistry of the grain boundaries could be different from the adjacent matrix due to the precipitation of intermetallics at the grain boundaries. The precipitation of AlCuMnFe(Si)-containing intermetallics on the grain boundaries results in a solute-depleted zone, typically Cu-depleted zone near the grain boundaries, making the adjacent matrix anodic to the grain boundaries, while the precipitation of S-phase or Mg segregation could make the grain boundaries anodic to the adjacent matrix [29]. Therefore, the corrosion propagates to grain boundaries by forming galvanic cells with the adjacent matrix (Figure 4.25).

Compared with the MA, different corrosion mechanism is revealed for the MMCs due to the difference in microstructures. According to the characteristics of the surface morphology during corrosion initiation, the SiC particles are revealed to have no direct effect on the corrosion behaviour of the MMCs but the θ-phase particles in the SiC/Al interfacial regions are the preferential site for corrosion initiation. The inert nature of the AlCuMnFe(Si)-containing particles in the MMCs could be due to the high percentage of Si and lower Cu/Fe ratio, which have been reported to cause a delay in corrosion initiation at these particles [30]. The θ-phase particles has a more positive OCP than the aluminium matrix and thus behaves as a cathode, leading to the dissolution of the surrounding aluminium, which has been extensively discussed [31]. Also, the θ-phase particles and Mg segregation are usually closely precipitated in the SiC/Al interfacial regions; they could form galvanic cells with each other and accelerate the corrosion initiation. The fact that the θ-phase particles act as the

corrosion initiation site is in agreement with previous reports [31-33]. Mg segregation to the SiC/Al interface has been also reported to be an important factor degrading the corrosion performance of the MMC [14]. Due to the dissolution of Mg segregation and Al matrix, crevices could form at the SiC/Al interfaces as shown in Figures 4.24(b) and 4.24(c). The formation of micro-crevices could accelerate the dissolution of the matrix around isolated SiC particles. The small pits eventually grow to be attached to each other to form larger pits as shown in Figures 4.25(d) and 4.25(e).

Due to the reduced interfacial precipitates in composite B, the active sites for corrosion initiation are reduced and thus the corrosion resistance of composite B is higher than that of composite A. In addition, although there is no evidence showing that the corrosion initiation is associated with the porosity in the MMCs, the contribution of the reduced porosity to the enhanced corrosion performance of composite B could not be ruled out.

4.5 Summary

In this chapter, the effect of SiC particles on the microstructure and corrosion behaviour of MMCs has been evaluated. Microstructural characterization reveals that the addition of SiC particles results in preferential precipitations, such as θ-phase and Mg segregation, in SiC/Al interfacial regions. The concentration of Si in the AlCuMnFe(Si)-containing particles is higher for the MMCs than the MA, which is attributed to the presence of SiC particles as a source of free Si. The incorporation of submicrometre-sized SiC particles reduces the preferential precipitation in SiC/Al interfacial regions in composite B.

Corrosion evaluation indicates that the corrosion resistance of composite B is close to that of the MA and higher than that of composite A. The corrosion initiation sites are S-phase and AlCuMnFe(Si)-containing particles for the MA whilst the corrosion

preferably initiates at the θ-phase particles and Mg segregation in SiC/Al interfacial regions for the MMCs. The improved corrosion resistance of the composite B is attributed to the decrease of the interfacial precipitation in SiC/Al interfacial regions, reducing the active sites for corrosion initiation.

References

[1]   R.G. Buchheit, R.P. Grant, P.F. Hlava, B. Mckenzie, G.L. Zender, *Local dissolution phenomena associated with S phase (Al₂CuMg) particles in aluminum alloy 2024-T3*, Journal of the Electrochemical Society, 144 (1997), 2621-2628.

[2]   C. Luo, Role of microstructure on corrosion control of AA2024-T3 aluminium alloy, 2011, Ph.D thesis, The University of Manchester

[3]   R.D. Evans, J.D. Boyd, *Near-interface microstructure in a SiC/Al composite*, Scripta Materialia, 49 (2003), 59-63.

[4]   J.C. Romero, L. Wang, R.J. Arsenault, *Interfacial structure of a SiC/Al composite*, Materials Science and Engineering a-Structural Materials Properties Microstructure and Processing, 212 (1996), 1-5.

[5]   Z.P. Luo, *Crystallography of SiC/MgAl₂O₄/Al interfaces in a pre-oxidized SiC reinforced SiC/Al composite*, Acta Materialia, 54 (2006), 47-58.

[6]   L.H. Hihara, R.M. Latanision, *Galvanic corrosion of aluminum-matrix composites*, Corrosion, 48 (1992), 546-552.

[7]   A.C. Balaskas, M. Curioni, G.E. Thompson, *Effectiveness of 2-mercaptobenzothiazole, 8-hydroxyquinoline and benzotriazole as corrosion inhibitors on AA 2024-T3 assessed by electrochemical methods*, Surface and Interface Analysis, (2015), early online.

[8]   S.C. Tjong, K.C. Lau, *Properties and abrasive wear of TiB₂/Al-4%Cu composites produced by hot isostatic pressing*, Composites Science and Technology, 59 (1999), 2005-2013.

[9]   O. El-Kady, A. Fathy, *Effect of SiC particle size on the physical and mechanical properties of extruded Al matrix nanocomposites*, Materials & Design, 54 (2014), 348-353.

[10]   D. Mandal, S. Viswanathan, *Effect of heat treatment on microstructure and interface of SiC particle reinforced 2124 Al matrix composite*, Materials Characterization, 85 (2013), 73-81.

[11]   W. Lucke, J. Comas, G. Hubler, K. Dunning, *Effects of annealing on profiles of aluminum implanted in silicon-carbide*, Journal of Applied Physics, 46 (1975), 994-997.

[12]   J.C. Romero, R.J. Arsenault, *Anomalous penetration of Al into SiC*, Acta Metallurgica Et Materialia, 43 (1995), 849-857.

[13]   M.M. Buarzaiga, S.J. Thorpe, *Corrosion behavior of as-cast, silicon-carbide particulate-aluminum alloy metal-matrix composites*, Corrosion, 50 (1994), 176-185.

[14]   D. Imeson, D.L. Bartlett, *Microstructural origins of corrosion in a 20% SiC$_p$/2124 aluminium alloy metal matrix composite*, Journal of Microscopy, 177 (1995), 347-356.

[15]   Z. Ahmad, B.J.A. Aleem, *Corrosion behavior of a discontinuously reinforced composite in salt water environment*, Journal of Reinforced Plastics and Composites, 25 (2006), 1507-1523.

[16]   H. Ribes, R. Dasilva, M. Suery, T. Bretheau, *Effect of interfacial oxide layer in Al-SiC particle composites on bond strength and mechanical-behavior*, Materials Science and Technology, 6 (1990), 621-628.

[17]   S. Candan, *Effect of SiC particle size on corrosion behavior of pressure infiltrated Al matrix composites in a NaCl solution*, Materials Letters, 58 (2004), 3601-3605.

[18]   J.S. Lin, P.X. Li, R.J. Wu, *Aging evaluation of cast particulate-reinforced SiC/Al(2024) composites*, Scripta Metallurgica Et Materialia, 28 (1993), 281-286.

[19]   T.W. Clyne, P.J. Withers. An introduction to metal matrix composites, 1993.

[20]   P.B. Prangnell, W.M. Stobbs, *The effect of internal stresses on precipitation behaviour in particulate reinforced Al matix MMCs, in: N. Hansen et al. (Eds.) Metal Matrix Composites—Processing, Microstructure and Properties, 12th Risϕ Int. Symp. on Metallurgy and Materials Science, Risϕ National Laboratory, Roskilde, Denmark, 1991, 603–610.*

[21]   C.T. Kim, J.K. Lee, M.R. Plichta, *Plastic relaxation of thermoelastic stress in aluminum/ceramic composites*, Metallurgical Transactions A, 21 (1990), 673-682.

[22]   S.D. Peteves, P. Tambuyser, P. Helbach, M. Audier, V. Laurent, D. Chatain, *Microstructure and microchemistry of the Al/SiC interface*, Journal of Materials Science, 25 (1990), 3765-3772.

[23]   A. Boag, A.E. Hughes, A.M. Glenn, T.H. Muster, D. McCulloch, *Corrosion of AA2024-T3 Part I. Localised corrosion of isolated IM particles*, Corrosion Science, 53 (2011), 17-26.

[24]   C. Blanc, A. Freulon, M.C. Lafont, Y. Kihn, G. Mankowski, *Modelling the corrosion behaviour of Al$_2$CuMg coarse particles in copper-rich aluminium alloys*, Corrosion Science, 48 (2006), 3838-3851.

[25]   L. Lacroix, L. Ressier, C. Blanc, G. Mankowski, *Statistical study of the corrosion behavior of Al$_2$CuMg intermetallics in AA2024-T351 by SKPFM*, Journal of the Electrochemical Society, 155 (2008), C8-C15.

[26]   O. Schneider, G.O. Ilevbare, J.R. Scully, R.G. Kelly, *In situ confocal laser scanning microscopy of AA 2024-T3 corrosion metrology - II. Trench formation around particles*, Journal of the Electrochemical Society, 151 (2004), B465-B472.

[27]   G.O. Ilevbare, O. Schneider, R.G. Kelly, J.R. Scully, *In situ confocal laser scanning microscopy of AA 2024-T3 corrosion metrology - I. Localized corrosion of particles*, Journal of the Electrochemical Society, 151 (2004), B453-B464.

[28]   P. Leblanc, G.S. Frankel, *A study of corrosion and pitting initiation of AA2024-T3 using atomic force microscopy*, Journal of the Electrochemical Society, 149 (2002), B239-B247.

[29]   V.S. Sinyavskii, V.V. Ulanova, V.D. Kalinin, *On the mechanism of intergranular corrosion of aluminum alloys*, Protection of Metals, 40 (2004), 481-490.

[30]   A. Boag, A.E. Hughes, A.M. Glenn, T.H. Muster, D. McCulloch, *Corrosion of AA2024-T3 Part I: Localised corrosion of isolated IM particles*, Corrosion Science, 53 (2011), 17-26.

[31]   Z. Feng, C. Lin, J. Lin, J. Luo, *Pitting behavior of SiC_p 2024 Al metal matrix composites*, Journal of Materials Science, 33 (1998), 5637-5642.

[32]   Z. Ahmad, P.T. Paulette, B.J.A. Aleem, *Mechanism of localized corrosion of aluminum-silicon carbide composites in a chloride containing environment*, Journal of Materials Science, 35 (2000), 2573-2579.

[33]   D. Nickel, G. Alisch, H. Podlesak, M. Hockauf, G. Fritsche, T. Lampke, *Microstructure, corrosion and wear behaviour of UFG-powder-metallurgical Al-Cu alloys, Al-Cu/Al$_2$O$_3$(p) and Al-Cu/SiC(p) composites*, Reviews on Advanced Materials Science, 25 (2010), 9.

Chapter 5 Microstructural characterization of the excimer laser-melted MA and MMC

5.1 Introduction

As discussed in Chapter 4, the microstructural heterogeneity, such as the intermetallics and grain boundary segregations, results in high susceptibility of MA to localised corrosion. The addition of SiC particles could further deteriorate the corrosion performance of the MMC if high content of precipitates is introduced to the SiC/Al interfaces. The rest of this research work investigates the capability of excimer LSM for improving the corrosion resistance of the MA and the MMC reinforced with micrometre-sized SiC particles. This chapter focuses on the microstructural characterization of the excimer laser-melted MA and MMC. The modelling of excimer LSM process is introduced to help understand the microstructure evolution upon laser irradiation.

5.2 Selection of laser operating parameters

Depending on the selection of laser operating parameters, different microstructures can be obtained. Laser fluence and NOP are two important parameters affecting the excimer LSM process. The surface morphology, roughness, melt depth and homogeneity of the melted layer significantly depend on the laser fluence and the NOP for both Al alloys [1-4] and MMCs [5, 6]. The operating parameters have to be controlled in reasonable ranges in order to achieve homogeneous melted layers and at the same time avoid any undesirable changes. To evaluate the influence of the laser operation parameters on the microstructures of the melted layer, the laser fluence varied from 1 to 7 J/cm^2, and eight levels of NOP from 5 to 40 with an interim of 5 pulses (P) between two neighbouring levels were selected.

Due to the extreme short time of laser-material interaction for a single laser pulse, two laser pulses in sequence are considered to have no effect on the materials

response for each laser pulse. Therefore, the frequency of the laser radiation was set at 10 Hz.

5.3 Microstructural characterization of excimer laser-melted MA

5.3.1 Surface morphology
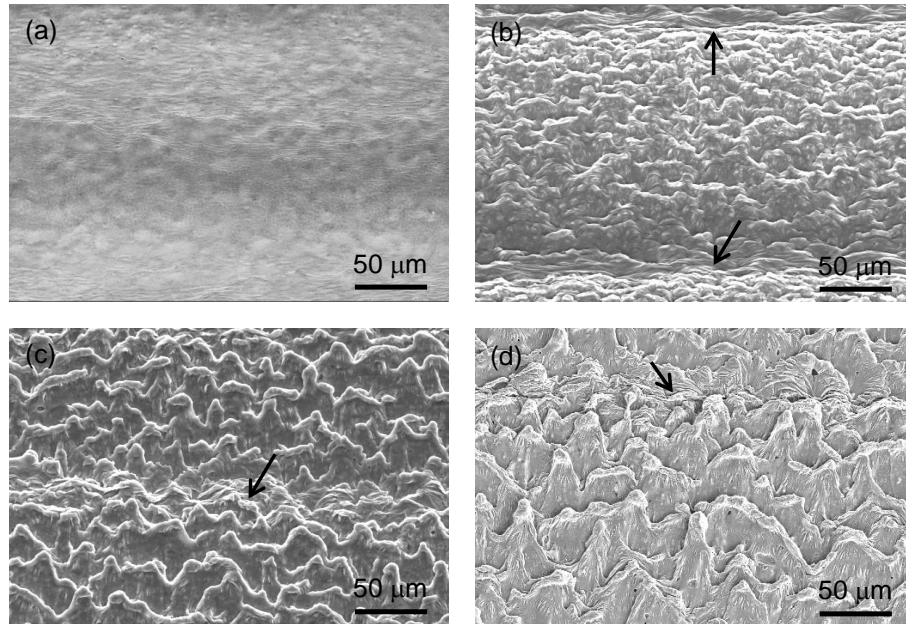
Figure 5.1 SE-SEM micrographs of excimer laser-melted MA treated with 10 P at different laser fluences: (a) 1 J/cm^2; (b) 3 J/cm^2; (c) 5 J/cm^2; and (d) 7 J/cm^2.

Figure 5.1 shows the surface morphology of the laser-melted MA treated with 10 P and various laser fluences from 1 J/cm^2 to 7 J/cm^2. The laser-melted surface appears flat when the laser fluence of 1 J/cm^2 is applied, as shown in Figure 5.1(a). By increasing the laser fluence, the laser-melted surfaces exhibit a rippled morphology. The oriented ripples are attributed to the surface tension of the melt and the shear stresses generated from the surface tension gradients [1]. Considering a single shot of the laser pulse, due to the higher energy intensity in the centre of beam spot than the circumference, a radial temperature gradient is generated. The temperature coefficient of the surface tension ($\partial\sigma/\partial T$) is written as $\partial\sigma/\partial T = -S$, where σ and S is the enthalpy and entropy, respectively. Therefore, the decrease of temperature from the beam centre contributes to the increase of surface tension as

the entropy *S* is always positive. After the melting of the alloy occurs, the melt is pulled away from the centre by the surface tension. It is evidently shown in Figure 5.2, which presents the laser-melted surface within a single beam spot. The central area is flat and the melt is pulled away from the centre to form the ripped structure. On the edge, the re-solidified melt is squeezed, corresponding to the squeezed ripples indicated in Figure 5.1(b)-(d) (black arrows). However, when the laser fluence is lower than 3 J/cm^2 with relative low NOP, the whole melted surface is free of significant ripples (Figure 5.2(b)).
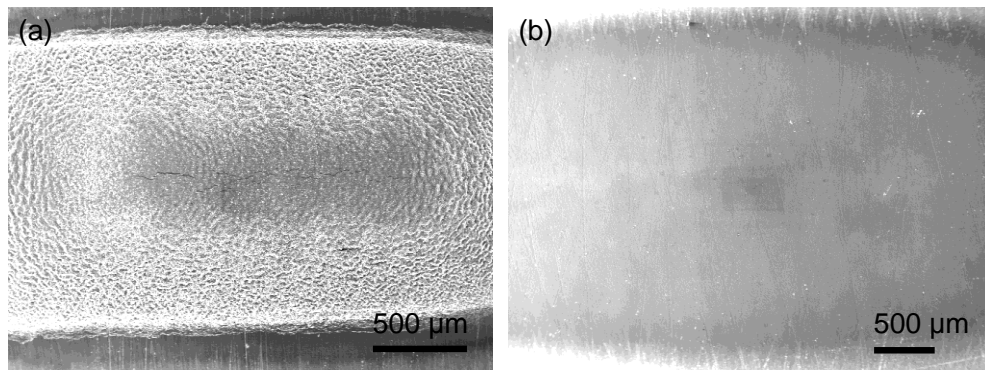
Figure 5.2 SE-SEM micrographs of laser-melted MA in the area of a single spot: (a) 7 J/cm^2, 5 P and (b) 2 J/cm^2, 5 P.
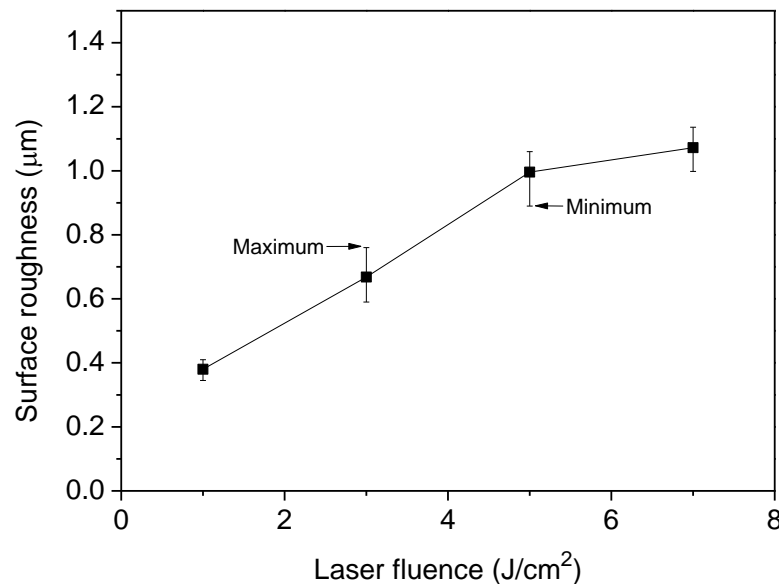
Figure 5.3 Surface roughness of laser-melted MA treated with 10 P at different laser fluences.

The surface roughness was measured using interferometry as described in Section 3.6. The results are shown in Figure 5.3, where the roughness values are average values of three measurements for each sample. The graph shows that the surface roughness increases with the increase of applied laser fluence. The deposited energy in the melt pool increases and therefore the temperature of the melt increases with increasing laser fluence. It is known that the higher the temperature of a system is, the higher the entropy S of the system is. The increase of laser fluence results in the increase in entropy of the melt and thus a larger surface tension gradient, causing significant ripples on the laser-melted surface as shown in Figure 5.1. Therefore, the formation of ripples could be the main factor that contributed to the increase of surface roughness of the laser-melted surface.
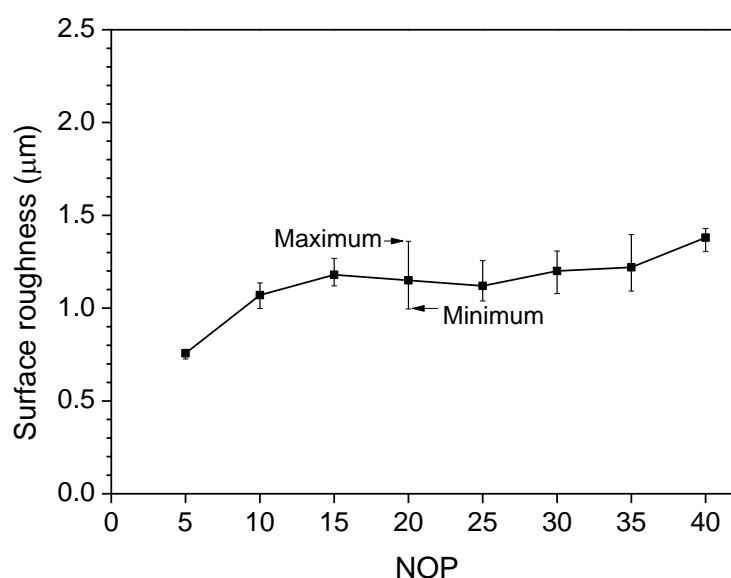
Figure 5.4 Surface roughness of laser-melted MA treated at 7 J/cm^2 with various NOP.

The surface roughness of the laser-melted MA is also related to the variation of NOP as shown in Figure 5.4. The corresponding surface morphologies are shown in Figure 5.5. With the laser fluence of 7 J/cm^2, the rippled structure is revealed on all the samples with the applied NOP varying from 5 to 40. An evident rise in surface roughness is shown when the NOP increased from 5 to 15. When further increasing the NOP, the surface roughness changes little. The initial increase in surface roughness could be due to the ripples growing closer as shown in Figure 5.5. With

the increase of NOP, pores eventually appear on the laser-melted MA surfaces, indicated by black arrows in Figures 5.5(d)-(h).
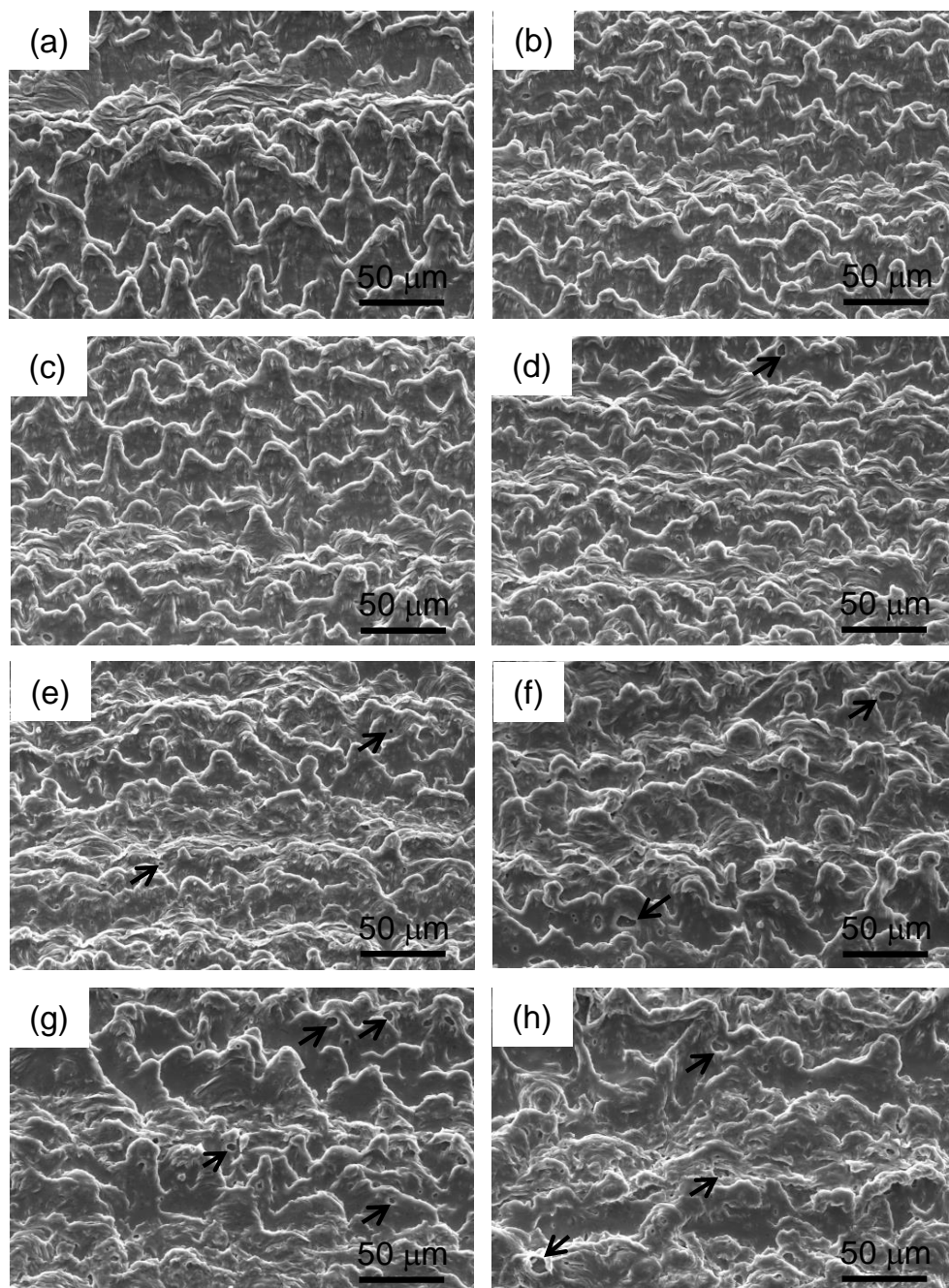
Figure 5.5 SE-SEM micrographs of excimer laser-melted MA at 7 J/cm^2 with different NOP: (a) 5 P; (b) 10 P; (c) 15 P; (d) 20 P; (e) 25 P; (f) 30 P; (g) 35 P; and (h) 40 P.

In the areas that the rippled structure is formed with high laser fluence or high NOP, the melt is squeezed during the flow of the melt upon laser irradiation as a result of the presence of surface tension gradients. When fast re-solidification takes place, there is not sufficient time for the ripples to be flattened and therefore, micro-crevices could be formed between the squeezed ripples as shown in Figure 5.6.

5.3.2 Cross-sectional morphology

Figure 5.7 shows the cross-sectional morphology of laser-melted MA treated with 10 P at various laser fluences from 1 J/cm^2 to 7 J/cm^2. The bright intermetallic particles, observed in the underlying substrate, disappear in the near-surface region, indicating the dissolution of intermetallic particles by laser irradiation. When the laser fluence of 1 J/cm^2 is applied, a thin melted layer can be achieved and the intermetallic particles are not completely dissolved as suggested by the presence of intermetallics with solute trails in the melted layer (Figure 5.7(a)). When the laser fluence increases to 3 J/cm^2, the solute trails are significantly reduced, indicating a more homogeneous dispersion of solutes in the melted layer. Complete dispersion of the solutes can be achieved when the laser fluence further increases to 5 J/cm^2 or higher with the NOP of 10.
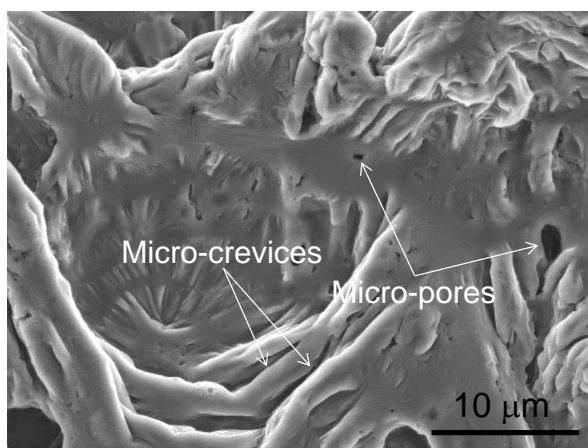
Figure 5.6 SE-SEM micrograph showing the micro-crevices formed between the ripples.

A linear relationship is indicated between the thickness of the melted layer and the laser fluence when the laser fluence increases from 1 J/cm^2 to 7 J/cm^2, as shown in

Figure 5.8. The maximum and minimum measurements of the thickness are shown in Figure 5.8 and the difference between the two values increases with the increase of laser fluence, which could be due to the increase of surface roughness. It is easy to understand that higher laser fluences result in larger melt depths because more energy is deposited in the melting pool, causing a larger volume of material to be melted. The changes in the melt depth indicate that higher laser fluences are desirable to obtain thicker melted layers. Many studies of the corrosion behaviour of excimer-laser melted aluminium alloys can be found in the literature using relative high laser fluences (> 5 J/cm^2) in order to achieve melted layers with considerable thicknesses [4, 7-13].
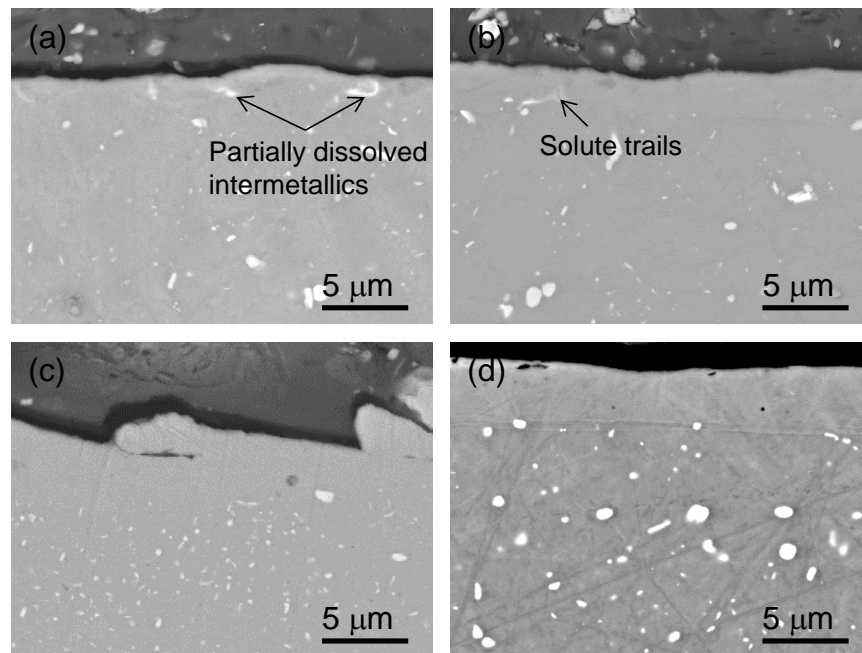
Figure 5.7 BSE-SEM micrographs of the cross-section of excimer laser-melted MA treated with 10 P at different laser fluences: (a) 1 J/cm^2; (b) 3 J/cm^2; (c) 5 J/cm^2; and (d) 7 J/cm^2.

Considering the melted layer of MA treated with different NOP at the fixed laser fluence of 7 J/cm^2, the intermetallics are revealed to be completely dissolved into Al matrix except the sample treated with 5 P, in which solute trails and undissolved intermetallics are shown in the melted layer (Figure 5.9). The solute trails are elongated along the moving direction of the melt (parallel to the sample surface),

being attributed to the incomplete dispersion of the solutes resulted from the melted intermetallics. The melted layer becomes porous when the applied NOP increases to 25 or higher and the significance of the porosity increases with the increase of NOP.
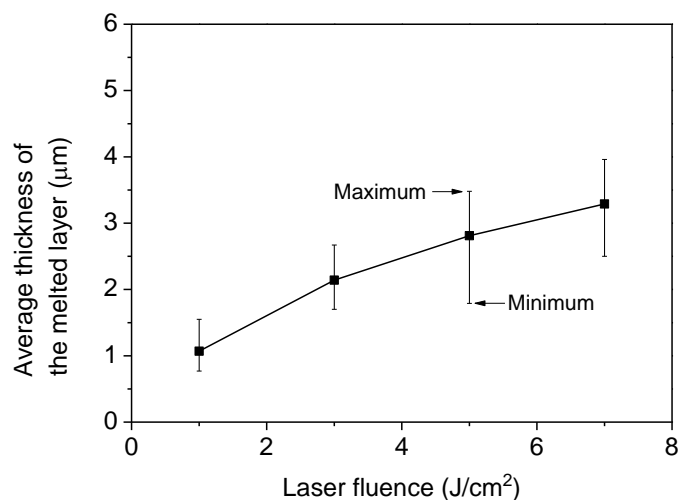
Figure 5.8 Correlation between the thicknesses of the melted layer of MA with the laser fluence. All the samples were treated with the fixed NOP of 10.

The variation of the thickness of the melted layer with NOP is shown in Figure 5.10. The difference between the maximum and minimum values under each condition indicates the rough nature of the laser-melted surfaces. The average thickness of the melted layer shows slight increase with increasing NOP from 5 to 40. This is probably because of the increase of laser beam absorptivity as a result of the increased roughness [14]. The increase of the melted layer thickness with increasing NOP is more apparent when the applied NOP is higher than 25. This is probably attributed to the porous nature of the melted layer. The higher porosity could result in larger volume of the melted layer and therefore, thicker melted layer was observed. The formation of the porosity in the melted layer can be attributed to the strong agitation of the melting pool due to the surface tension, trapping the air in the melted layer or resulting in crevices and passages related to the ripples (red arrows in Figures 5.9 (a) and (e)). An example showing the formation of porosity in the melted

155
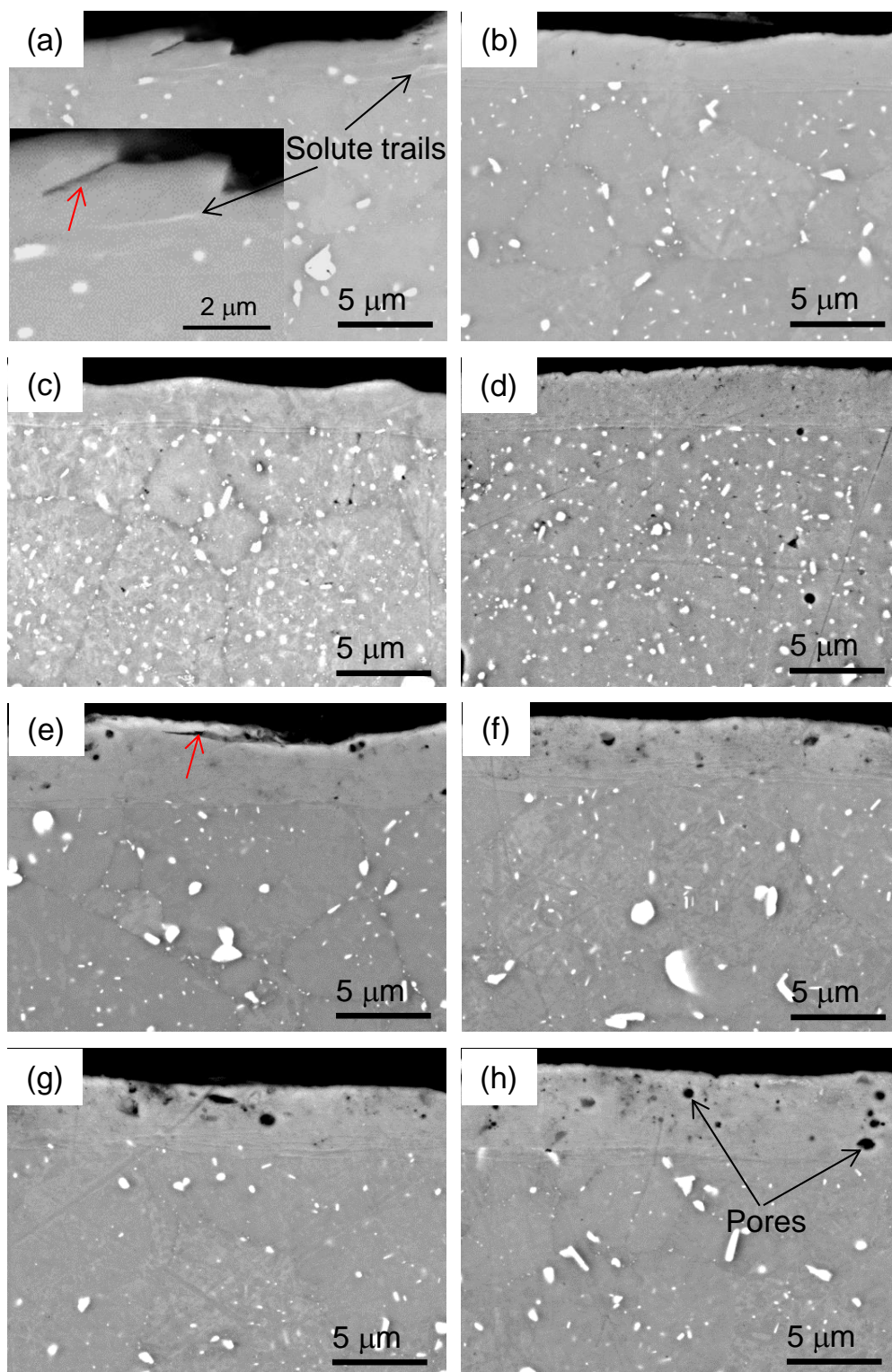
Figure 5.9 BSE-SEM micrographs of the cross-section of excimer laser-melted MA at the fixed laser fluence of 7 J/cm^2 with different NOP: (a) 5 P; (b) 10 P; (c) 15 P; (d) 20 P; (e) 25 P; (f) 30 P; (g) 35 P; and (h) 40 P.

layer is shown in Figure 5.11. Clearly, the rippled structure is formed due to the fast re-solidification of the melt during movement as a result of fast cooling rates. A gas pore is trapped between the ripple and the substrate. The trapped air could be then distributed in the melted layer after repeating the melting process by applying more laser pulses.
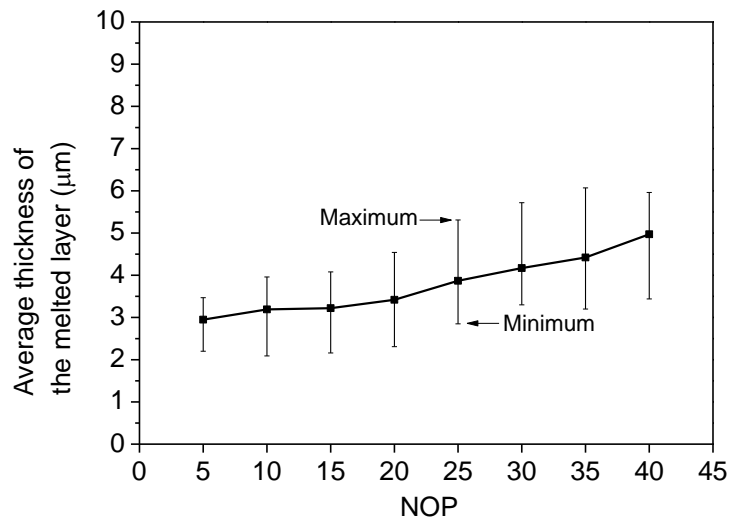
Figure 5.10 Correlation between the thicknesses of the melted layer of MA and the NOP. All the samples were treated at the fixed laser fluence of 7 J/cm^2.
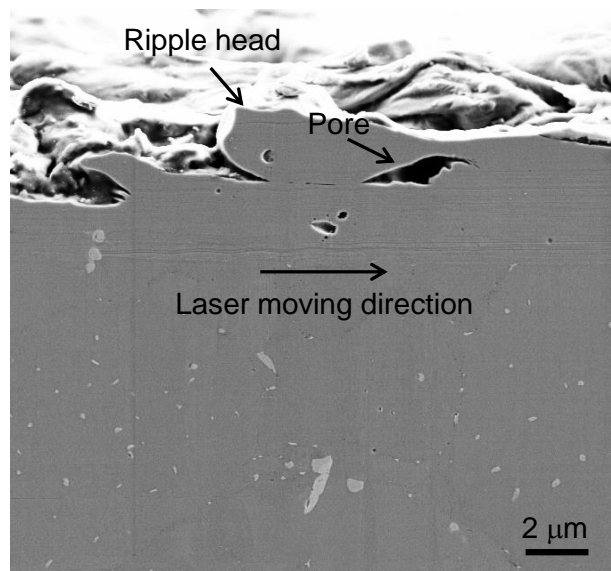
Figure 5.11 Cross-sectional SE-SEM micrograph showing the gas pore trapped between the rippled structure and the underlying substrate (7 J/cm^2, 25 P).

157
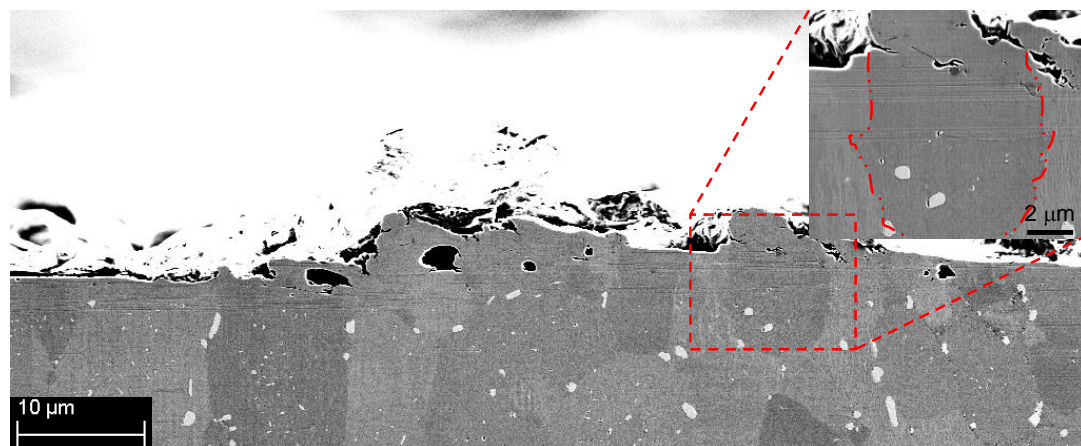
Figure 5.12 Cross-sectional SE-SEM micrograph showing the grain structure in the melted layer (7 J/cm^2, 10 P).
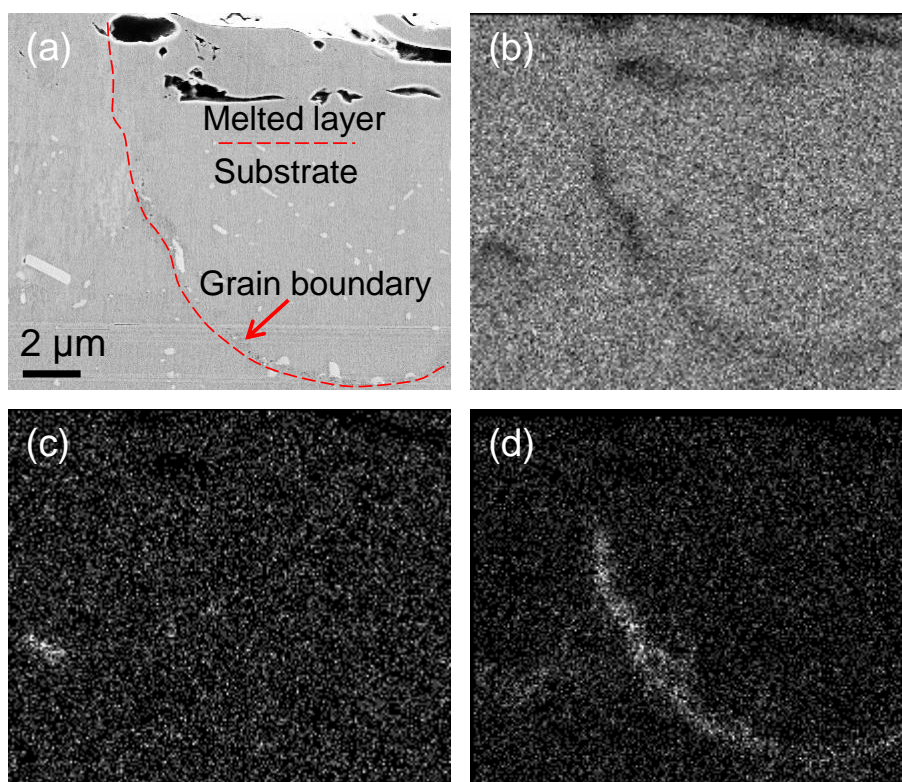
Figure 5.13 EDX elemental mapping analysis of the grain boundaries in the melted layer and substrate (7 J/cm^2, 25 P): (a) SE-SEM micrograph; and individual maps of (b) Al; (c) Cu; and (d) Mg.

Figure 5.12 is an SE-SEM micrograph showing the typical grain structures in the melted layer. Adjacent grains show a slight difference in their contrast so that the

158

grains can be readily distinguished. It is shown that the grain boundaries of the underlying substrate continued upwards through the melted layer. The grain size in the melted layer remains unchanged compared with that in the substrate but the intermetallic particles precipitated at the grain boundaries are dissolved in the melted layer. Further examination of the grain boundary composition with EDX elemental mapping analysis is shown in Figure 5.13. Cu and Mg are homogeneously distributed in the melted layer while significant segregation of Mg at the grain boundaries is shown in the substrate. This indicates the microstructural refinement by redistributing the alloying elements in the melted layer after excimer LSM.
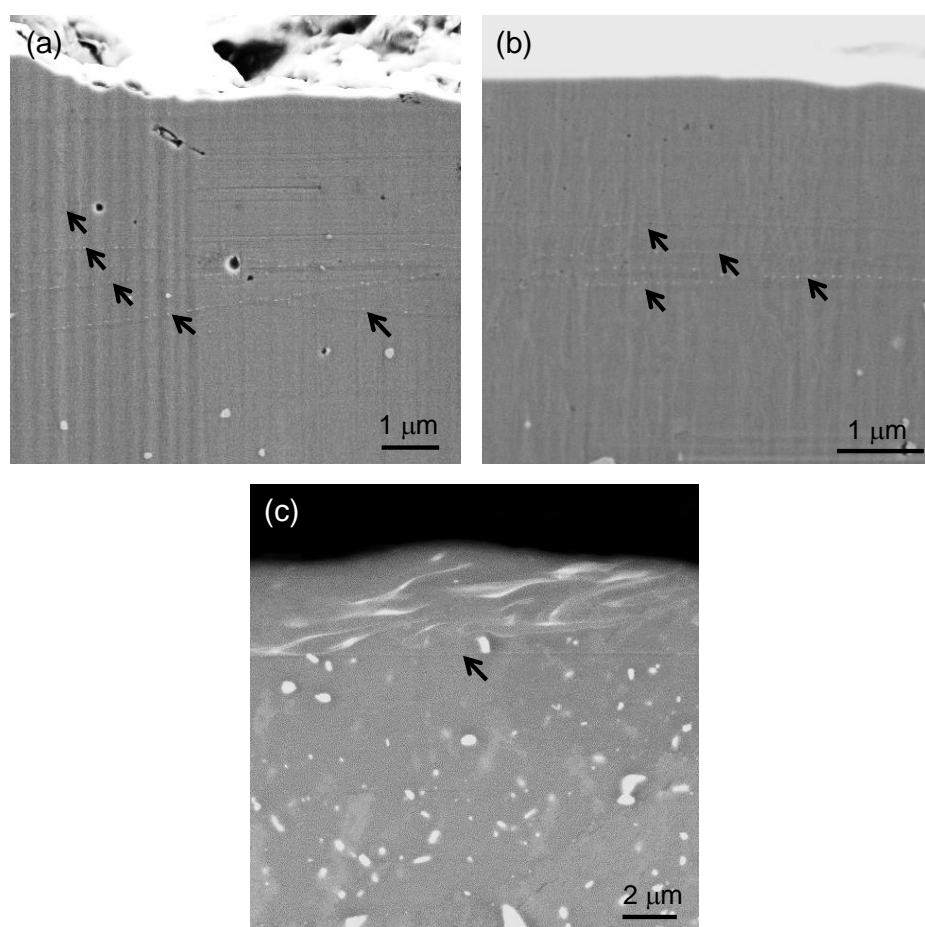
Figure 5.14 SEM micrographs showing the segregation bands in the melted layer: (a) 7 J/cm^2, 25 P; (b) 2 J/cm^2, 20 P; and (c) 7 J/cm^2, single pulse.

Banded structures were observed in the melted layer, as shown in Figure 5.14(a), revealing several light segregation bands parallel with the sample surface. The segregation bands are not continuous but composed of a stream of extra fine particles.

159

The segregation bands are normally concentrated at the bottom of the melted layer but also present in the middle area of the melted layer. They could intersect with the pores in the melted layer. The formation of the segregation bands is to some extent independent on the laser fluence. It is shown in the samples treated with both high and low laser fluences as indicated in Figure 5.14(a) and Figure 5.14(b). There is a correlation between the number of the segregation bands and the NOP reported by Ryan et al. [3], who found that the number of segregation bands linearly increased with the increase of the NOP. Nevertheless, it is difficult to count the number of the segregation bands as they could also intersect with each other and become one at the point of intersection. Therefore, the cross-section of the melted layer formed with a single laser pulse was examined, as shown in Figure 5.14(c). A large number of solute trails are revealed in the melted layer, being due to that a single laser pulse is not enough to fully disperse the solute atoms resulted from the dissolved intermetallics. However, only one straight segregation band is indicated. The segregation band is likely to be formed at the melted layer/substrate interface for the single laser pulse. This is a confirmation of the results in Ref. [3], which attributes the formation of the segregation bands to the morphological instability at the beginning of the solidification of the melt.

5.3.3 Large area coverage

By selecting proper laser operating parameters, compact melted layers with complete dispersion of solutes atoms could be achieved, although the thickness and surface morphology of the melted layers could be different by applying different combinations of laser fluence and NOP. As shown in Figure 3.1, the laser beam has a rectangular shape with the energy intensity lower at the two ends of the long side than the central area. Therefore, an overlapped ratio of 20% was selected to compensate the energy deficiency at the two ends for large area coverage.

Two typical surface morphologies are formed depending on the selected laser operating parameters when achieving compact and homogeneous melted layers. They are formed with the parameter set 7 J/cm^2, 10 P and 2 J/cm^2, 20 P, respectively, as shown in Figure 5.15. Two adjacent consecutive tracks of the laser beam with a 20% overlapped area are presented in both micrographs. The melted surface

generally exhibits a rippled morphology when high laser fluence (7 J/cm^2) is applied. There is a re-heated area with the width of a few tens of microns next to the overlapped area as indicated in Figure 5.15(a). However, when low laser fluence (2 J/cm^2) is applied, the rippled structure is significantly reduced and the reheated area is hardly observed as shown in Figure 5.15(b), although a higher NOP is applied.
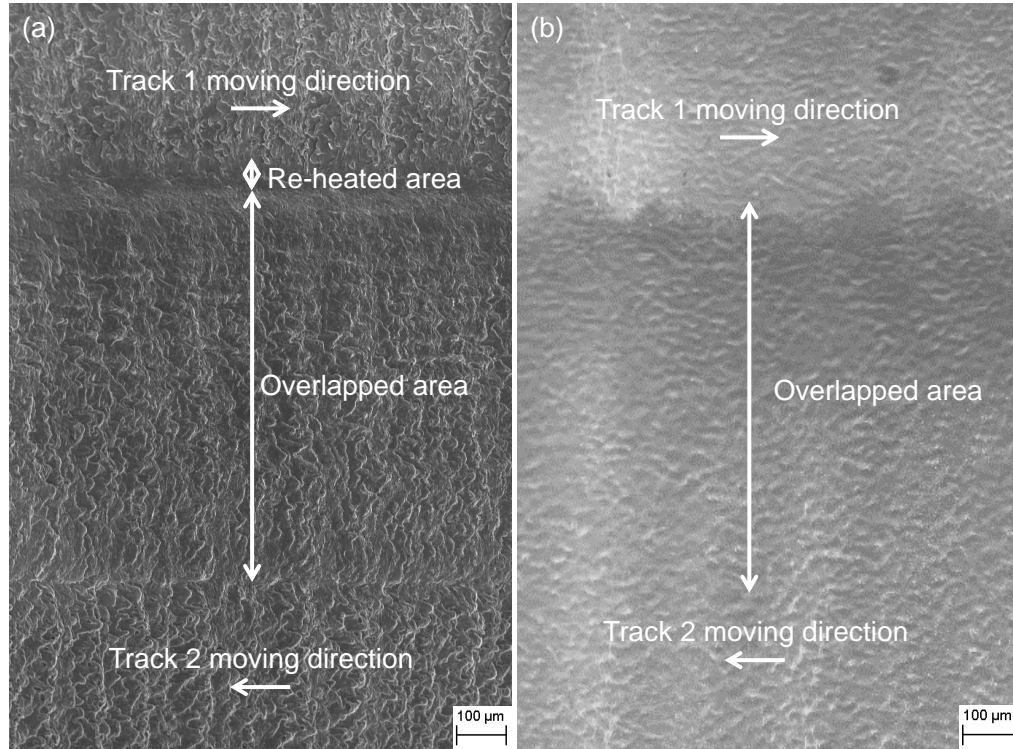
Figure 5.15 SE-SEM micrographs showing the typical surface morphologies of the excimer laser-melted MA, presenting two adjacent laser beam tracks with an overlapped area in-between: (a) 7 J/cm^2, 10 P and (b) 2 J/cm^2, 20 P.

Figures 5.16(a)-(b) show the microstructures of the central areas of the beam tracks with different laser operating parameters. With the high laser fluence, significant ripples are revealed whilst only slightly wrinkled surface is revealed with the low laser fluence. The overlapped areas exhibit similar morphologies as shown in Figures 5.16(c)-(d), but micro-pores are evident in the overlapped areas. The pore sizes of the sample treated with the laser fluence of 7 J/cm^2 are larger than that of the sample treated with the laser fluence of 2 J/cm^2. With the high laser fluence of 7 J/cm^2, the micro-pores are concentrated at the interface of the overlapped area and the re-heated area, which is also the interface of the two tracks as shown in Figure 5.16(e). The

interface of the two tracks treated with 2 J/cm^2 is free of micro-pores and the wrinkles are smoothed in the overlapped area in Figure 5.16(f).
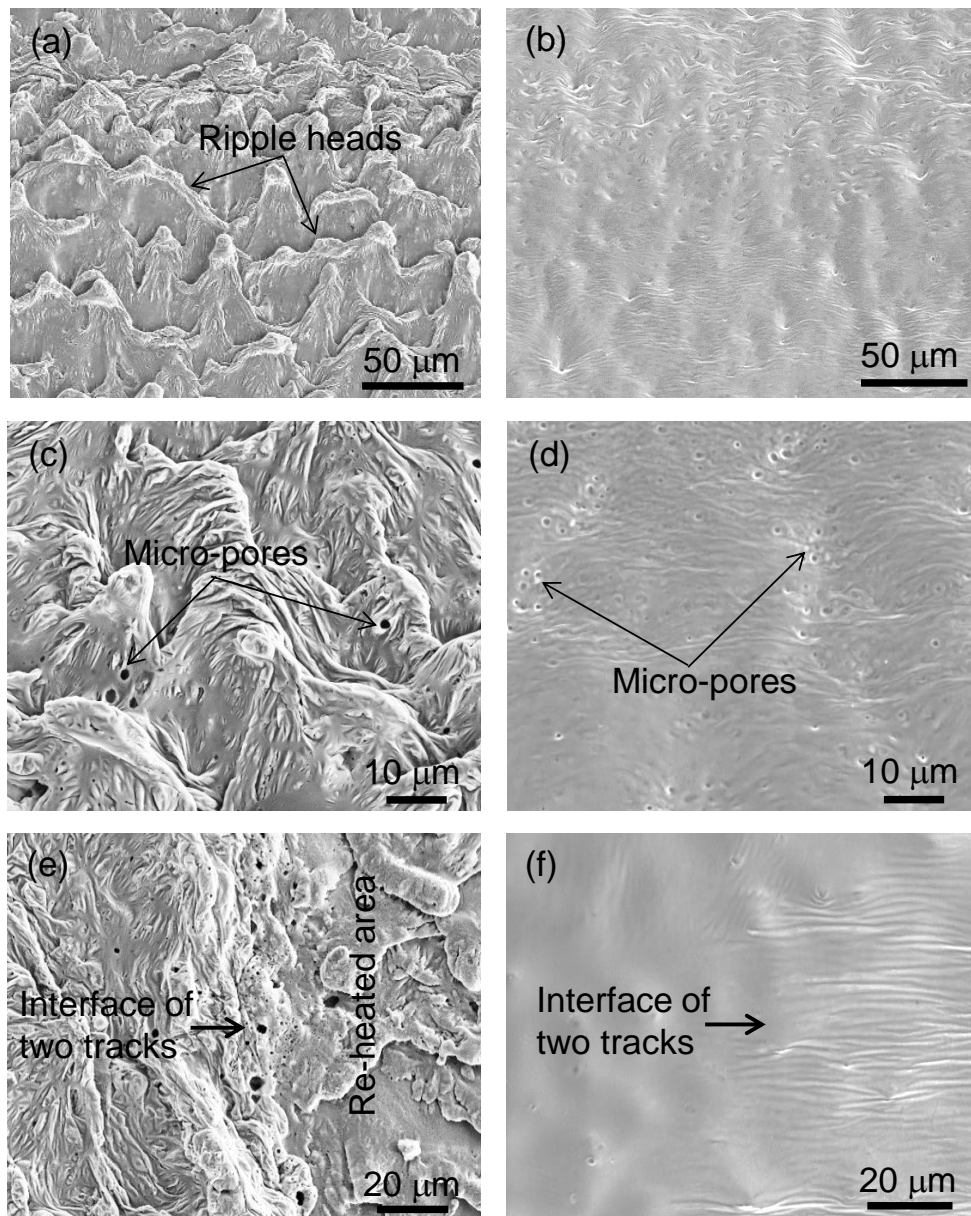
Figure 5.16 SE-SEM micrographs showing the morphology of the central areas of the laser beam tracks: (a) 7 J/cm^2, 10 P and (b) 2 J/cm^2, 20 P; overlapped areas: (c) 7 J/cm^2, 10 P and (d) 2 J/cm^2, 20 P; and interface of two tracks and the reheated areas: (e) 7 J/cm^2, 10 P and (f) 2 J/cm^2, 20 P.

Figure 5.17 shows the cross-sectional morphologies of the melted layer formed under the two conditions. The melted layers are free of intermetallic particles and the

solutes are fully dispersed in the melted layers for both samples. The thickness of the melted layer for the sample conducted at 7 J/cm^2 is larger than that conducted at 2 J/cm^2, being consistent with the results in Figure 5.8. Under both conditions, the melted layer in the overlapped area is thicker than that in the central area of the track as the measurements demonstrate in Figures 5.17(c) and 5.17(d). This could be due to the radial motion of the melt from the centre to the perimeter, making materials accumulated in the overlapped area. An increase in porosity is shown in the overlapped area for both samples, which also contributes to the increase of the thickness of the melted layer in this region. However, the pore sizes in the two samples are quite different from each other. In the sample treated with 7 J/cm^2, micro-sized pores were observed, but in the sample treat with 2 J/cm^2, much smaller nano-sized pores were observed in contrast (Figures 5.17(c)-(d)).
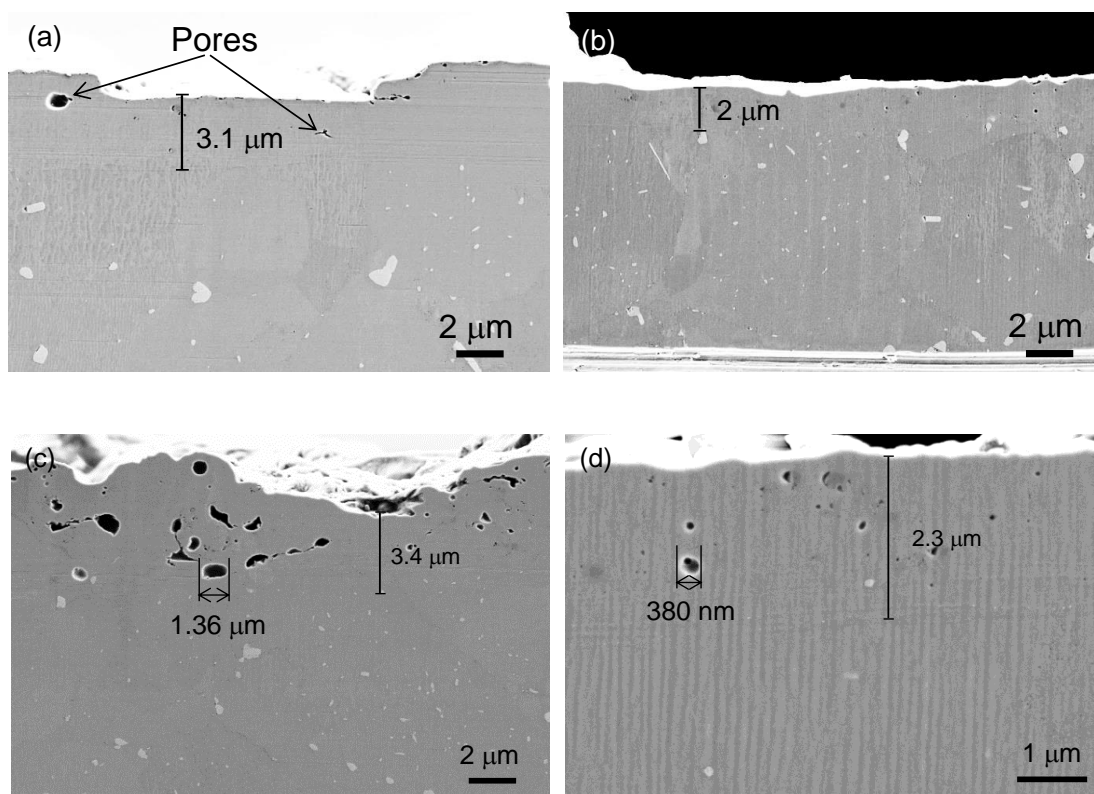
Figure 5.17 SE-SEM micrographs showing the cross-sectional morphology of the central areas of the laser beam tracks: (a) 7 J/cm^2, 10 P and (b) 2 J/cm^2, 20 P; and the overlapped areas: (c) 7 J/cm^2, 10 P and (d) 2 J/cm^2, 20 P.

5.3.4 TEM characterization

Figure 5.18 shows the presence of the segregation bands in the melted layer. Three light segregation bands at the bottom and one in the middle of the melted layer are shown in Figure 5.18(a). At a higher magnification, the segregation bands are approximately 20 nm wide and consisted of a string of extra-fine particles, which are typically elongated along the melted layer/substrate interface. Figure 5.19(a) is a HAADF image, which shows several segregation bands at the melted layer/substrate interface and within the melted layer. The chemical composition of the segregation bands was investigated using EDX line scan from A to B as shown in Figure 5.19(a). Figure 5.19(b) shows that the segregation band is rich in Cu. Figure 5.20(a) shows magnified image of the parallel segregation bands in Figure 5.18(b). Apart from copper, there is an increase in Mg detected using EDX in the segregation bands as indicated in Figure 5.20(b). Due to that Mg is not present in all the segregation bands, the segregation bands are generally termed as Cu-rich segregation bands in current work. The Cu-rich segregation bands have been reported in several researchers' work [3, 4, 8, 9]. However, no phase identification of the Cu-rich segregation bands has been reported. In the present work, the attempt to identify such phase is not successful. This could be due to the formation of non-equilibrium phases during fast re-solidification of the melt.
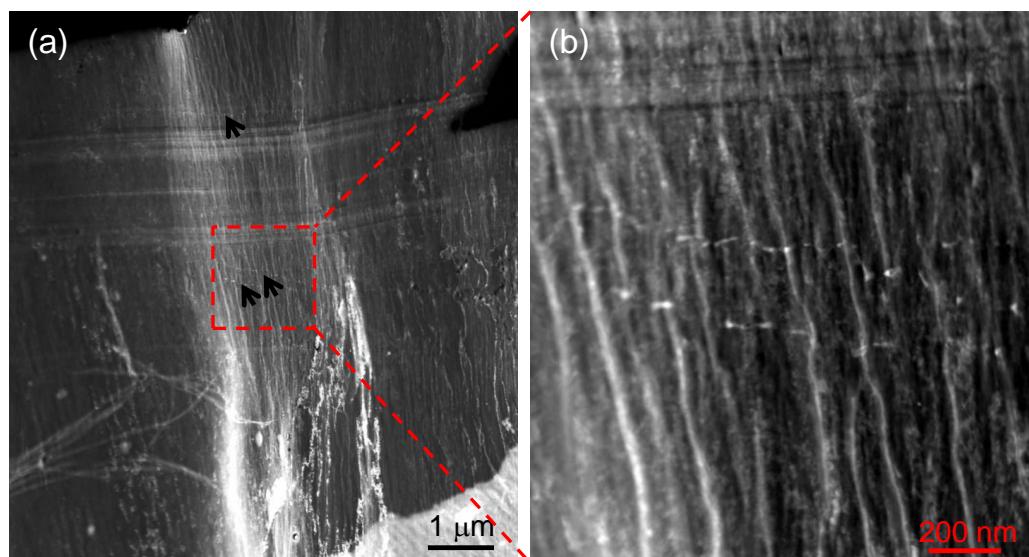
Figure 5.18 HAADF images showing the segregation bands in the melted layer.
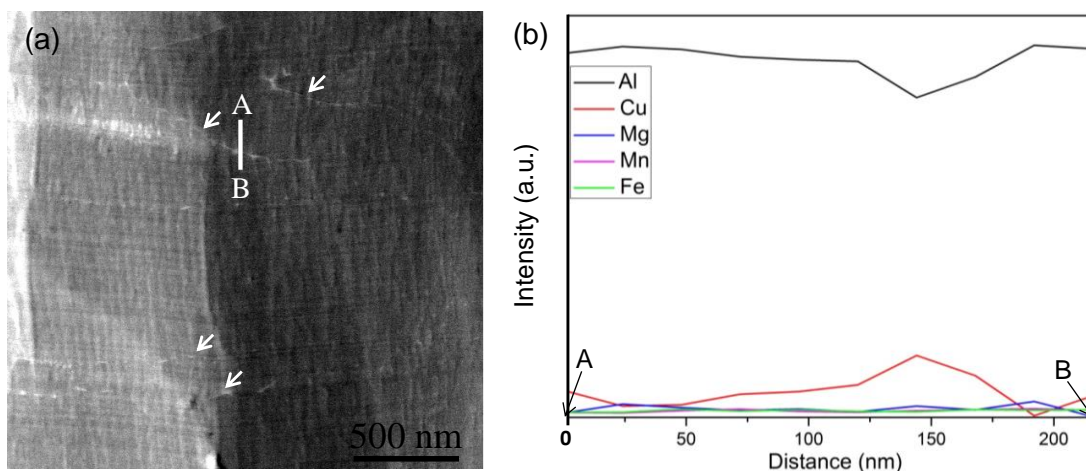
Figure 5.19 (a) HAADF image showing several segregation bands and (b) EDX elemental line profiles between A and B in (a).
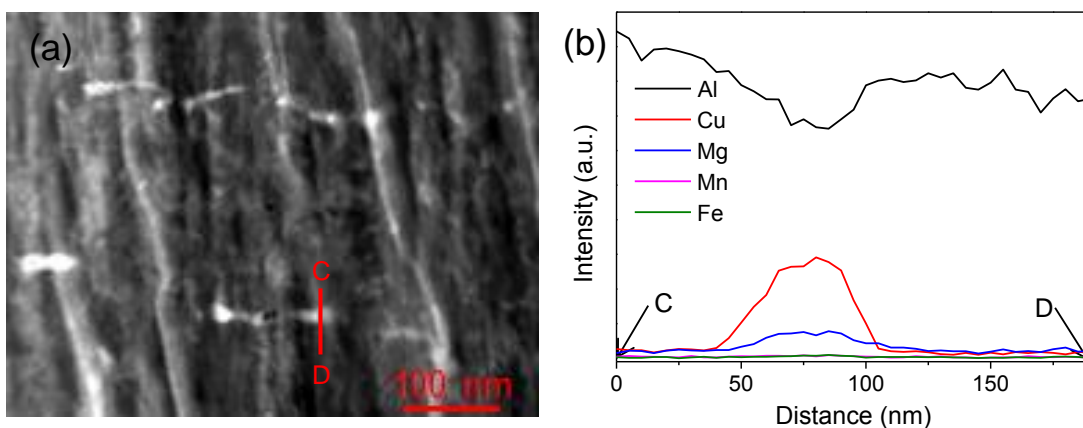
Figure 5.20 (a) HAADF image showing two parallel segregation bands and (b) EDX elemental line profiles between C and D in (a).

5.3.5 XRD analysis

Figure 5.21 shows the XRD patterns of as-received and laser-melted MA under different conditions. The XRD pattern of as-received MA presents Al_2CuMg and AlCuMnFe(Si)-containing phases apart from Al matrix, being in agreement with the observation in Chapter 4. The peaks of such intermetallic phases are eliminated or significantly reduced in the XRD patterns of laser-melted MA, indicating the dissolution of intermetallic particles after LSM. The solute elements exhibit extended solid solubility in the excimer laser-melted layer, leading to the formation

of supersaturated solid solution [15]. Thus, the solutes dissolve into Al matrix and are homogeneously dispersed in the melted layer as a result of the repeating melting process by a number of laser pulses. The XRD patterns of the samples treated at 7 J/cm^2 are similar to that of the sample treated at 2 J/cm^2, indicating that homogeneous microstructure is achieved under all selected conditions.
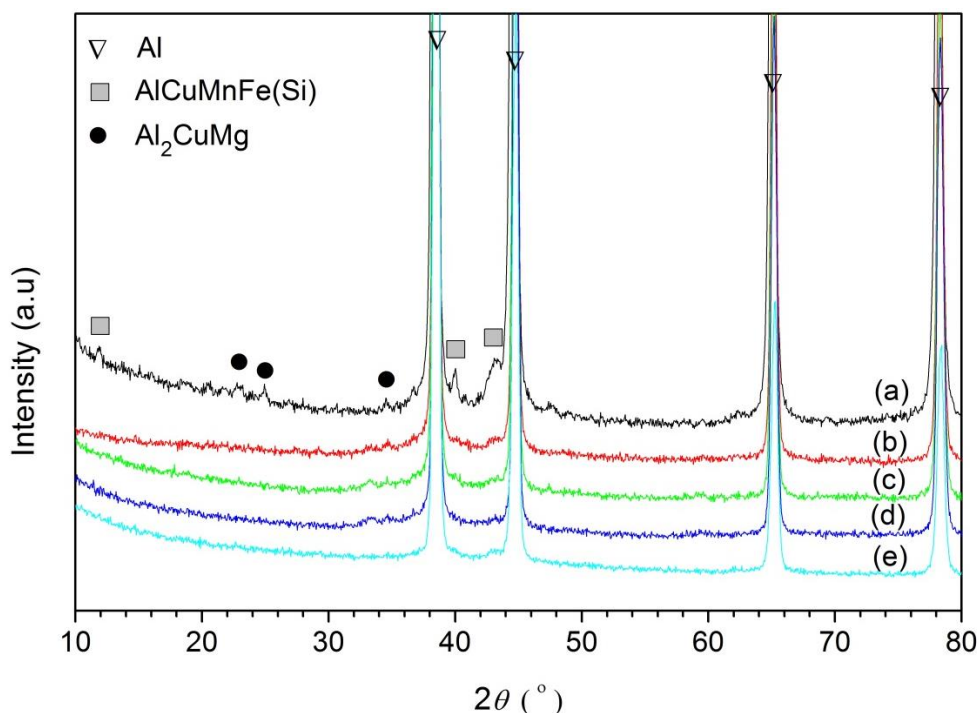
Figure 5.21 Low-angle XRD patterns of MA: (a) as-received; (b) 7 J/cm^2, 10 P; (c) 7 J/cm^2, 25 P; (d) 7 J/cm^2, 40 P and (e) 2 J/cm^2, 20 P. The glancing angle was 1 °.

5.3.6 SKPFM analysis

SKPFM analysis was performed in the cross-section plane of the laser-melted MA. Figure 5.22(a) is the height map of the cross-section, showing the presence of intermetallic particles in the substrate and the melted layer free of intermetallic particles on the top. Figure 5.22(b) presents the distribution of surface potential, which is inversely proportional to the actual Volta potential. In the substrate, all the intermetallic particles show lower surface potentials than the Al matrix, indicating more positive Volta potentials of the intermetallic particles. As is known, the AlCuMnFe(Si)-containing particles are inert or cathodic while the S-phase particles

are anodic to the Al matrix [16-18]. However, the S-phase particles, having higher surface potential, were not detected. This could be due to the fact that the measured surface potential of S-phase particles is very sensitive to the surface finishing; they may exhibit a cathodic nature in the air [18]. By dissolving the intermetallic particles, the melted layer shows a homogeneous surface potential distribution at the available resolution as shown in Figure 5.22(b). Figure 5.22(c) shows the two line profiles of the surface potential in the melted layer and the substrate, respectively. The line profile in the substrate shows that the difference of the surface potentials could be over 100 mV between the intermetallic particles and the Al matrix. On the contrary, the line profile in the melted shows small variations in surface potential.
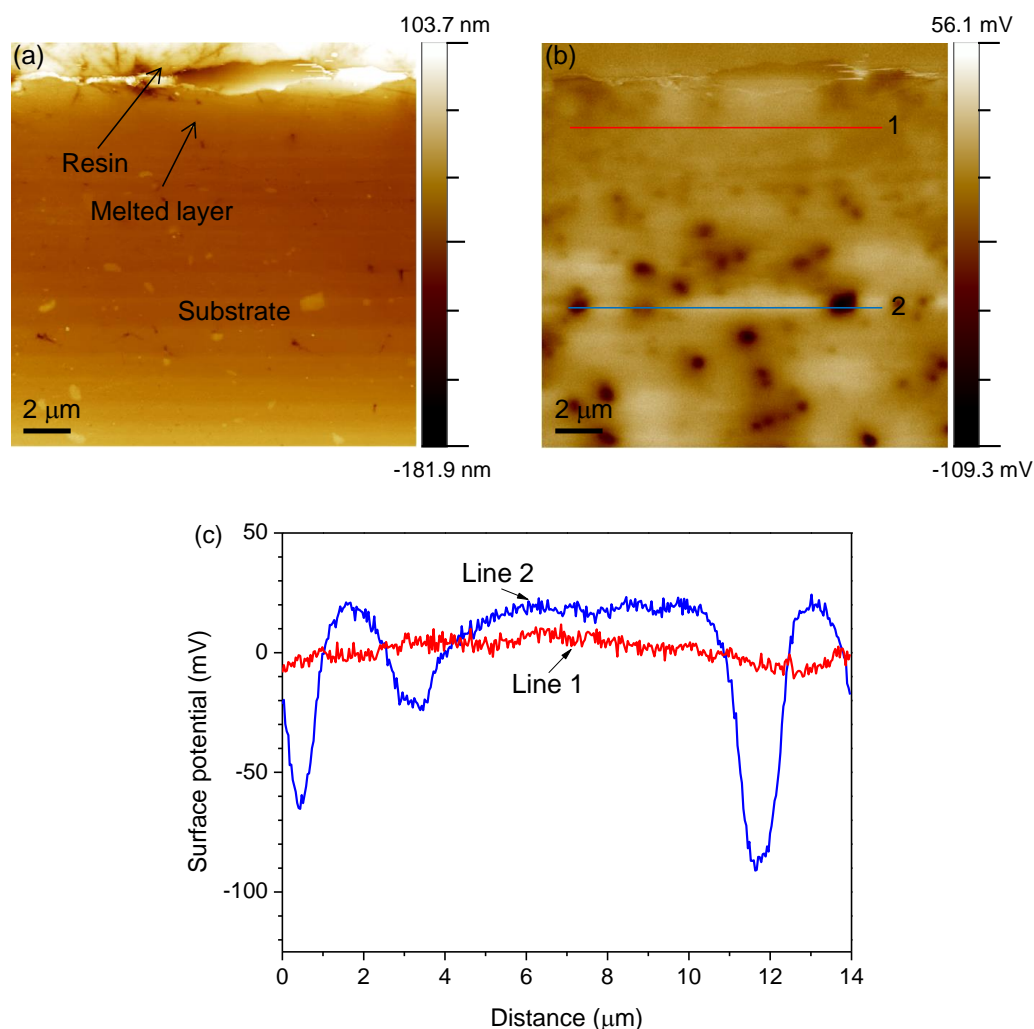
Figure 5.22 SKPFM study of the cross-section of the excimer laser-treated MA: (a) topography map; (b) surface potential map and (c) two line profiles of surface potential map, where Line 1 is from the melted layer and Line 2 is from the substrate.

5.4 Microstructural characterization of excimer laser-melted MMC

5.4.1 Surface morphology

Figure 5.23 SE-SEM micrographs of excimer laser-melted MMC with 10 P at different laser fluences: (a) 1 J/cm^2; (b) 3 J/cm^2; (c) 5 J/cm^2; and (d) 7 J/cm^2.

Figure 5.23 shows the surface morphology of the laser-melted MMCs treated with 10 P at various laser fluences from 1 J/cm^2 to 7 J/cm^2. The measured surface roughness of the laser-melted MMC is presented in Figure 5.24, which shows a linear increase of the surface roughness with the increase of laser fluence. Although the results indicate the surface roughening by increasing the laser fluence, there is no significant rippled structure formed on the surfaces for all the conditions. The reduced ripples could be due to the presence of SiC particles, acting as obstacles stopping the melt from flowing. By increasing the laser fluence from 1 J/cm^2 to 3 J/cm^2, crater-like morphology is revealed on the laser-melted surface and disappears by further increasing the laser fluence as shown in Figure 5.23. Such craters have been reported in Zhang's work with the laser fluence of 2.3 J/cm^2 [6]. The SiC particles on the surfaces are significantly reduced after laser irradiation. The particles observed on the laser-melted surfaces are remnants of SiC particles, being verified

using EDX elemental mapping analysis, as shown in Figure 5.25. The particles in Figure 5.25(a) are rich in silicon, indicating that they come from SiC particles. However, carbon enrichment is not shown at these particles, which suggests these remnants are not in the original form of the SiC (Figure 5.25(d)).
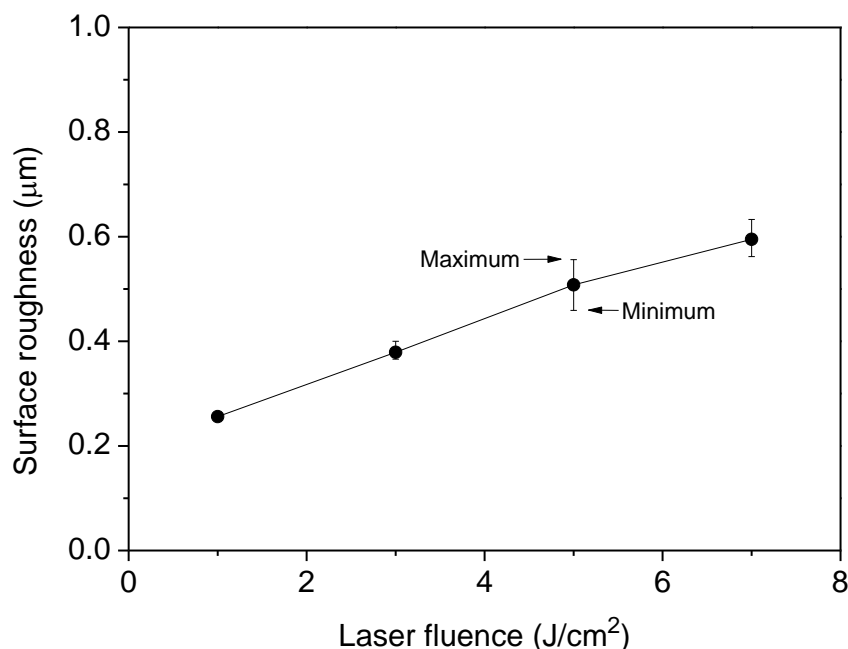
Figure 5.24 Surface roughness of laser-melted MMC treated with 10 P at different laser fluences.

Figure 5.26 shows the surface morphologies of the laser melted MMC at the fixed laser fluence of 7 J/cm^2 with various NOP. The sample treated with 5 P shows a fairly rough surface whilst other samples appear to be more flat in Figure 5.26. This is verified by the surface roughness measurements as shown in Figure 5.27, which shows an initial decrease in surface roughness with the NOP increased from 5 to 15. The surface roughness of the melted surface shows little change from 15 to 30, and then increases slightly from 30 to 40. The initial high roughness of the laser-melted MMC (5 and 10 P) is probably attributed to the boiling effect due to the presence of SiC particles on the surface, which resulted in high temperature over the boiling point of aluminium (see Figure 5.42). When the NOP increased to 30 or higher, networks of cracking are formed on the surface. The formation of networks of cracking could contribute to the slight increase in surface roughness when the NOP

exceeds 30. The SiC remnants on the laser-melted surface of the MMC reduce with the increase of NOP and are essentially eliminated with the NOP of 20 or higher (Figure 5.26).

Comparing the surface roughness values of laser-melted MA and the MMC in Figures 5.3, 5.4, 5.24 and 5.27, the MMC exhibits lower surface roughness than the MA under the same operating conditions. This could be due to the significantly reduced rippled structure on the laser-melted surfaces. It is postulated here that the SiC particles in the melted layer resist the motion of the melt, leading to the disappearance of significant rippled structure. This also explains the small variations of three measurements of surface roughness of laser-melted MMC for each condition.
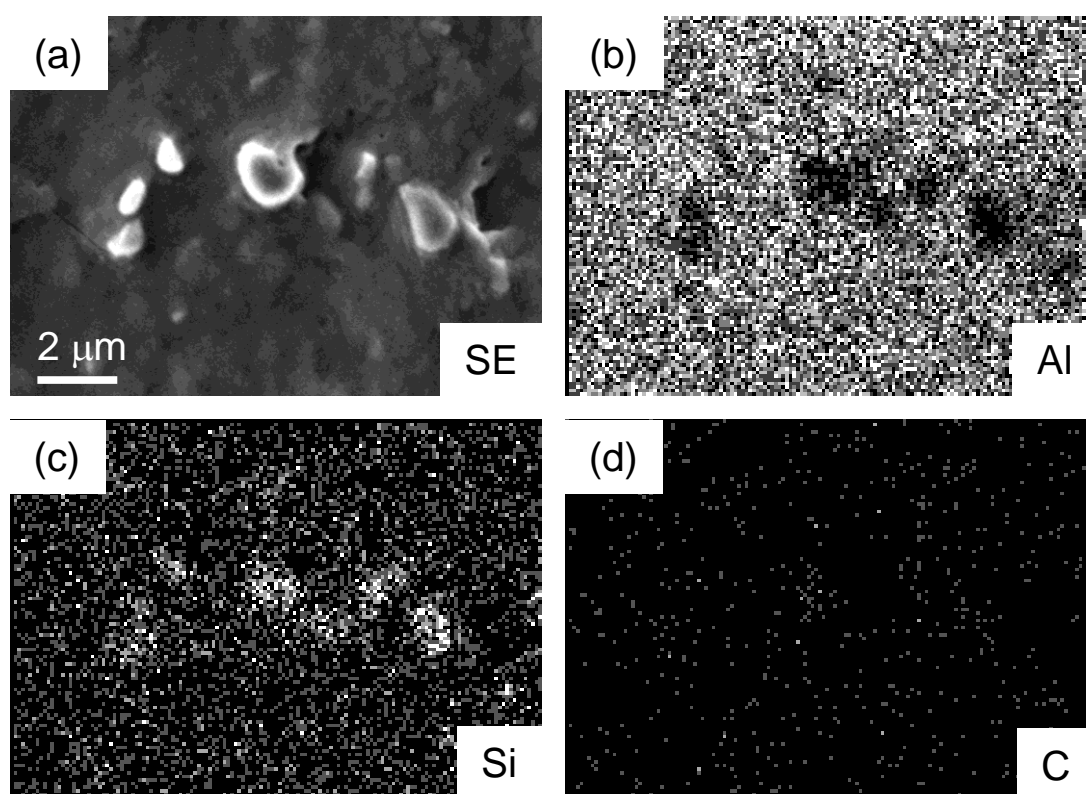
Figure 5.25 EDX elemental mapping analysis of laser-melted surface of MMC at the laser fluence of 7 J/cm^2 with the NOP of 10: (a) SE-SEM micrograph and individual map of (b) Al, (c) Si and (d) C.

5.4.2 Cross-sectional morphology
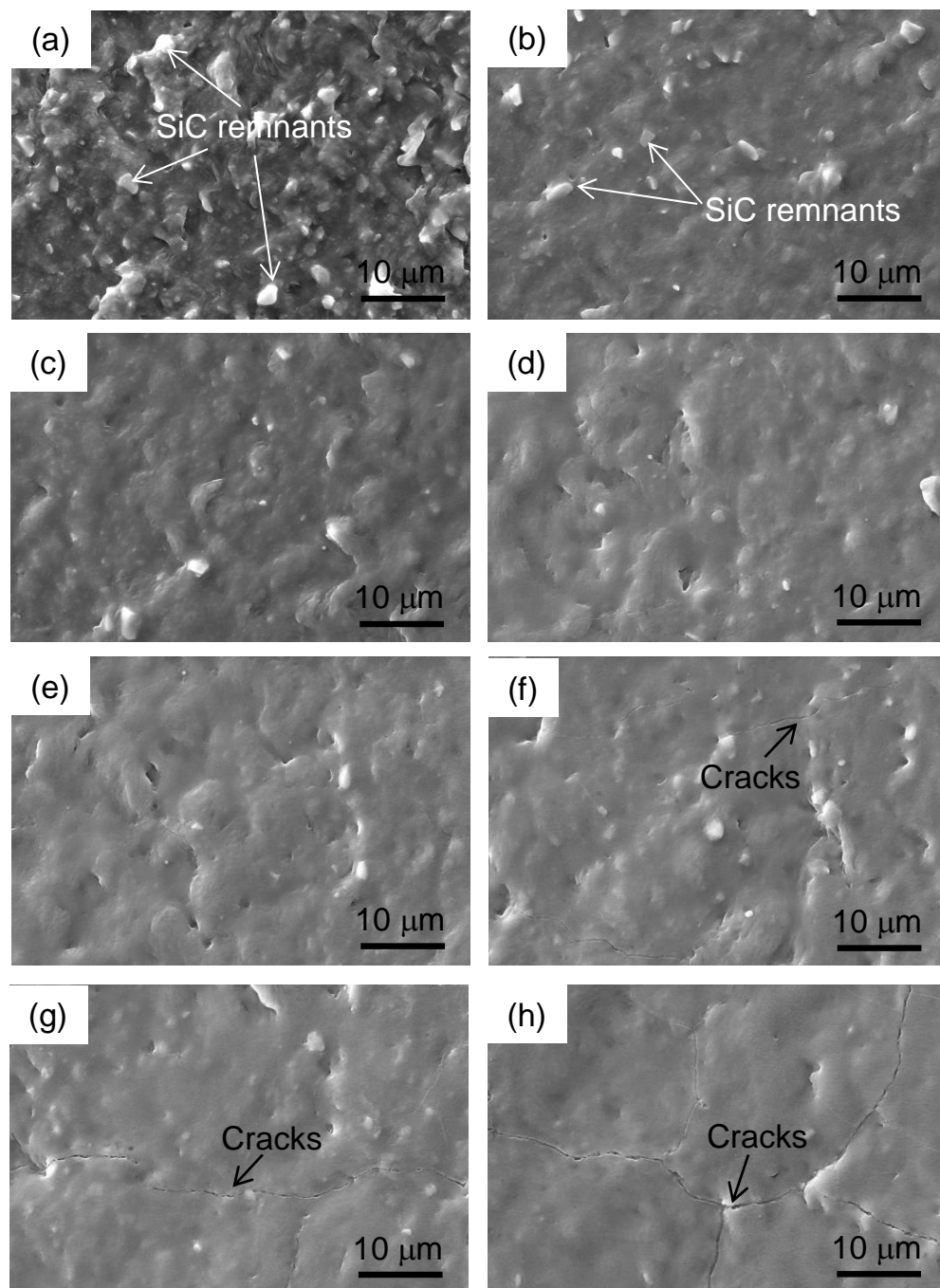
Figure 5.26 SE-SEM micrographs of excimer laser-melted MMC at the laser fluence of 7 J/cm^2 with different NOP: (a) 5 P; (b) 10 P; (c) 15 P; (d) 20 P; (e) 25 P; (f) 30 P; (g) 35 P; and (h) 40 P.

Figure 5.28 presents the cross-sectional morphologies of the laser-melted MMC treated with 10 P at various laser fluences from 1 J/cm^2 to 7 J/cm^2. The intermetallics are visible in the underlying substrate (black arrows) but are dissolved in the melted layer. It is noted that the thickness of the melted layer increases with the increase of laser fluence. SiC particles are revealed in the melted layer for all samples. However, a thin layer without SiC particles, which shows non-uniform thicknesses, is always present no matter which laser fluence is applied. This is in agreement with the disappearance of SiC particles on the laser-melted surfaces, which means that removal of SiC particles occurs upon laser irradiation but it does not occur in the same depth with the melt depth of the Al matrix. Hereby, the layer free of SiC particles is termed as "surface layer" in this chapter as a matter of unification. The removal of SiC particles contributes to the homogenization of the melted layer due to elimination of SiC/Al interfaces. The thickness and homogeneity of the surface layer could be important factors for obtaining improvement of corrosion properties. The thickness of the surface layer increases with the increase of laser fluence. Similar to the MA, the thickness of the surface layer shows a linear relation with the laser fluence as shown in Figure 5.29. The measurements of the thickness show significant variations, which is due to the presence SiC particles in the melted layer (Figure 5.28).
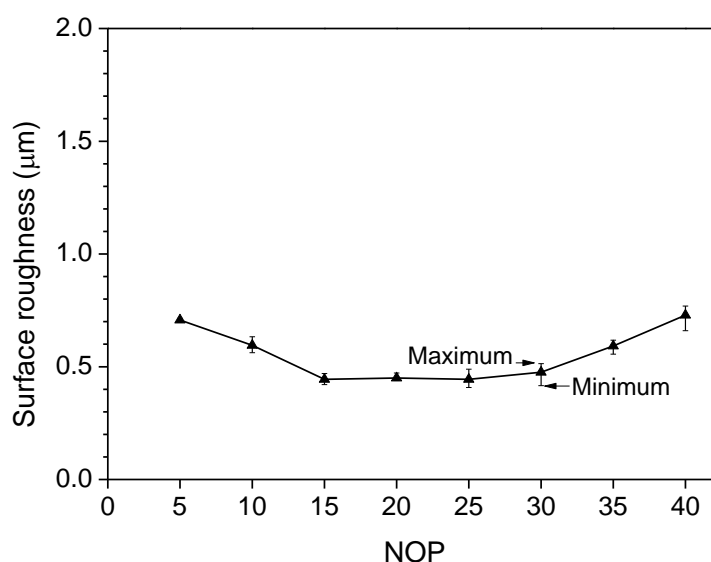
Figure 5.27 Surface roughness of laser-melted MMC treated at the laser fluence of 7 J/cm^2 and various NOP.
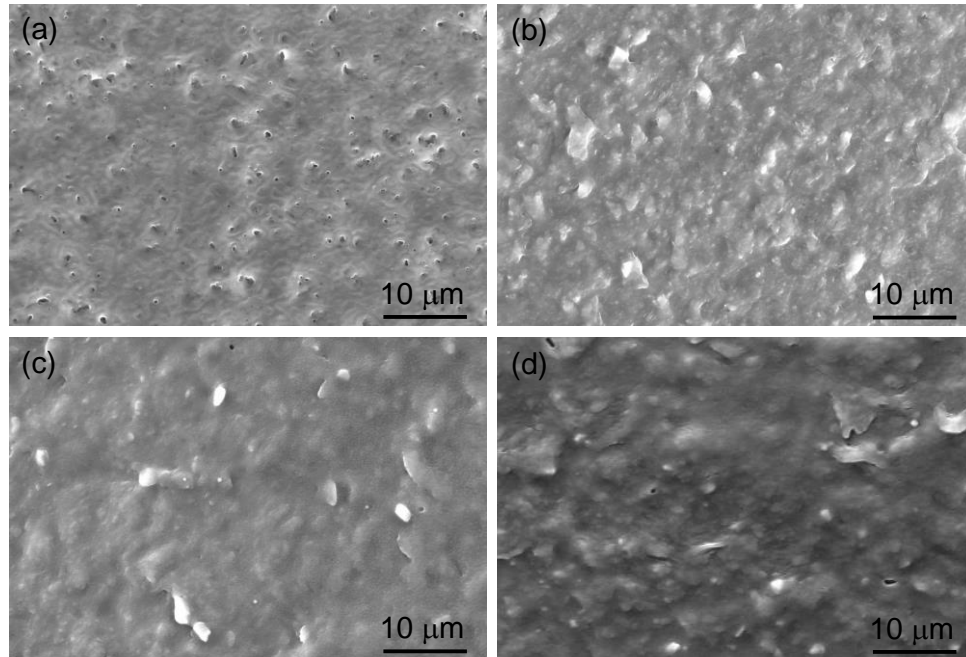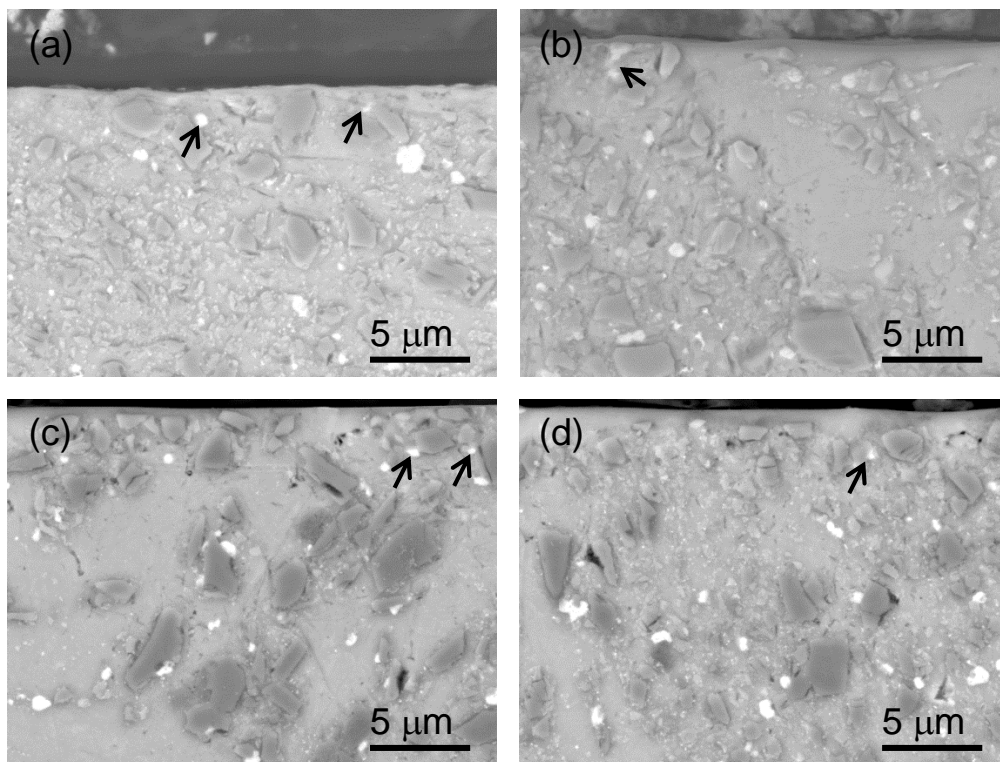
Figure 5.28 BSE-SEM micrographs of the cross-section of excimer laser-melted MMC with 10 P at different laser fluences: (a) 1 J/cm^2; (b) 3 J/cm^2; (c) 5 J/cm^2; and (d) 7 J/cm^2.
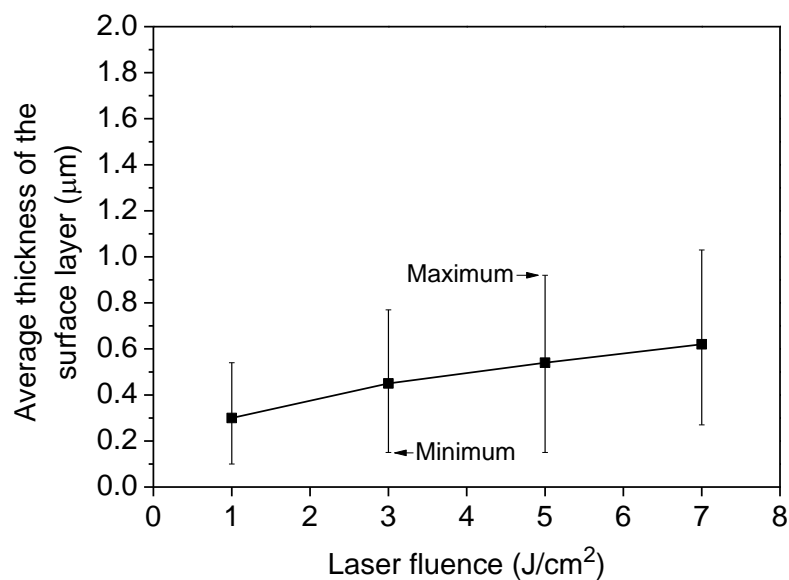
Figure 5.29 Correlation between the thicknesses of the surface layer with the laser fluence. All the samples were treated with the fixed NOP of 10.
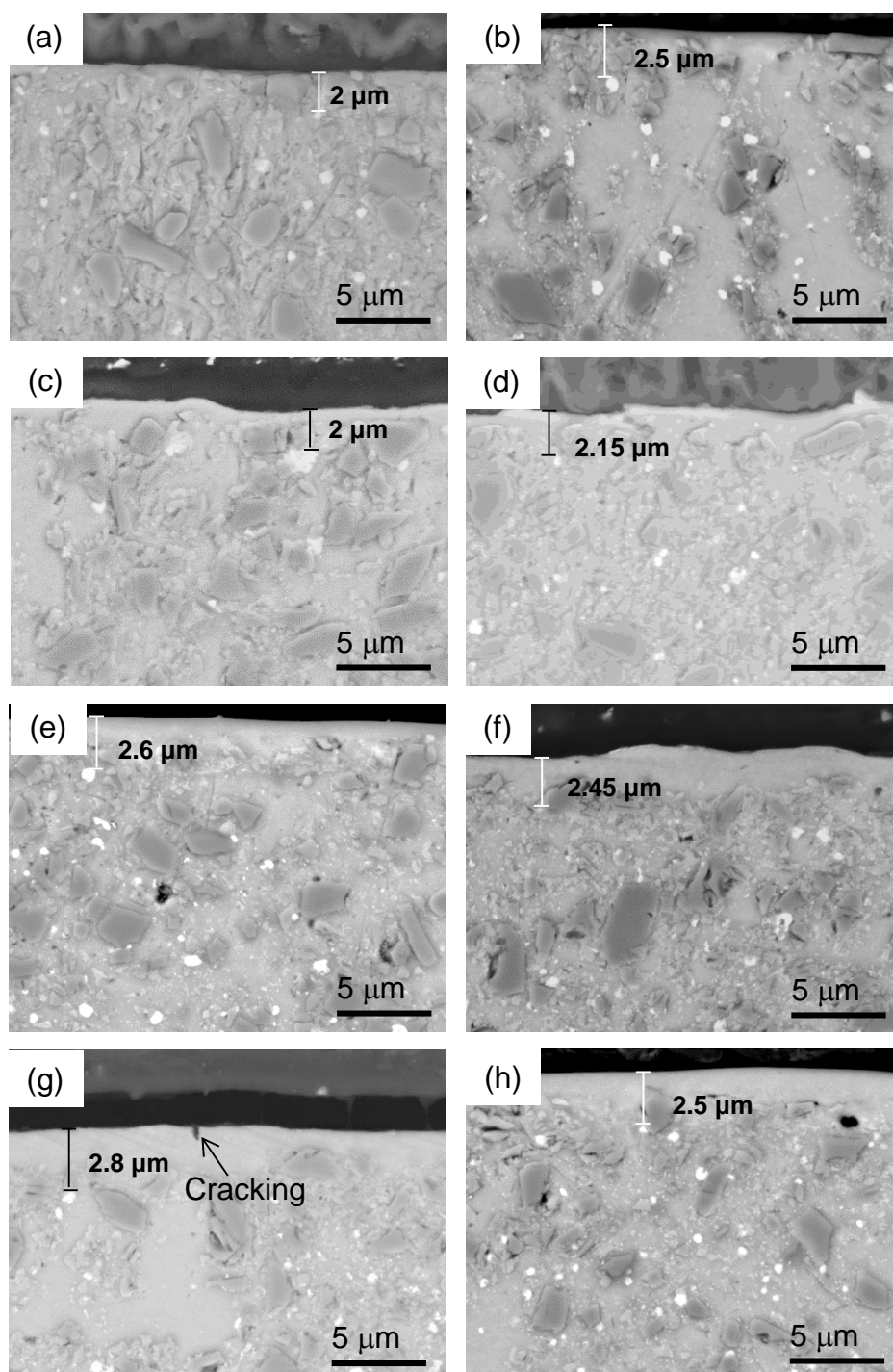
Figure 5.30 BSE-SEM micrographs of the cross-section of excimer laser-melted MMC at the fixed laser fluence of 7 J/cm^2 with different NOP: (a) 5 P; (b) 10 P; (c) 15 P; (d) 20 P; (e) 25 P; (f) 30 P; (g) 35 P; and (h) 40 P.

Figure 5.30 shows the cross-sectional morphology of the excimer laser-melted MMC with different NOP at the fixed laser fluence of 7 J/cm^2. The surface layer, covering

174

the substrate, is very limited in the thickness with relative low NOP, as shown in Figures 5.30(a) and (b). A number of SiC particles, which are hardly covered by the surface layer, were observed for the MMC treated with 5 P and 10 P. This is in agreement with the plan view observation, which indicates a large number of remaining SiC particles on the laser-melted surface with 5 P and 10 P (Figure 5.26). The total melt depths of the samples treated with 7 J/cm^2 are in the range of 2-3 μm, which does not vary much as shown in Figure 5.30, suggesting that the increase of NOP has no significant effect on the melt depth of Al matrix. However, the melted layer can be divided into two regions, upper region free of SiC particles (the surface layer) and lower region with SiC particles. The surface layer becomes thicker with higher NOP, which is verified by the measurements of its thickness in Figure 5.31, indicating a gradual increase of the thickness of the surface layer with the increase of NOP. The significant difference between the maximum and minimum thicknesses arises from the interruption of SiC particles in the surface layer. The cracks, which have been observed from the plan view of the laser-melted MMC with the NOP of 30 or higher, are occasionally revealed in the cross-sectional micrographs (Figure 5.30(g)).
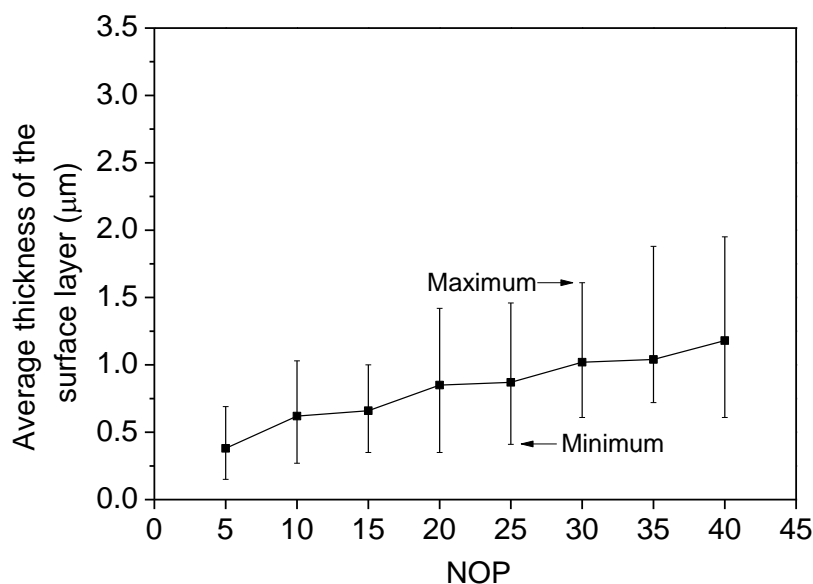
Figure 5.31 Correlation between the thickness of the surface layer of the MMC with the NOP. All the samples were treated with the fixed laser fluence of 7 J/cm^2.

Segregation bands similar to those in the laser-melted MA, concentrated at the bottom of the melted layer and parallel to the sample surface, were observed in the melted layer of the MMC as shown in Figure 5.32. The segregation bands exist in the regions free of SiC particles but are absent when encountering SiC particles in the melted layer.
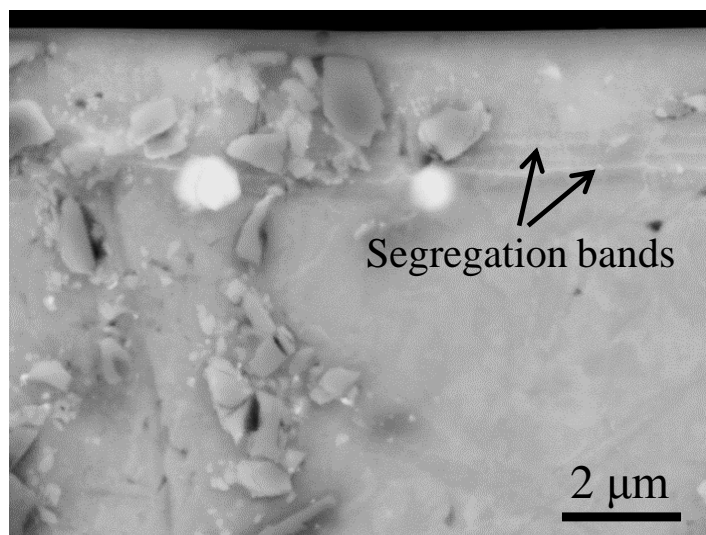
Figure 5.32 BSE-SEM micrograph showing the segregation bands in the melted layer of the MMC (7 J/cm^2, 25 P).

5.4.3 Large area coverage

The laser fluence of 7 J/cm^2 was applied for large area coverage of laser-melted MMC. A general view of the excimer laser-melted surface of the MMC is shown in Figure 5.33, which presents two laser tracks with an overlapped area in-between. There is a re-heated area with the width of ~100 μm next to the overlapped area in the first track and a ridge formed at the interface of the re-heated area and the overlapped area, being evidently shown in Figure 5.34. In the re-heated area next to the ridges, cracks were observed for the samples with 10 P and increased with the increase of NOP from 10 to 40, although cracking was not observed in the single track-melted MMC with 10 P as discussed above. Compared with the centre of the beam track, the remaining SiC particles are significantly reduced in the re-heated area and the overlapped area as shown in Figure 5.34(a). The ridges between the overlapped area and the re-heated area become more significant as the NOP

increases. The morphology of the ridges is shown in Figure 5.35, which shows the formation of micro-crevices when high NOP was applied.
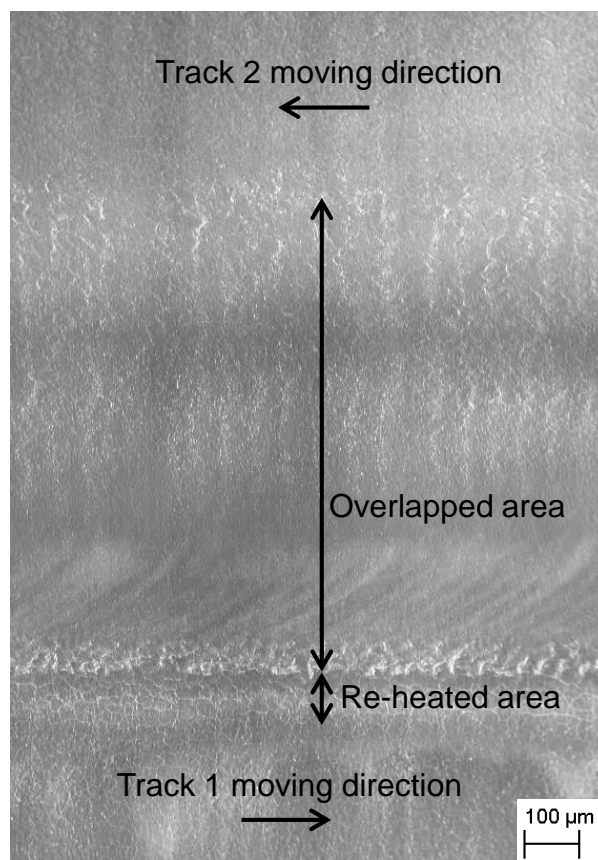
Figure 5.33 General view of the excimer laser-melted surface morphology of the MMC (7 J/cm^2, 25 P).

5.4.4 TEM characterization

According to the characteristics of the re-solidified microstructures, the melted layer can be divided into three regions, i.e. bottom, middle and top regions as indicated in Figure 5.36(a). Several segregation bands parallel to the top surface were observed in the bottom region. They are either locally continuous or composed of fine particles as shown at higher magnification in Figure 5.36(b). The compositional data from this bottom region was obtained using STEM-EDX analysis, as shown in Figure 5.37. The segregation bands are rich in copper, occasionally accompanied with silicon, (Figures 5.37(c) and 5.37(d)). In addition, STEM-EDX spectrum images of Mg and

O showing the distribution of magnesium and oxygen suggests the formation of magnesium oxides (Figures 5.37(e) and 5.37(f)).
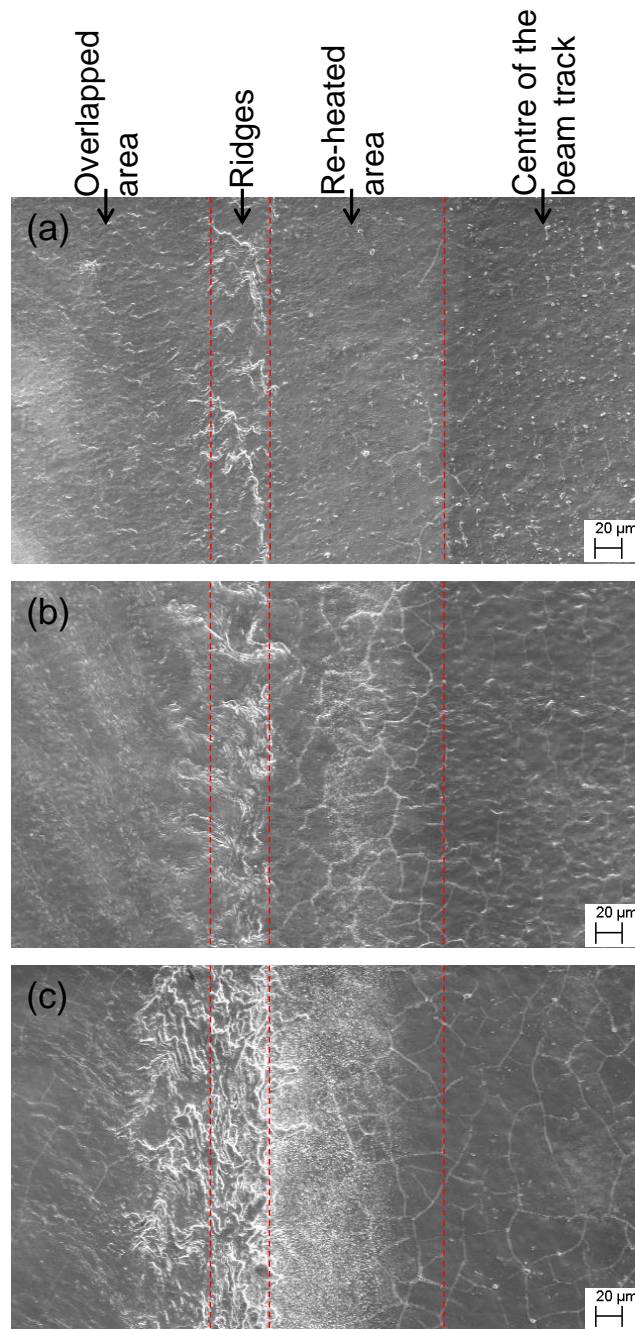
Figure 5.34 SE-SEM micrographs showing the morphology of the overlapped area and the re-heated area of the excimer laser-melted MMCs at the laser fluecne of 7 J/cm^2 with different NOP: (a) 10 P; (b) 25 P; and (c) 40 P.
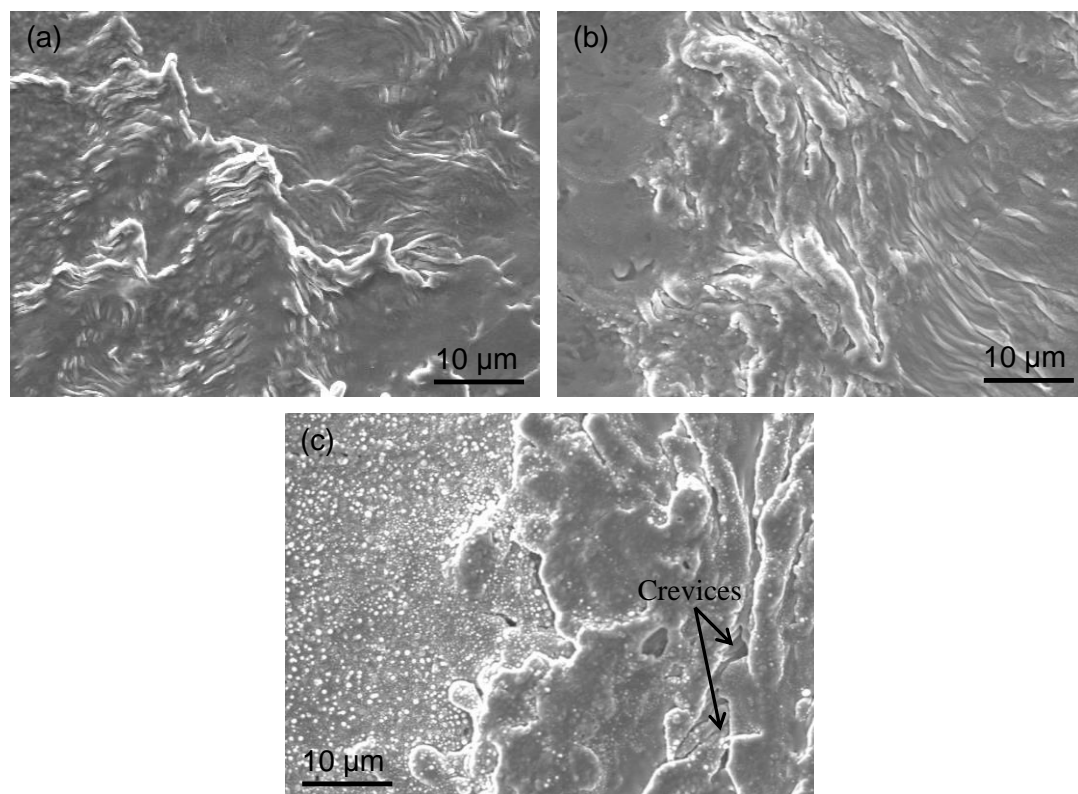
Figure 5.35 SE-SEM micrographs showing the ridges formed at the interface of re-heated area and the overlapped area: (a) 10 P; (b) 25 P; and (c) 40 P.

The middle zone of the melted layer is characterised with a highly refined "filamentary" structure, as well as the remaining SiC particles, as shown in Figure 5.36(c). In this area, the copper-rich segregation bands were not observed. The STEM-EDX spectrum images in Figure 5.38 show the partitioning of Al and Si. Cu and Mg enrichments were occasionally observed in the Si-rich areas as shown in Figures 5.38(d) and 5.38(e). The size of the fine Si microsegregation regions reduces gradually and finally disappears in the top zone of the melted layer, as shown in Figure 5.36(d). It is noticeable that the SiC/Al interface in Figure 5.36(d) is ambiguous, indicating that the SiC particle was partially removed (decomposed) during excimer LSM.

Figure 5.36(e) shows the typical morphology of the top region of the melted layer, which exhibits a homogeneous single-phase microstructure in terms of elemental segregation and intermetallic phases. Nano-sized remnants of SiC particles are revealed in the top region of the melted layer, as shown in Figure 5.36(f).

179
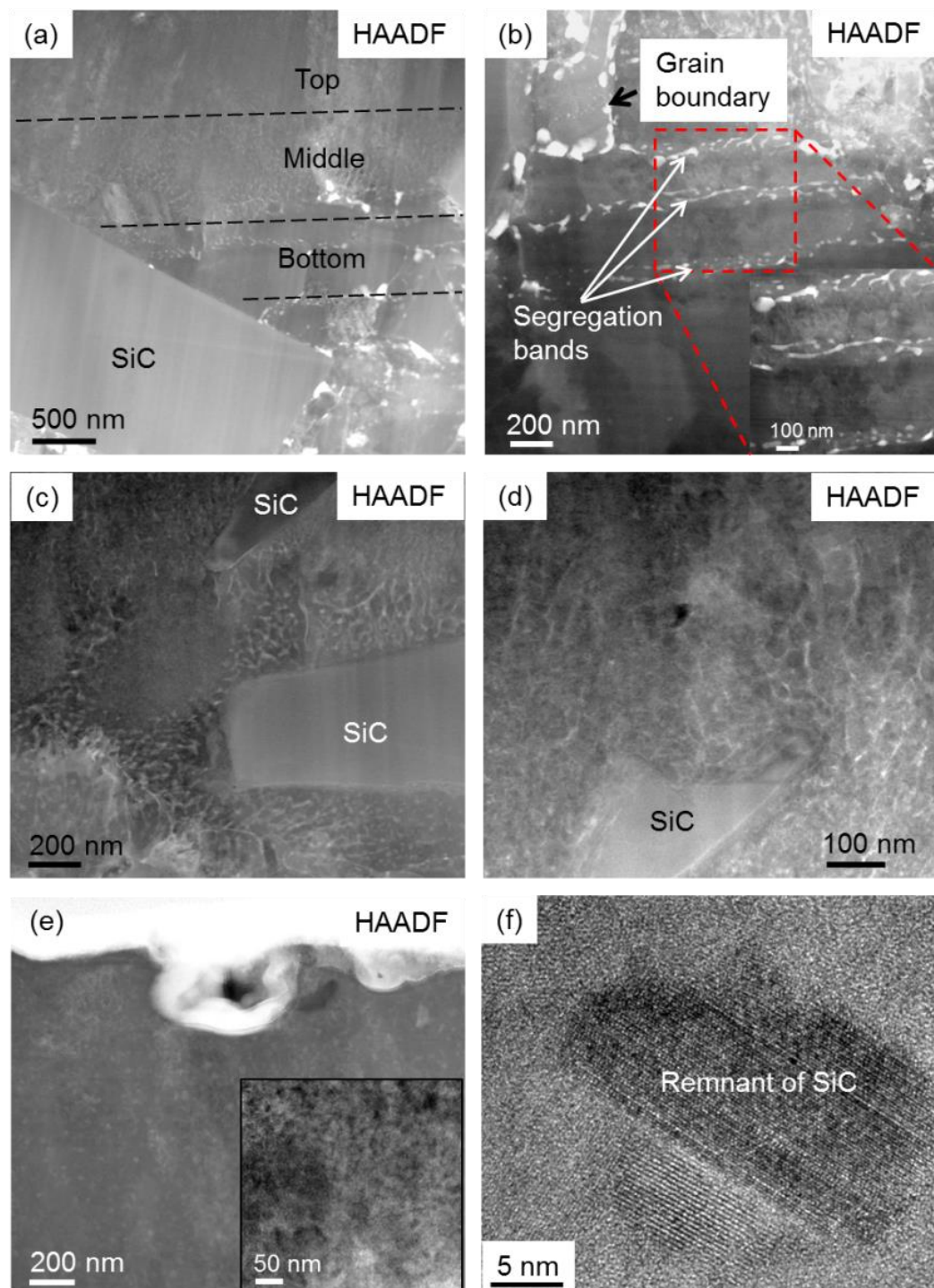
Figure 5.36 HAADF images from the melted layer of the MMC: (a) general view; (b) bottom region; (c) middle region; (d) transition from middle region to top region; (e) top region and (f) high-resolution TEM image of nano-sized SiC remnant in the top region (25 P).
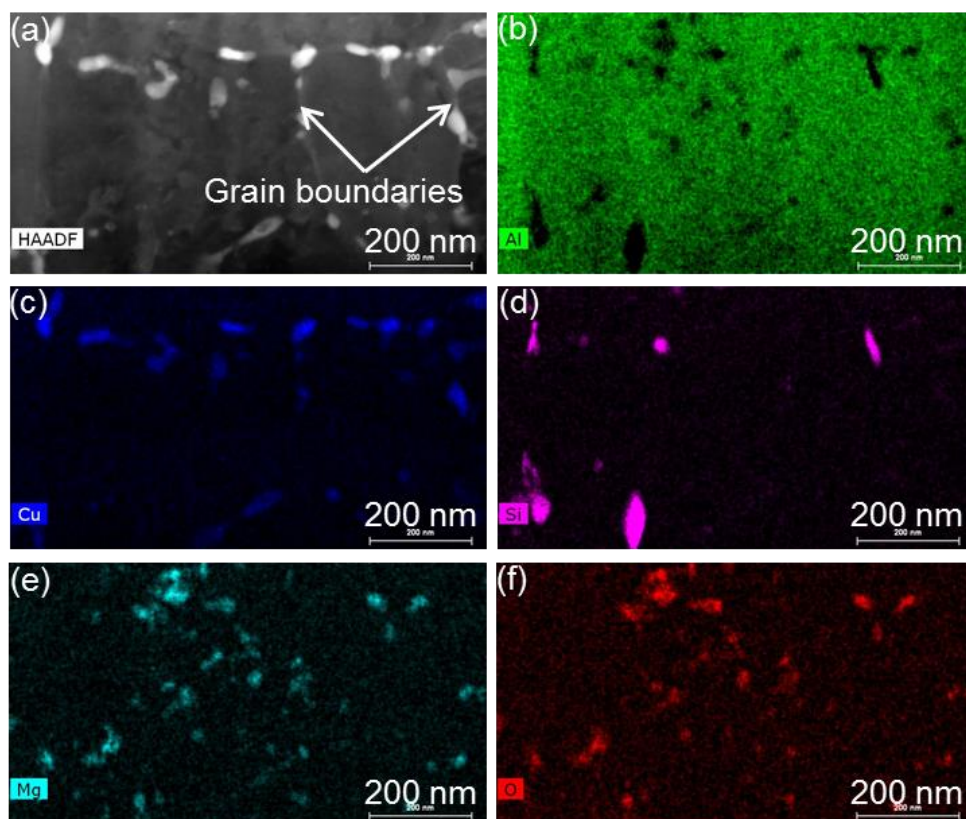
Figure 5.37 (a) HAADF image and corresponding STEM-EDX spectrum images of (b) Al; (c) Cu; (d) Si; (e) Mg and (f) O obtained from the bottom of the melted layer. Note the presence of the fine Cu precipitates and partially-dissolved SiC particles.
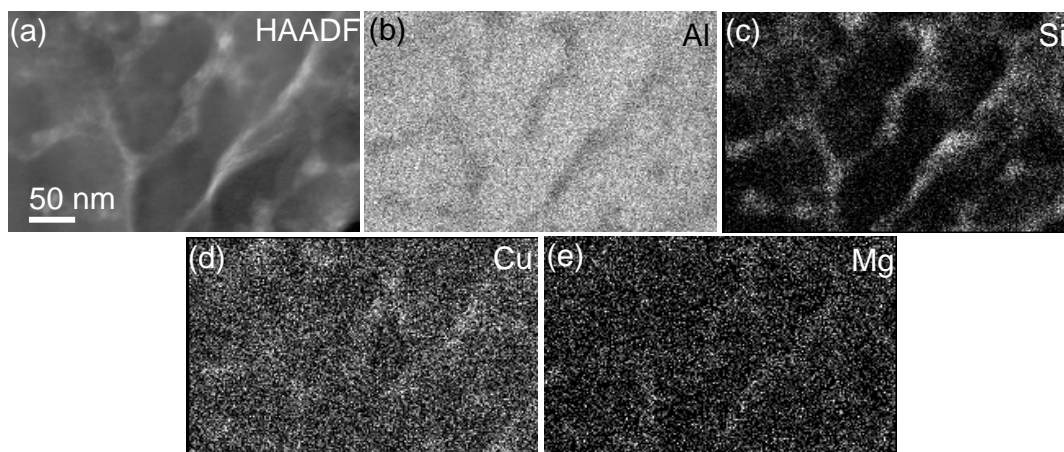
Figure 5.38 (a) HAADF image and corresponding STEM-EDX spectrum images of (b) Al; (c) Si; (d) Cu; and (e) Mg, showing the "filamentary" segregation.
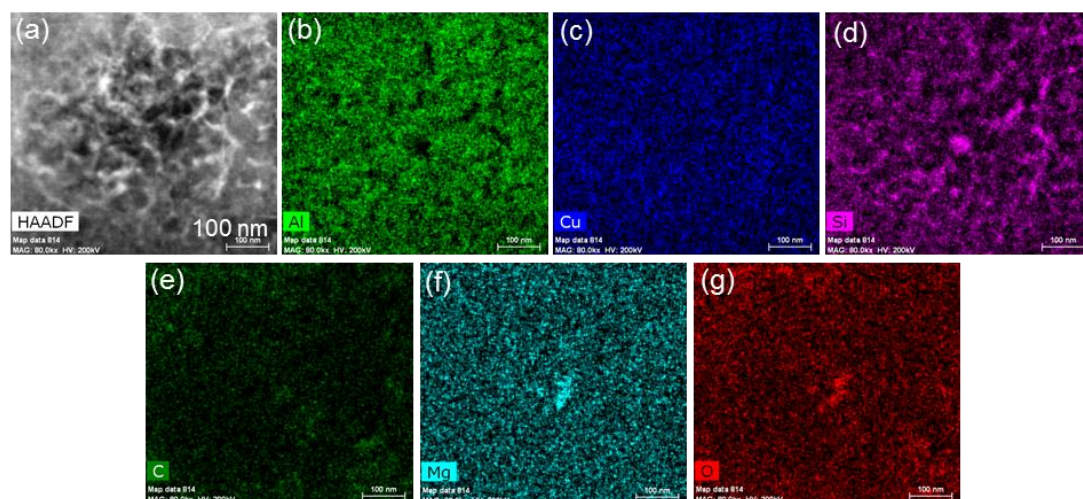
Figure 5.39 (a) HAADF image and corresponding STEM-EDX spectrum images of (b) Al; (c) Cu; (d) Si; (e) C; (f) Mg and (g) O, showing the site of the SiC decomposition.

Furthermore, in the middle and top regions of the melted layer, the SiC decomposition sites were detected (Figure 5.39(a)). It is noted that Al and Si partitioning is consistent with the observed image contrast in the HAADF image (Figures 5.39(b) and 5.39(d)), where the bright area and the grey-to-dark area (Figure 5.39(a)) correspond to Si and Al, respectively, implying intensively perturbed decomposition products. Copper is homogeneously distributed in the Al matrix (Figure 5.39(c)). No apparent Carbon enrichments (from the decomposition of SiC) are indicated and similar to the distribution of oxygen (Figures 5.39(e) and 5.39(g)). These observations could be interpreted that carbon in the melted layer is in the oxidation state, in agreement with Yue et al. [5], who suggested the oxidation of the alloying elements, as well as Si and C, on the excimer laser-treated surface by XPS analysis. Magnesium oxides, observed in the form of particles in the bottom region, are significantly reduced in the middle and top area of the melted layer, as shown in Figures 5.39(f) and 5.39(g).

5.4.5 XRD analysis

Figure 5.40 shows the XRD patterns of as-received and laser-melted obtained at the glancing angle of $2°$ and $1°$ respectively, both confirming the dissolution of the

intermetallic particles in the melted layer as the peaks for Al_2Cu and AlCuMnFe(Si)-containing phases disappear after LSM. It is noticeable that the XRD profiles obtain-
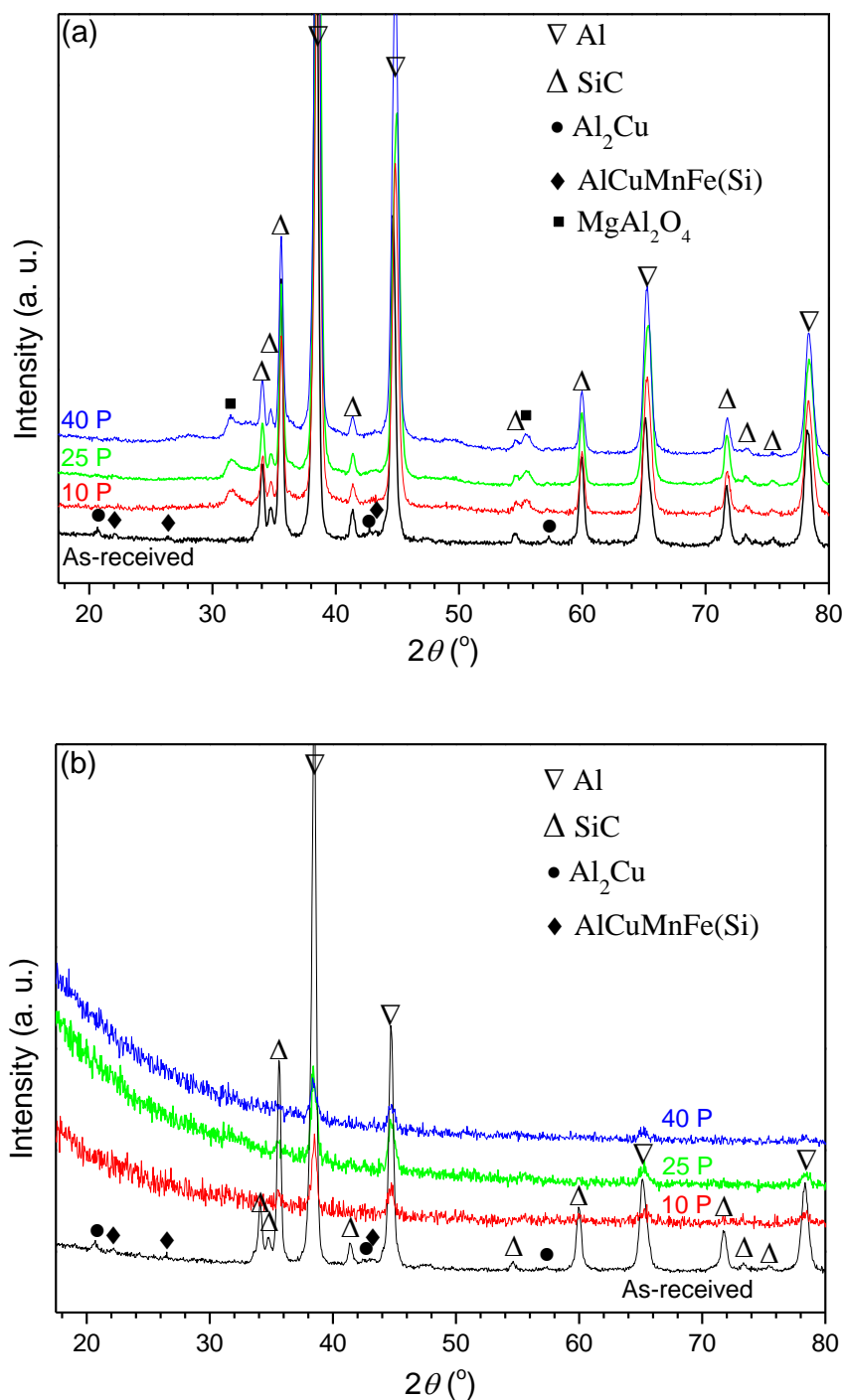
Figure 5.40 Low-angle XRD patterns of the as-received and laser-treated MMC with the glancing angle of (a) 2 ° and (b) 1 °.

ed with 1 ° show mainly Al phase but that obtained with 2 ° suggests the presence of SiC phase and spinel phase $MgAl_2O_4$. The peaks of SiC could be resulted from the presence of submerged SiC particles and the remnants in the melted layer. The presence of spinel phase $MgAl_2O_4$ corresponds to the observation of magnesium oxides at the bottom of the melted layer but the content of which has been revealed to decrease significantly at the top of the melted layer. Therefore, the peaks of $MgAl_2O_4$ were not observed when using the glancing angle of 1 °. The compound Al_4C_3, which was reported in LSM of SiC-reinforced MMCs with CO_2 or Nd: YAG lasers [19, 20], was not observed by either XRD or TEM after excimer LSM in the present study.

5.4.6 SKPFM analysis

SKPFM analysis of a cross-section of the MMC (25 P) is displayed in Figure 5.41. Figure 5.41(b) presents the surface potential distribution in the near-surface region measured via SKPFM. The bulk MMC displays evenly distributed SiC particles in Figure 5.41(a), resulting in great heterogeneity in surface potential. It is possible for the semi-conductive SiC particles to form galvanic cells with the matrix alloy [21, 22]. Since the SiC particles are typically protruding on the sample surface after mechanical polishing due to its high hardness, the information at the SiC/Al interfaces could be lost in SKPFM analysis. Therefore, the surface potential map of the fine precipitates at the SiC/Al interfaces was not obtained. However, similar to grain boundary precipitates in the MA, the precipitates close to the SiC/Al interfaces lead to solute depleted zone and thus the interfacial region could be either cathodic (Al_2Cu precipitates) or anodic (Mg segregation) to the vicinity, as discussed in chapter 4. The formation of the melted layer with homogeneous surface potential distribution, as shown in Figure 5.41(b), could significantly reduce the galvanic coupling effect. Line profiles of the surface potential in the melted layer and the substrate are shown in Figure 5.41(c), showing much smaller variations in surface potential in the melted layer than the substrate, which could reduce the possibility for galvanic corrosion.
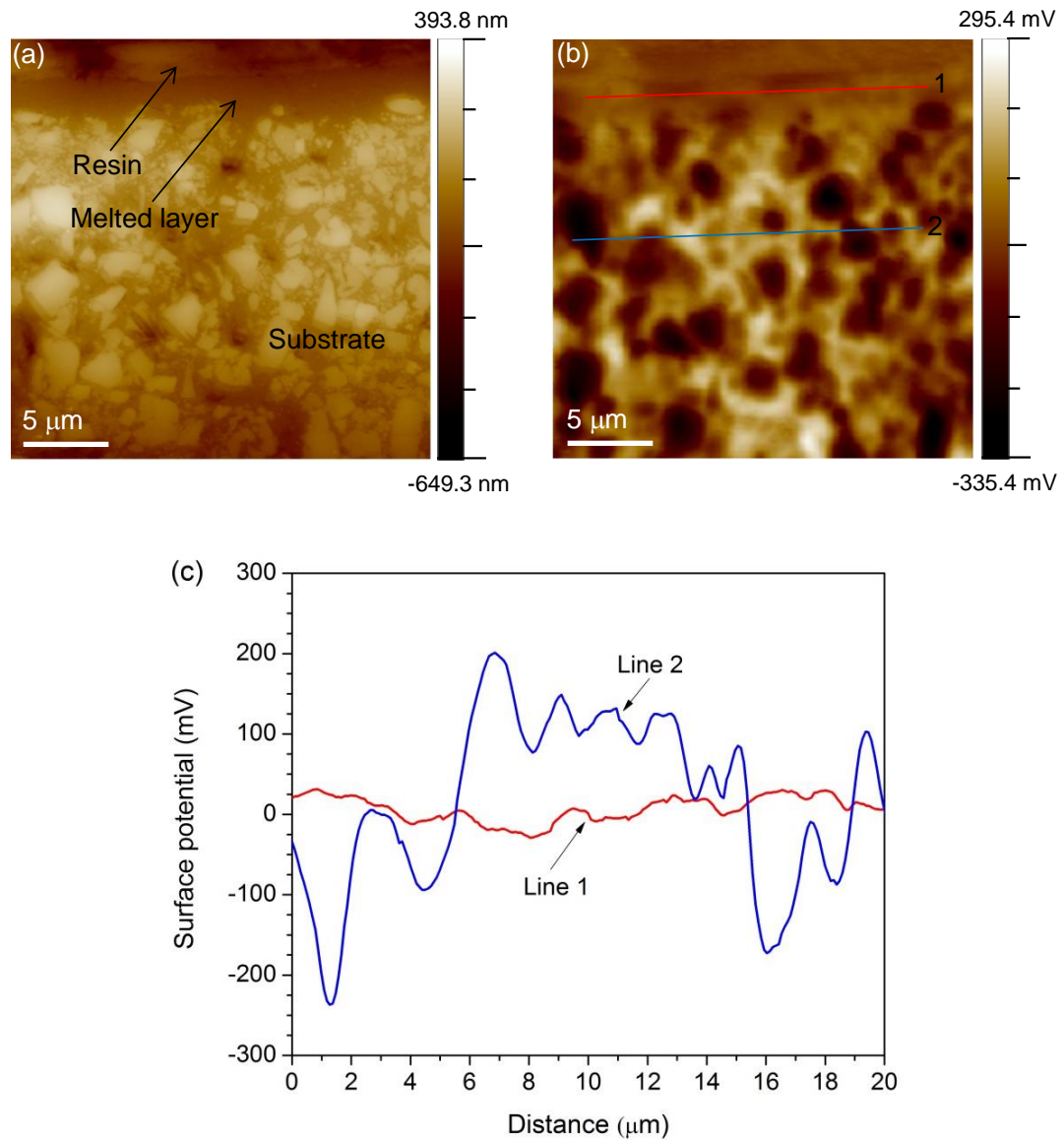
Figure 5.41 SKPFM study of the cross-section of the laser-treated MMC: (a) topography map; (b) surface potential map and (c) two line profiles of surface potential map.

5.5 Modelling of LSM process

5.5.1 Analytical model

Considering the dual-phase (i.e. AA2124 and SiC) in the MMC, the simple one-dimensional heat conduction equation described in Chapter 2 was employed to

evaluate the individual laser melt depth for the two phases. The materials properties used in current work are listed in Table 5.1. The absorptivity of SiC at 248 nm is deduced from the reflectivity calculated according to Ref. [28]. The temperature distribution along depth direction can be calculated according to Equations 2.4-2.8 for AA2124 and SiC, respectively.

Table 5.1 Materials properties used in the analytical modelling.

Properties	AA2124	SiC
Mass density (g/cm^3)	2.78 [23]	3.16 [24]
Thermal conductivity (W/m K)	152 [23]	114 [24]
Specific heat capacity (J/kg K)	900 [23]	715 [24]
Melting point (K)	908 [23]	-
Boiling point (K)	2792 [25]	3003 (decomposition) [26]
Absorptivity at 248 nm	0.07 [27]	0.73

The temperature distributions along the depth and evolution within 64 ns for AA2124 after the irradiation of a single laser pulse with the selected parameters are plotted in Figure 5.42. A molten layer around 1.2 μm is indicated to be formed in the near-surface region for AA2124 (point A) and the surface temperature could be around 2650 K at the end of the laser pulse (15 ns), as shown in Figure 5.42. Since the maximum surface temperature is lower than the boiling point of AA2124, it is implied that no significant evaporation of aluminium occurred. The melting of the alloy continued proceeding until 30 ns and the depth of the molten layer increased to 1.6 μm (point B), which indicates that the heat conduction from molten layer (melted before 15 ns) contributed to further melting of the underlying substrate after the laser beam was moved away. The temperature distribution on SiC upon the laser irradiation is also shown in Figure 5.42, which demonstrates that the temperature of SiC within 1.7 μm depth (point C) from the top surface is greater than its decomposing point (i.e. 3003 K). The high temperature on SiC could result in a melt

depth of the surrounding matrix alloy up to ~2.6 μm (point D). Note that the temperature of SiC exceeds its decomposition temperature at the end of the laser pulse. Therefore, the evolution of the temperature distribution in SiC is not given because the analytical model cannot predict the influence of decomposition/evaporation on the temperature evolution. The analytical model shows a significant difference in the thermal responses between AA2124 and SiC due to the different absorptivity and thermal properties of the two materials as shown in Table 5.1. The melt depth of AA2124 and the decomposing depth of SiC were deduced separately from the analytical model and the results were obtained without the thermal diffusion between the two materials taken into account when they are in the form of a composite.
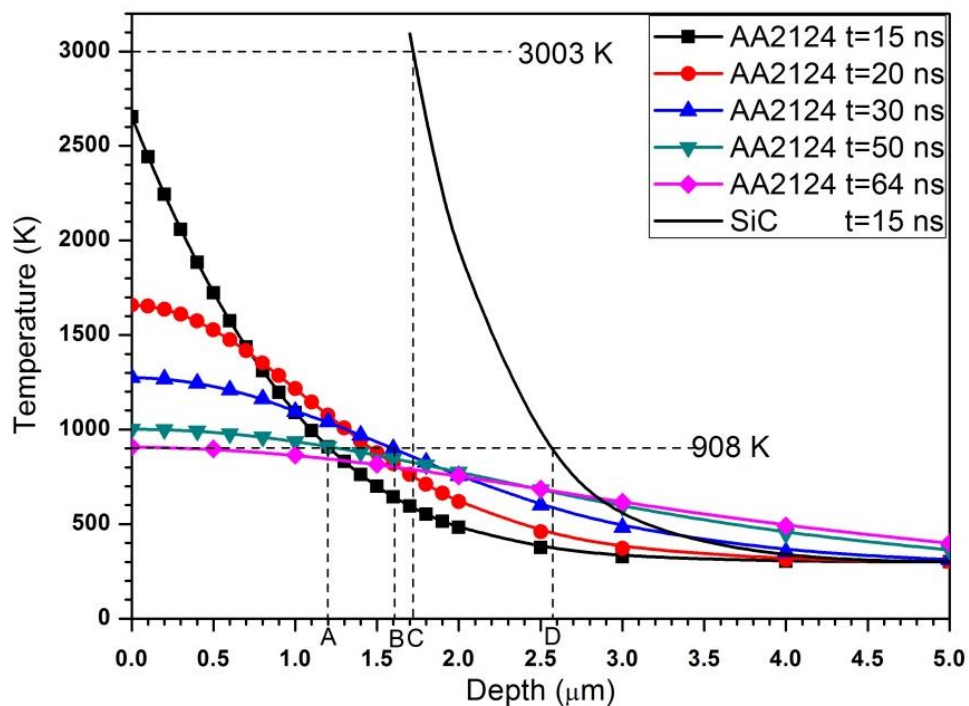
Figure 5.42 Temperature distributions along depth upon laser irradiation for AA2124 and SiC.

5.5.2 FEM
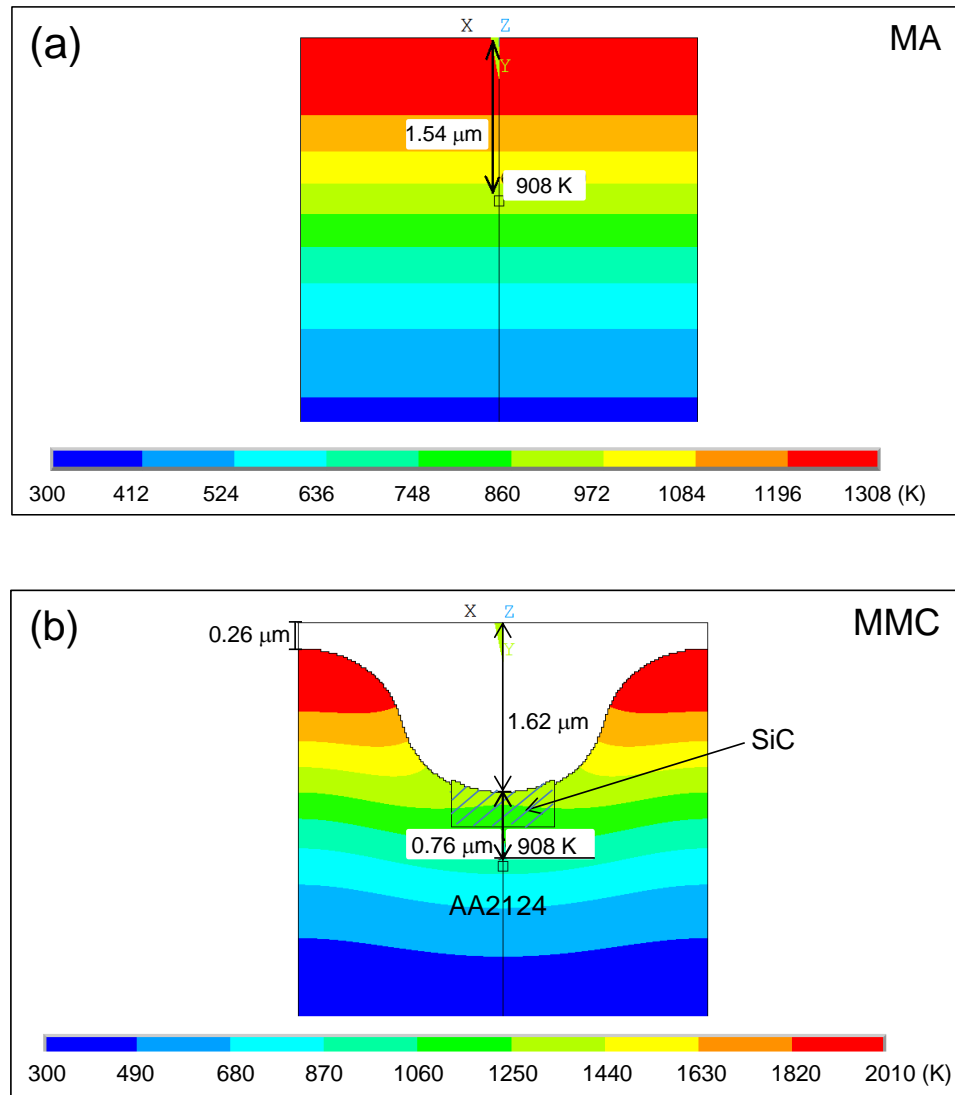
Figure 5.43 FEM simulation of the maximum melt depth in the MA and the MMC induced by a single laser pulse irradiation at 7 J/cm^2.

Considering the thermal conduction between SiC and AA2124, which is not able to be simulated using the analytical model, FEM was employed to evaluate the materials response of the MMC, as well as the MA. Figure 5.43 presents the temperature distribution in both materials when maximum melt depth is obtained. For the MA, the maximum melt depth is 1.54 μm as indicated in Figure 5.43(a), which is in good agreement with the result of the analytical model. For the MMC,

the results indicate that SiC could decompose within the depth of 1.62 μm and the temperatures of surrounding matrix could be over its melting temperature within 0.76 μm from the lowest point for the decomposition of the SiC. Therefore, the total melt depth is added up to 2.38 μm. The temperature on SiC is indicated to be much higher than that on AA2124 after the single pulse irradiation. Due to the thermal diffusion between SiC and AA2124, the matrix around the SiC particle could be evaporated, as shown in Figure 5.43(b). Within the dimension used for simulation, the evaporation depth of the matrix is 0.26 μm, within which the materials are supposed to be removed after laser irradiation, leading to the total thickness of the melted layer being reduced to 2.12 μm. Comparing the results in Figures 5.42 and 5.43(b), it is indicated that the maximum melt depth for the MMC is close to the melt depth right after the laser irradiation, suggesting different evolution of temperature with time for the MA and the MMC due to the presence of SiC particles.

5.5.3 SPH model

It should be noted that the molten matrix would flow into and fill the gaps formed by the evaporation of the matrix and the decomposition products of SiC after laser irradiation. The process was simulated with smoothed-particle hydrodynamics (SPH) modelling illustrating the hydrodynamics in SiC particles removal and their interaction with the molten matrix. The initial simulation setup is shown in Figure 5.44(a). The temperatures calculated via Equations 2.4-2.8 were used as the internal energy (initial conditions) of the vapour of the decomposition products or the over-heated SiC and the molten matrix in the SPH model. Figure 5.44 shows how the vapour was ejected and interacted with the surrounding molten matrix. Due to the heat conduction between the SiC and the matrix, the surrounding matrix became vapour and some evaporated materials were released from the bulk material in the early stage, as shown in Figure 5.44(b). Afterwards, the molten matrix around flowed towards the centre and filled the gap left by the release of the vapour, as shown in Figure 5.44(c). In this stage, some vapour might be re-solidified and

trapped in the melted layer and finally the melted layer was formed as shown in Figure 5.44(d). The simulation results support the TEM observation, which indicates nano-sized remnants from SiC particles in the melted layer.
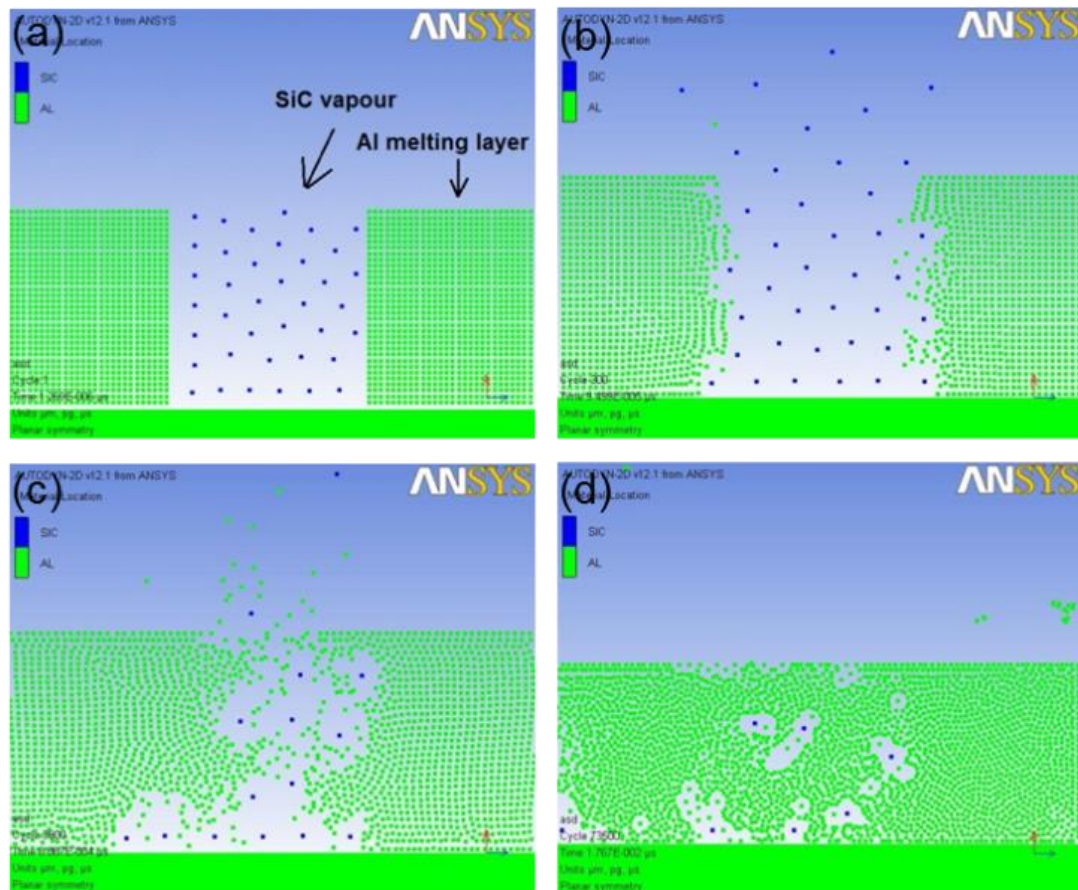
Figure 5.44 SPH simulation of excimer LSM of the MMC: (a) initial setup; (b) ejection of the vapour in early stage; (c) flow of the surrounding melted alloy and trapping of the re-solidified vapour; (d) the final melted layer formed by laser irradiation.

5.6 Discussion

5.6.1 Effect of SiC on the formation of the melted layer

As indicated in analytical and FEM modelling, SiC has great impact on the thermal and material responses of the MMC. The absorptivity of SiC to 248 nm laser beam is

ten times higher than that of AA2124 but the thermal conductivity of SiC is lower than that of AA2124 (Table 5.1). Therefore, the temperature obtained on SiC was much higher than that of AA2124 as shown in Figure 5.42, leading to distinct characteristics for the MMC upon laser irradiation due to the presence of SiC particles.

An important characteristic is the decomposition of SiC particles, leading to the removal of SiC particles from the melted layer. At the decomposition temperature, SiC decomposes into silicon vapour and solid carbon [29]. The analytical modelling shows a good consistence with the FEM simulation, suggesting a decomposition depth of ~1.7 μm. Although the temperature higher than the decomposition temperature of SiC is not given in the simulation results, other studies have suggested that the temperature of SiC exceeds 10000 K by excimer laser irradiation with similar operation conditions [29, 30], which could evaporate the decomposition products. The decomposition of SiC and evaporation of the decomposition products are believed to be the main mechanisms for the removal of SiC particles from the melted layer. It was reported that the power density threshold value for explosive boiling to occur in laser ablation of SiC using 248 nm KrF excimer laser is 2.2×10^8 W/cm^2 [31] and 3.3×10^8 W/cm^2 [29], corresponding to 3.3 J/cm^2 and 5 J/cm^2 for the laser used in the present study, respectively. Both values are lower than the fluence used in our investigation. Therefore, the explosive boiling cannot be ruled out as a driven force for the removal of SiC particles. The powder density threshold for explosive boiling to occur in aluminium was reported to be 5×10^{10} W/cm^2 [32] for a nanosecond pulsed laser, which is much higher than that used in present study, 4.7×10^8 W/cm^2. Therefore, the removal of the matrix is more likely due to the evaporation induced by thermal conduction from SiC particles, rather than the explosive boiling.

Another characteristic is that the high temperature on SiC particles contributes to further melting of the matrix along the depth direction. Prior to the analysis of the effect of SiC particles on the melt depth, the difference between the modelling work and the experimental observation is interpreted. It is revealed that the measured melt depths of the MA are larger than the calculated melt depths. This could be due to the

use of the theoretical absorptivity of Al based on an algorithm [27]. The actual absorptivity of AA2124 is dependent on the surface finish and the alloying elements. A rough surface and the alloying elements with higher absorptivity, such as Cu and Fe, could result in an increase in absorption of laser energy and therefore the increase of the melt depth. The actual absorptivity of aluminium to the 248 nm KrF excimer laser pulse can be as high as 0.16 [14]. Furthermore, considerable porosity in the melted layer can also increase the thickness of the melted layer. However, the modelling results are in good agreement with the experimental results when applied to the MMC. As shown in FEM results, the matrix around SiC particles and a part of the decomposition products are evaporated after laser irradiation but evaporation of Al are not likely to occur during LSM of the MA (Figure 5.43). The consumption of materials due to evaporation causes a decrease in the thickness of the melted layer, conceding the effect of the difference between the actual absorptivity and the theoretical absorptivity of the matrix. Also, the reduced porosity in the melted layer could contribute to a smaller thickness of the melted matrix in the MMC compared with that in the MA.

Based on above discussion, the formation of the melted layer with two regions, i.e. upper region with SiC removed and lower region with the presence of SiC, could be explained by subsequent thermal conduction from SiC to Al after laser irradiation. Both FEM and analytical modelling have shown a further melt depth of ~0.8 μm from the maximum depth of SiC decomposition (1.7 μm). However, the thickness of the upper region and the whole melted layer is not uniform, which could be due to the heterogeneity of the sample surface as explained by the schematic in Figure 5.45. According to Beer-Lambert law, the absorption depth for most metals undergoing UV irradiation is on the order of 10 nm [33]. Therefore, only the SiC particles exposed on the irradiated surface are directly subjected to laser irradiation, as shown in Figure 5.45(a). With this consideration, SiC particles merged under the irradiated surface can only be heated up by absorbing the heat from the covering matrix or irradiated by following laser pulses after the covering material is evaporated. As the temperature obtained on the matrix is much lower than that on SiC, most submerged SiC particles could not be heated up to as high temperature as the directly irradiated SiC particles. Therefore, SiC particles within the depth of ~1.7 μm from the surface

could not be completely removed by laser irradiation, as shown in Figure 5.45(b), resulting in the non-uniform depths observed.
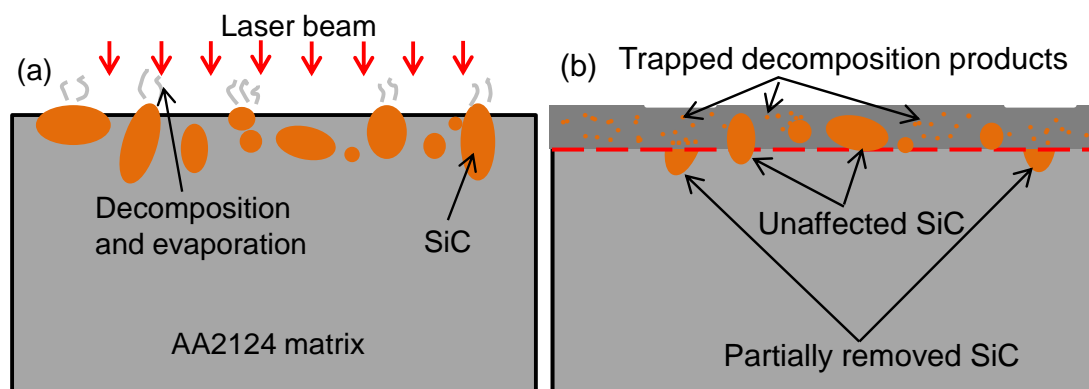
Figure 5.45 Schematic of the SiC removal by laser irradiation: (a) distribution of SiC particles before laser irradiation and laser-material interaction and (b) distribution of SiC particles after laser irradiation.

5.6.2 Oxidation of the elements
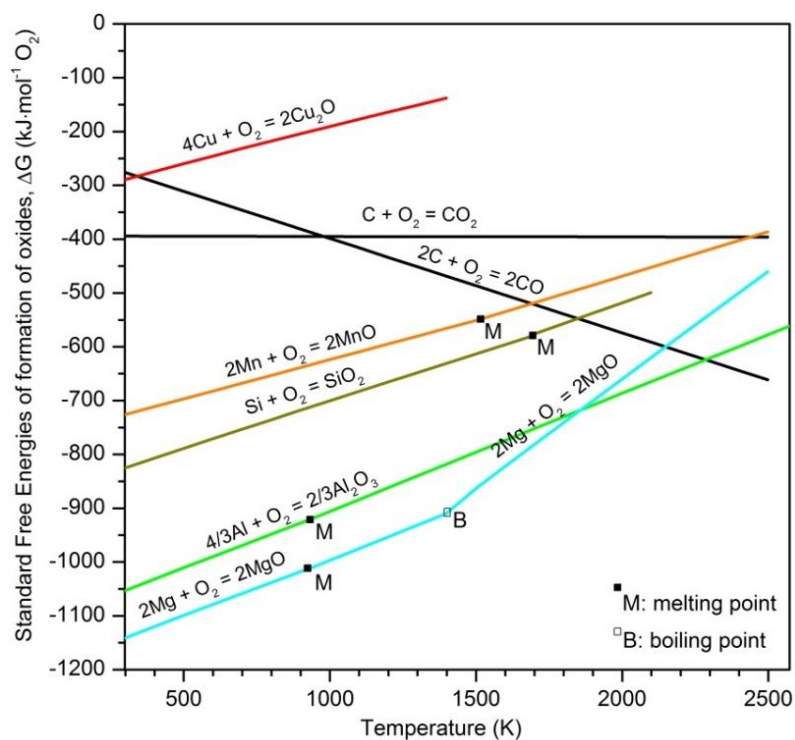
Figure 5.46 Ellingham diagram [34].

For the MMC, the XRD results suggest the formation of $MgAl_2O_4$ spinel in the melted layer and the EDX analysis shows the presence of $MgAl_2O_4$ spinel at the bottom of the melted layer. Due to the evaporation process, as well as the effect of surface tension [1], disturbance was obtained in the melting pool so that oxygen could be introduced to the melting pool by convection and react with the melt or vapour. The well-known Ellingham diagram was employed to analyse the thermodynamics of the oxidation of the alloying elements. According to Figure 5.46, plotted with the data from [34], there is a strong tendency for the formation of one or more oxides in the AA2124 aluminium alloy system. However, the Gibbs energy variations indicate that MgO is the most stable oxide at relative low temperatures (lower than 1870 K) as the Gibbs energies for the formation of MgO are the lowest in this temperature range. This explains the formation of magnesium oxides at the bottom of the melted layer. At the bottom of the melted layer, decomposition of SiC is not likely to occur as suggested by the FEM and analytical model and the temperature is relatively low. Therefore, the amount of free carbon at the bottom could be negligible and the formation of MgO is thermodynamically favourable. However, the content of magnesium in the alloy system is small and it is kinetically possible for the formation of Al_2O_3, which is the second stable oxide in Figure 5.46. The MgO could react with the Al_2O_3 to form $MgAl_2O_4$ spinel under laser irradiation, being consistent with previous report [35]. However, at the top of the melted layer close to the surface, the temperature is much higher than that at the bottom of the melted layer and the decomposition of SiC prevails upon laser irradiation. The decomposition products, especially carbon, could significantly impact the oxidation process of the alloying elements. It is noticeable that CO becomes the most stable oxide when the temperature exceeds 2270 K as shown in Figure 5.46. Therefore, carbon is the element that is most prone to react with oxygen. The carbon resulted from the decomposition of SiC could be oxidized to form CO, and then released to the environment, leaving Si enrichments at the decomposing sites (Figure 5.39). On the other hand, Mg and Al may be also subjected to oxidation but they are evenly distributed in the melted layer due to the intense disturbance at the top of the melted layer and no significant spinel is formed that has been confirmed by the XRD results with the glancing angle of 1 $^\circ$(Figure 5.40(b)).

However, there is no evidence for the formation of $MgAl_2O_4$ spinel in the melted layer of the MA. This could be probably related to the different temperature fields in the melting pool of the MA and the MMC. The reaction for the formation of $MgAl_2O_4$ spinel is as follows [36]:

$$Al_2O_3 \text{ (s)} + MgO \text{ (s)} = MgAl_2O_4 \text{ (s)} \qquad \text{(Reaction 5.1)}$$
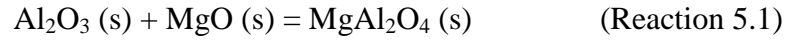
$$\Delta G = -35600 - 10.9T \text{ (J/mol)}$$

Here ΔG is the Gibbs energy change and T is the temperature. This reaction is spontaneous at any temperature because ΔG is always negative. However, the increase of temperature results in more negative ΔG, making the reaction easier to take place in the laser-melted MMC. The $MgAl_2O_4$ spinel is present in the melted layer as nanoparticles, indicating that the reaction occurred locally, which could be attributed to the local segregation of Mg in the MMC. This is also an indication of that the homogeneity of the melted layer is higher for the MA than the MMC.

5.6.3 Cu-rich segregation bands

Cu segregation was observed at the bottom region of the melted layer for both the MA and the MMC. Such Cu-rich segregation bands were reported in excimer laser-melted 2xxx aluminium alloys and the mechanisms for the formation of such bands were discussed [3, 4, 8, 9, 37]. Viejo et al. [4, 9, 37] attributed the formation of the copper-rich segregation bands to the application of insufficient laser pulses that did not allow the solute-rich liquid to be fully dispersed. In this case, solute trails, rich in manganese and iron as well, were observed at the partially melted coarse intermetallic phases. However, the segregation bands in current work are not evidently related to partially dissolved intermetallics because the solute trails are rarely revealed. Therefore, there could be another mechanism responsible for the formation of the Cu-rich segregation bands.

As suggested by Ryan and Prangnell [3] and indicated in Figure 5.14(c), the Cu-rich segregation bands are related to the start of the solidification. By tracing the melting temperature of the MA in the analytical model (Figure 5.42), the position of the

liquid-solid interface was determined, according to which the evolution of growth front velocity (solidification rate) was obtained, as shown in Figure 5.47. It is shown that the growth front velocity increases rapidly to over 200 m/s during the solidification process. When the growth front velocity is higher than some critical values, the microsegregation-free structure is achieved by the mechanism of absolute stability [38]. The theoretical minimum growth front velocity for the formation of the microsegregation-free structure for Al-5% Cu alloy was calculated to be 5.33 m/s [39]. Ryan et al. [3] also reported the agreeable growth front velocity of ~5 m/s for AA2024 alloy to achieve absolute stability. When the growth front velocity approaches to the critical value for absolute stability, an oscillatory instability could appear as suggested by Coriell and Sekerka [40] and Merchant and Davis [41], leading to the formation of the banded structure before the microsegregation-free structure is achieved (Figure 2.6). As shown in Figure 5.47, there is a short period for the growth velocity to increase from zero to a considerably high value (~5 m/s indicated in [3] and [39]) for the MA to achieve absolute stability. The Cu-rich segregation bands could be formed during this short period as a result of the oscillatory morphological stability.
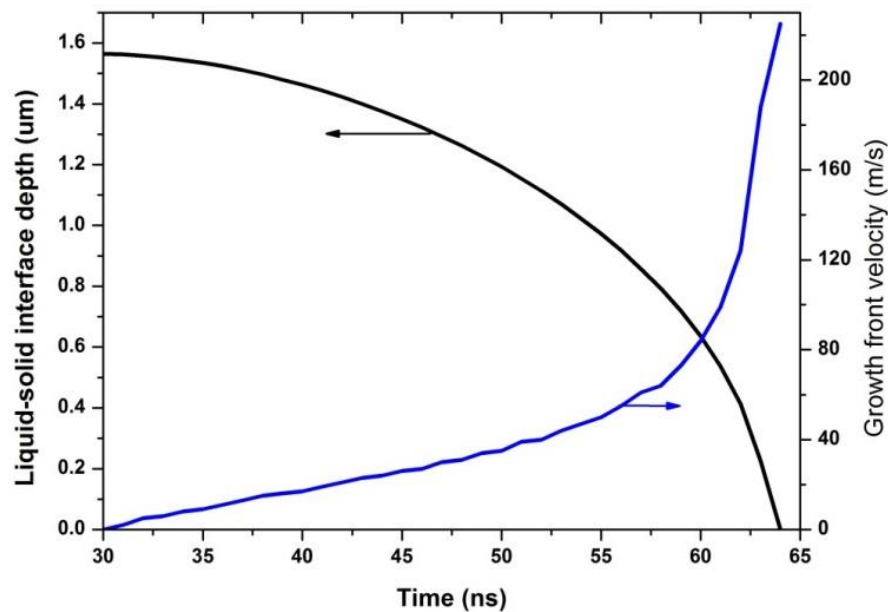
Figure 5.47 Evolution of liquid-solid interface and growth front velocity with time in excimer LSM of the MA. Note that the solidification process starts at 30 ns when the maximum melt depth is reached, as indicated in Figure 5.42.

5.6.4 Al-Si eutectic in the melted layer of MMC

The filamentary microstructure, present in the middle region of the melted layer of MMC (Figure 5.36(c)), is attributed to an Al-Si eutectic structure formed during solidification of the melt. The average chemical composition of the middle and top regions of melted layer, where decomposition of SiC occurred, was determined by EDX analysis and is shown in Table 5.2. The high Si percentage is resulted from the decomposition of the SiC particles. Consulting with the Al-Si phase diagram, the Si content, 11.5 wt.%, in the melted layer is close to that of the eutectic Al-Si alloy, which contains ~12.2 wt.% Si. This is an indication of the tendency for the formation of Al-Si eutectic microstructure when the temperature decreases to the range for the formation of Al-Si eutectic during solidification. According to M. Gündüz et al. [42], the inter-spacing of the Si precipitations in eutectic Al-Si alloy decreases with the increase of growth front velocity. Therefore, the Si segregation became much finer as the growth front velocity increased when the solidification proceeded from the bottom to the top of the melted layer (Figures 5.36(c) and 5.36(d)). However, during such rapid solidification, continuous decrease of inter-spacing with the increasing growth front velocity is not possible, restricted by the absolute stability resulting in the planar front morphology, indicated by Zimmermann et al. [43]. Therefore, the coupled eutectic structure was only formed in the middle zone of the melted layer and the top area was formed with the microsegregation-free structure.

Table 5.2 Chemical composition of the melted layer by EDX quantitative analysis.

Element	Al	Si	Cu	Mg	Mn	Fe	C	O
Wt.%	74.36	11.47	2.93	0.94	0.32	0.19	7.15	2.64

5.6.5 Microsegregation-free structure

For the MA, microsegregation-free structure was observed throughout the melted layer except those Cu-rich segregation bands concentrated at the bottom of the melted layer. As illustrated above, the growth front velocity rapidly increased to enable the solidification to proceed with absolute stability (Figure 5.47). For the MMC, the microsegregation-free structure was formed in the top region of the

melted layer which was essentially free of SiC particles. However, in the middle region of the melted layer, it was missing due to the formation of the Al-Si eutectic. This could be due to the presence of SiC particles in the middle to bottom region altering the temperature distribution in these areas.
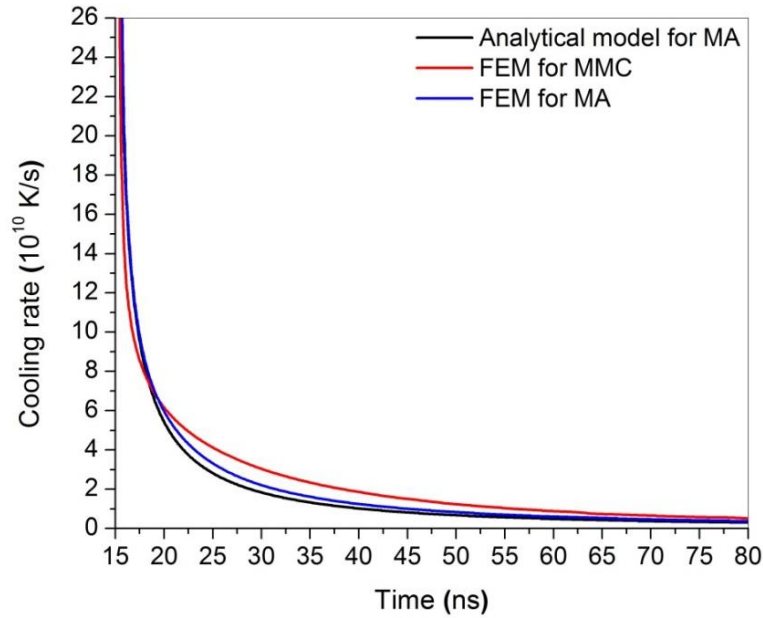
Figure 5.48 Evolution of the cooling rate at the surface after laser irradiation.

The calculation of the growth front velocity could not include the effect of SiC particles for the MMC and therefore the formation of the microsegregation-free structure in the top region will be interpreted in the view of fast cooling rates resulted from excimer LSM. The magnitude of the cooling rates can reflect the speed of solidification. It is generally accepted that the fast cooling rate resulted from excimer LSM, leading to the formation of the microsegregation-free structure, is the key advantage of excimer lasers compared to the CW CO2 or Nd:YAG lasers [3, 4, 37]. The evolution of the surface cooling rate was obtained from the analytical and FEM modelling for the MA and the FEM modelling for the MMC, as shown in Figure 5.48. For the MA, the curves obtained from the analytical model and the FEM are close to each other, indicating good consistence between the two modelling methods. The MMC exhibits similar evolution of cooling rates. It is noticeable that the surface cooling rate is over 10^9 K/s, up to 10^{11} K/s, throughout the solidification process for both materials. The results are in good agreement with previous research

[3], which suggested that the cooling rate of 10^9 K/s resulted in the formation of the microsegregation-free structure. For the MMC, the evaporated materials could be re-solidified and trapped in the melted layer before they are released to the environment as a result of the fast cooling rates. This could explain the presence of nano-sized remnants of SiC (Figure 5.36(f)) and high content of Si and C in the melted layer (Table 5.2).

5.7 Summary

The microstructures of the MA and the MMC after excimer LSM have been studied. Two parameters, i.e. laser fluence and NOP, have significant influence on the microstructures of the melted layer for both materials. High laser fluence contributes to the complete melting in near-surface regions and the thick melted layer. High NOP improves the homogeneity of solutes dispersion but results in high porosity (MA) or networks of cracking (MMC). For the MA, significant rippled structure is formed, which can be reduced by reducing the laser fluence, whilst no significant rippled structure is observed for the MMC after LSM.

The effect of SiC particles on microstructures of the melted layer has been discussed. Dissolution of intermetallic particles occurred during LSM and a homogeneous melted layer with complete dispersion of solute atoms could be formed for the MA. Apart from the dissolution of intermetallic particles, removal of SiC particles is revealed for the MMC. According to the modelling results, the high temperature on SiC particles causes decomposition of SiC and evaporation of surrounding matrix Al and the decomposition products. The high temperature on SiC also contributes to further melting of the matrix along the depth direction.

Due to the presence of SiC particles, the microstructure of the melted layer of the MMC is different from that of the MA. Except the Cu-rich segregation bands, microsegregation-free structure is revealed throughout the melted layer of the MA. However, the melted layer of the MMC can be divided into three regions, which are characterized with copper-rich segregation bands and $MgAl_2O_4$ spinel in the bottom region, Al-Si eutectic in the middle region, and microsegregation-free structure in

the top region, respectively. The formation of copper-rich segregation bands in both materials is attributed to the oscillatory instability before the absolute stability is obtained during solidification. In the MMC, the oxidation of aluminium and magnesium at the bottom of the melted layer results in the formation of $MgAl_2O_4$ spinel and is suppressed in the middle and the top area of the melted layer. No $MgAl_2O_4$ spinel is formed in the melted layer of the MA. The decomposition of SiC provides significant amount of Si close to the eutectic composition, leading to growth of Al-Si eutectic in the MMC. The formation of the microsegregation-free microstructure as a result of the fast cooling rate is believed to contribute to the improvement of corrosion resistance of the MA and the MMC, which will be investigated in the next chapter.

References

[1]   T.R. Anthony, H.E. Cline, *Surface rippling induced by surface-tension gradients during laser surface melting and alloying*, Journal of Applied Physics, 48 (1977), 3888-3894.

[2]   M. Bonelli, A. Miotello, P. Mosaner, *Morphological changes induced on aluminum surfaces by excimer laser irradiation*, Applied Surface Science, 186 (2002), 211-215.

[3]   P. Ryan, P.B. Prangnell, *Grain structure and homogeneity of pulsed laser treated surfaces on Al-aerospace alloys and FSWs*, Materials Science and Engineering a-Structural Materials Properties Microstructure and Processing, 479 (2008), 65-75.

[4]   F. Viejo, A.E. Coy, F.J. Garcia-Garcia, Z.L.P. Skeldon, G.E. Thompson, *Relationship between microstructure and corrosion performance of AA2050-T8 aluminium alloy after excimer laser surface melting*, Corrosion Science, 52 (2010), 2179-2187.

[5]   A.H. Wang, T.M. Yue, *Surface characteristic change of SiC reinforced Mg-alloy composite induced by excimer laser surface treating*, Journal of Materials Science Letters, 20 (2001), 1965-1967.

[6]   X.M. Zhang, H.C. Man, T.M. Yue, *Corrosion properties of excimer laser surface treated Al-SiC metal matrix composite*, Scripta Materialia, 35 (1996), 1095-1100.

[7]   Z. Aburas, Microstructural characterisation and corrosion studies of excimer laser-treated aluminium alloy AA2024-T351, 2013, Ph.D Thesis, The University of Manchester

[8]   C. Padovani, A.J. Davenport, B.J. Connolly, S.W. Williams, E. Siggs, A. Groso, M. Stampanoni, *Corrosion protection of AA2024-T351 friction stir welds by laser surface melting with Excimer laser*, Corrosion Engineering Science and Technology, 47 (2012), 188-202.

[9]   F. Viejo, A.E. Coy, F.J. Garcia-Garcia, M.C. Merino, Z. Liu, P. Skeldon, G.E. Thompson, *Enhanced performance of the AA2050-T8 aluminium alloy following excimer laser surface melting and anodising processes*, Thin Solid Films, 518 (2010), 2722-2731.

[10]   C.P. Chan, T.M. Yue, H.C. Man, *Effect of excimer laser surface treatment on corrosion behaviour of aluminium alloy 6013*, Materials Science and Technology, 18 (2002), 575-580.

[11] C.P. Chan, T.M. Yue, H.C. Man, *The effect of excimer laser surface treatment on the pitting corrosion fatigue behaviour of aluminium alloy 7075*, Journal of Materials Science, 38 (2003), 2689-2702.

[12] T.M. Yue, C.P. Chan, L.J. Yan, H.C. Man, *Effect of excimer laser surface melting on intergranular corrosion cracking of the aluminum-lithium alloy 8090*, Journal of Laser Applications, 16 (2004), 31-39.

[13] T.M. Yue, L.J. Yan, C.P. Chan, C.F. Dong, H.C. Man, G.K.H. Pang, *Excimer laser surface treatment of aluminum alloy AA7075 to improve corrosion resistance*, Surface & Coatings Technology, 179 (2004), 158-164.

[14] L.K. Ang, Y.Y. Lau, R.M. Gilgenbach, H.L. Spindler, *Analysis of laser absorption on a rough metal surface*, Applied Physics Letters, 70 (1997), 696-698.

[15] Z. Liu, H. Liu, F. Viejo, Z. Aburas, M. Rakhes, *Laser-induced microstructural modification for corrosion protection*, Proceedings of the Institution of Mechanical Engineers Part C-Journal of Mechanical Engineering Science, 224 (2010), 1073-1085.

[16] A. Boag, A.E. Hughes, A.M. Glenn, T.H. Muster, D. McCulloch, *Corrosion of AA2024-T3 Part I. Localised corrosion of isolated IM particles*, Corrosion Science, 53 (2011), 17-26.

[17] G.O. Ilevbare, O. Schneider, R.G. Kelly, J.R. Scully, *In situ confocal laser scanning microscopy of AA 2024-T3 corrosion metrology - I. Localized corrosion of particles*, Journal of the Electrochemical Society, 151 (2004), B453-B464.

[18] P. Leblanc, G.S. Frankel, *A study of corrosion and pitting initiation of AA2024-T3 using atomic force microscopy*, Journal of the Electrochemical Society, 149 (2002), B239-B247.

[19] J.A. Vreeling, V. Ocelik, G.A. Hamstra, Y.T. Pei, J.T.M. De Hosson, *In-situ microscopy investigation of failure mechanisms in Al/SiC$_p$ metal matrix composite produced by laser embedding*, Scripta Materialia, 42 (2000), 589-595.

[20] C. Hu, T.N. Baker, *Laser processing to create in-situ Al-SiC$_p$ surface metal-matrix composites*, Journal of Materials Science, 30 (1995), 891-897.

[21] L. Díaz-Ballote, L. Veleva, M.A. Pech-Canul, M.I. Pech-Canul, D.O. Wipf. *Activity of SiC particles in Al-based metal matrix composites revealed by SECM*, Journal of the Electrochemical Society, 151 (2004), B299.

[22] H.B. Ding, L.H. Hihara, *Galvanic corrosion and localized degradation of aluminum-matrix composites reinforced with silicon particulates*, Journal of the Electrochemical Society, 155 (2008), C226-C233.

[23] J.G. Kaufman. Aluminum Alloy Database. Knovel.

[24]   R.G. Munro, *Material properties of a sintered α-SiC*, Journal of Physical and Chemical Reference Data, 26 (1997), 1195-1203.

[25]   Melting, Boiling, Triple, and Critical Point Temperatures of the Elements. in: W. M. Haynes e, (Ed.). CRC Handbook of Chemistry and Physics, 95th Edition (Internet Version 2015), CRC Press/Taylor and Francis.

[26]   P. Patnaik. Handbook of Inorganic Chemicals, McGraw-Hill, 2003.

[27]   A.D. Raki, *Algorithm for the determination of intrinsic optical constants of metal films: application to aluminum*, Applied Optics, 34 (1995), 4755-4767.

[28]   W.J. Choyke, E.D. Palik. Silicon Carbide (SiC). in: Palik ED, (Ed.). Handbook of Optical Constants of Solids, Academic Press, 1997. pp. 587-595.

[29]   S. Gupta, B. Pecholt, P. Molian, *Excimer laser ablation of single crystal 4H-SiC and 6H-SiC wafers*, Journal of Materials Science, 46 (2010), 196-206.

[30]   R. Reitano, P. Baeri, N. Marino, *Excimer laser induced thermal evaporation and ablation of silicon carbide*, Applied Surface Science, 96-8 (1996), 302-308.

[31]   F. Neri, F. Barreca, S. Trusso, *Excimer laser ablation of silicon carbide ceramic targets*, Diamond and Related Materials, 11 (2002), 273-279.

[32]   A. Bogaerts, Z. Chen, R. Gijbels, A. Vertes, *Laser ablation for analytical sampling: what can we learn from modeling?*, Spectrochimica Acta Part B: Atomic Spectroscopy, 58 (2003), 1867-1893.

[33]   M. Brown, C. Arnold. Fundamentals of laser-material interaction and application to multiscale surface modification. in: Sugioka K, Meunier M, Piqué A, (Eds.). Laser Precision Microfabrication, Springer Berlin Heidelberg, 2010. pp. 91-120.

[34]   http://www.engr.sjsu.edu/ellingham/

[35]   I.V. Beketov, A.I. Medvedev, O.M. Samatov, A.V. Spirina, K.I. Shabanova, *Synthesis and luminescent properties of $MgAl_2O_4$:Eu nanopowders*, Journal of Alloys and Compounds, 586, Supplement 1 (2014), S472-S475.

[36]   Z.P. Luo, Y.G. Song, S.Q. Zhang, *A TEM study of the microstructure of SiC_p/Al composite prepared by pressureless infiltration method*, Scripta Materialia, 45 (2001), 1183-1189.

[37]   F. Viejo, Z. Aburas, A.E. Coy, F.J. Garcia-Garcia, Z. Liu, P. Skeldon, G.E. Thompson, *Performance of Al alloys following excimer LSM-anodising approaches*, Surface and Interface Analysis, 42 (2010), 252-257.

[38]   W. Kurz, D.J. Fisher. Fundamentals of solidification, Trans Tech Publications, 1986.

[39]   M. Zimmermann, M. Carrard, M. Gremaud, W. Kurz, *Characterization of the banded structure in rapidly solidified Al-Cu alloys*, Materials Science and Engineering: A, 134 (1991), 1278-1282.

[40]   S.R. Coriell, R.F. Sekerka, *Oscillatory morphological instabilities due to non-equilibrium segregation*, Journal of Crystal Growth, 61 (1983), 499-508.

[41]   G.J. Merchant, S.H. Davis, *Morphological instability in rapid directional solidification*, Acta Metallurgica Et Materialia, 38 (1990), 2683-2693.

[42]   M. Gündüz, H. Kaya, E. Çadırlı, A. Özmen, *Interflake spacings and undercoolings in Al–Si irregular eutectic alloy*, Materials Science and Engineering: A, 369 (2004), 215-229.

[43]   M. Zimmermann, M. Carrard, W. Kurz, *Rapid solidification of Al-Cu eutectic alloy by laser remelting*, Acta Metallurgica, 37 (1989), 3305-3313.

Chapter 6 Corrosion performance of excimer laser-melted MA and MMC

6.1 Introduction

In Chapter 5, microstructure refinement in the melted layer has been demonstrated for both the MA and the MMC after excimer LSM. This chapter studies the corrosion performance of the laser-melted materials by comparison with that of the as-received materials, with particular interest in the correlation between the laser-induced microstructural changes and the corrosion behaviour of the laser-melted MA and MMC.

6.2 Selection of laser operating parameters for corrosion evaluation

Table 6.1 Laser operation parameters for corrosion evaluation of the laser-melted MA and MMC.

	Parameters	Microstructures
MA	2 J/cm^2, 20 P	Thin; compact; no significant ripples.
	7 J/cm^2, 10 P	Medium; compact; significant ripples.
	7 J/cm^2, 25 P	Medium; porous; significant ripples.
	7 J/cm^2, 40 P	Thick; more porous; significant ripples.
MMC	7 J/cm^2, 10 P	Thin[*]; compact; a number of SiC remnants on the surface.
	7 J/cm^2, 25 P	Medium; compact; reduced SiC remnants on the surface.
	7 J/cm^2, 40 P	Thick; networks of cracking; further reduced SiC remnants on the surface.

[*] refers to the thickness of the surface layer of laser-melted MMC.

As discussed in Chapter 5, the laser fluence and the NOP have significant influence on LSM of the MA and the MMC. By adjusting the operating parameters, several important characteristics such as surface morphology, melt depth, porosity and cracking of the melted layer can be changed. To investigate the corrosion performance of the laser-melted materials, several typical combinations of the laser fluence and the NOP were selected to form desirable microstructures of the melted layer, by which means the effect of the laser-induced characteristics on the corrosion performance of the laser-melted materials can be evaluated. The selected laser operating parameters and the corresponding microstructures of the melted layer, including the melt depth, the integrity and surface morphology of the melted layer, are shown in Table 6.1.

6.3 Corrosion evaluation of excimer laser-melted MA

6.3.1 Open circuit potential

Figure 6.1 shows the open circuit potential (OCP) evolution of the MA with time in the duration of 1 h after immersion in 0.6 M NaCl solution. The stable OCP of all the samples after the immersion of 1 h indicates that the samples have obtained a steady state. The laser-melted MA samples exhibit more electrochemical positive steady OCPs than the as-received MA. The samples treated with 7 J/cm^2 share a characteristic that the OCP graphically has an initial drop and then rises gradually to the steady OCP values as shown in Figure 6.1. One possible explanation is associated with the rippled structure of the samples treated with 7 J/cm^2, leading to the formation of micro-crevices and micro-pores (Figure 5.5 and Figure 5.6). The initial shift of OCP to more electrochemical negative values during immersion of first 5 min or less can be attributed to the penetration of the solution into the micro-crevices and micro-pores, which actually increases the contact area with the solution. The increase of the exposed area could increase the total metal dissolution rate on the sample surface, leading to the shift of OCP to the electrochemical negative direction. As the immersion time increased, the oxygen in the crevices and pores was depleted

due to the difficulty of oxygen diffusion into the passages caused by the geometry and could not support the cathodic reaction; and therefore the cathodic reaction and anodic reaction were separated at the outer surface and inside the crevices and pores. The outer surface acted as the cathode and the crevice area exhibited the anodic nature. The enhanced cathodic reaction at the outer surface could play such a role in making the OCP shift back to the electrochemical positive direction according to the mixed potential theory, as shown in Figure 6.1. As discussed in Chapter 5, the rippled structure becomes more significant as suggested by the increase of surface roughness with increasing the NOP. Correspondingly, the increase of NOP results in longer duration for the samples to obtain the steady state.
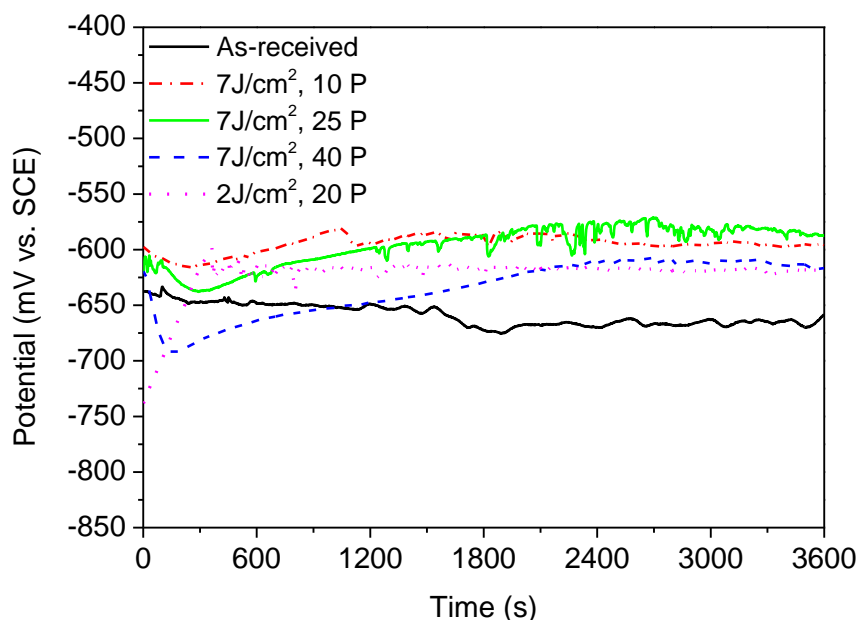
Figure 6.1 Evolution of the OCP of as-received and laser-melted MA in naturally aerated 0.6 M NaCl solution.

The sample treated with the laser fluence of 2 J/cm^2 shows different OCP evolution from those treated with the laser fluence of 7 J/cm^2, which is due to the absence of significant rippled structure. The initial shift of OCP to the positive direction could be attributed to the passivation of the surface exposed to the solution, limiting the

anodic dissolution. The steady OCP afterwards indicates the equilibrium between the passivation and the metal dissolution.

6.3.2 Potentiodynamic polarization
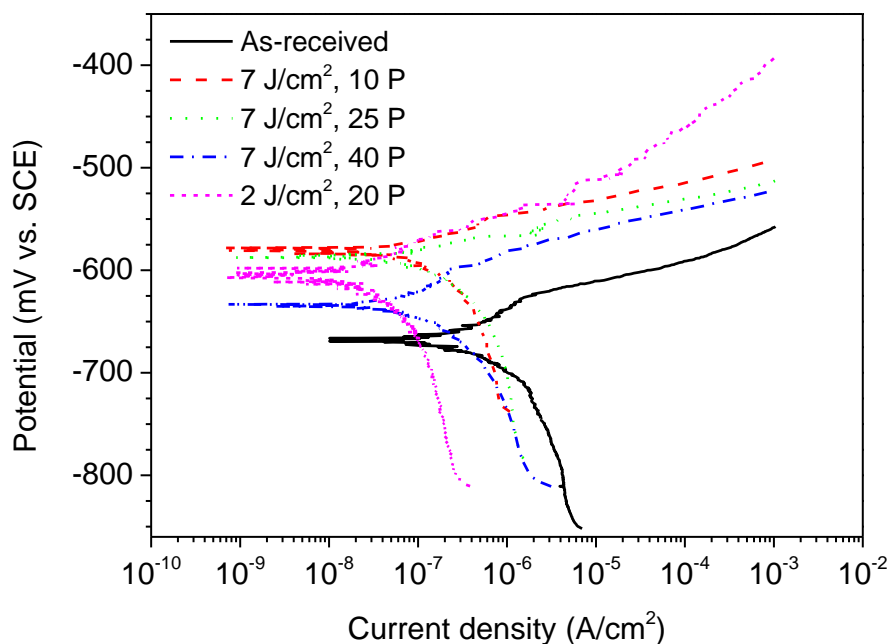
Figure 6.2 Potentiodynamic polarization curves of as-received and laser-melted MA in naturally aerated 0.6 M NaCl solution.

The potentiodynamic polarization curves of as-received and laser-melted MA following the immersion of 1 h in naturally aerated 0.6 M NaCl solution are presented in Figure 6.2. No passivation was observed in the anodic branch of polarization curves for all the samples, indicating the active nature of the surface during anodic polarization. This is different from the results of Padovani *et al.*'s work, which showed a passivation range in anodic branch for the samples after LSM [1]. It is probably due to the fact that the potentiodynamic polarization in their work was conducted in 0.1 M NaCl solution, which is less aggressive than the 0.6 M NaCl solution used in the present work. Comparing the cathodic branches of the polarization curves, the curves for laser-melted samples shift to the left in the graph,

suggesting smaller cathodic current density for the laser-melted samples than the as-received sample. The electrochemical heterogeneity caused by intermetallics and grain boundary segregations could result in galvanic coupling effect in the as-received MA, as discussed in Chapter 4. However, the melted layer in the MA exhibits highly refined homogeneous microstructure so that the cathodic reaction associated with the intermetallics could be significantly reduced, leading to the reduction of cathodic current density.

Table 6.2 Average electrochemical parameters interpreted from the polarization curves of three measurements of as-received and laser-melted MA.

	E_{corr} (mV vs. SCE)	i_{corr} (μA/cm^2)
As-received	-658±10	0.55±0.22
7 J/cm^2, 10 P	-582±3	0.14±0.06
7 J/cm^2, 25 P	-599±15	0.19±0.11
7 J/cm^2, 40 P	-629±6	0.21±0.06
2 J/cm^2, 20 P	-600±4	0.036±0.02

The electrochemical parameters interpreted from the potentiodynamic polarization curves are shown in Table 6.2. At the corrosion potential (E_{corr}), the laser-melted samples exhibit smaller corrosion current density than the as-received sample (i_{corr}). The i_{corr} is 2-4 times smaller for the samples treated with the laser fluence of 7 J/cm^2 than the as-received sample and follows the sequence 10 P < 25 P < 40 P. Compared with the as-received sample, a fifteenth-fold smaller i_{corr} is registered for the sample treated with the laser fluence of 2 J/cm^2. It is evident that the corrosion resistance of AA2124 has been improved after LSM and the sample treated with the laser fluence of 2 J/cm^2 is of the highest corrosion resistance among the laser-melted samples.

Figure 6.3 shows the surface morphology of the as-received and laser-melted MA after potentiodynamic polarization. Pitting has initiated on all the samples. For the as-received sample, the corrosion initiated at the intermetallics as shown in Figure

6.3(a). The results in Chapter 4 have demonstrated that the intermetallics are mainly AlCuMnFe(Si)-containing particles and S-phase particles, which act as local cathodes and local anodes regarding to Al matrix, respectively [2-4]. Therefore, these intermetallics are susceptible for corrosion initiation in chloride solution. After excimer LSM, the intermetallics dissolved into the Al matrix to form a homogeneous melted layer, eliminating the galvanic coupling effect between the intermetallic particles and the matrix [1, 5-8].
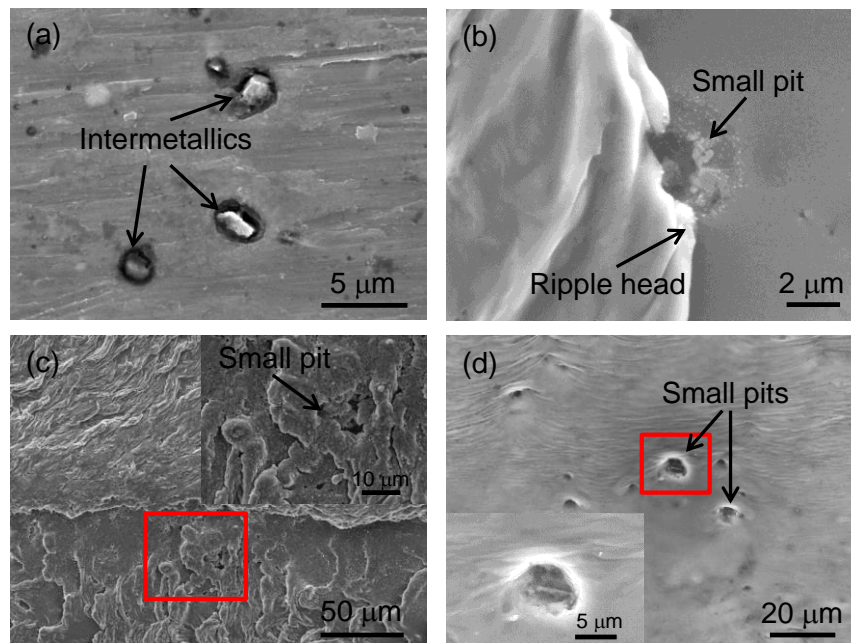
Figure 6.3 SE-SEM micrographs showing the surface morphology of the MA after potentiodynamic polarization: (a) as-received; (b) 7 J/cm^2, 25 P, the track centre; (c) 7 J/cm^2, 25 P, the re-heated area close to the overlapped area; and (d) 2 J/cm^2, 25 P.

Figure 6.3(b) shows a small pit initiated close to the ripple head. Figure 6.3(c) shows a pit formed in the re-heated area close to the overlapped area. The results indicate that the pitting initiation of the laser-melted samples is more associated with the artefact caused by excimer LSM. Yilbas et al. [9] has demonstrated that the rough surface morphology resulted from LSM by a pulsed CO_2 laser could even decrease the corrosion resistance of AA8022 aluminium alloy. In the present study, the

rippled structure has been found to be able to create narrow passages underneath the ripples and thus introduce significant porosity in the melted layer (Figure 5.11). The crevice environment makes such sites preferential for corrosion initiation by promoting crevice corrosion. The corroded morphology reveals the pits close to the ripple head (Figure 6.3(b)), which is likely resulted from the corrosion initiation at the underneath crevices, agreeing with the discussion of the OCP evolution in the previous section.

Figure 6.3(d) presents the surface morphology of the laser-melted sample treated with the laser fluence of 2 J/cm^2 after potentiodynamic polarization. Although the rippled structure was significantly reduced compared with those treated with the laser fluence of 7 J/cm^2, the slightly wrinkled area also generated a few small pits. This indicates that the laser-induced morphology played an important role in initiating pitting.

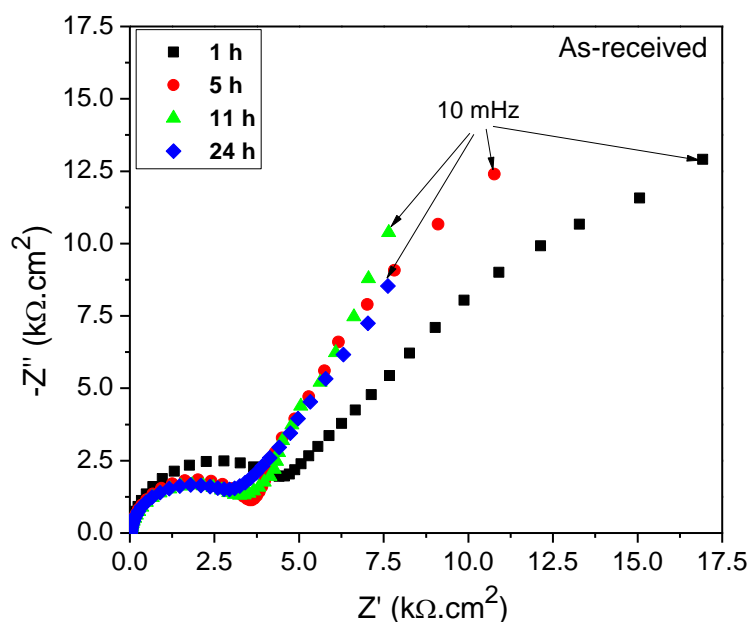### 6.3.3 Electrochemical impedance spectroscopy

Figure 6.4 Nyquist plots of the EIS responses of as-received MA up to 24 h during immersion in 0.6 M NaCl solution.

Figures 6.4-6.8 show the Nyquist plots of the EIS responses of the as-received and laser-melted MA during the immersion in 0.6 M NaCl solution up to 24 h. All the Nyquist plots are characterized by one capacitive loop at high-medium frequencies and another capacitive loop or a diffusion tail at low frequencies, except the samples treated with the laser fluence of 2 J/cm^2 after immersion in the solution for 1 h, which exhibited only one capacitive loop in the plot. The high-medium frequency capacitive loop corresponds to the electrolyte-metal interface behaviour and the diameter of the semicircle measures the charge transfer resistance, which is proportionally related to the corrosion resistance of the alloy when the surface undergoes corrosion in aggressive media. The low frequency capacitive loop is related to the mass transport during corrosion and when it is depressed to present a diffusion tail it represents the Warburg diffusion impedance. For quantitative analysis of the EIS spectra, fittings were carried out using the equivalent circuit as shown in Figure 6.9, where R_s is the electrolyte resistance, Q_{dl} is the constant phase element (CPE) related to the double layer capacitance, R_{ct} is the charge transfer resistance and R_w and Q_w are diffusion related Warburg elements.

Figure 6.5 Nyquist plots of the EIS responses of laser-melted MA (7 J/cm^2, 10 P) up to 24 h during immersion in 0.6 M NaCl solution.

Figure 6.6 Nyquist plots of the EIS responses of laser-melted MA (7 J/cm^2, 25 P) up to 24 h during immersion in 0.6 M NaCl solution.

Figure 6.7 Nyquist plots of the EIS responses of laser-melted MA (7 J/cm^2, 40 P) up to 24 h during immersion in 0.6 M NaCl solution.

The use of CPE has been described previously and the impedance of CPE (Z_{CPE}) is written as:

$$Z_{\text{CPE}(\omega)} = (Cj\omega^{-n})^{-1} \qquad \text{(Equation 6.1)}$$

where j^2=-1, and n is an empirical exponent between 0 and 1. Particularly, when n=0.5, the group of R_w and Q_w can be converted to the Warburg impedance [10]. With the varying n, the EIS plots at low frequencies which exhibit non-ideal diffusion tail can be better fitted [11].
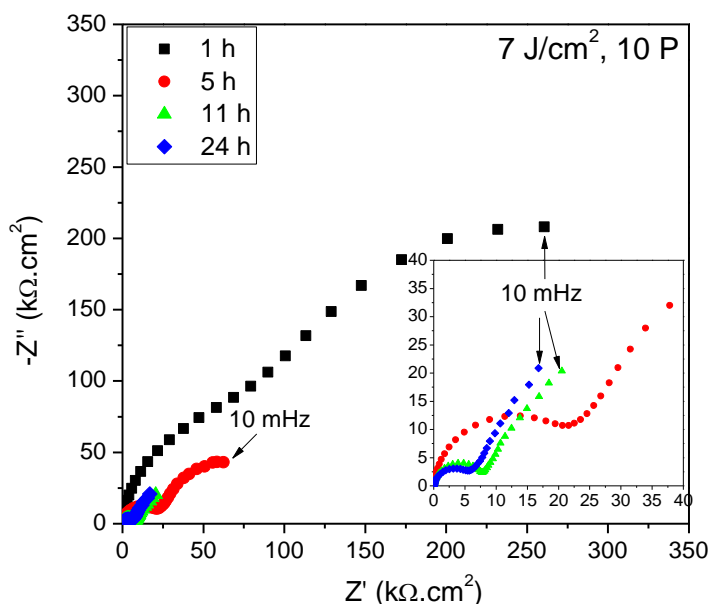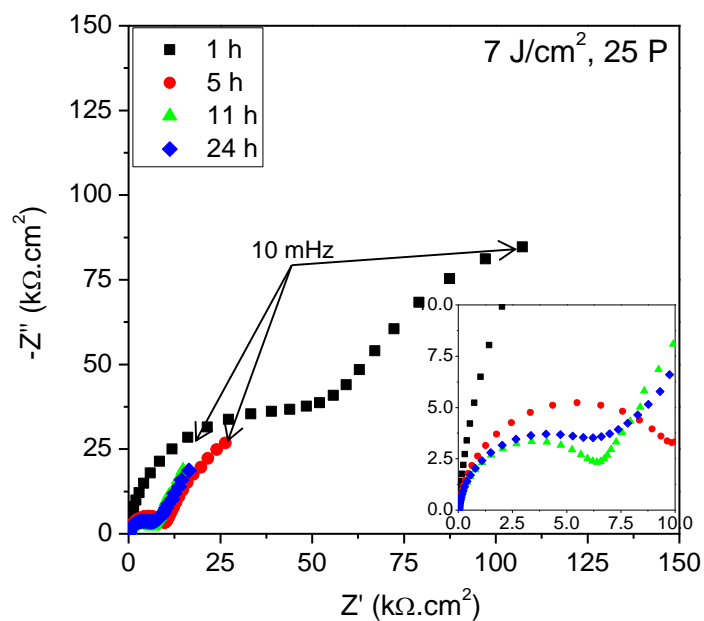

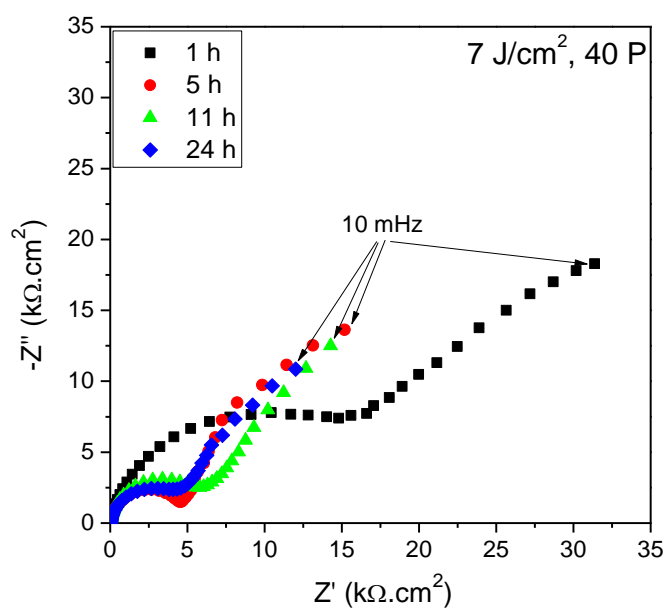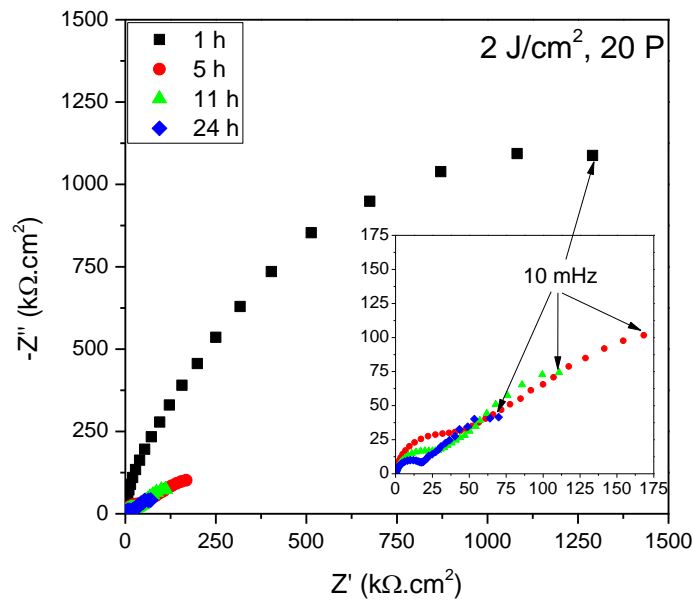Figure 6.8 Nyquist plots of the EIS responses of laser-melted MA (2 J/cm^2, 20 P) up to 24 h during immersion in 0.6 M NaCl solution.
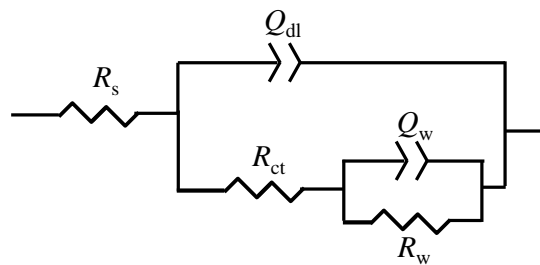

Figure 6.9 Equivalent circuit used to fit the EIS spectra.

The fitting was carried out using the Zview software. The complete fitting results for EIS spectra in Figures 6.4-6.8 are listed in Appendix A. The simulated data are in

good agreement with the experimental data, indicated by the small χ^2 in the range of 10^{-4}-10^{-3}. Figure 6.10 shows the good agreement between the experimental results and the fitted results for both the modulus of impedance and phase angle with frequency using the equivalent circuit in Figure 6.9. The scatter of the results obtained from three measurements for each condition is less than 35% for the R_{ct} and Q_{dl}. However, the Q_w and R_w show large variations in the three measurements, probably being due to the fact that they are assigned as the result of diffusion process of the chloride and aluminium ions.
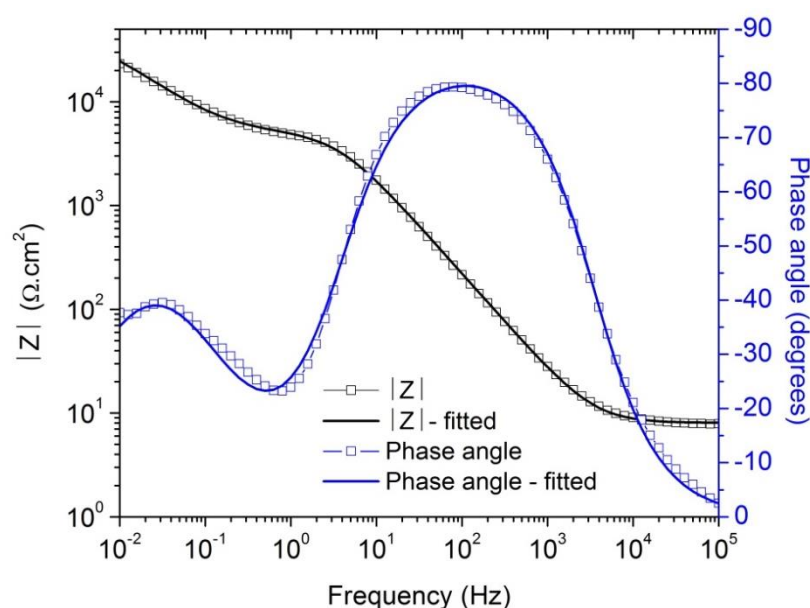
Figure 6.10 Bode plots of as-received MA after immersion in 0.6 M NaCl solution for 1 h showing good agreement between the raw data and the fitted results.

R_{ct} has considerable importance to the corrosion rate measurements and is used to characterise the corrosion resistance of the investigated samples. Figure 6.11 shows the evolution of R_{ct} with immersion time up to 24 h for the MA before and after excimer LSM. The R_{ct} of the as-received sample decreases with increasing immersion time, indicating that the corrosion resistance decreases with the increase of immersion time due to the aggravated pitting corrosion. Throughout the immersion in the solution up to 24 h, the R_{ct} values of the laser-melted samples are

higher than those of the as-received sample, although the laser-melted samples are also subjected to the decrease of the R_{ct} with increasing immersion time. This suggests that the corrosion resistance of the MA is improved by excimer LSM. From Figure 6.11, it is implied that the corrosion resistance of the laser-melted samples treated at 7 J/cm^2 with different NOP initially follows the sequence: 10 P > 25 P > 40 P, due to increased porosity with increasing NOP, and then falls to similar values after 24 h immersion. It is notable that the laser-melted sample treated at 2 J/cm^2 with 20 P has a remarkably higher R_{ct} than all other samples throughout the immersion test, indicating the highest corrosion resistance among all investigated samples. It can be concluded that the rippled structure played an important role in corrosion initiation, covering up the effect of porosity after relative long immersion.
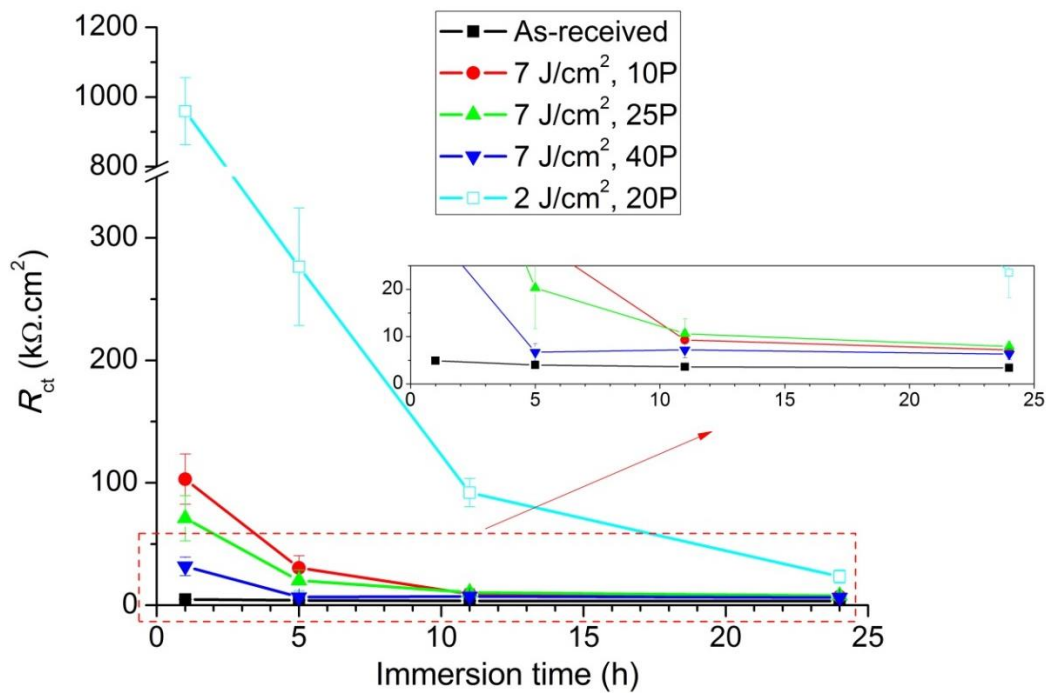

Figure 6.11 Evolution of R_{ct} with immersion time for the MA before and after excimer LSM under different conditions.

Figure 6.12 shows the evolution of Q_{dl} with immersion time up to 24 h. The increase of Q_{dl} with increasing immersion time for all the samples suggests increased corroded area or intensified absorption of chloride ions [12], being in accordance

with the decreasing corrosion resistance. The laser-melted sample treated at 2 J J/cm^2 with 20 P showed little increase in Q_{dl} after immersion for 24 h, suggesting that the sample corroded at very low corrosion rates. The results of EIS measurements are in agreement with that of potentiodynamic polarization.
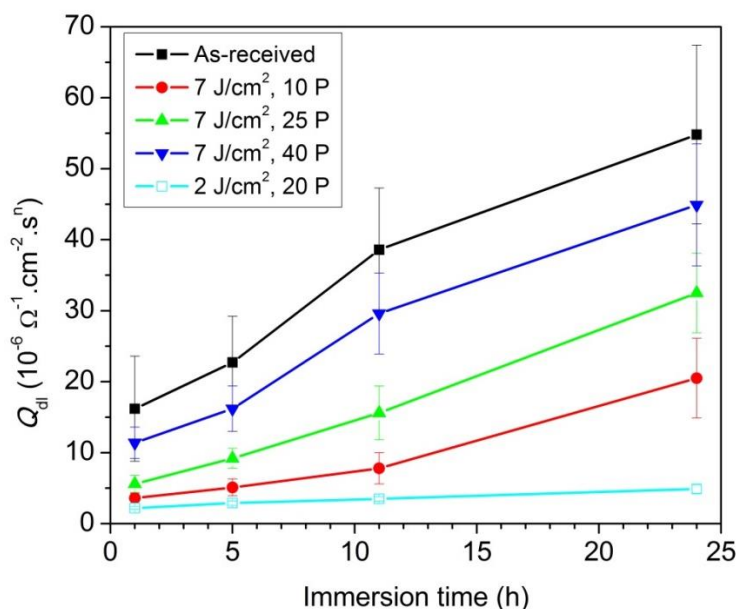
Figure 6.12 Evolution of Q_{dl} with immersion time for the MA before and after excimer LSM under different conditions.

6.3.4 Immersion test

Figure 6.13 presents the SEM micrographs showing the surface morphology of as-received and laser-melted MA after immersion in 0.6 M NaCl solution for 24 h. Large open pits are randomly distributed on the surface of as-received sample and a large amount of corrosion products accumulate at the open mouth of the pits (Figure 6.13(a)). Severe intergranular attack can be observed in Figure 6.13(b), revealing a number of ellipsoidal or round α-Al grains in the pit. The SEM micrograph of the cross-section of the as-received sample shows deep pitting attack with the depth more than 100 μm in Figure 6.14(a). The intergranular attack has propagated much deeper than the depth of the pit itself.
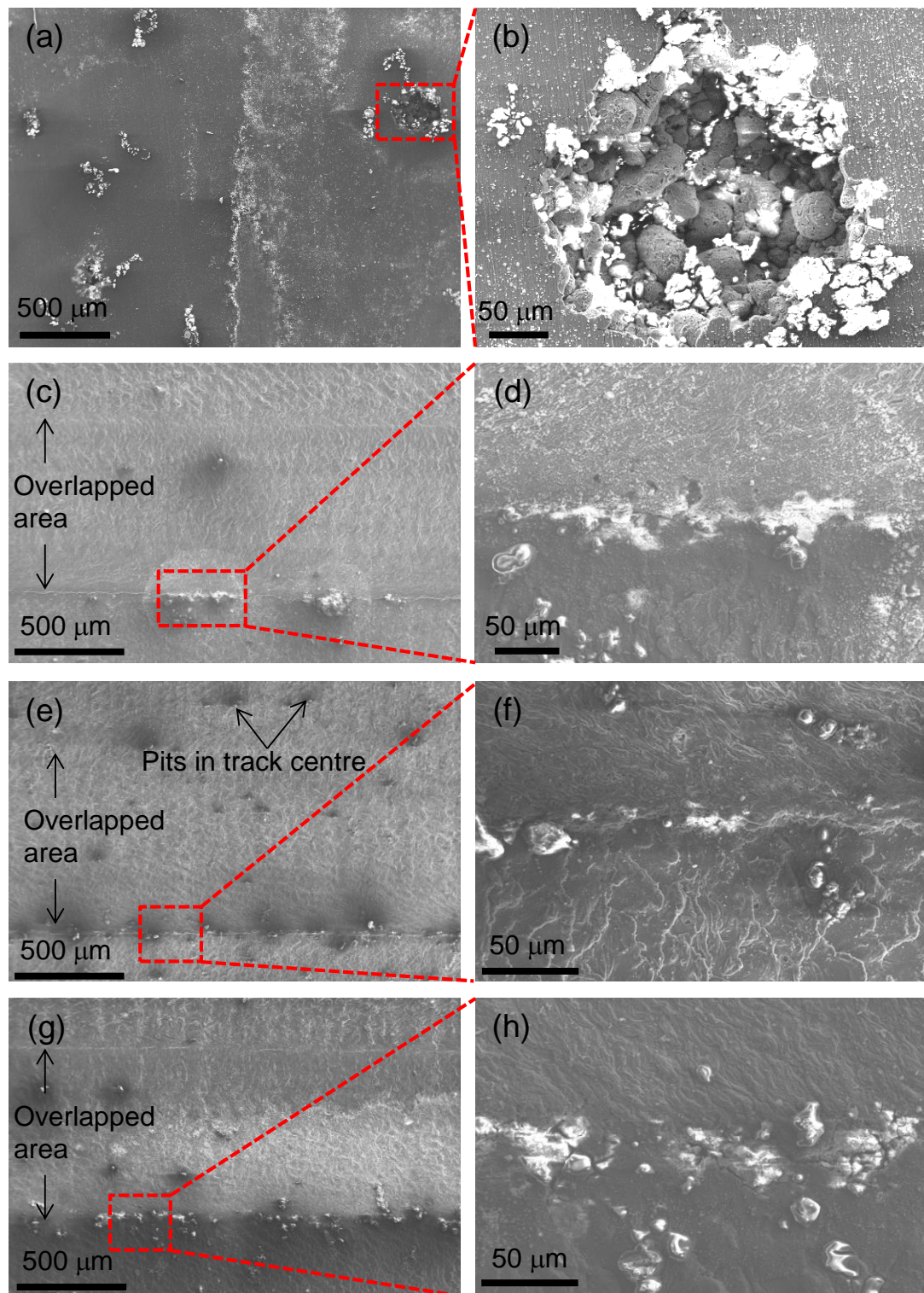
Figure 6.13 SE-SEM micrographs showing the surface morphology of as-received and laser-melted MA after immersion in 0.6 M NaCl solution for 24 h: (a)-(b) as-received; (c)-(d) 7 J/cm^2, 10 P; (e)-(f) 7 J/cm^2, 25 P; (g)-(h) 7 J/cm^2, 40 P; and (i)-(j) 2 J/cm^2, 20 P.
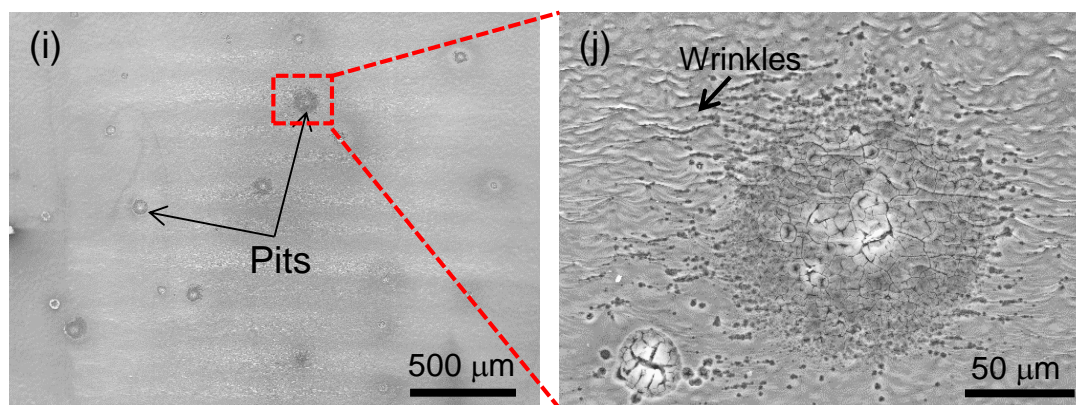
Figure 6.13 Continued.

Figures 6.13(c)-(h) show the corroded surface morphology of the laser-melted MA treated with the laser fluence of 7 J/cm^2. There are no visible open pits observed on the corroded surface and the corrosion products on the surface are reduced compared with the as-received sample. The pits are randomly distributed on the corroded surface but much more concentrated at the interface between the overlapped area and the re-heated area, which is shown in Figures 6.13(d), 6.13(f) and 6.13(h) for the samples treated with 10 P, 25 P, and 40 P, respectively. The interface between the overlapped area and the re-heated area is more likely to be attacked because of a highly porous microstructure as shown in Figure 5.16. This is in agreement with Viejo et al. [8], who revealed intensified corrosion attack associated with the porosity in the overlapped area of excimer laser-melted AA2050-T8 aluminium alloy. The trend of increasing corrosion attack is revealed with the increase of the NOP from 10 to 40. The corresponding cross-sectional morphology of the corroded samples is shown in Figures 6.14(b)-(g). Corrosion attack of the melted layers is observed in Figures 6.14(b), 6.14(d) and 6.14(f) and no deep pits are revealed. However, delamination of the melted layers is indicated, where the attack of the melted layers seems to be prevented when the chloride solution penetrates the melted layer but the whole melted layer is delaminated from the underlying substrate, as shown in Figures 6.14(c), 6.14(e) and 6.14(g). Viejo et al. [8] and Yuan et al. [13] firstly reported such delamination for excimer laser-melted AA2050 aluminium alloy

and AA2024 aluminium alloy, respectively, during immersion tests in EXCO solution. Padovani et al. later reported the delamination of the melted layer for excimer laser-melted AA7449 welds [5] and AA2024 welds [1] in 0.1 M NaCl solution. This phenomenon is attributed to the presence of solute-rich segregation bands at the bottom of the melted layer [1, 5, 6, 8, 13], i.e. Cu-rich segregation bands in current work. The underlying substrates are attacked along the grain boundaries but the attacking depth is significantly reduced compared with the as-received sample.

The intergranular attack in both as-received and laser-melted MA is resulted from the electrochemical heterogeneity of the grain boundaries. As discussed in Chapter 4, the grain boundaries of the MA are precipitated with a large number of intermetallic particles and Mg segregation. The precipitation of intermetallic particles cathodic to Al matrix, e.g. AlCuMnFe(Si)-containing particles, makes the adjacent matrix act as an anode, which could be dissolved during immersion in chloride media. The Mg segregation to the grain boundaries results in the anodic nature of the grain boundaries themselves compared with the grains and thus the grain boundaries is subjected to preferential dissolution during corrosion attack. Take the as-received sample for example, both types of intergranular attack is indicated in Figure 6.15.

The corroded surface of the laser-melted sample treated with the laser fluence of 2 J/cm^2 is rather clean but with a few small pits observed on the surface. There is almost no corrosion product accumulation on the surface after immersion in 0.6 M NaCl solution for 24 h as shown in Figure 6.13(i). Closer examination of the pitted sites indicates that the pitting attack is associated with the wrinkles on the surface (Figure 6.13(j)), which is in agreement with the observation after potentiodynamic polarization. The cross-sectional examination reveals shallow pits with the depth less than 20 μm as shown in Figure 6.14(h). Although the pit depth exceeds the thickness of the melted layer, no delamination of the melted layer is indicated for the sample treated with the laser fluence of 2 J/cm^2. Without the delamination phenomenon, the

melted layer formed with the laser fluence of 2 J/cm^2 could provide better protection to the substrate than that formed with the laser fluence of 7 J/cm^2.

Figure 6.14 BSE-SEM micrographs showing the cross-sectional morphology of as-received and laser-melted MA after immersion in 0.6 M NaCl solution for 24 h: (a) as-received; (b)-(c) 7 J/cm^2, 10 P; (d)-(e) 7 J/cm^2, 25 P; (f)-(g) 7 J/cm^2, 40 P; and (h) 2 J/cm^2, 20 P.
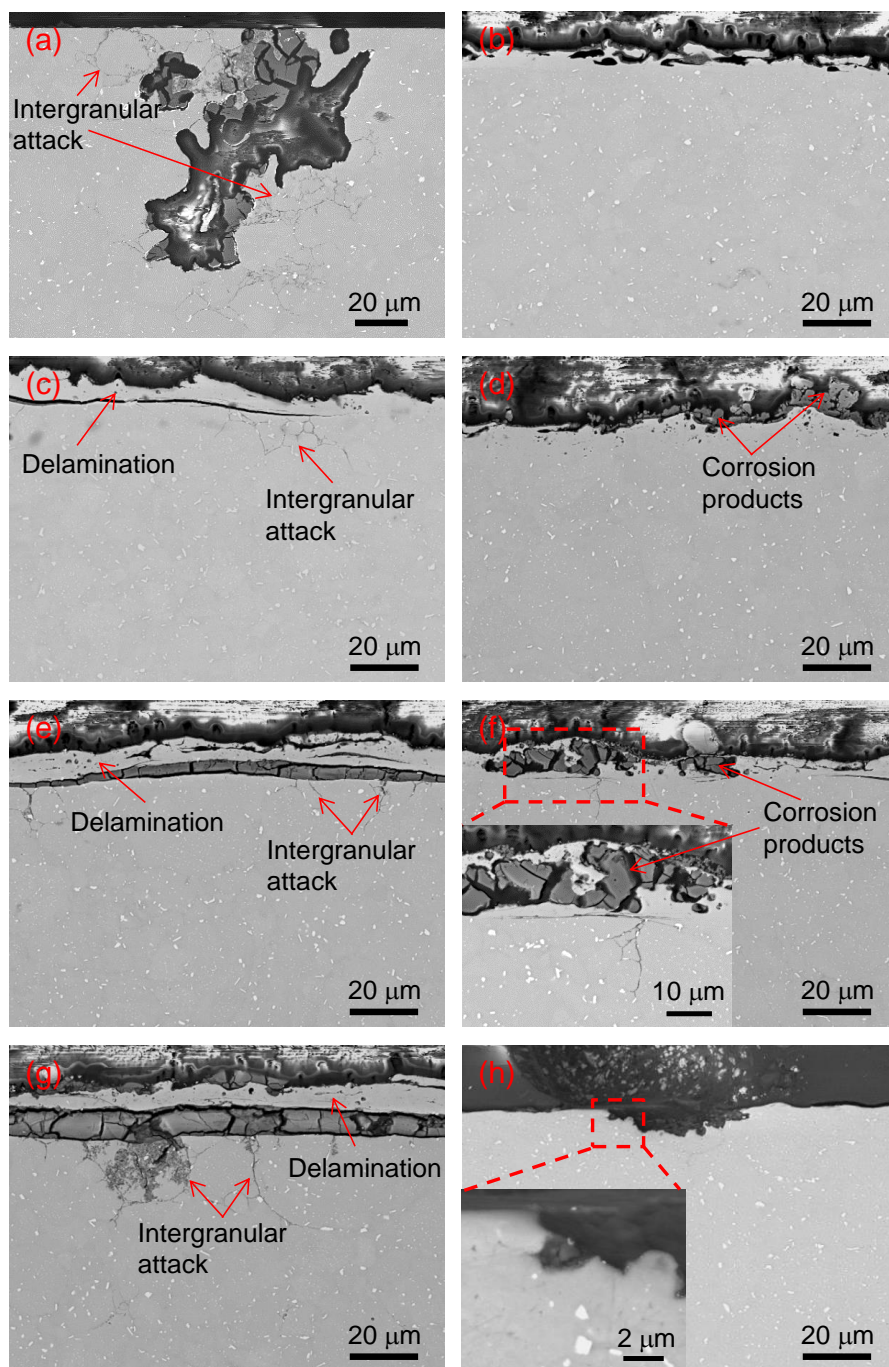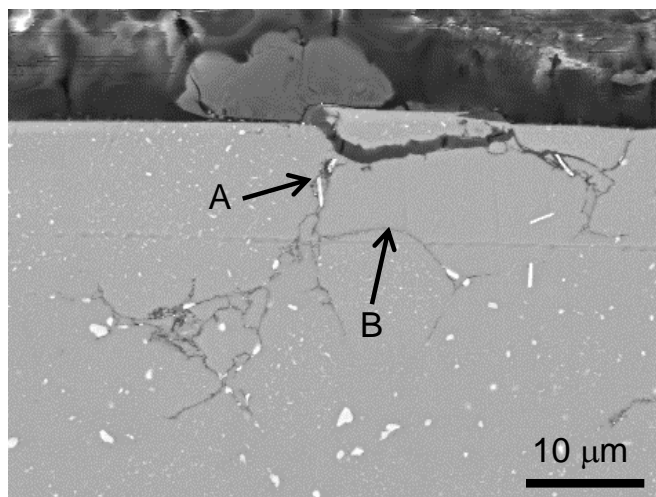
Figure 6.15 BSE-SEM micrograph showing the intergranular attack in as-received MA after immersion in 0.6 M NaCl solution for 24 h. Site A indicates the intergranular attack caused by the cathodic intermetallic particles at the grain boundaries. Site B indicates the preferential dissolution of the anodic grain boundaries due to the Mg segregation to the grain boundaries.

Regarding the delamination of the melted layer formed with the laser fluence of 7 J/cm^2, the corrosion mechanism of the laser-melted MA is proposed for better understanding of the phenomenon. It has been demonstrated that the corrosion initiation is associated with the micro-pores and micro-crevices caused by the formation of the rippled structure. Therefore, the first step could be pitting or crevice corrosion initiated in the micro-pores and micro-crevices as shown in Figure 6.16(a). With longer immersion time, the dissolution of the melted layer could result in the exposure of the Cu-rich segregation bands to the chloride solution. Some micro-pores intersected with the Cu-rich segregation bands in Figure 5.14 also cause easy contact between the Cu-rich segregation bands and the chloride solution, which results in the formation of galvanic cells between the Cu-rich segregation bands and Al matrix. The Cu-rich segregation bands could act as an effective cathode and the adjacent as the anode [7], promoting the corrosion at the interface of the melted layer and the substrate, as schematically shown in Figure 6.16(b). The corrosion tends to propagate laterally and delamination of the melted layer could occur. The important
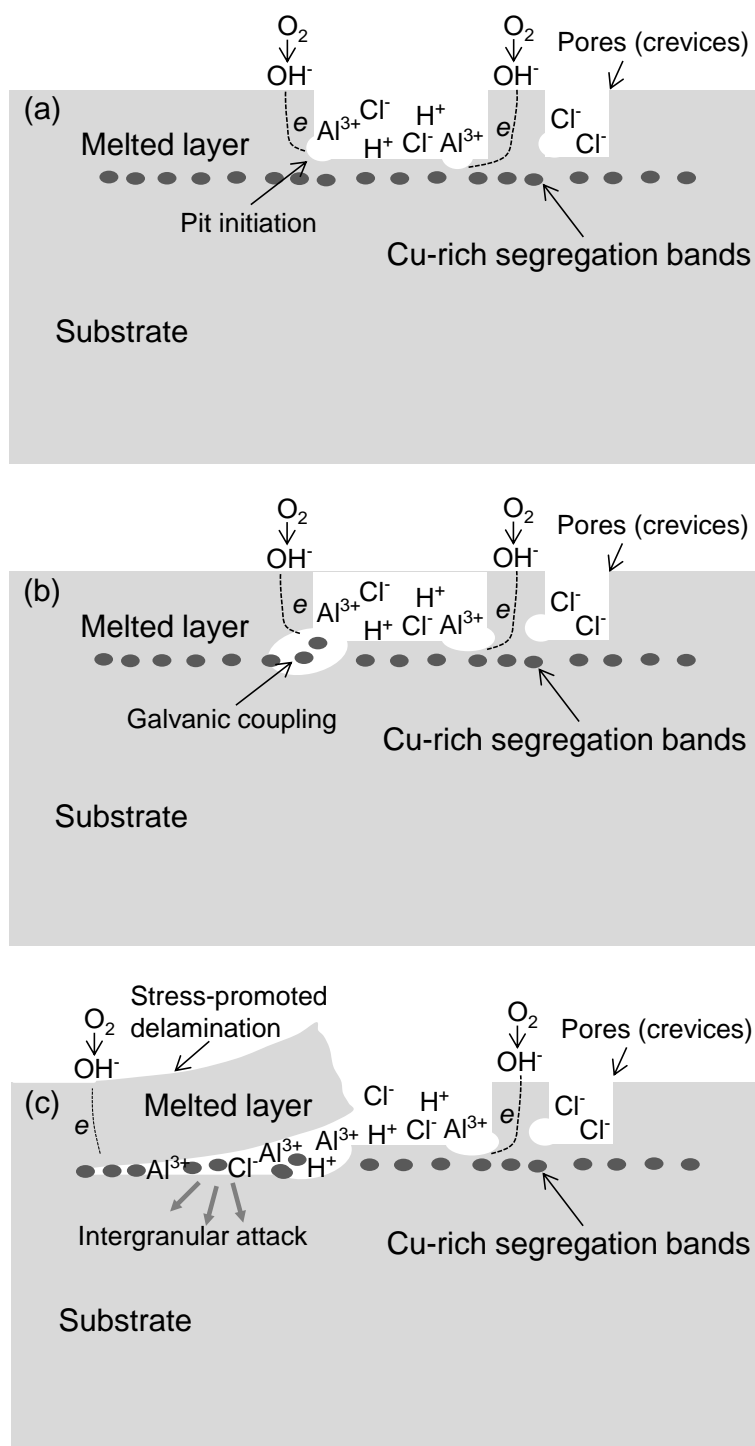
Figure 6.16 Schematic of the corrosion mechanism of laser-melted MA: (a) pit initiation; (b) galvanic corrosion at the Cu-rich segregation bands; and (c) stress-promoted delamination of the melted layer. The cathodic reaction indicated in the schematic is the reduction of oxygen: $O_2 + 2H_2O + 4e = 4OH^-$. The anodic reaction is the dissolution of aluminium: $Al - 3e = Al^{3+}$.

factors facilitating the delamination of the melted layer could be the tensile residual stress induced by excimer LSM, which was reported previously [13]. At the same time, corrosion attack propagates into the substrate in the form of severe intergranular corrosion as shown in Figure 6.16(c). The absence of the delamination of the melted layer for the sample treated at the laser fluence of 2 J/cm^2 may be related to different degree of residual stress, which needs further investigation.

6.4 Corrosion performance of excimer laser-melted MMC

6.4.1 Open circuit potential
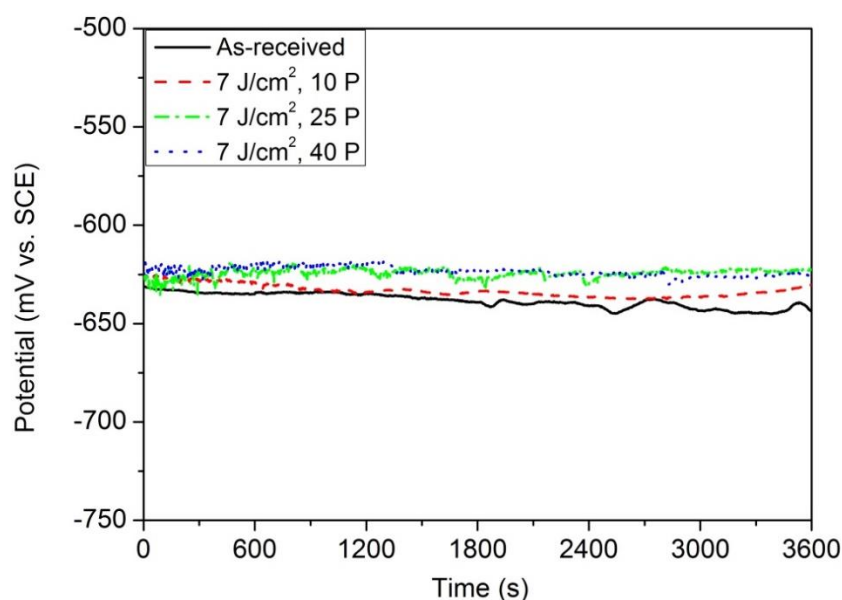
Figure 6.17 Evolution of the OCP of as-received and laser-melted MMC in naturally aerated 0.6 M NaCl solution.

Figure 6.17 presents the OCP evolution of the MMC before and after excimer LSM in 0.6 M NaCl solution. All samples remain at steady OCPs during immersion for 1 h. The steady OCP values of the laser-melted MMC are slightly higher than that of the as-received MMC, which is in agreement with Yue at al. [14]. However, it is difficult to interpret the change in OCP after excimer LSM because the OCP can be affected by many factors, such as the removal of SiC particles, the Si and C resulted

from the decomposition of SiC particles and the oxidation of the alloying elements. The increase in OCP is resulted from the combined effect of these factors.

6.4.2 Potentiodynamic polarization

The potentiodynamic polarization curves of as-received and laser-melted MMC are shown in Figure 6.18, which shows that the polarization curves shift to the upper left after excimer LSM compared with the as-received MMC. The shift of corrosion potential (E_{corr}) is in line with the changes of OCP after excimer LSM. The corrosion current density (i_{corr}) is significantly reduced according to the curves and the values of i_{corr} obtained from the curves are listed in Table 6.3. The samples treated with the NOP of 10, 25 and 40 exhibit much smaller i_{corr} values, which were reduced to about 1/5, 1/7 and 1/6 of the i_{corr} of the as-received sample, indicating the improvement of corrosion performance of the MMC after excimer LSM. Among the three conditions, the sample treated with 25 P shows best corrosion performance as indicated by the lowest corrosion current density.
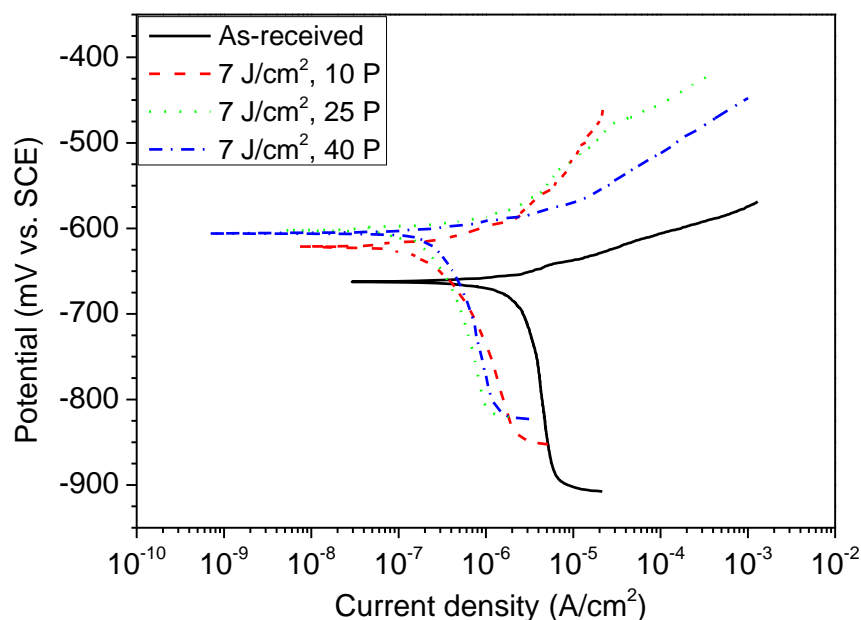
Figure 6.18 Potentiodynamic polarization curves of as-received and laser-melted MMC in naturally aerated 0.6 M NaCl solution.

Table 6.3 Average electrochemical parameters interpreted from the polarization curves of three measurements of as-received and laser-melted MMC.

	E_{corr} (mV vs. SCE)	i_{corr} (μA/cm^2)
As-received	-655±16	1.84±0.85
7 J/cm^2, 10 P	-620±5	0.37±0.09
7 J/cm^2, 25 P	-609±5	0.26±0.01
7 J/cm^2, 40 P	-599±12	0.29±0.07
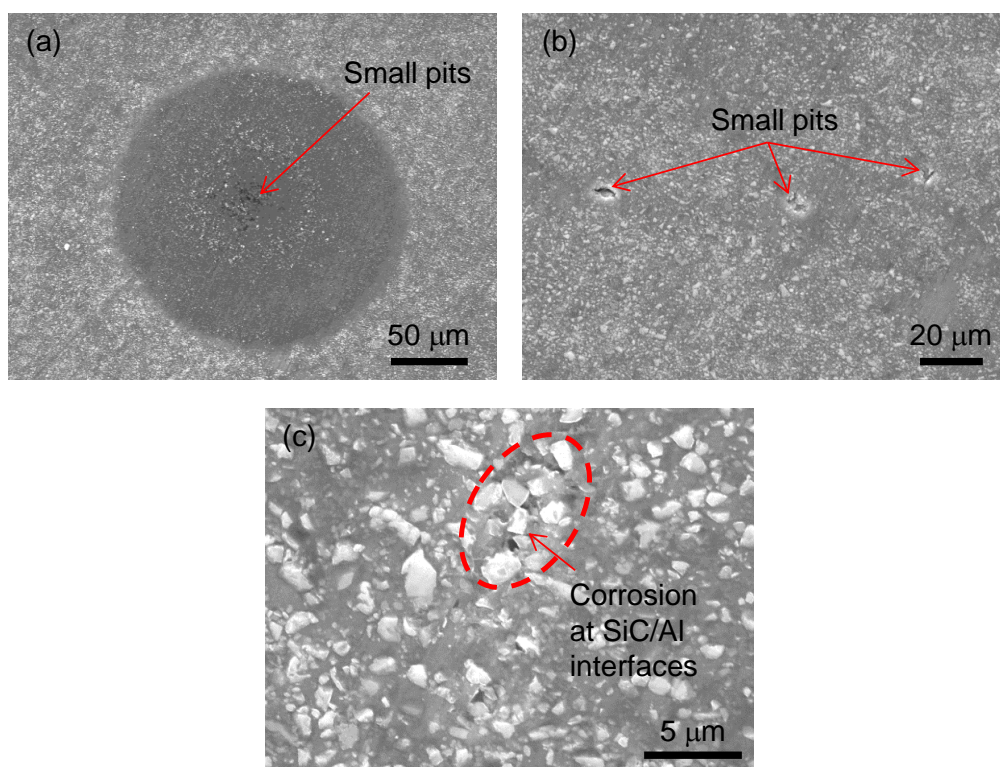
Figure 6.19 SEM micrographs showing the pit initiation of as-received MMC after potentiodynamic polarization.

Figure 6.19(a) shows a pit initiated during potentiodynamic polarization. It is formed with a central pitted area and a concentric ring with reduced corrosion. Figure 6.19(b) shows a few small pits in as-received MMC. Closer examination indicates the occurrence of the dissolution of matrix alloy at the SiC/Al interfacial regions, as shown in Figure 6.19(c). This is in accordance with the results in Chapter 4, which concluded that the corrosion initiated at the Al$_2$Cu intermetallic particles in the

SiC/Al interfacial regions. The improvement of corrosion resistance of the MMCs after excimer LSM could be attributed to the dissolution of the Al_2Cu phases, as well as other intermetallics, and the reduction of SiC/Al interfaces. Similar conclusions have been drawn by Yue et al. [14] and Zhang et al. [15].
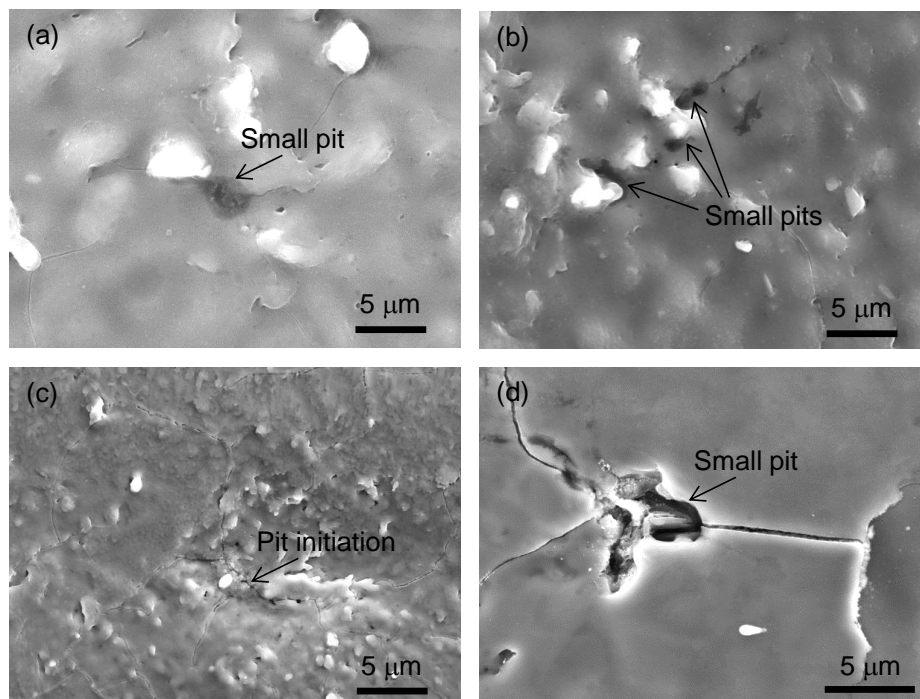
Figure 6.20 SEM micrographs showing the pit initiation of laser-melted MMC after potentiodynamic polarization: (a)-(b) 10 P, (c) 25 P and (d) 40 P.

Figure 6.20 shows two typical corroded morphologies of the laser-melted MMC after potentiodynamic polarization. Figures 6.20(a) and 6.20(b) show the corrosion initiation in the matrix around the SiC remnants (bright particles) in the sample treated with 10 P. As shown in Figure 5.39, the SiC decomposing area could be inhomogeneous due to the incomplete dispersion of Si, which could result in the formation of galvanic cells between Si and Al. The incomplete dispersed Si could act as the cathode and the Al matrix as the anode, leading to the preferential dissolution of the matrix around the SiC remnants. Figures 6.20(c) and 6.20(d) show the pits initiated at the cracks on the laser-melted surface treated with 25 P and 40 P, respectively. This indicates that apart from the corrosion initiation around the SiC

remnants, another corrosion mechanism related to the cracking is also revealed. This could explain the increase of corrosion resistance by increasing the NOP from 10 to 25; and then the decrease of corrosion resistance by further increasing the NOP from 25 to 40. The reduced SiC remnants and the averted networks of cracking give rise to the best corrosion performance of the laser-melted sample treated with 25 P.

6.4.3 Electrochemical impedance spectroscopy

Figures 6.21-6.24 show the Nyquist plots of the EIS responses for the MMCs before and after LSM during the immersion in 0.6 M NaCl solution up to 24 h. The Nyquist plots for all the samples at all soaking time are characterized by a capacitive loop at high-medium frequencies and another capacitive loop or a diffusion tail at low frequencies. This means that the MMC samples exhibited similar corrosion behaviour to the MA samples and can be fitted using the same equivalent circuit as shown in Figure 6.9.
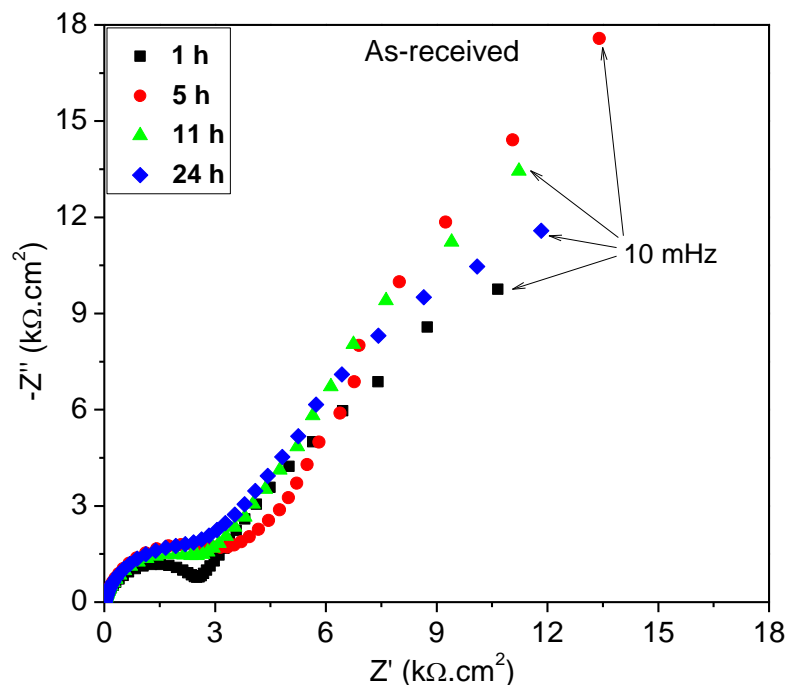
Figure 6.21 Nyquist plots of the EIS responses of as-received MMC up to 24 h during immersion in 0.6 M NaCl solution.

Figure 6.22 Nyquist plots of the EIS responses of laser-melted MMC (7 J/cm^2, 10 P) up to 24 h during immersion in 0.6 M NaCl solution.

Figure 6.23 Nyquist plots of the EIS responses of laser-melted MMC (7 J/cm^2, 25 P) up to 24 h during immersion in 0.6 M NaCl solution.
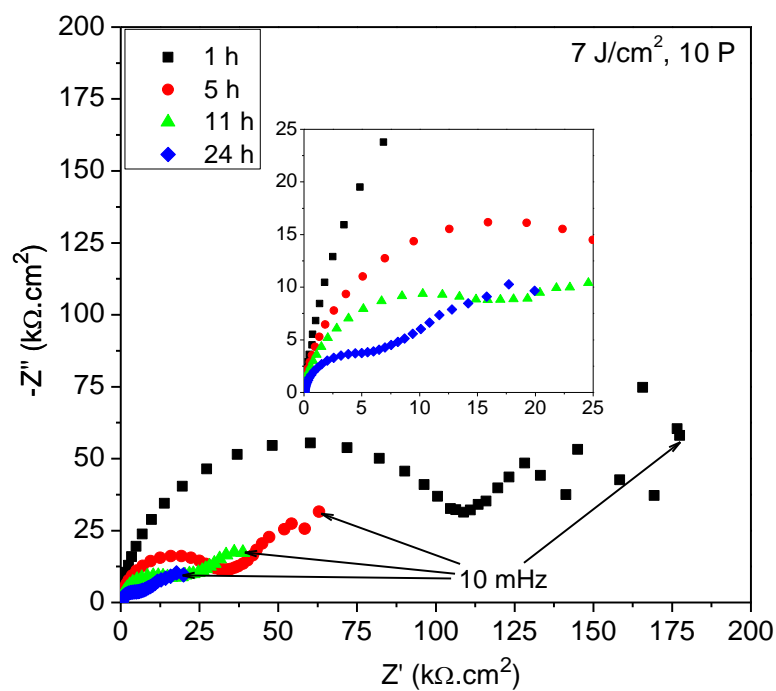
Figure 6.24 Nyquist plots of the EIS responses of laser-melted MMC (7 J/cm^2, 40 P) up to 24 h during immersion in 0.6 M NaCl solution.
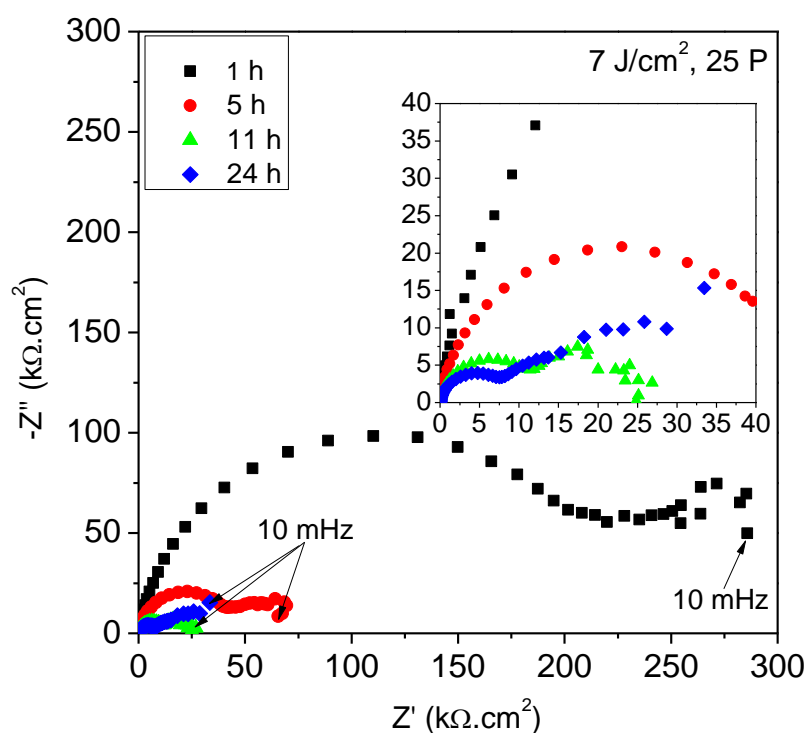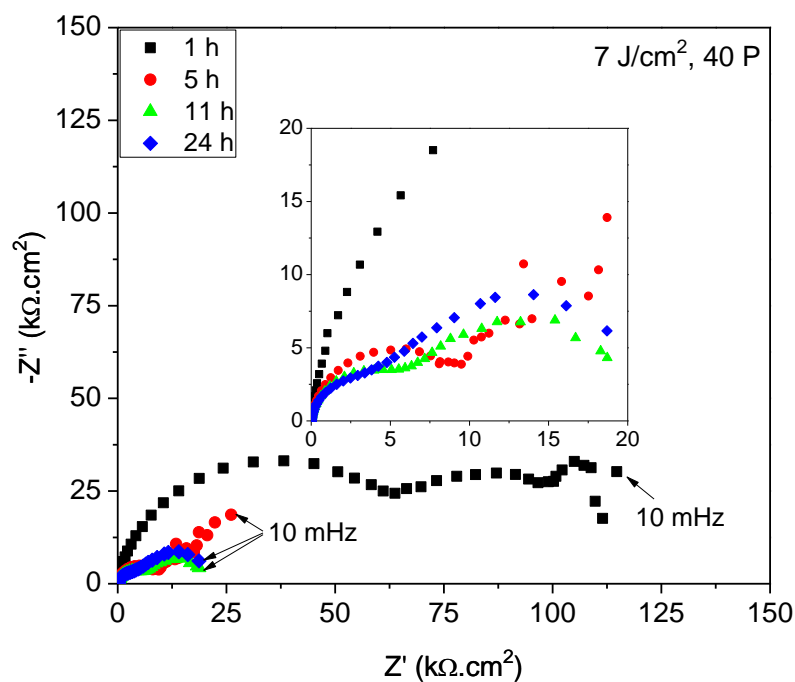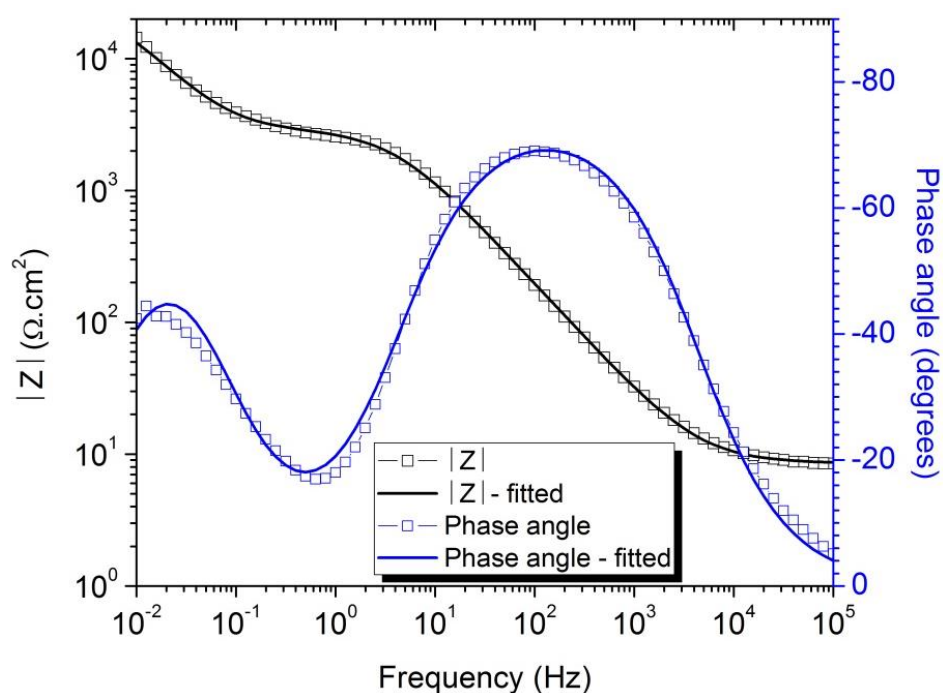

Figure 6.25 Bode plots of as-received MMC after immersion in 0.6 M NaCl solution for 1 h showing good agreement between the raw data and the fitted results.

The complete fitting results for EIS spectra in Figures 6.21-6.24 are listed in Appendix B. The simulated data are in good agreement with the experimental data, indicated by the small χ^2 in the range of 10^{-4}-10^{-3}. Figure 6.25 shows the good agreement between the experimental results and the fitted results for both the modulus of impedance and phase angle with frequency. The scatter of the results obtained from three measurements for each condition is less than 30% for the R_{ct} and Q_{dl}. However, the Q_w and R_w exhibit large variations in the three measurements due to the fact that they are related to the diffusion process of the chloride and aluminium ions as mentioned before.

Figure 6.26 show the evolution of R_{ct} and Q_{dl} with immersion time up to 24 h for the MMC before and after excimer LSM. The R_{ct} of the as-received sample slightly increases after immersion for 24 h. The increase of R_{ct} is an indication for the formation of corrosion product covering the sample surface, which is supported by the corresponding increase of Q_{dl} with increasing immersion time. The R_{ct} of the laser-melted samples decreases with increasing immersion time, suggesting the decrease of corrosion resistance; correspondingly, the Q_{dl} of the laser-melted sample increases with the increase of immersion time as shown in Figure 6.26(b). However, the monotonic decreasing of R_{ct} implies that no dense corrosion product was formed on the surface of laser-melted samples during immersion. Throughout the immersion in the solution up to 24 h, the R_{ct} values of the laser-melted samples are higher than those of the as-received sample suggesting that the improvement of corrosion resistance by excimer LSM. After immersion for 1 h, the sample treated with 25 P shows the highest R_{ct}, followed by the sample treated with 10 P, and the lowest for the sample treated with 40 P. The sample treated with 25 P is likely to possess the highest corrosion resistance throughout the immersion test, which could be attributed to the formation of a more homogeneous surface without generating obvious networks of cracking.
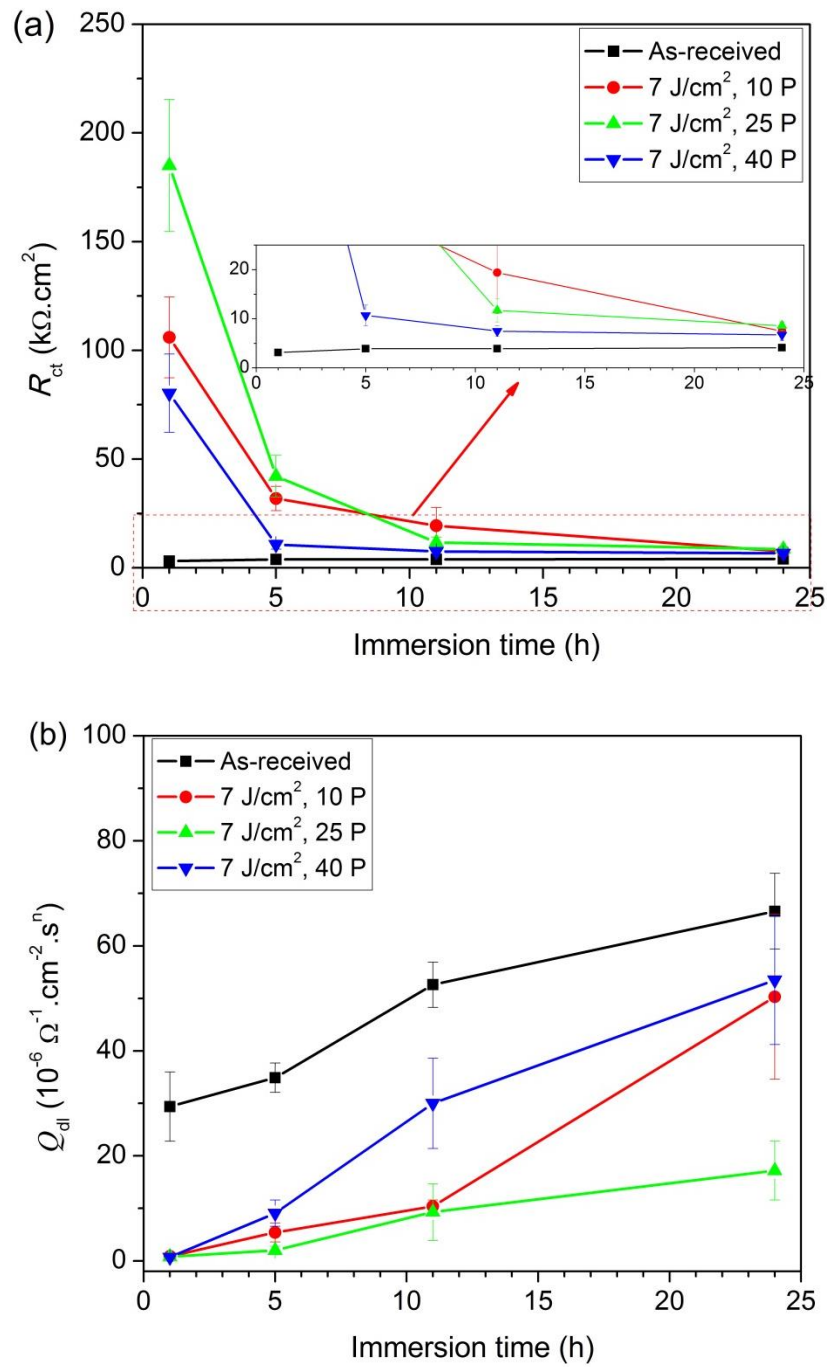
6.4.4 Immersion test

Figure 6.26 Evolution of (a) R_{ct} and (b) Q_{dl} with immersion time for the MMC before and after excimer LSM under different conditions.

Figure 6.27 shows the corroded surface morphology of as-received and laser-melted MMCs after immersion in 0.6 M NaCl solution for 24 h. The as-received sample

shows some open pits and the whole surface seems to be covered with corrosion products (Figure 6.27(a)). The observation is in agreement with speculation made from the R_{ct} evolution in EIS measurements. The corrosion is reduced for the laser-melted MMCs compared with the as-received sample as shown in Figures 6.27(b)-(d). Corrosion products are significantly reduced on the surface of laser-melted samples. Closer examination reveals the morphology in cracked blisters at the pitted area for all laser-melted samples as shown in Figure 6.28. The pitted sites of the samples treated with 10 P and 25 P are apparently associated with the fine SiC remnants on the surface, as indicated in Figure 6.28(a) and (b), respectively. As discussed in Chapter 5, the vicinity of SiC remnants could be rich in Si due to incomplete decomposition of SiC and incomplete dispersion of resultant free Si. The Si-rich phase could form galvanic couples with the Al matrix, resulting in the initiation of corrosion. This was verified by EDX elemental mapping analysis of the pitted areas. The distribution of elements in Figure 6.29 suggests high concentration of Si at the pitting sites. The oxygen distribution displayed in Figure 6.29(e) implies low concentration of oxygen, indicating no dense corrosion products were formed.

The SiC remnants were not observed on the surface treated with 40 P, but corrosion still initiated (Figure 6.28(c)). The dominant cracks spread over the surface could probably be the corrosion initiation sites. The EDX elemental mapping analysis (Figure 6.30) reveals reduced Si but increased O at the pitting sites, compared with the sample treated with 25 P. The reduction of Si is attributed to the enhanced dispersion effect when high NOP is applied. The increase of O is resulted from the formation of significant corrosion products. The pits are covered with cracked corrosion products as shown in Figure 6.28(c) indicating that the sample treated with 40 P was subjected to more severe corrosion attack than other laser-melted samples.

The observations suggest that, unlike the excimer laser-melted MA, the corrosion initiation in excimer laser-melted MMCs is not related to the morphological aspect but associated with the chemical segregation resulted from the incomplete dispersion

233

of Si, although the networks of cracking could lead to corrosion initiation. The different corrosion mechanisms for the excimer laser-melted MA and MMC are attributed to the different surface morphology and different degree of homogeneity in the melted layer.
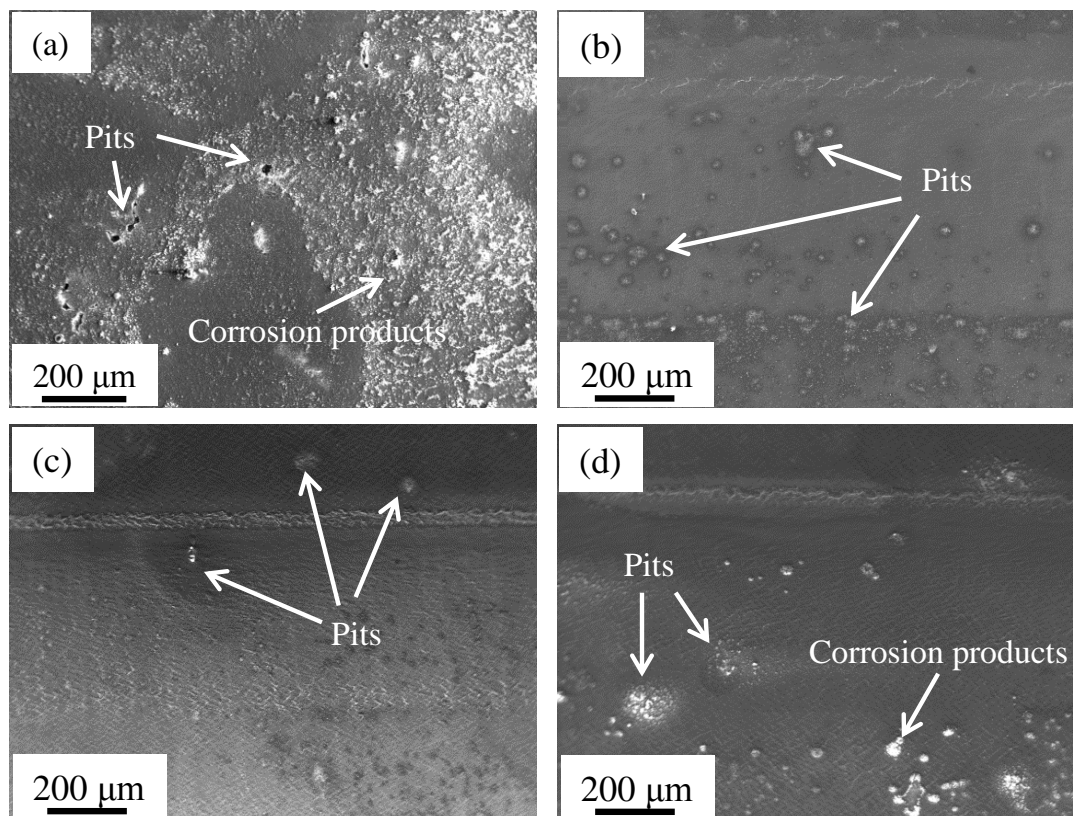
Figure 6.27 SEM micrographs of surface morphology of the MMC after immersion in 0.6 M NaCl for 24 h: (a) as-received; (b) 7 J/cm^2, 10P; (c) 7 J/cm^2, 25P; and (d) 7 J/cm^2, 40P.

Cross-section examination revealed deep pits with significant accumulation of corrosion products in the as-received sample, while the pits in the laser-melted samples were typically confined within the melted layer after immersion for 24 h (Figure 6.31). The excimer LSM effectively stopped the corrosive media from attacking the bulk material during the immersion tests.
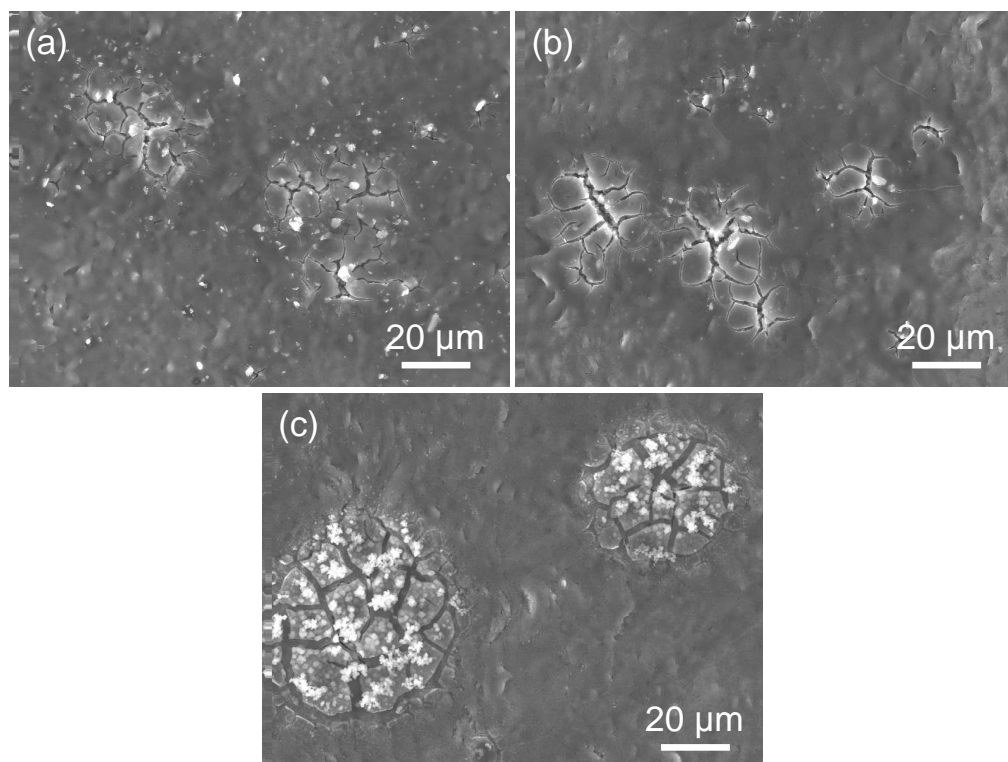
Figure 6.28 SEM micrographs showing the morphology of the pitted area of the laser-melted MMC: (a) 7 J/cm^2, 10P; (b) 7 J/cm^2, 25P; and (c) 7 J/cm^2, 40P.
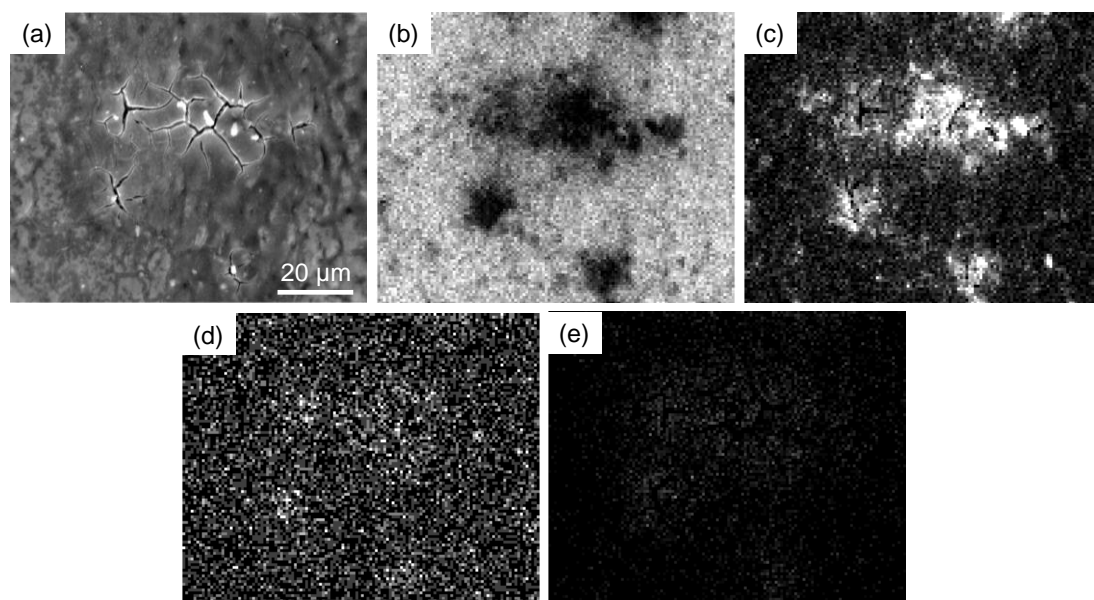
Figure 6.29 Distribution of elements at the pitted areas of the sample treated with 25 P obtained by EDX elemental mapping analysis: (a) SE-SEM micrograph; and individual map of (b) Al; (c) Si; (d) Cu; and (e) O.
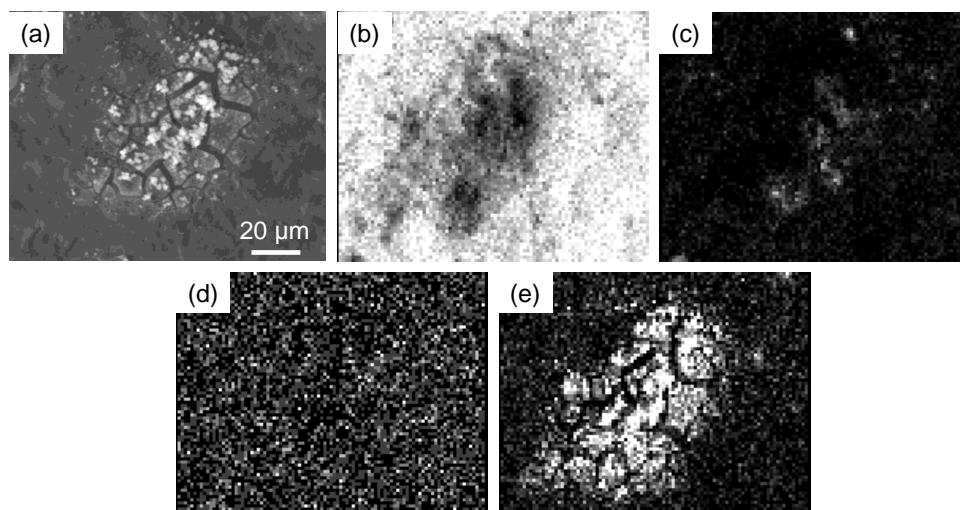
Figure 6.30 Distribution of elements at the pitted areas of the sample treated with 40 P obtained by EDX elemental mapping analysis: (a) SE-SEM micrograph; and individual map of (b) Al; (c) Si; (d) Cu; and (e) O.
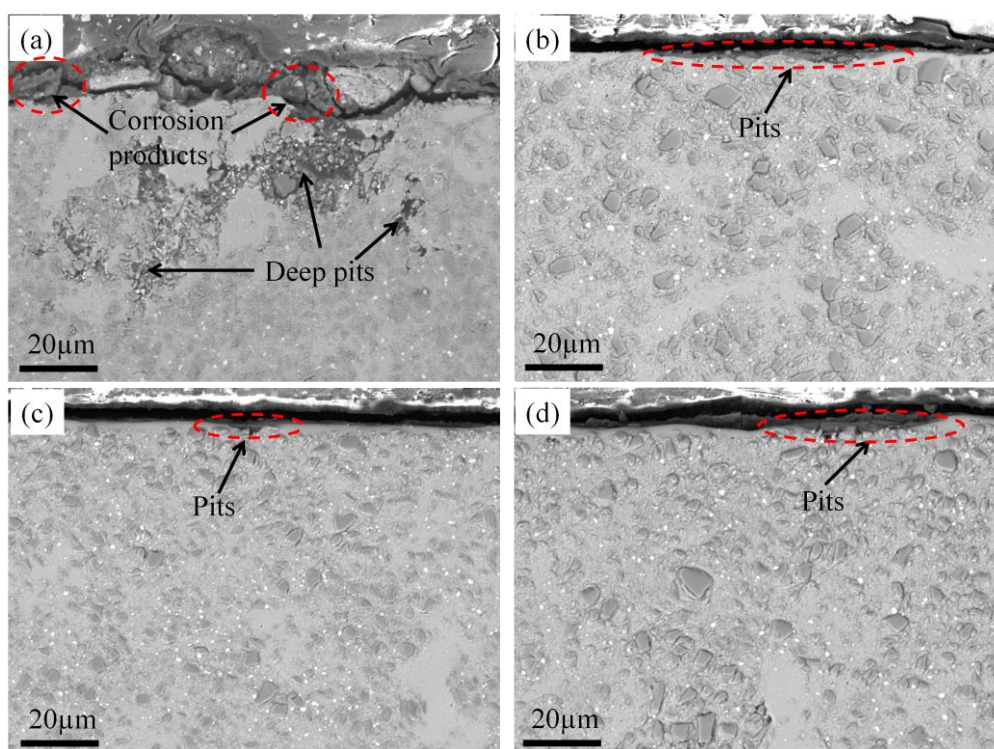
Figure 6.31 SEM micrographs of cross-sections of the corroded MMCs after immersion in 0.6 M NaCl for 24 h: (a) as-received; (b) 7 J/cm^2, 10P; (c) 7 J/cm^2, 25P; and (d) 7 J/cm^2, 40P.

6.5 Summary

The corrosion behaviour of the excimer laser-melted MA and MMC has been studied by comparison with the as-received materials in this Chapter. Improvement of corrosion performance by excimer LSM is revealed for both materials.

After excimer LSM, the corrosion resistance of MA is in the following sequence:

2 J/cm^2, 20P > 7 J/cm^2, 10P > 7 J/cm^2, 25P > 7 J/cm^2, 40P > as-received sample.

The improvement of corrosion resistance after excimer LSM is due to the dissolution of intermetallics and homogeneous distribution of alloying elements in the melted layer. For the samples treated with 7 J/cm^2, the corrosion initiation is governed by the rippled structure and the corrosion resistance can be reduced by increasing NOP. The failure of the melted layer is related to the final delamination of the melted layer. The corrosion resistance of the sample treated with 2 J/cm^2 is greatly improved compared with the as-received sample as a result of a homogeneous surface without the formation of significant ripples.

For the MMC, corrosion evaluation suggests that the MMC treated with 25 P exhibits the highest corrosion resistance among the laser-melted samples. The improvement of corrosion resistance of the MMC after excimer LSM is attributed to the dissolution of intermetallics, reduction/elimination of SiC/Al interfaces and the related porosity, reducing the active sites for localized corrosion. Insufficient NOP (10 P) causes the enrichment of Si around the SiC remnants, being the dominant mechanism for corrosion initiation. Excessive NOP (40 P) gives rise to the networks of cracking that resulted in corrosion initiation at the cracks.

References

[1]   C. Padovani, A.J. Davenport, B.J. Connolly, S.W. Williams, E. Siggs, A. Groso, M. Stampanoni, *Corrosion protection of AA2024-T351 friction stir welds by laser surface melting with excimer laser*, Corrosion Engineering Science and Technology, 47 (2012), 188-202.

[2]   A. Boag, A.E. Hughes, A.M. Glenn, T.H. Muster, D. McCulloch, *Corrosion of AA2024-T3 Part I. Localised corrosion of isolated IM particles*, Corrosion Science, 53 (2011), 17-26.

[3]   G.O. Ilevbare, O. Schneider, R.G. Kelly, J.R. Scully, *In situ confocal laser scanning microscopy of AA 2024-T3 corrosion metrology - I. Localized corrosion of particles*, Journal of the Electrochemical Society, 151 (2004), B453-B464.

[4]   P. Leblanc, G.S. Frankel, *A study of corrosion and pitting initiation of AA2024-T3 using atomic force microscopy*, Journal of the Electrochemical Society, 149 (2002), B239-B247.

[5]   C. Padovani, A.J. Davenport, B.J. Connolly, S.W. Williams, E. Siggs, A. Groso, M. Stampanoni, *Corrosion protection of AA7449-T7951 friction stir welds by laser surface melting with an Excimer laser*, Corrosion Science, 53 (2011), 3956-3969.

[6]   P. Ryan, P.B. Prangnell, *Grain structure and homogeneity of pulsed laser treated surfaces on Al-aerospace alloys and FSWs*, Materials Science and Engineering a-Structural Materials Properties Microstructure and Processing, 479 (2008), 65-75.

[7]   F. Viejo, A.E. Coy, F.J. Garcia-Garcia, M.C. Merino, Z. Liu, P. Skeldon, G.E. Thompson, *Enhanced performance of the AA2050-T8 aluminium alloy following excimer laser surface melting and anodising processes*, Thin Solid Films, 518 (2010), 2722-2731.

[8]   F. Viejo, A.E. Coy, F.J. Garcia-Garcia, Z.L.P. Skeldon, G.E. Thompson, *Relationship between microstructure and corrosion performance of AA2050-T8 aluminium alloy after excimer laser surface melting*, Corrosion Science, 52 (2010), 2179-2187.

[9]   B.S. Yilbas, M. Khaled, C. Karatas, *Corrosion Properties and Morphology of Laser Melted Aluminum Alloy 8022 Surface*, Journal of Materials Engineering and Performance, 18 (2009), 1-7.

[10]   E.S.M. Sherif, H.R. Ammar, K.A. Khalil, *Effects of copper and titanium on the corrosion behavior of newly fabricated nanocrystalline aluminum in natural seawater*, Applied Surface Science, 301 (2014), 142-148.

[11]   J.H. Chang, J. Park, Y.K. Pak, J.J. Pak, *Fitting improvement using a new electrical circuit model for the electrode-electrolyte interface*, 2007 3rd International IEEE/EMBS Conference on Neural Engineering, Vols 1 and 2, (2007), 572-574.

[12]   J.A. Moreto, C.E.B. Marino, W.W. Bose, L.A. Rocha, J. Fernandes, *SVET, SKP and EIS study of the corrosion behaviour of high strength Al and Al-Li alloys used in aircraft fabrication*, Corrosion Science, 84 (2014), 30-41.

[13]   Y. Yuan, Z. Aburas, T. Hashimoto, Z. Liu, P. Skeldon, G. Thompson, *Microstructure analysis and corrosion study of excimer laser modified AA2024-T351*, ECS Transactions, 11 (2008), 49-58.

[14]   T.M. Yue, S.M. Mei, K.C. Chan, H.C. Man, *The effect of excimer laser surface treatment on corrosion resistance of aluminium 2009/SiC$_w$ composite*, Materials Letters, 39 (1999), 274-279.

[15]   X.M. Zhang, H.C. Man, T.M. Yue, *Corrosion properties of excimer laser surface treated Al-SiC metal matrix composite*, Scripta Materialia, 35 (1996), 1095-1100.

Chapter 7 Main conclusions and future work

7.1 Conclusions

- *Effect of SiC on the microstructure and corrosion behaviour of the MMCs*

Microstructural characterization of AA2124-T4 aluminium alloy and SiC_p/AA2124-T4 MMCs has revealed that the addition of SiC particles significantly altered the microstructure of the matrix. The main intermetallics in the monolithic aluminium alloy include AlCuMnFe(Si)-containing phases and S (Al_2CuMg) phase, plus numerous fine dispersiods. The addition of SiC particles results in preferential precipitations, including θ (Al_2Cu) phase and Mg segregation, in the SiC/Al interfacial regions. The AlCuMnFe(Si)-containing phases in the MMCs are revealed with increased content of Si compared to those in the monolithic aluminium alloy, being due to the presence of SiC particles. The incorporation of submicrometre-sized SiC particles reduces the preferential precipitations in the SiC/Al interfacial regions, compared to the coarser micrometre-sized SiC particles.

The corrosion behaviour of the MMCs and the monolithic aluminium alloy has been evaluated in the 0.6 M NaCl solution. Potentiodynamic polarization and EIS measurements have revealed that the MMC reinforced with micrometre-sized SiC particles possesses corrosion resistance inferior to the monolithic aluminium alloy while the MMC reinforced with submicrometre-sized SiC particles close to the monolithic alloy. Examination of the corroded surfaces suggests different corrosion mechanisms for the MMCs and the monolithic aluminium alloy. The S phase and AlCuMnFe(Si)-containing intermetallics are preferential sites for corrosion initiation in the monolithic aluminium alloy; The intermetallics and Mg segregation at the grain boundaries facilitate the intergranular attack. On the contrary, the AlCuMnFe(Si)-containing intermetallics remains relative inert and the SiC/Al interfacial regions show high susceptibility to corrosion initiation due to the presence

of θ phase and Mg segregation in the MMCs. Therefore, the higher corrosion resistance of the MMC reinforced with submicrometre-sized SiC particles than that reinforced with micrometre-sized SiC particles is interpreted as a result of the reduction of precipitates in the SiC/Al interfacial regions, reducing the active sites for corrosion initiation.

- *Microstructure of the excimer laser-melted AA2124 aluminium alloy and MMC*

Microstructural refinement has been achieved for the monolithic aluminium alloy and the MMC by excimer LSM. Two laser operating parameters, i.e. laser fluence and NOP, show significant influence on the microstructures of the melted layer for both materials. High laser fluence contributes to the increase of the thickness of the melted layers and enhances solute dispersion in the melted layer. High NOP slightly increases the thickness of the melted layers and also improves the homogeneity of solutes dispersion, but results in high porosity for the monolithic aluminium alloy and networks of cracking for the MMC. The laser-melted aluminium alloy exhibits significant rippled structure, which can be reduced by reducing the laser fluence, whilst no significant rippled structure is formed for the MMC after excimer LSM.

Dissolution of intermetallic particles occurred during excimer LSM and a homogeneous melted layer with complete dispersion of solute atoms could be formed for the monolithic aluminium alloy. For the MMC, removal of SiC particles occurs, apart from the dissolution of intermetallic particles. According to the modelling work, the high temperature on SiC particles results in the decomposition of SiC and evaporation of surrounding matrix and the decomposition products; the decomposition products can be trapped in the melted layer for form a Si- and C-rich melted layer.

The melted layer in the monolithic aluminium alloy is characterized with a homogeneous microstructure except the Cu-rich segregation bands concentrated at the bottom of the melted layer. The melted layer in the MMC can be divided into three regions, which involve the copper-rich segregation bands and $MgAl_2O_4$ spinel in the bottom region, Al-Si eutectic in the middle region, and microsegregation-free

structure in the top region, respectively. The formation of copper-rich segregation bands in both materials could be attributed to the oscillatory instability before the absolute stability was obtained during solidification. In the MMC, the oxidation of aluminium and magnesium at the bottom of the melted layer results in the formation of $MgAl_2O_4$ spinel. The decomposition of SiC provides significant amount of Si close to the eutectic composition, leading to growth of Al-Si eutectic in the MMC. The formation of the microsegregation-free microstructure in both materials is believed to be attributed to the fast cooling rates, enabling the solidification to proceed with absolute stability.

- *Corrosion behaviour of excimer laser-melted AA2124 aluminium alloy and MMC*

Improvement of corrosion performance by excimer LSM has been revealed in 0.6 M NaCl solution for both materials. For the monolithic aluminium alloy, the improvement of corrosion resistance after excimer LSM is believed to be due to the dissolution of intermetallics and homogeneous distribution of alloying elements in the melted layer. However, the corrosion behaviour of laser-melted aluminium alloys is significantly dependent on the surface morphology induced by excimer LSM. For the samples treated at the laser fluence of 7 J/cm^2, the corrosion initiation is associated with the rippled structure and the corrosion resistance can be reduced by increasing NOP from 10 to 40. The failure of the melted layer is related to the final delamination of the melted layer due to the presence of the Cu-rich segregation bands at the bottom of the melted layer. The corrosion resistance of the sample treated at the laser fluence of 2 J/cm^2 is greatly improved compared to those treated at the laser fluence of 7 J/cm^2, being due to the homogeneous surface without significant ripples.

For the MMC treated at the laser fluence of 7 J/cm^2, the improvement of corrosion resistance is attributed to the dissolution of intermetallics, reduction/elimination of SiC/Al interfaces and the related porosity. The MMC treated with 25 P exhibits the highest corrosion resistance among the laser-melted samples, being due to the

essentially reduced SiC particles on the surface without obvious cracking. Application of insufficient NOP (10 P) results in considerable remaining SiC particles on the surface. Around these partially decomposed SiC particles shows the enrichment of Si, which is the dominant mechanism for corrosion initiation of the laser-melted MMC. Networks of cracking arise when excessive NOP (40 P) is applied. The cracks are subjected to corrosion initiation during immersion test.

7.2 Suggestions for future work

From the results of current work, the following are suggested for future work.

- Considering the as-received AA2124-T4 aluminium alloy and MMCs, the MMCs exhibit finer grain sizes and grain boundaries. The amount of the precipitates on the grain boundaries also seems to be altered by the addition of SiC particles. It would be interesting to investigate the intergranular corrosion behaviour of these materials and thus to evaluate the effect of the SiC particles on the intergranular corrosion resistance of the MMCs.

- As the delamination of the melted layer leads to the failure of the melted layer in AA2124 aluminium alloy, it is very important to fully understand the mechanism for this phenomenon. It is attributed to the combined effect of the presence of Cu-rich segregation bands and the tensile stress induced by excimer LSM. However, the sample treated at the laser fluence of 2 J/cm^2 is free of delamination of the melted layer, providing a method to avoid this phenomenon. It gives a hint that different laser fluence might result in different degree of residual stress or deformation in the melted layer. Further investigation can be carried out to confirm these assumptions.

- In current work, considering the excimer laser-melted MMCs, the Si resulted from the decomposition of SiC is difficult to be fully dispersed in the melted layer since Si-rich decomposition sites have been observed even when applying 25 or

243

more laser pulses. However, application of high NOP results in cracking of the surface. Thus, the improvement of the corrosion resistance is limited. Some initial work has been done and shows that the crack-free surface can be recovered by a re-scan at low laser fluence. Also, the re-scan could further enhance the solute dispersion in the melted layer. It could be very interesting work to evaluate the corrosion performance of the laser-melted MMCs treated under such conditions.

• Due to the presence of SiC reinforcement, the conventional protection methods have been reported to be less effective for the MMCs than the monolithic aluminium alloys, as indicated in the literature review. Therefore, by removing the SiC particles exposed on the surface, excimer LSM could potentially find applications as a pre-treatment before carrying out the conventional surface treatment, such as anodising and chemical conversion coatings.

Appendix A

Average fitting values from the EIS spectra of as-received and laser-melted MAs.

t (h)	R_s ($\Omega.cm^2$)	R_{ct} ($k\Omega.cm^2$)	Q_{dl} (10^{-6}) ($\Omega^{-1}.cm^{-2}.s^n$) (n_1)	R_w ($k\Omega.cm^2$)	Q_w (10^{-6}) ($\Omega^{-1}.cm^{-2}.s^n$) (n_1)
	As-received				
1	8.4±0.3	4.9±0.3	16.2±7.4 (0.92±0.02)	45.2±9	404±114 (0.8±0.04)
5	8.1±0.02	4±0.2	22.7±6.5 (0.94±0.02)	63.8±20	537±118 (0.8±0.11)
11	8.2±0.02	3.6±0.3	38.6±8.7 (0.92±0.01)	96.2±27.3	735±137 (0.78±0.08)
24	8±0.03	3.4±0.4	54.8±12.6 (0.92±0.02)	89.2±33.3	603±98 (0.7±0.04)
	7 J/cm², 10 P				
1	10.3±0.2	103±20.6	3.6±0.7 (0.94±0.01)	385±85	18.6±5.9 (0.89±0.03)
5	10.4±0.1	30.5±10	5.1±1.2 (0.93±0.01)	156.2±38.3	98.3±20.4 (0.82±0.02)
11	10.5±0.1	9.3±2.1	7.8±2.2 (0.93±0.01)	183.9±45.6	395±72 (0.8±0.04)
24	10.2±0.2	7.2±0.9	20.5±5.6 (0.92±0.02)	144.6±30.7	325±54 (0.75±0.09)
	7 J/cm², 25 P				
1	10.5±0.3	71±18.5	5.6±1.2 (0.95±0.01)	213±56.6	36.5±9.3 (0.85±0.07)
5	10.6±0.3	20.3±8.6	9.2±1.4 (0.93±0.02)	123±34.5	303.6±72.5 (0.8±0.08)
11	10.8±0.2	10.6±3.2	15.6±3.8 (0.92±0.01)	133.8±24.9	403.2±68.2 (0.82±0.03)
24	10.5±0.4	7.9±1.1	32.5±5.6 (0.93±0.01)	184.4±40.2	362.5±88.6 (0.78±0.09)
	7 J/cm², 40 P				
1	8.2±0.02	31.8±7.5	11.4±2.2 (0.93±0.02)	85.9±19.3	70.7±12.5 (0.78±0.07)
5	8.4±0.01	6.7±1.8	16.2±3.2 (0.92±0.01)	40.6±8.6	482.3±78.3 (0.85±0.04)
11	8.3±0.01	7.2±1.7	29.6±5.7 (0.92±0.02)	37.9±8.8	523±56.8 (0.83±0.03)
24	8.2±0.02	6.3±1.1	44.9±8.6 (0.91±0.02)	49.6±10.3	584.3±38.8 (0.81±0.04)

Appendix A continued.

	2 J/cm^2, 20 P				
1	6.5 ±0.01	959 ±96.5	2.2 ±0.2 (0.97 ±0.01)	1760 ±420	1 ±0.2 (0.91 ±0.02)
5	6.5 ±0.02	276.4 ±48	2.9 ±0.3 (0.95 ±0.01)	978 ±146	6.6 ±1.4 (0.72 ±0.08)
11	6.4 ±0.01	92 ±11.6	3.5 ±0.3 (0.95 ±0.01)	475 ±102	29.6 ±6.9 (0.8 ±0.04)
24	6.2 ±0.02	23.5 ±5.3	4.9 ±0.6 (0.93 ±0.01)	193.7 ±45.2	53 ±12.5 (0.75 ±0.07)

Appendix B

Average fitting values from the EIS spectra of as-received and laser-melted MMCs.

t (h)	R_s ($\Omega.cm^2$)	R_{ct} ($k\Omega.cm^2$)	Q_{dl} (10^{-6}) ($\Omega^{-1}.cm^{-2}.s^n$) (n_1)	R_w ($k\Omega.cm^2$)	Q_w (10^{-6}) ($\Omega^{-1}.cm^{-2}.s^n$) (n_1)
	As-received				
1	8.5±0.2	3.1±0.1	29.4±6.6 (0.86±0.03)	24.8±13	689±80 (0.83±0.04)
5	8.4±0.2	3.9±0.6	34.9±2.8 (0.87±0.02)	68.1±23.2	522±71 (0.83±0.02)
11	8.8±0.2	3.9±0.5	52.6±4.3 (0.87±0.01)	50.6±10.6	512±130 (0.82±0.01)
24	8.2±0.2	4.1±0.2	66.6±7.2 (0.87±0.01)	38.6±14.7	477±86 (0.8±0.02)
	7 J/cm^2, 10 P				
1	10.2±0.2	106±18.6	0.9±0.1 (0.94±0.01)	128.7±51.7	41.5±9.1 (0.8±0.06)
5	10.2±0.1	31.9±5.6	5.4±1.8 (0.95±0.01)	102.8±21.4	184±80 (0.75±0.05)
11	10.4±0.3	19.4±8.4	10.4±1.2 (0.94±0.01)	73.6±23.6	166±65 (0.69±0.1)
24	10±0.3	7.5±1.8	50.3±15.7 (0.93±0.01)	36.1±17.9	406±101 (0.71±0.05)
	7 J/cm^2, 25 P				
1	10.5±0.4	185±30.4	0.8±0.3 (0.93±0.02)	144.9±38.6	23.6±7.2 (0.79±0.04)
5	10.1±0.1	42.1±9.6	2±0.8 (0.94±0.01)	47.6±12.4	78.3±20.3 (0.8±0.1)
11	10±0.2	11.7±2.4	9.3±5.4 (0.94±0.02)	24.3±7.8	234±86 (0.88±0.07)
24	10.2±0.1	8.6±0.9	17.2±5.6 (0.93±0.01)	34±8.1	265±78 (0.75±0.08)
	7 J/cm^2, 40 P				
1	10.5±0.1	80.3±18	0.7±0.3 (0.93±0.01)	43.6±18.4	25.9±7.9 (0.9±0.08)
5	10.2±0.1	10.7±2.1	9.1±2.5 (0.94±0.02)	25.9±9.6	206±37 (0.83±0.04)
11	10±0.2	7.5±1.1	30±8.6 (0.94±0.01)	15.1±3.8	312±76 (0.83±0.09)
24	9.8±0.2	6.7±1.2	53.5±12.3 (0.93±0.01)	15.2±6.2	390±120 (0.82±0.08)